ANL-75-82

ANL-75-82

INL Technical Library
241315

CONTRIBUTION TO THE THEORY OF THE TWO-PHASE BLOWDOWN PHENOMENON

by

Michael N. Hutcherson

RETURN TO REFERENCE FILE
TECHNICAL PUBLICATIONS
DEPARTMENT

U of C-AUA-USERDA

ARGONNE NATIONAL LABORATORY, ARGONNE, ILLINOIS

Prepared for the U. S. NUCLEAR REGULATORY COMMISSION
under Contract W-31-109-Eng-38

The facilities of Argonne National Laboratory are owned by the United States Government. Under the terms of a contract (W-31-109-Eng-38) between the U. S. Energy Research and Development Administration, Argonne Universities Association and The University of Chicago, the University employs the staff and operates the Laboratory in accordance with policies and programs formulated, approved and reviewed by the Association.

MEMBERS OF ARGONNE UNIVERSITIES ASSOCIATION

The University of Arizona
Carnegie-Mellon University
Case Western Reserve University
The University of Chicago
University of Cincinnati
Illinois Institute of Technology
University of Illinois
Indiana University
Iowa State University
The University of Iowa
Kansas State University
The University of Kansas
Loyola University
Marquette University
Michigan State University
The University of Michigan
University of Minnesota
University of Missouri
Northwestern University
University of Notre Dame
The Ohio State University
Ohio University
The Pennsylvania State University
Purdue University
Saint Louis University
Southern Illinois University
The University of Texas at Austin
Washington University
Wayne State University
The University of Wisconsin

NOTICE

This report was prepared as an account of work sponsored by the United States Government. Neither the United States nor the United States Energy Research and Development Administration, nor any of their employees, nor any of their contractors, subcontractors, or their employees, makes any warranty, express or implied, or assumes any legal liability or responsibility for the accuracy, completeness or usefulness of any information, apparatus, product or process disclosed, or represents that its use would not infringe privately-owned rights. Mention of commercial products, their manufacturers, or their suppliers in this publication does not imply or connote approval or disapproval of the product by Argonne National Laboratory or the U. S. Energy Research and Development Administration.

Printed in the United States of America
Available from
National Technical Information Service
U. S. Department of Commerce
5285 Port Royal Road
Springfield, Virginia 22161
Price: Printed Copy $7.50; Microfiche $2.25

Distribution Category:
Water Reactor Safety Research
Systems Engineering (NRC-2)

ANL-75-82

ARGONNE NATIONAL LABORATORY
9700 South Cass Avenue
Argonne, Illinois 60439

CONTRIBUTION TO THE THEORY OF THE TWO-PHASE BLOWDOWN PHENOMENON

by

Michael N. Hutcherson*

Reactor Analysis and Safety Division

Based on a dissertation presented to the
Faculty of the Graduate School of
University of Missouri
in partial fulfillment of the
requirements for the degree
Doctor of Philosophy

December 1975

*Now at McDonnell Aircraft Corp., St. Louis, Missouri

TABLE OF CONTENTS

Page

NOMENCLATURE 16

ABSTRACT 17

I. INTRODUCTION 17

II. BACKGROUND 21

- A. Analytical Investigations 21
- B. Experimental Investigations 25

III. ANALYSIS 37

- A. General Considerations 37
- B. Critical Flow 39
  - 1. Single-phase Critical Flow 39
  - 2. Generalized Single- and Two-phase, One- and Two-component, Critical Flow 41
- C. Subcooled-blowdown Model 55
- D. Bubble-growth Blowdown Model 58
- E. Dispersed Blowdown Model 63

IV. EXPERIMENTAL APPARATUS 65

- A. Description of Experimental Apparatus 65
  - 1. Blowdown Vessel and Internal Geometry 65
  - 2. Rupture-disk Assembly 72
  - 3. Measurement of Fluid Weight 72
  - 4. Thrust Measurement 72
  - 5. Pressure Measurement 73
  - 6. Measurement of Void Fraction 73
  - 7. Temperature Measurement 73
  - 8. Electrical Heating System 76
  - 9. Data-acquisition System 76
- B. Operating Procedure 76

V. CALIBRATION TEST OF EXPERIMENTAL APPARATUS 78

VI. EXPERIMENTAL RESULTS FOR TWO-PHASE BLOWDOWN 91

TABLE OF CONTENTS

Page

VII. DISCUSSION OF RESULTS 97

A. The Role of Incipient Vaporization in the Decompression Process 97

B. Thermodynamics of the Vaporization Process 104

C. Effect of the Internal Vessel Geometry on the Blowdown 130

1. Detection of Internal Choking 130
2. External Choking 131
3. Internal Flow Regimes 132
4. Upstream Fluid Quality 134
5. Interpretation of the Internal Flow Regime 139

D. Comparison of Our Transient, Large-duct, Critical-flow Data with Steady-state, Small-duct, Critical-flow Data 141

E. Comparison of Other Transient, Large-duct, Critical-flow Data with the Steady-state, Small-duct, Critical-flow Data . . 145

F. Comparison of Predictions to the Steady-state, Small-duct, Critical-flow Data from Various Critical-flow Analytical Models 147

1. Comparison of the Homogeneous-equilibrium Model to the Steady-state, Small-duct Data 147
2. Comparison of the Homogeneous-frozen Model to the Steady-state, Small-duct Data 148
3. Comparison of the Henry-Fauske Model to the Steady-state, Small-duct Data 150
4. Comparison of the Moody Model to the Steady-state, Small-duct Data 151

G. Comparison of Various Predictions of the Critical-flow Analytical Model to Our Transient, Large-duct, Critical-flow Data 152

H. Comparison of Predictions of Various Critical-flow Analytical Models to Other Transient, Large-duct, Critical-flow Data 157

VIII. CONCLUSIONS AND RECOMMENDATIONS 160

A. Conclusions 160

B. Recommendations for Future Work 162

TABLE OF CONTENTS

Page

APPENDIXES

A. Data Reduction 163

B. Verification of Internal Vessel Pressures Being Stagnation Pressures 165

C. Experimental Data. 167

ACKNOWLEDGMENTS 180

REFERENCES 181

LIST OF FIGURES

No. Title Page

1. Schematic of Flow Path due to Break in PWR Cold Leg 18
2. Schematic Flow Path in a Two-loop System due to Break in PWR Cold Leg 19
3. Critical-flow Criterion 39
4. Schematic of Blowdown Vessel and Internals 66
5. Front View of Blowdown Apparatus 67
6. Side View of Blowdown Apparatus 67
7. Small-size Blowdown Vessel and Internals 68
8. Top View of Internal Geometry of Blowdown Vessel 69
9. Internal Geometry and Mounting of Blowdown Vessel 70
10. External Trace Heaters for Blowdown Vessel 71
11. Immersion Heaters for Blowdown Vessel 71
12. Pressure-tap Locations 74
13. Thermocouple Locations 75
14. System Configuration for the Calibration Run 78
15. Remaining Mass in the Calibration Run 79
16. Thrust Developed in the Calibration Run 79
17. Flow Rates in the Calibration Run 80
18. Internal Vessel Pressure in the Calibration Run 80
19. Span-reduction Method of the Remaining Mass in the Calibration Run 81
20. Span-reduction Method of the Thrust in the Calibration Run 81
21. Comparison of the Mass Flow Rates Determined from the Mass Decay Signal and Those from the Thrust and Upstream Pressure Signals in the Calibration Run 82
22. Comparison of the Measured Internal Vessel Pressures in the Calibration Run 83
23. Comparison of the Measured and Calculated Remaining Mass in the Calibration Run 85
24. Comparison of the Measured Internal Vessel Pressure and That Calculated from the Measured Mass Decay History, Considering Heat Transfer from the Entrained Liquid to the Expanding Gas in the Calibration Run 88

LIST OF FIGURES

No. Title Page

25. Comparison of the Mass Flow Rates Determined from the Experimental Measurements and the Calculated Mass Flow Rates in the Calibration Run. 88
26. Comparison of the Measured and Calculated Thrust in the Calibration Run. 89
27. Comparison of the Measured and Calculated Internal Vessel Pressure in the Calibration Run 89
28. Remaining Mass in Test 1 91
29. Remaining Mass in Test 2 91
30. Thrust in Test 1 92
31. Thrust in Test 2 92
32. Pressures Upstream of the Entrance to the Exhaust Duct in Test 1 92
33. Pressures Upstream of the Entrance to the Exhaust Duct in Test 2 92
34. Internal Vessel Pressures in Test 1 93
35. Internal Vessel Pressures in Test 2 93
36. Pressures Upstream and Downstream of the Area Expansion in the Annulus in Test 1 93
37. Pressures Upstream and Downstream of the Area Expansion in the Annulus in Test 2 93
38. Pressures Up the Downcomer Annulus in Test 1 94
39. Pressures Up the Downcomer Annulus in Test 2 94
40. Pressures on Opposite Sides of the Internal Skirt in Test 1 95
41. Pressures on Opposite Sides of the Internal Skirt in Test 2 95
42. Pressures Upstream and Near the Exit of the Exhaust Duct in Test 1 95
43. Pressures Upstream and Near the Exit of the Exhaust Duct in Test 2 95
44. Internal Vessel Temperatures in Test 1. 96
45. Internal Vessel Temperatures in Test 2. 96
46. Limits of Stability of a Surface Cavity 97
47. Equilibrium Concentration of Air in Water 99

LIST OF FIGURES

No. Title Page

48. Maximum Stable Cavity Radius during Heatup in Test 1 101
49. Maximum Stable Cavity Radius during Heatup in Test 2 101
50. Growth Characteristics of Vapor Bubble during the Inertially and Thermally Controlled Growth Periods 102
51. Unstable Thermal Growth of a Bubble Resulting from a Surface Cavity 103
52. Comparison of the Measured Pressures and the Saturation Pressures Corresponding to the Measured Temperatures in Test 1. . . 104
53. Comparison of the Measured Pressures and the Saturation Pressure Corresponding to the Measured Temperature in Test 2 104
54. Comparison of the Measured and Inferred Remaining Mass in Test 1 105
55. Comparison of the Measured and Inferred Remaining Mass in Test 2 105
56. An Indication of When Thermodynamic Equilibrium of the Remaining Fluid in the Internal-Skirt Region Was Reached in Test 1 . 107
57. An Indication of When Thermodynamic Equilibrium of the Remaining Fluid in the Internal-Skirt Region Was Reached in Test 2 . 108
58. Comparison of the Subcooled Blowdown Model to the Data of BNWL Run 25 109
59. Comparison of the Subcooled Blowdown Model to the Data of BNWL Run 52 110
60. Comparison of the Subcooled Blowdown Model to the Data of Battelle-Frankfurt Run 13 110
61. Predicted Internal Vessel Pressure Histories for Various Initial Liquid Superheats for the Maximum Number of Nucleation Sites per Unit Surface Area by the Bubble-growth Blowdown Model . . . 111
62. Comparison of the Predicted Internal Vessel Pressure Histories for Various Numbers of Nucleation Sites per Unit Surface Area for a Constant Initial Liquid Superheat by the Bubble-growth Blowdown Model 112
63. Comparison of the Predicted Internal Vessel Pressure Histories by the Bubble-growth Blowdown Model for Various Numbers of Nucleation Sites per Unit Surface Area as Compared to the Measured Internal Vessel Pressure History in Test 1 113

LIST OF FIGURES

No. Title Page

64. Comparison of the Predicted Internal Vessel Pressure Histories by the Bubble-growth Blowdown Model for Various Numbers of Nucleation Sites per Unit Surface Area as Compared to the Measured Internal Vessel Pressure History in Test 2 113

65. Comparison of the Inferred Vapor Volume in the Vessel in Test 1 and that Calculated by the Bubble-growth Blowdown Model 114

66. Comparison of the Inferred Vapor Volume in the Vessel in Test 2 and that Calculated by the Bubble-growth Blowdown Model 114

67. Comparison of the Measured and Calculated Internal Vessel Pressure by the Bubble-growth Blowdown Model in Test 1 115

68. Comparison of the Measured and Calculated Internal Vessel Pressure by the Bubble-growth Blowdown Model in Test 2 115

69. Comparison of the Measured and Predicted Pressure Histories by the Bubble-growth Blowdown Model in BNWL Run 20 116

70. Comparison of the Measured and Predicted Pressure Histories by the Bubble-growth Blowdown Model in BNWL Run 25 117

71. Comparison of the Measured and Predicted Pressure Histories by the Bubble-growth Blowdown Model in BNWL Run 52 117

72. Comparison of the Measured and Predicted Pressure Histories by the Bubble-growth Blowdown Model in the Battelle-Frankfurt Run 13 118

73. Comparison of the Measured and Predicted Pressure Histories by the Bubble-growth Blowdown Model in Ungerer's Experiment . 118

74. Prediction of the Pressure History during the Initial Stage of Decompression for the Proposed Bubble-growth Blowdown Model. 119

75. Prediction of the Void Fraction during the Initial Stage of Decompression for the Proposed Bubble-growth Blowdown Model . . 120

76. Predictions of the Internal Vessel Pressure and Void-fraction Histories during the Initial Stage of Decompression of a PWR Vessel from the Bubble-growth Blowdown Model 121

77. Comparison of the Dispersed-regime Blowdown Model to the Data of BNWL Run 20 122

78. Comparison of the Dispersed-regime Blowdown Model to the Data of BNWL Run 25 123

79. Comparison of the Dispersed-regime Blowdown Model to the Data of BNWL Run 52 123

LIST OF FIGURES

No. Title Page

80. Comparison of the Dispersed-regime Blowdown Model to the Data of Battelle-Frankfurt Run 13 124

81. Comparison of the Subcooled, Bubble-growth, and Dispersed Blowdown Models to the Measured Pressure in the Battelle-Frankfurt Run 13 124

82. Cross Section of the Blowdown Vessel Illustrating the Proposed Flow Regimes inside the Vessel during the Various Stages of Decompression in These Tests 125

83. Temperature of the Vessel Structure after Blowdown in Test 1 . . . 127

84. Temperature of the Vessel Structure after Blowdown in Test 2 . . 127

85. Pressures Upstream and Downstream of the Area Expansion in Test 1 130

86. Pressures Upstream and Downstream of the Area Expansion in Test 2 130

87. Pressures Up the Downcomer Annulus in Test 1 131

88. Pressures Up the Downcomer Annulus in Test 2 131

89. Comparison between the Pressure Upstream of the Exhaust Duct and the Average Internal Skirt Pressure in Test 2 132

90. Choking at the Exhaust Plane in Test 2 132

91. Comparison of Predictions of the Homogeneous-equilibrium and Homogeneous-frozen Critical-flow Models for the Remaining Mass for the Internal Vessel Quality Being the Isentropic Quality Corresponding to the Measured Pressure in Test 1 133

92. Comparison of Predictions of the Homogeneous-equilibrium and Homogeneous-frozen Critical-flow Models for the Remaining Mass for the Internal Vessel Quality Being the Isentropic Quality Corresponding to the Measured Pressure in Test 2 133

93. Comparison of the Inferred Fluid Quality and the Inlet Isentropic and Isenthalpic Qualities at the Inlet Based on the Measured Pressure in Test 1 134

94. Comparison of the Inferred Fluid Quality and the Inlet Isentropic and Isenthalpic Qualities at the Inlet Based on the Measured Pressure in Test 2 134

95. Normalized Blowdown Characteristics in Test 1 139

96. Normalized Blowdown Characteristics in Test 2 139

LIST OF FIGURES

No.	Title	Page
97.	Comparison of the Transient, Large-duct, Critical-flow Rates in Test 1 and the Corresponding Steady-state, Small-duct, Critical-flow Rates in Refs. 15 and 16	141
98.	Comparison of the Transient, Large-duct, Critical-flow Rates in Test 2 and the Corresponding Steady-state, Small-duct, Critical-flow Rates in Refs. 15 and 16	142
99.	Comparison of the Transient, Large-duct, Critical-exit-pressure Ratio in Test 1 and the Corresponding Steady-state, Small-duct, Critical-throat-pressure Ratio of Refs. 15 and 16	142
100.	Comparison of the Transient, Large-duct, Critical-exit-pressure Ratio in Test 2 and the Corresponding Steady-state, Small-duct, Critical-throat-pressure Ratio of Refs. 15, 16, and 18	143
101.	Axial Pressure Distribution at Critical Flow near the Exit of a Constant-area Duct Having a Gradual and Rapid Divergence Downstream of the Exit	143
102.	Radial Pressure Distribution near the Exit of a Constant-area Duct at Critical Flow	144
103.	Comparison of Ungerer's Transient, Large-duct, Critical-flow Rates for $A_e/A_{bv} = 0.025$ and the Corresponding Steady-state, Small-duct, Critical-flow Rates in Refs. 15 and 16	145
104.	Comparison of Ungerer's Transient, Large-duct, Critical-flow Rates for $A_e/A_{bv} = 0.013$ and the Corresponding Steady-state, Small-duct, Critical-flow Rates in Refs. 15 and 16	145
105.	Comparison of the Transient, Large-duct, Critical-flow Rates in the CSE Test 7 and the Corresponding Steady-state, Small-duct, Critical-flow Rates in Refs. 15 and 16	146
106.	Comparison of the Transient, Large-duct, Critical-flow Rates in the CSE Test 11 and the Corresponding Steady-state, Small-duct, Critical-flow Rates in Refs. 15 and 16	146
107.	Comparison of the Homogeneous-equilibrium Critical-flow Model to the Steam-Water Critical-flow-rate Data of Refs. 15 and 16	147
108.	Comparison of the Homogeneous-equilibrium Critical-flow Model to the Steam-Water Critical-pressure-ratio Data of Refs. 15, 16, and 18	148
109.	Comparison of the Homogeneous-frozen Critical-flow Model to the Steam-Water Critical-flow-rate Data of Refs. 15 and 16	149

LIST OF FIGURES

No.	Title	Page
110.	Comparison of the Homogeneous-frozen Critical-flow Model to the Steam-Water Critical-pressure-ratio Data of Refs. 15, 16, and 18	149
111.	Comparison of the Henry-Fauske Critical-flow Model to the Steam-Water Critical-flow-rate Data of Refs. 15 and 16	150
112.	Comparison of the Henry-Fauske Critical-flow Model to the Steam-Water Critical-pressure-ratio Data of Refs. 15, 16, and 18	151
113.	Comparison of the Moody Critical-flow Model to the Steam-Water Critical-flow-rate Data of Refs. 15 and 16	151
114.	Comparison of the Moody Critical-flow Model to the Steam-Water Critical-pressure-ratio Data of Refs. 15, 16, and 18	152
115.	Pressures Upstream of the Exhaust Duct in Test 1	153
116.	Pressure Upstream of the Exhaust Duct in Test 2	153
117.	Comparison of the Measured and Predicted Critical Flow Rates in Test 1	154
118.	Comparison of the Measured and Predicted Critical Flow Rates in Test 2	154
119.	Comparison of the Measured and Predicted Critical Pressure Ratios in Test 1	155
120.	Comparison of the Measured and Predicted Critical Pressure Ratios in Test 2	155
121.	Comparison of the Measured and Predicted Remaining Mass in Test 1	155
122.	Comparison of the Measured and Predicted Remaining Mass in Test 2	155
123.	Comparison of the Measured and Predicted Thrust in Test 1	156
124.	Comparison of the Measured and Predicted Thrust in Test 2	156
125.	Comparison of the Critical-flow-model Predictions to Ungerer's Transient, Large-duct, Critical-flow-rate Data for A_e/A_{bv} = 0.025	157
126.	Comparison of the Critical-flow-model Predictions to Ungerer's Transient, Large-duct, Critical-flow-rate Data for A_e/A_{bv} = 0.013	158

LIST OF FIGURES

No.	Title	Page
127.	Comparison of the Critical-flow-model Predictions to the Measured, Transient, Large-duct, Critical Flow Rates in the CSE Test 7	159
128.	Comparison of the Critical-flow-model Predictions to the Measured, Transient, Large-duct, Critical Flow Rates in the CSE Test 11	159
A.1.	The Span-reduction Method of the Remaining Mass in Test 1.	163
A.2.	The Span-reduction Method of the Remaining Mass in Test 2.	163
A.3.	The Span-reduction Method of the Thrust in Test 1	164
A.4.	The Span-reduction Method of the Thrust in Test 2	164
B.1.	Schematic of the Exhaust Geometry	165
C.1.	Remaining-mass Signal in the Calibration Test.	167
C.2.	Remaining-mass Signal in Test 1	167
C.3.	Remaining-mass Signal in Test 2	168
C.4.	Overall Thrust Signal in the Calibration Test	168
C.5.	Thrust Signal at the Initiation of the Calibration Test.	169
C.6.	Overall Thrust Signal in Test 1	169
C.7.	Thrust Signal at the Initiation of Test 1	169
C.8.	Overall Thrust Signal in Test 2	170
C.9.	Thrust Signal at the Initiation of Test 2	170
C.10.	Overall P_1 Signal in the Calibration Test	171
C.11.	P_1 Signal at the Initiation of the Calibration Test.	171
C.12.	Overall P_2 Signal in Test 1	171
C.13.	P_2 Signal at the Initiation of Test 1	172
C.14.	Overall P_3 Signal in Test 1	172
C.15.	P_3 Signal at the Initiation of Test 1	173
C.16.	Overall P_1 Signal in Test 2	173
C.17.	P_1 Signal at the Initiation of Test 2	174
C.18.	Overall P_8 Signal in the Calibration Test	174
C.19.	P_8 Signal at the Initiation of the Calibration Test.	175
C.20.	Overall P_8 Signal in Test 1	175

LIST OF FIGURES

No.	Title	Page
C.21.	P_8 Signal at the Initiation of Test 1	175
C.22.	Overall P_8 Signal in Test 2	176
C.23.	P_8 Signal at the Initiation of Test 2	176
C.24.	Overall P_{14} Signal in the Calibration Test	177
C.25.	Overall P_{14} Signal in Test 1	177
C.26.	P_{14} Signal at the Initiation of Test 1	177
C.27.	Overall P_{14} Signal in Test 2	178
C.28.	P_{14} Signal at the Initiation of Test 2	178
C.29.	Overall T_8 Signal in Test 1	179
C.30.	Overall T_7 Signal in Test 2	179

LIST OF TABLES

No.	Title	Page
I.	Summary of Literature on Two-phase Blowdown	21
II.	Comparison of Energy Remaining in Vessel with Upstream Fluid Quality in Test 1	135
III.	Comparison of Energy Remaining in Vessel with Upstream Fluid Quality in Test 2	135
IV.	Comparison of Inferred Upstream Fluid Quality with Velocity Ratio in Test 1	137
V.	Comparison of Inferred Upstream Fluid Quality with Velocity Ratio in Test 2	138

NOMENCLATURE ➡

NOMENCLATURE

[illegible]	[illegible]; acceleration
[illegible]	[illegible] area
C	Solute concentration in Henry's Law
c	Specific heat capacity
C_d	Discharge coefficient
D	Diameter
D_h	Hydraulic diameter
E	Elasticity; energy
f	General function
F	Thrust
F_r	Friction force
g	Gravitational acceleration
G	Mass flow rate per unit area
h	Specific enthalpy; heat-transfer coefficient
i	Specific internal energy
k	Velocity or slip ratio; thermal conductivity
K	Inverse of Henry's Law constant
L	Length
m	Mass
M	Momentum
$\dot{m}$	Mass flow rate
N	Nonequilibrium parameter in the Henry-Fauske[1] Model
n	Exponent in the surface tension relation; polytropic exponent
P	Static pressure
q	Thermal energy per unit mass
$\dot{Q}$	Heat-transfer rate
r	Radius
R	Radius; gas constant in Eq. 18
s	Specific entropy
S	Surface area
t	Time
T	Temperature
u	Linear speed
v	Specific volume
V	Volume
$\dot{W}$	Time rate of change of work, or power
x	Flowing fluid quality
z	Axial length
Z	Vertical height
α	Void fraction
α_ℓ	Thermal diffusivity of liquid
α_w	Thermal diffusivity of vessel wall material
β	Factor in Henry-Fauske[1] critical flow model
γ	Isentropic exponent for vapor
Δ	Finite change or difference
δ	Wall thickness
ϵ	Strain
ζ	Axial direction
η	Ratio of exit pressure to inlet stagnation pressure
θ	Inclination angle from horizontal position
ρ	Fluid density
σ	Normal stress; surface tension
$\underline{\tau}$	Present time step
$\underline{\tau}'$	Present time step in the growth of a bubble generation from a solid surface
τ	Time step; time; shear stress of a fluid at a solid boundary
τ'	Time step during the growth of a bubble generation from a solid surface
∞	Free stream

Subscripts

a	Ambient or atmospheric; surface-cavity activation
b	Bubble
BV	Blowdown vessel, also bv
c	Critical or extreme value; thermodynamic critical-point value
d	Surface-cavity deactivation
e	Exit plane, or exhaust
E	Equilibrium
ED	Exhaust duct
EM	Empty of original fluid mass in discharge duct
ext	External
g	Gas; bubble generation
G	Given flow rate per unit area; current bubble generation at a given time step
HE	Homogeneous Equilibrium
HF	Homogeneous Frozen
h	Hydraulic; isenthalpic
i	Inlet or inflow, internal; given sector or volume of a system
IS	Internal skirt
j	Nozzle inlet location
ℓ	Subcooled liquid
L	Saturated liquid
LT	Long tube
meas	Measured
M	Momentum
o	Stagnation, initial, or reference condition
P	Produced
p	Constant pressure
s	Isentropic
sat	Saturation
t	Throat
T	Total
v	Constant volume
ves	Vessel material
V	Saturated vapor
VL	Difference between saturated vapor and saturated liquid thermodynamic property
w	Wall or solid surface

CONTRIBUTION TO THE THEORY OF THE TWO-PHASE BLOWDOWN PHENOMENON

by

Michael N. Hutcherson

ABSTRACT

Isothermal blowdown experiments have been conducted in a 5.40-ft^3 pressure vessel with an internal configuration similar to the downcomer annulus typical of current pressurized-water-reactor designs. The working fluid was water, and the decompressions were initiated from a high-pressure, stagnant, saturated-liquid state by breaking a rupture disk in the exhaust duct. In addition to a calibration run conducted with room-temperature water, two-phase transients were recorded and analyzed with initial pressures of 300 and 400 psia.

The experimental results show that choking occurred only at the exit of the exhaust duct and that no appreciable compressible effects were experienced within the vessel during the transient. The vaporization process within the vessel appears to be a strong function of the surface-to-volume ratio for the coolant, and the principal vapor-production process early in the transient is one of thermally dominated vapor bubbles growing in a liquid matrix. A comparison of the experimental results for the transient, large-duct, critical flow rates from this investigation reveals an excellent comparison with data of other steady-state, small-duct, critical flow studies available in the literature.

Simplistic, analytical models have been developed to predict the vessel characteristics during a blowdown transient. The analysis is based on thermally dominated bubble growth early in the transient with the transition to the dispersed liquid phase in a vapor matrix, with a subsequent relaxation to equilibrium, at a void fraction of ~0.40.

I. INTRODUCTION

This study is concerned with the two-phase decompression and associated two-phase critical-flow phenomena that occur as the result of a break in a high-pressure, high-temperature system. Critical flow governs the rate at which fluid will be discharged from a system during most of a depressurization and thus largely controls the time of blowdown. The two-phase critical-flow phenomenon has been extensively investigated[1-33] because of its relevance to nuclear-reactor safety, fossil-fired boiler operation, turbine operation, the operation of refrigeration systems, and the flow of cryogenic fluids.

This study considers the effect of internal vessel geometry on the inlet conditions to the exhaust duct during the critical-flow period of blowdown. This case is considered because of its relevance to the decompression process in a pressurized-water, nuclear-reactor (PWR) system.

Nuclear-reactor safety has provided a large impetus for understanding the two-phase blowdown phenomenon in more detail. The case of a break in the primary circulating coolant loop of a reactor system has generated much analytical and experimental simulation on both the large and small scale. It is generally considered that the break in a light-water nuclear-reactor system occurs in an inlet duct of the primary coolant loop to the reactor vessel. Figures 1 and 2 illustrate the general configuration of a PWR system and the location of a postulated break in an inlet duct to the reactor vessel.

The break is considered to occur in the inlet duct of the primary loop to the reactor vessel for two principal reasons. First, because the inlet fluid to the reactor vessel is at a lower temperature than the outlet fluid, it will start to flash at a lower pressure, and it will be less compressible during the early period of the decompression. Thus, the exhaust flow rate early in the blowdown from a break in the inlet line would be greater than that from the outlet line. Second, for a break in the inlet line, the flow in the reactor vessel,

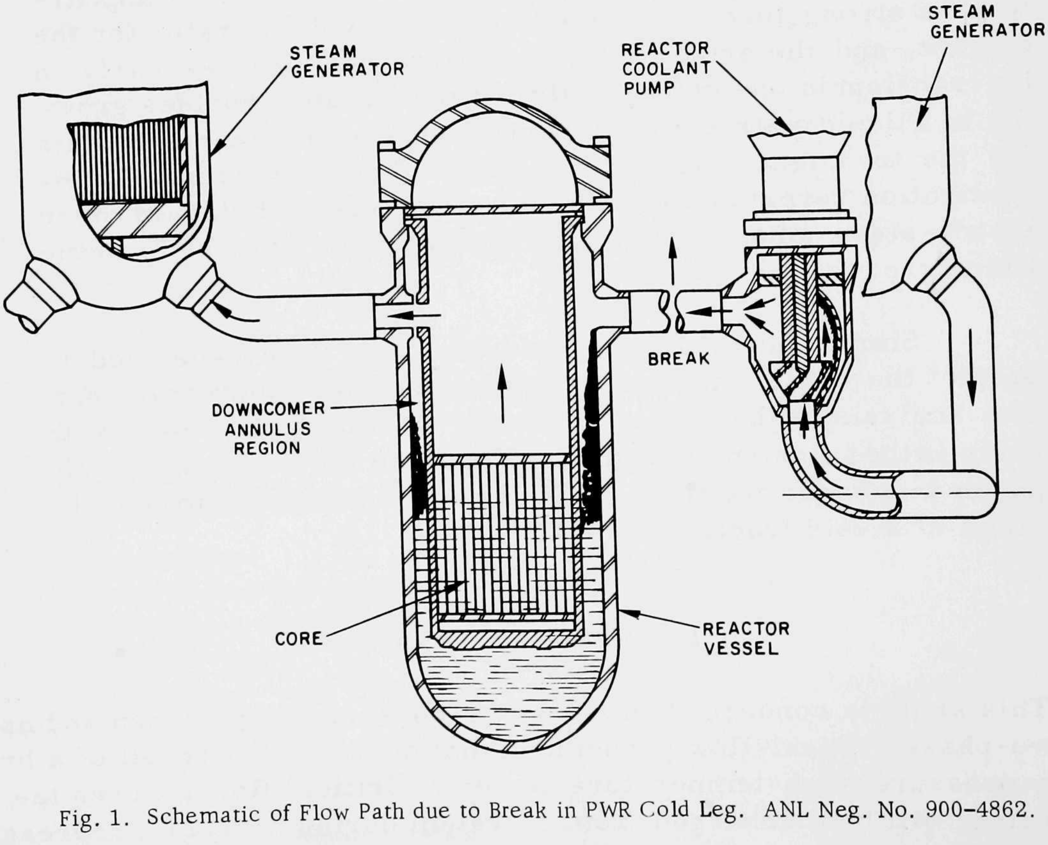

Fig. 1. Schematic of Flow Path due to Break in PWR Cold Leg. ANL Neg. No. 900-4862.

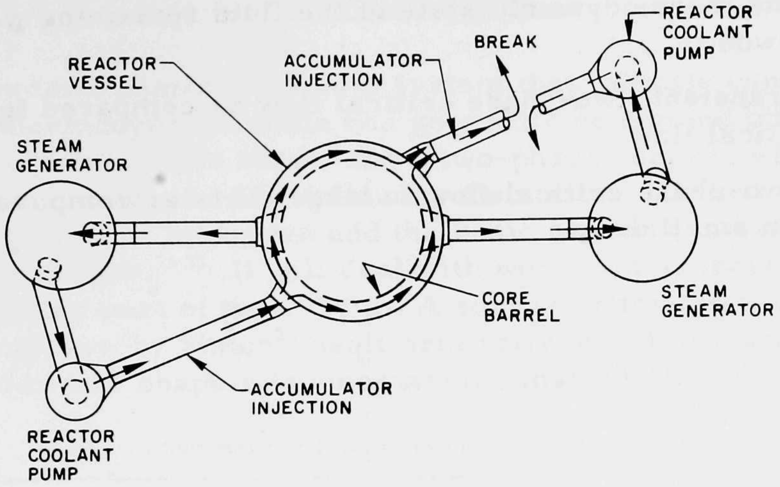

Fig. 2. Schematic Flow Path in a Two-loop System due to Break in PWR Cold Leg. ANL Neg. No. 900-4860 Rev. 1.

and particularly in the core, has to reverse flow direction to exhaust from the inlet. This period of fluid deceleration, stagnation, and reversal determines when critical heat flux (CHF) is reached locally. After CHF has been reached, the fuel-cladding temperature will increase. These are the two primary reasons for considering the inlet break as compared to the outlet break in a Loss of Coolant Accident (LOCA).

The variables of interest during two-phase blowdown are the characteristics of the transient coolant-discharge phenomenon, which determine the flow rate from the system and the pressure history within the system. From a reactor safety and licensing viewpoint, questions are continually being posed regarding (1) the applicability of the available two-phase critical-flow models and experimental data to the postulated accident, (2) the possibility and magnitude of nonequilibrium thermodynamic states during blowdown, and (3) the possibility of secondary choking locations within the system. Thus, to assess the effects of a decompression transient upon a given system, a detailed knowledge of the fluid behavior within the system during the blowdown is required.

This investigation was undertaken to examine transient, two-phase critical flow from a small pressure vessel containing internal geometry for a double-ended, guillotine break in a relatively large duct.

The objectives of this investigation were to determine the following:

1. The effect of internal vessel geometry on the decompression transient. In other words, does choking occur within the system? What magnitude of pressure difference exists between the various sectors of the system during the blowdown? Is the pressure immediately upstream of the inlet to the break significantly different from the pressure inside the internal region of the vessel? Is there a nonuniform flow distribution produced anywhere within the vessel during the depressurization?

2. The thermodynamic state of the fluid remaining within the vessel during the blowdown.

3. Transient, two-phase critical flow as compared to steady-state, two-phase critical flow.

4. Two-phase critical flow in large ducts as compared to two-phase critical flow in small ducts.

II. BACKGROUND

The blowdown phenomenon in a system that initially contains a liquid at an elevated thermodynamic state can generally be divided into a subcooled liquid regime, which is quite short, and a two-phase regime, which comprises most of the decompression. The following discussion will primarily address the two-phase regime of blowdown and the basic phenomena associated with it, such as critical flow.[1-33] It will deal with work that appeared in the literature since the latter part of the 1950's. A survey article on two-phase blowdown and critical flow by Simon[34] dealt primarily with European work. The literature cited in this chapter is summarized in Table I.

TABLE I. Summary of Literature on Two-phase Blowdown

Year	Analytical	Experimental
1955		LOFT and Semiscale[52-61]
1959	Harris[35]	Etheimer[66]
1960		Humboldt Bay[62]
1962	Nahavandi[38]	Bodega Bay[63]
1966	Margolis and Redfield[39] Moody[41]	Chen and Isbin[6] Fugie et al.[64] Tagami[65] Ungerer[67]
1968	Moore and Rettig[40] Goulding[42]	
1969	Moody[43] Nahavandi[44]	Carzaniga[68]
1970	Wilburn[45]	White[69] Allemann et al.[70] Gallagher[71]
1971	Hoppner[50]	Hoppner[50] Battelle Institut[72-78] Allemann et al.[79] Simon[34]
1972		Rudiger[80] Shimamune et al.[81] Tokumitsu[82]
1973		Bettis FLASK Experiment[83] Choi[84]
1975		Banerjee et al.[51] Leung[85]

A. Analytical Investigations

Harris[35] performed blowdown analyses dealing primarily with a vessel of initially stagnant, saturated liquid, and the Benjamin-Miller[36] and Allen[37] relations were used to describe the break flow rate. Thermodynamic equilibrium of the remaining fluid inside the vessel was assumed to exist during the decompression. To my knowledge, this was the first recognition of the effect of the break flow area on phase separation within the vessel. Separated and uniform flow-regime blowdowns were analyzed, and it was concluded that these calculations would bracket the actual blowdown event. It was further concluded that, for the more probable small breaks, the separated flow analysis would likely be the most valid.

Nahavandi[38] formulated a 25-finite-element, lumped-parameter computer code to calculate the response of a four-loop, PWR system to a double-ended, guillotine break in one of the primary flow loops. The remaining fluid within the vessel was assumed to always be uniformly dispersed. The code did not account for the relative motion between the vapor and liquid phases, nor did it include a neutron-kinetics analysis of the accident. The analysis assumed a one-dimensional, quasi-steady-state condition during the transient, no heat transfer to or from the coolant envelope, and no heat exchange to the coolant when passing through the pumps.

Margolis and Redfield[39] formulated the first version of the FLASH computer code to simulate the subcooled liquid and two-phase regimes of a blowdown transient. Moore and Rettig[40] developed a similar computer code, RELAP. In both codes, the continuity, momentum, and energy equations were formulated in integral form for prescribed control volumes which made up the entire system. The two-phase critical-flow formulation presently employed in both the FLASH and RELAP codes is the Moody[2] model.

Moody[41] proposed a model for calculating the response of a system to a depressurization from an initially stagnant, elevated pressure-temperature fluid condition. In formulating the two-phase blowdown model, he considered a straight exhaust duct with constant flow area, adiabatic walls, and liquid friction at the walls of the duct. He also assumed that the liquid and vapor phases were in thermodynamic equilibrium at all flow sections in the duct, and that there was no slip between the liquid and vapor phases remaining within the blowdown vessel. The blowdown analysis considered an adiabatic, constant-volume reservoir containing a uniformly distributed, liquid-vapor mixture in thermodynamic equilibrium. By simultaneously solving the continuity and energy equations, he determined a relation for the pressure history inside the vessel. This was used to determine the system response to saturated liquid, saturated vapor, and uniformly distributed two-phase-mixture blowdowns. The model produced the best results when pipe friction dominated. It was suggested that if geometric flow resistances were predominant, an equivalent length of pipe based on incompressible-flow considerations should be used to produce an equivalent flow resistance in order to predict the blowdown rate. The calculated flow rates underpredicted low-quality flows and overpredicted high-quality flows.

Goulding[42] analyzed the decompression phenomenon from an initially high-energy, subcooled liquid state, down through the subcooled decompression regime, and on to the two-phase blowdown regime. Various pertinent physical observations were made concerning the transition into the two-phase decompression regime. The method of characteristics was used to solve the three quasi-linear, hyperbolic differential equations that described the system response. The analysis assumed one-dimensional thermodynamic equilibrium, isentropic, nonsteady flow (which inherently accounted for the fluid inertia), and acoustic effects at the initiation of the transient. The effects of transient fluid friction were considered to be essentially the same as steady-state friction evaluated at the same Reynolds number. During the two-phase portion of the transient, two-phase friction was accounted for based on all-liquid, single-phase flow modified with the Lockhart-Martinelli relation. The effects of heat exchange between the fluid and the fluid envelope were disregarded, and the two-phase fluid was assumed to be homogeneously mixed at all times and locations. The analysis also included the effect of flow-area changes. The analysis was applied to some of the initial semiscale experiments, and the comparison of measured and calculated results was reasonably good for the initially high-pressure, subcooled liquid period of the decompression for which the analysis was applicable. The decompression times of the sited experimental runs were similar to those of the present study, about 3 sec. Of the 3-sec blowdown time, the subcooled decompression period lasted for about the first 10 msec, and then the two-phase choked and unchoked regimes took up the balance of the blowdown time. The analysis was unable to predict the upstream pressure undershoot below the bulk saturation pressure seen in the experimental results because of the thermodynamic-equilibrium assumption used in formulating the model. However, the analysis was able to predict the increase in the exhaust-duct exit pressure during the transition period into the two-phase regime.

Moody[43] proposed a model to calculate the liquid-vapor action in a pressure vessel during an adiabatic blowdown. The parameters of primary interest were the history of the two-phase-mixture level and the local fluid properties in the vessel. The assumptions used in the model were (1) thermodynamic equilibrium, (2) uniform pressure distribution throughout the vessel at any given time, (3) uniform distribution of the net rate of vapor formation in the liquid phase, except at points of local heating, (4) uniform time-dependent mixture properties at a given elevation, and (5) constant average bubble-rise speed relative to the liquid. Moody concluded that calculated results fit the data best when the analysis used a bubble-rise speed of 0.5-1.0 ft/sec. When the bubble-rise speed was 1.0 ft/sec, the mixture level reached its maximum height in 20-25 sec. Since the initial liquid level in the vessel for the data being compared to was about 20 ft, it was reasoned that the mixture apparently swelled until the quality or void fraction was sufficiently high to permit a vapor-separation rate from the surface that was essentially equal to the vapor-blowdown rate from the vessel for the case of a top blowdown. Moody also concluded that if the vapor-blowdown rate exceeded the vapor separation rate from the surface, the mixture level would rise.

Nahavandi[44] extended his previous analysis[38] of a LOCA by considering the various flow regimes that may exist in the various components of the reactor system; the neutronics aspects of such an accident were also included.

He concluded that the present critical-flow models were developed and verified under steady-state flow conditions and, therefore, are not applicable in a transient analysis.

One objective of the present study was to determine if transient, two-phase critical flow is any different from steady-state, two-phase critical flow. Two semiscale experimental runs with different initial stagnation pressures and different exhaust flow areas were analyzed. The comparison of the pressures and temperatures was reasonably good. An attempt was made to account for the nonequilibrium nature of the fluid furing the initiation of the transient when the pressure undershoots the bulk saturation pressure. Metastability correction terms were derived from the experimental results, and these brought the numerical and experimental results into better agreement.

Wilburn[45] performed an analytical investigation into the liquid-vapor action inside a vessel during blowdown. The phenomenon was assumed to be one-dimensional in nature. The complicated problem of bubble formation was idealized by assuming all the bubbles were formed uniformly throughout the vessel in such a manner that they instantaneously attained a terminal rise speed. The investigation centered on the questions of the position of the interface between the high- and low-density fluids, and the vertical void-fraction profile. The numerical simulation employed two empirical parameters: the discharge coefficient and the bubble-rise speed. The discharge coefficient was determined through iteration by best fitting the calculated stagnation-pressure history to the measured stagnation-pressure history. The bubble-rise speed used was a best guess, and the resulting liquid-vapor model was then incorporated into the BURP computer code. The calculated results for the system pressure history were slightly higher than those calculated by Moody for a bottom blowdown,[43] and they were essentially equal to the calculated results from FLASH-2 for a middle blowdown.[46] They corresponded well with the Containment System Experiment (CSE)[47-49] data for a top blowdown. The BURP-calculated results for the foam level essentially corresponded with Moody's[43] calculated results in magnitude, but varied in instantaneous slope for a bottom blowdown. They corresponded closely with the FLASH-2 predictions[46] for a middle blowdown; they also agreed reasonably well with the CSE[47-49] data for a middle blowdown. They were slightly below the FLASH-2 predictions[46] for a top blowdown, and demonstrated good agreement with the CSE[47-49] data for a top blowdown. The predictions of the flow rate from the break by the BURP and FLASH-2 codes were within 10% for a middle blowdown. The predictions of the two codes for the mass of the remaining fluid in the vessel for a middle blowdown also agreed within 10%. Moody concluded that the assumption of a linear void-fraction profile in the remaining fluid was not valid for all types of blowdowns. The assumption of a linear or constant void-fraction profile in the remaining fluid led to a satisfactory prediction of the foam level by the lumped-parameter codes for a middle and bottom blowdown, but similar agreement was not seen for a top blowdown.

Hoppner[50] analyzed the various decompression regimes that exist during a blowdown transient. The numerical simulation technique formulated the continuity and energy equations for finite elements of the system using lumped parameters to characterize each control volume. The simulation, a computer code named DYLOC, calculated the spatial and transient thermodynamic states and flows in each control volume of the system. When the calculated results for the temperature response were compared to the measured values, the best comparison was effected for a simulation using four elements and a discharge coefficient in the Moody[2] critical-flow model of 0.625. This comparison was only good for about the first one-third of the time after the temperature had dropped from its initial, nearly constant value.

Banerjee et al.[51] used the Canadian-developed computer code RODFLOW to predict the thermal-hydraulic response of their experimental system during a decompression transient. In this code, the continuity, momentum, and energy equations are formulated in finite-difference form, and the flow is considered to be one-dimensional. The program considers transient flow boiling with the liquid and vapor phases in thermal equilibrium. The local void fraction is determined by considering slip between the liquid and vapor phases, and the modified Martinelli-Nelson two-phase friction model is used. The homogeneous-equilibrium and Henry-Fauske[1] two-phase critical flow models were used to calculate the critical flow rate from the system. The code prediction of the measured pressure history was reasonably good, but it failed to calculate the observed undershoot of the system pressure below the saturation pressure because of the assumption of thermodynamic equilibrium. The drop in the system pressure below the saturation pressure was attributed to a delay in bubble nucleation. Because of the assumption of thermodynamic equilibrium, the predicted void fraction was also greater than the measured value. The measured and calculated remaining mass within the system compared reasonably well, and the prediction of when critical heat flux occurred was fairly good. The measured pressure and remaining mass were best predicted when the homogeneous-equilibrium model rather than the Henry-Fauske critical-flow model was used. The predicted pressure and remaining mass were essentially independent of whether the two-phase friction was determined from the modified Martinelli-Nelson or homogeneous models.

B. Experimental Investigations

Starting about 1955, the National Reactor Testing Station (NRTS in Idaho (now the Idaho National Engineering Laboratory) began large-scale experimental simulations of the LOCA. The first experimental program that considered the LOCA in particular was the Safety Test Engineering Program (STEP). The ultimate plan in the LOCA experimental series is to perform such a test in a small-scale, PWR system (LOFT).

To gain preliminary understanding of the fluid dynamics, thermodynamics, and heat transfer of such a decompression, the semiscale experimental series was initiated. The purpose of this experiment is to simulate the LOFT system geometry without the actual fuel and then to study the system response during a LOCA. A more detailed explanation of the problem and program definition and some of the experimental and numerical results is given in Refs. 52-61.

To my knowledge, the first systematically executed blowdown experimental program was that performed on a full-scale, 1/48 segment of the Pacific Gas and Electric, Humboldt Bay[62] pressure-suppression containment vessel in 1960. The blowdown system was a vessel containing initially stagnant, saturated water at 1250 psia. The transients were initiated by failing one of the rupture disks of a two-disk system on the end of the $5\frac{3}{4}$-in.-dia exhaust duct. The decompressions were from a bottom location in the blowdown vessel, and the vessel had no internal structure in it. Various orifices were used to produce different rates of flow decay, but the instantaneous flow rate from the system was not measured.

In 1962, blowdown tests were performed on a full-scale, 1/112 segment of the Bodega Bay[63] nuclear power plant. These tests were similar to the Humboldt Bay runs. The blowdown vessel and exhaust duct were figured in a similar manner, except that the exhaust duct was a $12\frac{1}{8}$-in.-dia pipe. The tests were also initiated in a manner similar to that in the previous experiment. The system consisted of a blowdown vessel containing an initially stagnant fluid. Both saturated and slightly subcooled liquid initial stagnation conditions were generated before the decompressions were initiated, and the initial stagnation pressure in all the runs was 1250 psia. Both nozzles and orifices were used to produce the desired flow-decay rates; however, the instantaneous flow rate was not measured.

Chen and Isbin[6] conducted two-phase critical-flow tests in a vessel and manner similar to the present study. The hardware used was a pressure vessel which was 16 in. in inside diameter and 5 ft^3 in volume. The maximum operating condition of the facility was about 215-psia saturated water, and both steady-state and transient runs were performed. The vessel and associated hardware were suspended from a weight transducer, and the thrust was monitored with another load cell. Various pressures and temperatures were also recorded. Single-phase all-liquid calibration runs were performed to check the system-instrumentation response. The tests were initiated by breaking a single rupture disk which contained the entire system pressure, and the runs were performed with diverging and also constant-diameter exhaust ducts. All the tubes had a sharp entrance, and the exit of the constant diameter ducts was a 180° divergence. The experimental results compared well with those of Fauske.[3,7] A large degree of nonequilibrium existed in the liquid jet as it accelerated from an initially nearly saturated liquid state through the short tubes.

The data also indicated that the superheated liquid jet constricted to a vena contracta before it began to break up. It was deduced from the experimental results that an exit quality of only about half the exit equilibrium quality existed in the tests. In the rapidly diverging tubes, since the axial pressure distribution was nearly constant, the critical exit-plane pressure ratio was taken to be the ratio of the measured axial pressure to the inlet stagnation pressure. In the constant-diameter short tubes, the critical pressure ratio was taken to be the average pressure that existed over the upstream half of the tube to the inlet stagnation pressure. This was done because of the rapid exit divergence. As the divergence angle of the tapered tubes decreased, the critical pressure ratio became more a function of the inlet stagnation pressure.

For all the tubes, the critical flow rate could be calculated with good accuracy with the incompressible momentum equation when the proper exit or back pressure was used. A model was formulated to calculate the back pressure in the tapered tubes. It assumed a two-dimensional flow field, a liquid contracted area of 0.61 of the total initial flow area at the entrance plane, a turbulent boundary layer on the outer perimeter of the jet, and vapor generated only at the liquid jet surface. Entrainment was neglected, and the flow was considered to be homogeneous. The calculated critical flow rates were less than the measured values; the predicted exit or back pressures were higher than the measured pressures, making the calculated thrust greater than the measured thrust. The data from this experiment indicated that for a constant length-to-diameter (L/D) ratio for a short tube, the critical flow rate increased slightly as the diameter of the duct decreased. This is in contrast to Fauske's[3] observation that, for a constant L/D of a short tube, the critical flow rate increases and the critical pressure ratio decreases with increasing diameter of the duct.

Fugie et al.[64] and Tagami[65] measured the flow rates of initially saturated water and two-phase steam-water mixtures through orifices 0.394-2.756 in. in diameter for initial stagnation pressures from 150 to 1000 psia from a one-tenth-model reactor-pressure-vessel decompression system. The blowdown vessel was a cylinder which was 2 ft in inside diameter and 10 ft tall, and its internal volume was about 31 ft^3. There were exhaust ports at both the bottom and top of the vessel, but most of the blowdowns were performed from the bottom port. The mass flow rate from the system was indirectly measured with a load cell from which the blowdown vessel and its contents were suspended. For the bottom blowdowns, the level of the remaining fluid in the vessel was monitored with a differential pressure transducer. The void fraction in the exhaust duct was measured with a solenoid-type void transducer.

In the initial two-phase runs, the critical flow rate decreased as the orifice diameter increased. This was attributed to an excessive amount of steam being swept into the exhaust area. When the Moody[2] predictions were compared to the measured results, the predicted flow rates had to be corrected to account for the effect of the exhaust flow area on the flow rate. For the small orifices, of 0.394-in. diameter, the Moody model considerably underpredicted the measured flow rates because the inlet qualities were very small and the assumption of thermodynamic equilibrium in the model was not valid in this range. The Moody model predicted the flow rates through the 1.181-in.-dia orifice relatively well. As the orifice diameter was increased to 2.756 in., the Moody predictions exceeded the measured flow rates because of the increased inlet qualities and overpredicted slip ratios.

Etheimer,[66] Ungerer,[67] and Carzaniga,[68] conducted similar blowdown experiments to study the effect of the vessel and exhaust-duct geometry on the critical flow rate from the system. Cylindrical pressure vessels were used, and the blowdowns were from bottom exhaust ports. The experimental results indicated that for given initial stagnation conditions and L/D of the exhaust duct, the measured critical flow rate increased as the ratio of the exhaust-duct flow area to the internal-vessel flow area decreased. For a given L/D of the exhaust duct and ratio of the discharge to vessel flow area, the critical flow rate also increased as the L/D of the vessel increased for these bottom blowdowns. The diameter of the pressure vessel itself did not significantly effect the blowdown. All the characteristics of the blowdown vessel geometry that were conducive to increasing the critical flow rate basically permitted adequate time for significant phase separation to occur within the vessel. This left fluid of lower quality than the bulk liquid of uniformly distributed quality in the lower region of the vessel from where it was discharged at a rate greater than the homogeneous critical flow rate. The critical flow rate decreased as the L/D of the exhaust duct increased, all other parameters being constant. The flow approached a homogeneous-equilibrium flow as the length of the discharge duct increased sufficiently.

White[69] conducted blowdown tests of initial, two-phase, steam-water mixtures through a tube 15 ft long and of 0.621-in. inside diameter (L/D = 290). This was a considerably longer exhaust duct than had been previously used. The flow regime that was established in the initial, steady-state, flowing system was a two-phase, annular flow pattern which is characteristic of BWR conditions. The steady-state initial qualities and void fractions ranged from 0.08 to 0.31 and from 0.64 to 0.87, respectively, and the operating, steady-state initial system pressures were 485 and 1002 psia. An expansion wave propagated away from the break, and the fluid exhausted during the first 100 msec of the transient was recorded. The expansion wave fronts propagated away from the break at 1520-1570 ft/sec, a speed that was nearly independent of the initial pressure and quality. The fluid discharged within the first 100 msec could be predicted better with the homogeneous-critical-flow model than an annular-critical-flow model,[5] even though the initial, steady-state flow regime was an annular flow pattern.

Allemann et al.[70] performed a blowdown experiment simulating a LOCA in both PWR and BWR systems. The blowdowns were from the bottom of a 17-ft-high, $3\frac{1}{2}$-ft ID, 150-ft^3 cylindrical vessel. The design pressure and temperature of the system were 2750 psig and 650°F, and the discharge duct was a $6\frac{13}{16}$-in.-ID circular pipe. The exit of the exhaust duct was equipped with an orifice arrangement so the exit flow area could be changed from 0.0156 ft^2 to full open at 0.253 ft^2. A double-rupture-disk system on the end of the exhaust duct initiated the decompressions. The blowdowns were started with the vessel full of nearly saturated water that ranged from 6800 to 7000 lb_m. The initial stagnation conditions ranged from 600 to 2500 psig and 70 to 600°F.

True subcooled decompressions were not experienced in the Allemann et al. tests because nitrogen gas, which was used to pressurize the system during heatup, came out of solution before the saturation pressure was reached. The measurements of the two-phase critical flow rate were also suspect because of the effect of the nitrogen gas in solution. Experimental results were obtained for pressure, temperature, interface between the high- and low-density fluids, flow rate, void fraction, thrust, and local structural stresses. The interface between the high- and low-density fluids was measured with a time-domain reflectometer. Both the remaining fluid weight and the thrust were monitored with strain-gauge load cells, and the void fraction in the exhaust duct was determined with a neutron detector.

The primary questions of interest during the 20 tests were an evaluation of the interface between the high- and low-density fluids, and a determination of the vertical void-fraction profile. Thermodynamic equilibrium of the remaining fluid was reported to exist for the major portion of the two-phase period of the blowdown. The quality of the exhausting fluid increased as the ratio of the break flow area to the internal-vessel flow area increased, and also as the initial stagnation temperature increased.

Gallagher[71] performed a blowdown experiment with an air-water shock tube. The 2-in.-ID tube ranged in length from 6 to 17 ft. The low-pressure chamber was a cylindrical vessel, 8 ft long and of 42-in. inside diameter. The decompressions were initiated by breaking glass rupture disks, which were 1/4 to 3/8 in. thick. The initial stagnation conditions of the driver fluid were 300-2000 psig, 400-600°F, and 0-75% void fraction. The parameters investigated were initial stagnation fluid condition, size and location of the break, shape and location of various flow obstructions, the length of the driver tube, heat addition to the fluid during the blowdown, and the effect of an external circulating loop.

One of the primary objectives of the investigation was to study the loading on simulated vessel internals during the subcooled liquid and early portions of the two-phase regimes of the blowdown. The effect of flow obstructions such as rods or bundles of rods increased the decompression time, and obstructions that imposed rather small flow-area constrictions were not severely loaded. When the obstructed flow area was greater than about 70% of the remaining unobstructed flow area, the loads exerted on such an obstruction became significant. When the local constricted flow area was considerably larger than anywhere downstream, choking occurred at the upstream constriction.

For a large downstream break area compared to an upstream unobstructed flow area, there was appreciable loading on the upstream obstruction during the subcooled liquid and for a major portion of the two-phase regime of the decompression. When the downstream flow area was as small as or smaller than the upstream unobstructed flow area, the flow choked downstream of the obstruction, and a smaller load was exerted on the upstream obstruction. It was concluded that the load exerted on a flow obstruction did not significantly increase with increased length of the obstruction. When the obstruction was a rod or a bundle of rods, whether or not the rods were heated made no significant difference.

The Battelle Institute[72-78] conducted a blowdown experiment to simulate decompression transients in both BWR and PWR systems. The tests were primarily directed at understanding the saturated portion of the decompression with very simple or no internal structure inside the blowdown vessel. The vessels had many exhaust-port locations, but the decompressions were primarily from exhaust ports slightly above the midplane of the vessels, and there were no internal rods or obstructions in the vessels. The preliminary stage of the experimental program was performed with 6-in.-ID, 21-51-in.-high, glass, cylindrical pressure vessels. The discharge ducts were of 0.6- and 1.0-in. inside diameter and were 5-15 in. long. The initial tests were performed with 45-psia saturated water, and subsequent runs went to about 660-psia saturated water. During the blowdown, high-speed motion pictures were taken of the flow regimes established inside the glass vessels and in the exhaust duct. The parameters measured during the decompressions were the pressure and temperature of the remaining fluid inside the vessel. The parametric study included varying the initial water level in the vessel, the initial stagnation pressure inside the vessel, the height of the vessel, the diameter of the discharge duct, and the diameter of the orifice that was used at the end of the exhaust duct to control the flow decay.

The second part of the investigation used a 32-in.-ID, 13-ft-high, steel cylindrical vessel, which contained internal structure. The operating conditions of the tests performed with this vessel were as high as 1030-psia saturated water. The discharge duct was 5.906 in. in diameter and 244 in. long (L/D = 41). The data from these tests were in good agreement with the trends observed in the runs with the glass pressure vessel. In the tests performed with an initially partially full vessel of water, a short delay was detected between the time the rupture disks broke and the time the internal-vessel pressure recovered to nearly the initial saturation pressure. Such a delay was not evident in the runs with an initially nearly full vessel of water. The foam level inside the vessel rose at about 20 ft/sec toward the discharge duct. No pronounced hammer effect was detected in the two-phase system when the discharge duct was rapidly closed once flow had been established. No significant pressure differences were established between the various regions of the internal structure in the vessel during the decompressions. The maximum pressure difference between the various internal regions was about 14.5 psi.

The third part of the experimental program was directed at simulating both BWR and PWR initial conditions. A 31-in.-ID, 36-ft-high steel cylindrical pressure vessel, with no internal structure was used. The operating conditions in this vessel were from 1045- to 1925-psia saturated water and two-phase steam-water mixtures. The exhaust ducts were of 1.969- and 5.709-in. inside diameter, 8.858-11.204 in. long, with L/D ratios of 1.656-4.50. Both the initially subcooled liquid and two-phase decompressions exhibited nearly the same behavior, except at the very first of the blowdown. This was the same observation made by Fugie et al.[64] and Tagami.[65] Thermodynamic equilibrium of the remaining fluid inside the vessel existed for most of the decompression. For most of the blowdown, the foam level remained at approximately the elevation of the discharge duct. More pronounced separation of the liquid and vapor phases existed for smaller discharge areas relative to the internal-vessel flow area.

Allemann et al.[79] performed 21 blowdown tests similar to those described in Ref. 70. The experimental facility was the same as described in Ref. 70, except where noted. The initial stagnation conditions were 869-2165 psia and 496-601°F. The amount of water contained in the blowdown vessel at the time of rupture was 3400-7400 lb_m. The exhaust ducts were 0.815, 1.687, 3.438, and 5.188 in. in inside diameter, and the L/D of the ducts varied from 1 to 15. The blowdowns were executed from top, middle, and bottom exhaust ports. A sieve-plate separator in the blowdown vessel divided it into an upper and lower region. It was installed in the vessel to simulate the resistance the flow would experience when passing through the core structure in a prototypic geometry.

The same experimental measurements were recorded in these tests as in the previous runs,[70] except that the void-fraction measurement was omitted in place of measuring the movement of the sieve plate in these runs. The system was again pressurized with nitrogen gas during the entire heatup period, and the fluid was again in a stagnant state at the initiation of the decompressions. The dissolved nitrogen gas made the demineralized water significantly compressible and appreciably altered the blowdown characteristics in all regimes. This is consistent with the previous remarks concerning the effect of dissolved gas on the results in Ref. 70. The length of the exhaust duct had little effect on the measured critical flow rates for similar initial stagnation conditions. Orifices on the end of the exhaust duct were again used to control the break flow area from 0.0156 ft^2 to full open at 0.253 ft^2. When the Moody[2] critical-flow model was used to predict the critical-flow-rate data, the discharge coefficient (C_d) required to obtain a reasonable comparison between the measured and predicted histories ranged from 0.6 to 1.09. The required C_d to effect a reasonable comparison also decreased for increasing break size. The position of the interface between the high- and low-density fluids could be predicted reasonably well with a constant-bubble-rise model when the "proper" C_d was used.

The amount of water remaining in the vessel after the decompression was less than that predicted by the FLASH-2 code,[46] and the difference between the calculated and measured remaining liquid increased for blowdowns from successively lower exhaust ports from the vessel. The L/D of the exhaust duct had significantly less effect on the critical flow rate than that predicted by the Moody model.[41] The forces exerted on the sieve plate during the decompression were much less than the predicted values. The sieve-plate response did not match the calculated wave forms, nor did the predicted deflection of the sieve plate occur.

Hoppner[50] performed an experimental investigation into the various decompression regimes that exist during a blowdown transient. The experimental portion of the study was performed in a 4-ft-long, 1.5-in.-ID vertical shock tube in which the maximum initial condition was 74 psia and 270°F distilled water. The system was pressurized to 74 psia with nitrogen gas and then was electrically heated to 270°F. The blowdown was initiated by breaking a rupture disk at the upper end of the shock tube. During the decompression, the pressure was monitored at three axial locations, the temperature of the remaining fluid was measured, and the bubble nucleation, growth, and flow-regime development were observed with a high-speed (3000-frame/sec) motion-picture camera. Four distinct stages of decompression were observed in these blowdowns: (1) From 0 to about 10 msec, the system nearly depressurized as a single-phase, all-liquid fluid; (2) for about 10-100 msec, the internal-vessel pressure dropped slightly below the bulk saturation pressure, causing the liquid to superheat about 10°F, and vapor nucleation was generated; (3) from about 100 msec to some time t_c, the fluid in the blowdown vessel was a two-phase mixture, and the exhaust flow rate from the test section was controlled by two-phase critical flow at the exit; (4) for $t > t_c$, the two-phase flow from the system was subcritical until the flow ceased.

The largest bubbles observed during nucleation were about 0.007 in. in diameter. When the system contained more internal surface area, more nucleation occurred, and the internal-vessel pressure regained more rapidly. There was normally a short delay of about 2 msec from the time the rupture disk failed to when a bubble first appeared. The smallest detectable bubble size was about 0.002 in. in diameter, so the delay of 2 msec could have been the time required for the nuclei to have grown to 0.002-in. diameter. After about 2 msec, bubbles appeared on the surface, collapsed, reappeared at the same location, grew slightly, decreased in size somewhat, and finally grew rapidly.

This oscillatory motion of the bubbles, which occurred for about 10 msec, was attributed to the effect of the strongly reflected pressure waves on the growing nuclei. At about 10 msec, the bubbles changed shape from spheres to nearly oblate spheroids. It was concluded that for few and small nuclei the system pressure would decrease sufficiently below the saturation pressure to provide a large liquid superheat, which would promote fast bubble growth. For more and larger nuclei, the superheat would be less; therefore the bubble growth rate would not be as rapid. Nucleation, bubble growth, and an evolving bubbly-flow pattern was observed in the test section for $0 < t < 100$ msec. For

$100 < t < 300$ msec, bubble coalescence, nucleation, and transition to irregularly shaped large bubbles occurred. This was followed by an irregular, violent, slugging motion, local flow reversal, and chugging. The final flow regime was more violent and irregular when there were less initial surface-nucleation sites.

Rudiger[80] presented the results of some bottom blowdown tests performed by the Battelle Institut in Germany from a vessel that had no internal geometry. The vessel, which was suspended from a load cell, was a cylinder 36 ft 8 in. tall of 31-in. inside diameter; it had a 5.906-in.-ID exhaust duct, which was about two diameters long. The internal volume of the vessel was about 183 ft^3, and the maximum operating conditions of the apparatus were 2350 psia and 570°F. There were six different vertical levels on the vessel from which the blowdowns could be performed.

By comparing the results from these bottom blowdowns in which a low-quality fluid was exhausted first to some of the previous middle and top blowdowns in Refs. 72-78 in which a high-quality fluid was exhausted first, Rudiger observed that the initial decompression rates were significantly different. He also noticed that the drop in the internal-vessel pressure at the start of the decompression was a function of the vessel volume and the initial internal phase distribution. In addition, a liquid superheat of about 18°F was experienced during the initial period of the blowdown. Following this period, the fluid depressurized in a nearly equilibrium manner. This was the same observation made by Fugie[64] and Tagami[65] and in Refs. 72-78. Comparison between analytical-model predictions and the measurements revealed that the Moody[2] model overpredicted the flow rates, whereas the homogeneous-equilibrium model predicted the data reasonably well. An experiment directed at simulating both BWR and PWR initial conditions was also outlined, but no results were available at this time.

Shimamune et al.[81] presented some of the results of the Rosa I experiment conducted from 1970 to 1972 by the Japanese Atomic Energy Institute. About 65 blowdown tests were performed from a vessel 28-ft 3-in.-tall, 22-in.-ID vessel, which was equipped with both top and bottom exhaust ports (of 13.780-in. inside diameter). The length of the exhaust duct was 17 ft 2 in., making the $L/D \simeq 15$. Variously sized orifices were used to control the break flow area (0.984- to 4.921-in. diameter), and the initial stagnation pressure of the tests was 595-1438 psia. The parameters varied during the experiment were the initial stagnation pressure, break flow area, location of the break, vessel internals, the circulating flow rate through the vessel, and the circulating loop with and without a pressurizer when the vessel was in the loop. The experimental results were analyzed with the RELAP-3 computer code. The code used the Moody critical-flow model,[2] and the discharge coefficient C_d used in the model had to be decreased as the break area increased to predict the data properly. This was the same observation made by Allemann.[79] It was also noticed that the C_d used in the model had to be changed as the initial stagnation pressure of the test decreased for a constant break flow area. No substantial pressure differences were detected between the various regions of the vessel when internals were used in the blowdown vessel. This was the same observation made in Refs. 72-78.

Tokumitsu[82] summarized some of the preliminary safety tests performed in a 1/8th-scale model of the Fugen reactor, a 165-MWe, heavy-water-moderated BWR, built in Japan. The small-scale model system contained all the components of the full-size system, the primary objective of the experiment being to evaluate various emergency-core-cooling (ECC) injection methods. The parameters investigated in the experiment were the initial stagnation pressure, the exhaust area, and the rupture site. The initial stagnation pressure was varied up to 1068 psia, the exhaust diameters were 2.453, 3.937, 5.906, 7.874, and 9.843 in., and the rupture locations were in the downcomer pipe from the steam drum to the pump, the inlet duct from the pump to the reactor, and in the main steam line from the steam drum to the turbine. The core heat capacity was simulated with 28 stainless steel heaters that were 146 in. long, and the fluid was in a stagnant state at the initiation of the blowdown. The breaks were initiated with a quick-opening valve in the inlet feeder line, and with rupture disks in the downcomer pipe and in the main steam line. The inlet feeder pipe had two discharge ducts, so that either single or double breaks could be performed. The break flow areas in both exhaust ducts originating from the inlet feeder line were varied from full open at 2.453-in. diameter to one-half and one-third open. The rupture disks were broken with an electric-arc technique. For the break in the downcomer pipe, the initial depressurization rate in the steam drum was very rapid because saturated water was initially exhausted. This was followed by a more gradual decrease in the pressure due to flashing in the steam drum. The inlet-feeder pipe break simulated the difference in heat-removal ability of ruptured and unruptured pressure tubes in the reactor. The ruptured pressure tubes dried out at the bottom first; the unruptured ones dried out at the top first. The effect of loss of flow while still at full power was also investigated. In this case, the liquid level in the pressure tubes decreased to about half the height of the effective heating length of the fuel before dryout started to occur.

Starting in about 1973, the Bettis Flask tests[83] were performed at the NRTS by the Aerojet Nuclear Company. The purposes of this experimental program were to investigate certain heater performance characteristics during a LOCA and to examine various ECC injection techniques. The system consisted of an 8-ft^3 cylindrical vessel with no internals. It was positioned in a circulating loop in which the water was heated outside the blowdown vessel and than circulated through it. The system was designed to operate at 2500 psig and 650°F, and the exhaust-duct geometry was similar to the LOFT-blowdown configuration. The exhaust duct, originating from the bottom of the vessel, consisted of a combination of three different sections of pipe. The exit of the discharge duct was equipped with either a quick-response valve or a rupture-disk assembly to initiate the decompressions. During heatup, the fluid was maintained in a subcooled liquid state at the desired initial test pressure by pressurizing the system with nitrogen gas. This method of pressurizing the system while the fluid temperature is increased forces gas into solution. The mass flow rate from the system was measured with a drag-disk assembly near the end of the discharge duct. The fluid density was measured by an attenuation technique at the drag-disk location and also at two upstream locations in the exhaust duct. The homogeneous-equilibrium model best predicted the measured critical flow rates because the discharge duct was rather long, L/D ≃ 100. Various ECC systems were also investigated during the experiment.

Choi[84] applied similitude theory to the experimental modeling of the Containment System Experiment.[70,79] A number of isothermal blowdown tests with initially saturated and slightly subcooled water were performed from both top and bottom exhaust ports of a small vessel. The initial water conditions were 45-100 psia and 250-320°F; the vessel originally contained 23-28 lb_m of water. It was of 6-in. ID, 27 in. tall, and was designed to operate up to 100 psia and 400°F. It had no internal structure, its quotient of internal surface area to volume was about 10 ft^2/ft^3, and it was about one-seventh the height of the CSE vessel. The exhaust duct, which was the same for both top and bottom blowdowns, was of 0.66-in. ID and 27 in. long (that is, L/D ≃ 41), and this produced an exit-to-vessel flow-area ratio of 0.0121. The top and bottom exhaust ports were each about 5.5 in. from the top and bottom of the vessel.

The decompressions were initiated by mechanically breaking a single rupture disk on the end of the constant-area exhaust duct. The water in the blowdown vessel was heated by circulating it through an external heating loop with a heating capability of 2 kW. The initial conditions for the subcooled liquid were generated by pressurizing the system with air during heatup. The air came out of solution during decompression, and it effected the subcooled period of blowdown the most.

The measured parameters were pressure and temperature in the vessel and exhaust duct, remaining fluid weight, and the void fraction in the exhaust duct. Pressure and temperature measurements were made at both the upper and lower regions of the vessel, and also at two different axial locations in the exhaust duct. The two vessel-pressure measurements were made at the end of 3-in.-long standoff tubes from the vessel. The remaining fluid weight was measured by suspending the vessel and contents from a strain-gauge specimen for the top blowdowns, and by resting the vessel and contents on a supporting load cell for the bottom blowdowns. The void fraction in the exhaust duct was monitored with a gamma-ray-attenuation technique.

The internal vessel pressure dropped below the saturation pressure at the start of both the initially saturated and subcooled decompressions, and it recovered in about 1 sec. This was attributed to a short, subcooled blowdown period in such runs, and also to thermodynamic nonequilibrium behavior required to start vapor generation.

Many ot the reported pressure histories were nearly constant for a large portion of the decompression, which indicated that much of the remaining fluid was probably superheated liquid. However, thermodynamic equilibrium was reported for most of the latter period of the blowdown, but this is not consistent with the measured pressure histories. This is probably because the thermocouples served as nucleation surfaces, and thermodynamic equilibrium did nearly exist in the immediate vicinity of the thermocouple, but the remaining fluid away from the thermocouple was still superheated liquid.

There was a distinct "knee" in the measured pressure histories of the bottom blowdowns; however, it was not present in the top blowdowns. In the upper decompressions, the exit-fluid quality was greater because of phase separation, which reduced the critical flow rate and increased the blowdown time compared to the bottom blowdowns. The internal vessel temperature decreased more rapidly in the top blowdowns than in the bottom blowdowns. The fraction of the initial water content remaining within the vessel after decompression was approximately one-tenth in the bottom blowdowns and one-third in the top blowdowns. Phase separation within the vessel increased for reduced area ratios in the bottom blowdowns, and the critical flow rate decreased for increased area ratios because of enhanced sweep-in of the vapor phase from the vessel to the exhaust duct. The measured critical flow rates were less than those predicted by the Moody model.[2,41] The measured void fraction at the exit increased as the area ratio increased and the initial stagnation temperature increased.

Banerjee et al.[51] performed an adiabatic blowdown experiment with initially subcooled water. The system was an upward-flowing configuration in the initially steady-state condition; the flow was then forced to reverse direction by a valving arrangement similar to that described in Ref. 85. The test section consisted of an inlet and exit unheated section, and also a vertical, electrically heated center section. The parameters varied during the experiment were the heat flux to the fluid, the break area, and the initial subcooling of the water. The power to the heater was held constant during the decompression in order to generate a critical-heat-flux condition. The local pressure, fluid temperature, and the heater wall temperature were measured. The mass inventories in various regions of the test section were measured at selected stages during the blowdown by isolating a given section with the fast-acting valves. This was how the remaining mass history in the test section during the decompression was determined. The break flow rate was controlled by orifices and venturies. The system pressure dropped below the initial saturation pressure at the beginning of the blowdown, and this was interpreted as a delay in bubble nucleation.

III. ANALYSIS

A. General Considerations

The general analytical treatment of a system containing a fluid starts with the statement of the conservation equations. In light of the experimental information gained from this investigation, which will be dealt with in more detail in Chapters VI and VII, the following assumptions are made regarding the physical nature of the fluid within a system during blowdown:

1. The controlling mechanism for most of the decompression is two-phase choking at the exit of the exhaust duct.
2. There is an insignificant amount of heat transfer between the fluid and fluid envelope.
3. The decompression can be idealized as a set of quasi-steady states.

To analyze the response of a system during blowdown, the conservation equations for the system response are formulated upon the assumptions listed above. The system is defined as the fluid envelope and everything contained within it. The continuity equation is

$$\dot{m}_i - \dot{m}_e = \frac{\partial m}{\partial t}, \tag{1}$$

the dot above a symbol indicating time differentiation of the quantity represented. Since there is no mass flow into the system, Eq. 1 becomes

$$\frac{\partial m}{\partial t} = -GA_e. \tag{2}$$

The momentum equation can be written for an Eulerian reference frame as

$$\dot{M}_i - \dot{M}_e + \sum F_{ext} = \frac{\partial}{\partial t}(mu). \tag{3}$$

Since there is no momentum flow into the system, and since the time rate of change of the flow rate is small compared to the thrust and forces due to pressure differences, Eq. 3 can be approximated as

$$F = A_e(P_e - P_a + G^2 v_e). \tag{4}$$

The energy equation can also be formulated for an Eulerian frame of reference as

$$\dot{Q} - \dot{W} + \dot{E}_i - \dot{E}_e = \frac{\partial E}{\partial t}, \tag{5}$$

where the typical sign convention of heat transfer into the system and work done by the system is positive. By assuming negligible heat exchange between the fluid and fluid envelope, no performance of external mechanical work, and no energy flow into the system, Eq. 5 is reduced to

$$\frac{\partial}{\partial t}(m_e) = -\left[\rho A u(i + \tfrac{1}{2}u^2 + gz + Pv)\right]_e . \tag{6}$$

By neglecting elevation changes and incorporating the definition of specific enthalpy,

$$h = i + Pv, \tag{7}$$

we can write Eq. 6 as

$$\frac{\partial}{\partial t}(mh) = -\left[GA(h + \tfrac{1}{2}u^2)\right]_e . \tag{8}$$

Equation 8 can be integrated from the beginning to the end of the decompression to produce

$$m(0)h(0) - m(\tau)h(\tau) = A_e \int_0^T G\left(h + \tfrac{1}{2}G^2v^2\right)_e dt. \tag{9}$$

For a homogeneous two-phase mixture, the specific enthalpy and specific volume become

$$h = h_V x + h_L(1 - x) \tag{10}$$

and

$$v = v_V x + v_L(1 - x), \tag{11}$$

where the fluid quality is defined as $x \equiv \dot{m}_V/\dot{m}_T$. Substituting these relations into Eq. 9 produces

$$m(0)h(0) - m(\tau)h(\tau) = A_e \int_0^T G\Big\{h_V x + h_L(1 - x) + \tfrac{1}{2}G^2\left[v_V x + v_L(1 - x)\right]^2\Big\}_e dt, \tag{12}$$

which is the energy equation describing the overall energy lost from the system during the decompression.

B. Critical Flow

1. Single-phase Critical Flow

The flow rate through a duct becomes a maximum, or its critical value, when a reduction in the downstream pressure no longer increases the flow rate for given upstream fluid conditions and duct geometry. At this condition, as illustrated in Fig. 3, the ratio of the throat pressure to the upstream stagnation pressure is termed the critical pressure ratio. Mathematically, the throat pressure is reduced until the maximum or critical flow rate is reached. For frictionless, adiabatic flow, and thus isentropic flow, this can be stated as

$$\left(\frac{dG}{dP_e}\right)_s = 0. \tag{13}$$

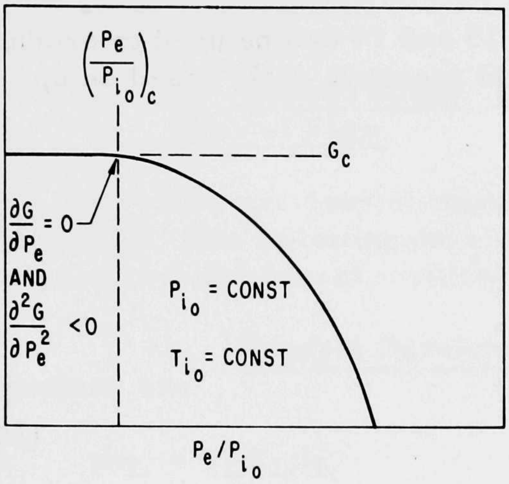

Fig. 3. Critical-flow Criterion. ANL Neg. No. 900-4861.

The specification of constant entropy in Eq. 13 is a result of an approximation in the momentum equation. Since the effect of gravity is negligible in high-speed flow, the one-dimensional momentum equation can be written as

$$-v\frac{dP}{dz} - \frac{d}{dz}\frac{\tau_w S}{\rho A} = u\frac{du}{dz}. \tag{14}$$

The frictionless assumption reduces this equation to

$$-v_e\left(\frac{dP}{dz}\right)_{e,s} = u_e\left(\frac{du}{dz}\right)_{e,s} \tag{15}$$

for the throat or exit location of a duct. The frictionless assumption indicates the process is reversible, and this coupled with the adiabatic assumption implies, from the Second Law of Thermodynamics, that the flow is isentropic. The general relation for the single-phase critical flow rate can be obtained by differentiating the continuity equation for a constant area duct, $G = \rho u$, and applying the critical-flow criterion in Eq. 13 to produce

$$\left(\frac{du_e}{dP_e}\right)_s = G_c\left(\frac{dv_e}{dP_e}\right)_s. \tag{16}$$

The assumption is made that the fluid speed and specific volume are composite functions of pressure and position so that $u = u[P(z)]$ and $v = v[P(z)]$. By employing this assumption and substituting Eq. 16 into Eq. 15, the general relation for the critical flow rate becomes

$$G_c = \left[\frac{-1}{\left(\dfrac{dv_e}{dP_e}\right)_s}\right]^{1/2} . \tag{17}$$

For the isentropic flow of an ideal gas, Eqs. 15 and 17 can be used to produce the single-phase critical flow rate and critical pressure ratio based on upstream stagnation conditions as given by[86]

$$G_c^2 = \frac{\gamma P_{i_0}^2}{RT_{i_0}}\left(\frac{2}{\gamma + 1}\right)^{(\gamma+1)/(\gamma-1)} \tag{18}$$

and

$$\eta = \left(\frac{2}{\gamma + 1}\right)^{\gamma/(\gamma-1)} . \tag{19}$$

Thus, the single-phase critical flow rate and critical-throat-pressure ratio are determined for given upstream stagnation conditions and fluid properties.

For isentropic flow in a constant-area duct, the momentum equation (Eq. 15) can be rearranged to the form of Eq. 17 without using the critical-flow criterion (Eq. 13). This implies that the only finite fluid speed that can exist under these conditions in a duct at critical flow is the acoustic propagation speed given by

$$a^2 = \left(\frac{\partial P}{\partial \rho}\right)_s . \tag{20}$$

Thus, for single-phase isentropic critical flow, the fluid speed at the choking location is precisely the propagation speed of the local acoustic pressure wave at that location.

For isentropic critical flow, the stream chokes at the minimum flow area. The continuity equation,

$$\frac{d\rho}{\rho} + \frac{dA}{A} + \frac{du}{u} = 0, \tag{21}$$

the frictionless momentum equation (Eq. 15), the isentropic acoustic propagation speed (Eq. 20), and the fact that the fluid speed at the choking location is equal to the local acoustic propagation speed in the fluid can be combined to indicate that $dA/dz = 0$ at that position. This implies an extreme in the flow area, and physical evidence reveals that the area is a minimum at this condition. Therefore, an isentropic critical flow will choke at the minimum flow area, or at the exit of a constant flow area.

Thus, the single-phase critical-flow phenomenon is well understood with the relation between the flowing fluid properties at the choking location and the pressure-wave-propagation characteristics at that position well established.

2. Generalized Single- and Two-phase, One- and Two-component, Critical Flow

The previous discussion has dealt with the critical flow of a single-phase fluid. The following development is valid for both single- and two-phase, one- and two-component, critical flow.[8]

a. General Development. The liquid and vapor or gas continuity equations are

$$\dot{m}_L = \rho_L A_L u_L \tag{22}$$

and

$$\dot{m}_V = \rho_V A_V u_V. \tag{23}$$

The momentum equation is

$$-A\frac{dP}{dz} = \frac{d}{dz}(\dot{m}u) + \frac{dF_r}{dz} + \frac{d}{dz}(mg \sin \theta). \tag{24}$$

As in the single-phase case, the pressure drop near the exit is considered to be primarily due to an increase in fluid momentum rather than to frictional and elevation pressure losses. This reduces the momentum equation to

$$-\left(\frac{dP}{dz}\right) = G\frac{d}{dz}\left[u_V x + u_L(1 - x)\right]. \tag{25}$$

It is assumed for given upstream conditions that u_V, u_L, and x are composite functions of P and z so that they can be formulated as $f = f[P(z)]$. This permits Eq. 25 to be written as

$$G^{-1} = -\frac{d}{dP}\left[u_V x + u_L(1 - x)\right]. \tag{26}$$

Employing the definitions of the velocity ratio, $k \equiv u_V/u_L$; the quality, $x \equiv \dot{m}_V/\dot{m}_T$; and the void fraction $\alpha \equiv A_V/A_T$; we can rearrange the continuity equations (Eqs. 22 and 23) to produce

$$(1 - x)G = \frac{u_L}{v_L}(1 - \alpha) \tag{27}$$

and

$$xG = \frac{u_V}{v_V}\alpha . \tag{28}$$

Combining Eqs. 27 and 28 and using the definition of the velocity ratio produce

$$\alpha = \frac{v_V x}{v_V x + v_L(1 - x)k} . \tag{29}$$

Using the velocity ratio in Eq. 26 produces

$$G^{-1} = -\frac{d}{dP}\Big\{\big[kx + (1 - x)\big]u_L\Big\} . \tag{30}$$

The total flow rate can be rearranged from Eqs. 27 and 28 into the form

$$G = \left(\frac{k\alpha}{v_V} + \frac{1 - \alpha}{v_L}\right)u_L . \tag{31}$$

Equation 29 can be substituted into Eq. 31 to give

$$G = \frac{ku_L}{v_V x + v_L(1 - x)k} . \tag{32}$$

Substitution of the continuity equation (Eq. 32) into the momentum equation (Eq. 30) produces

$$-G^{-1} = \frac{d}{dP}\left\{\frac{G}{k}\Big[v_V x + v_L(1 - x)k\Big]\Big[1 + x(k - 1)\Big]\right\} . \tag{33}$$

Expanding Eq. 33 and invoking the critical-flow criterion (Eq. 13) produce

$$-G_c^{-2} = \frac{d}{dP}\left\{\frac{1}{k}\Big[v_V x + v_L(1 - x)k\Big]\Big[1 + x(k - 1)\Big]\right\}_e . \tag{34}$$

Expanding Eq. 34 yields

$$G^2 = -k_e\left\{x\left[1 + x(k - 1)\right]\frac{dv_V}{dP} + k\left[1 + x(k - 2) - x^2(k - 1)\right]\frac{dv_L}{dP}\right.$$

$$+\left\{v_V\left[1 + 2x(k - 1)\right] + v_L k\left[(k - 2) - 2x(k - 1)\right]\right\}\frac{dx}{dP}$$

$$\left. + x(1 - x)\left(v_L k - \frac{v_V}{k}\right)\frac{dk}{dP}\right\}_e^{-1}. \qquad (35)$$

Equation 35 is the complete, general relation for the one-dimensional, steady-state, single- and two-phase, one- and two-component, critical flow rate per unit area. At this point various investigators have made different assumptions regarding the thermodynamic state of the fluid, the expansion process path, and the flow regime, and this has produced the various critical-flow models.

By comparing Eqs. 35 and 17, the compressibility of a two-phase, one-component mixture is seen to be, in general, a function of

$$\frac{dv}{dP} = f\left(v_V, \frac{dv_V}{dP}, v_L, \frac{dv_L}{dP}, x, \frac{dx}{dP}, k, \frac{dk}{dP}\right). \qquad (36)$$

Thus, the critical-flow phenomenon in a two-phase system is a complex combination of interphase heat, mass, and momentum exchange.

The general requirements of a two-phase, critical-flow model that will accurately predict the two-phase blowdown phenomenon are: (1) It must be able to handle upstream conditions from nearly saturated liquid to almost all vapor flow; (2) it must be based only on upstream stagnation conditions; (3) it must be able to predict both the critical flow rate and critical throat pressure; (4) it should be able to account for the discharge-duct geometry. The various currently available two-phase critical-flow models are summarized in Refs. 1, 2, 4, 5, 8, 10, 11, 26, 41, 87, 88, 89, and 90.

The two-phase critical flow models that will be discussed are the Homogeneous Equilibrium (HE), Homogeneous Frozen (HF), Moody,[2] and Henry-Fauske[1] predictions. These models will be assessed in terms of their applicability to the two-phase regime of decompression.

b. Specific Initially Two-phase Analytical Models

(1) Homogeneous-equilibrium Model. The initial approach taken to two-phase critical flow was similar to that described for single-phase

critical flow. The flow was assumed to be in thermodynamic equilibrium, adiabatic, and frictionless, and, hence, isentropic. The liquid and vapor or gas phases were assumed to travel at equal velocities; thus, the flow was termed "homogeneous." This permits the fluid specific volume to be formulated as in Eq. 11. By using this specific volume in the critical-flow relation, Eq. 17, the homogeneous-equilibrium critical flow rate becomes

$$G_{c_{HE}} = \left\{-\left[x_E \frac{dv_V}{dP} + (v_V - v_L)\left(\frac{dx_E}{dP}\right)_s + (1 - x_E)\frac{dv_L}{dP}\right]\right\}_e^{-1/2}, \tag{37}$$

where the exit equilibrium quality x_{E_e} is determined from

$$x_{E_e} = \frac{s_i - s_L(P_e)}{s_{VL}(P_e)} \tag{38}$$

and

$$-\left(\frac{dx_E}{dP}\right)_s = \frac{(1 - x_E)}{s_{VL}}\frac{ds_L}{dP} + \frac{x_E}{s_{VL}}\frac{ds_V}{dP}. \tag{39}$$

For low pressure, for which $v_L << v_V$, and an assumption that the liquid is incompressible, Eq. 37 simplifies to

$$G_{c_{HE}} = \left\{-\left[x_E \frac{dv_V}{dP} + v_V\left(\frac{dx_E}{dP}\right)_{s_i}\right]\right\}_e^{-1/2}. \tag{40}$$

Equation 40 is the relation for the homogeneous-equilibrium critical flow rate based on exit conditions.

The homogeneous-equilibrium critical flow rate can be related to the upstream stagnation conditions by use of the momentum equation. The flow is assumed to be frictionless and, hence, reversible; if this is coupled with the adiabatic assumption, the implication is that the flow process is isentropic. The frictionless assumption, together with negligible elevation-energy changes, permits the momentum equation to be written as

$$-v\ dP = u\ du. \tag{41}$$

For reversible processes, we may express the First and Second Laws of thermodynamics as

$$T\ ds + v\ dP = dh. \tag{42}$$

For an isentropic process, Eq. 42 simplifies; when it is combined with the momentum equation (Eq. 41) the result is

$$dh = -u\,du. \tag{43}$$

Integrating Eq. 43 from inlet to exit locations yields

$$h_{i_0} - h_e = \tfrac{1}{2}G_e^2 v_e^2. \tag{44}$$

Equation 44 can be expanded for a homogeneous two-phase mixture by using the definitions of the specific enthalpy, Eq. 10, and specific volume, Eq. 11, so that

$$h_{i_0} = \left\{h_V x_E + h_L(1 - x_E) + \tfrac{1}{2}G^2\left[v_V x_E + v_L(1 - x_E)\right]^2\right\}, \tag{45}$$

where x_E is determined by an isentropic expansion in Eq. 38. To ensure a maximum flow rate, the critical-flow criterion, Eq. 13, must be satisfied. From a knowledge of the upstream stagnation conditions, the exit pressure is reduced from the upstream pressure until the flow rate exhibits a maximum, as shown in Fig. 3. The critical flow rate is thus determined for the given upstream stagnation conditions. The ratio of the exit pressure at which the flow rate becomes a maximum to the upstream stagnation pressure is then the critical-exit-pressure ratio.

(2) Homogeneous Frozen Model. Another approach that has been taken to adiabatic, two-phase critical flow is the homogeneous frozen model.[26] Negligible wall friction is again assumed in the momentum equation, making it reversible. The reversible and adiabatic assumptions then imply that the expansion process is isentropic. There is considered to be no phase change within the duct, and the flow is assumed to be homogeneous. The kinetic energy of the stream is considered to be due only to the vapor expansion, and the critical flow rate can be defined by gas-dynamic principles. The frictionless momentum equation is

$$-\left[v_V x_i + v_{L_i}(1 - x_i)\right]dP = d\left(\frac{u^2}{2}\right). \tag{46}$$

Integrating this equation from the entrance to the exit of the duct while noting the isentropic expansion of the vapor phase, $v_{V_e} = v_{V_i}\eta^{-1/\gamma}$, produces

$$\frac{\gamma}{\gamma - 1}\left[1 - \eta^{(\gamma-1)/\gamma}\right] + \frac{v_{L_i}(1 - x_i)}{v_{V_i}x_i}(1 - \eta) = \frac{G_e^2 x_i v_{V_i}}{2P_{i_0}}\left[\frac{(1 - x_i)v_{L_i}}{x_i v_{V_i}} + \eta^{-1/\gamma}\right]^2. \tag{47}$$

The flow rate in Eq. 47 can be obtained by assuming no mass transfer (frozen), $x_i = x_e$ = constant in Eq. 40, and an isentropic expansion of the vapor phase, so that

$$G_c^2 = \left(\frac{\gamma P}{x_i v_V}\right)_e . \tag{48}$$

Equation 48 can also be derived from Eq. 47 by differentiating Eq. 47 and setting $dG/d\eta = 0$. Substituting Eq. 48 into Eq. 47 results in the following transcendental relation for the critical pressure ratio:

$$\frac{v_{L_i}(1 - x_i)}{v_{V_i} x_i}(1 - \eta) + \frac{\gamma}{\gamma - 1}\left[1 - \eta^{(\gamma-1)/\gamma}\right] = \frac{\gamma}{2}\eta^{(\gamma+1)/\gamma}\left[\frac{v_{L_i}(1 - x_i)}{v_{V_i} x_i} + \eta^{-1/\gamma}\right]^2 . \tag{49}$$

The energy equation for the stream is

$$h_{i_0} - h_e = \tfrac{1}{2}u_e^2 . \tag{50}$$

The right side of Eq. 50 can be evaluated from the momentum equation (Eq. 46), so that

$$\tfrac{1}{2}u_e^2 = x_i v_{V_i} P_{i_0}\frac{\gamma}{\gamma - 1}\left[1 - \eta^{(\gamma-1)/\gamma}\right] + v_{L_i} P_{i_0}(1 - x_i)(1 - \eta). \tag{51}$$

Referring to the assumption that the kinetic energy of the stream is due entirely to the expansion of the vapor phase simplifies Eq. 51, so that Eq. 50 becomes

$$h_{i_0} - h_e = x_i v_{V_i} P_{i_0}\frac{\gamma}{\gamma - 1}\left[1 - \eta^{(\gamma-1)/\gamma}\right]. \tag{52}$$

From the continuity equation, $G_c = u_e/v_e$, and the energy equations (Eqs. 50 and 52), the homogeneous frozen critical flow rate can be determined as

$$G_{c_{HF}} = \frac{1}{v_e}\left[2(h_{i_0} - h_e)\right]^{1/2} \tag{53}$$

or

$$G_{c_{HF}} = \frac{1}{v_{L_i}(1 - x_i) + v_{V_i} x_i \eta^{-1/\gamma}}\left[2 x_i v_{V_i} P_{i_0}\frac{\gamma}{\gamma - 1}\left(1 - \eta^{(\gamma-1)/\gamma}\right)\right]^{1/2} . \tag{54}$$

To evaluate the critical flow rate and critical pressure ratio based only on upstream stagnation conditions, Eq. 49 is solved for the critical pressure ratio, and it is used in Eq. 54 to determine the critical flow rate.

(3) Moody Model. The minimum-kinetic-energy, two-phase critical-flow model of Moody[2] is presently widely used to predict the two-phase critical flow rate and critical pressure ratio. The assumptions used in this model are as follows:

(a) The flow is one-dimensional.

(b) Both phases experience the same local static pressure.

(c) The phases are everywhere in thermodynamic equilibrium.

(d) The flow is adiabatic.

(e) The slip ratio and pressure at the exit plane are independent variables.

(f) The flow is isentropic from the entrance to the exit; hence, the stagnation enthalpy is constant through the duct.

(g) The liquid phase is incompressible.

The energy equation (Eq. 42) and the momentum equation (Eq. 41) were combined to produce the two-phase flow rate, Eq. 44. The mixture specific volume was formulated with the nonhomogeneous void fraction, Eq. 29. The fluid quality was evaluated isentropically, Eq. 38, and the mixture specific enthalpy was that in Eq. 10. These relations were combined to produce the following flow rate per unit area:

$$G(P,k) = \left\{ \frac{2\left[h_{i_0} - h_L - \frac{h_{VL}}{s_{VL}}(s_i - s_L)\right]}{\left[\frac{k(s_V - s_i)v_L}{s_{VL}} + \frac{(s_i - s_L)v_V}{s_{VL}}\right]^2 \left(\frac{s_i - s_L}{s_{VL}} + \frac{s_V - s_i}{k^2 s_{VL}}\right)} \right\}_e^{1/2} . \qquad (55)$$

To test for a maximum flow rate, the function G(P, k) must satisfy

$$\frac{\partial G(P,k)}{\partial P_e} = 0, \qquad (56)$$

$$\left[\frac{\partial G(P,k)}{\partial k}\right]_e = 0, \qquad (57)$$

and

$$\left[\frac{\partial^2 G(P, k)}{\partial P_e^2}\right] < 0. \tag{58}$$

Solving Eq. 57 for k_e indicates that the flow rate exhibits an extremum with respect to k when

$$k_e = \left[\frac{v_V(P_e)}{v_L(P_e)}\right]^{1/3}. \tag{59}$$

The critical flow rate and critical pressure ratio are determined for given upstream stagnation conditions by reducing the exit pressure below the upstream stagnation pressure until the flow rate indicates a maximum, satisfying Eq. 56. The flow rate is monotonically increasing up to the critical flow rate for reduced exit pressures (see Fig. 3); therefore, Eq. 58 is also satisfied.

(4) Henry-Fauske Model. The significant features of this model[1] are: (1) It handles upstream fluid conditions ranging from subcooled liquid to superheated vapor, and (2) it treats the expansion in the low-quality range as a nonequilibrium process. The assumptions used in this model are:

(a) The flow is one-dimensional.

(b) Wall friction is negligible compared to the momentum and pressure gradients near the exit.

(c) The flow is adiabatic.

(d) There is negligible slip between the phases ($k \simeq 1$).

(e) The system entropy remains constant during the expansion.

(f) There is insufficient time during the expansion process for appreciable interphase mass transfer to occur ($x_i \simeq x_t$).

(g) There is a negligible amount of interphase heat transfer during the expansion process, so that $T_{\ell_i} \simeq T_{\ell_t}$.

(h) Combination of conditions d-g implies that each phase expands individually in an isentropic manner; in particular, the vapor phase expands isentropically as an ideal gas from the stagnation location to the throat: $Pv_V^{\gamma} = \text{constant}$.

(i) The liquid phase is incompressible during the expansion: $dv_L/dP = 0$.

(j) The vapor phase at the throat expands in a polytropic manner to account for some of the heat transfer rate at that location:

$$\left(\frac{dv_V}{dP}\right)_t = \left(\frac{-v_V}{nP}\right)_t . \tag{60}$$

It is assumed that the thermal-equilibrium, two-component, polytropic exponent n, derived by Tangren et al.[91] and given by

$$n = \frac{(1 - x)\frac{cp_\ell}{cp_V} + x}{(1 - x)\frac{cp_\ell}{cp_V} + \frac{x}{\gamma}} , \tag{61}$$

can be used in Eq. 60 to account for some of the heat-transfer rate at the throat.

The interphase momentum transfer rate is indicated by the factor $(dk/dP)_t$. Since it is assumed that there is negligible mass transfer at the throat, $x_i \simeq x_t$, this implies that the actual one-component mixture behaves as a two-component fluid. The velocity ratio is also considered a composite function of pressure and position, $k = k[P(z)]$, so that $(dk/dP)_t$ can be expressed as the quotient of the position rate of change of the velocity ratio and pressure. Since the one-component mixture is assumed to behave in a two-component manner, the two-component, air-water, critical-flow data of Vogrin[92] were analyzed. These data indicated that the velocity ratio is a minimum at the throat, and the pressure gradient at the throat is finite. This implies that

$$\left(\frac{dk}{dP}\right)_t \simeq 0. \tag{62}$$

With the homogeneous assumption, the interphase heat-transfer process, described by Eq. 60, the assumption of negligible mass transfer from entrance to exit, $x_i \simeq x_t$, and the nearly constant v_L from entrance to exit, Eq. 35 reduces to

$$G_c = \left[\frac{x_i v_V}{nP} - (v_V - v_{L_i})\frac{dx}{dP}\right]_t^{-1/2} . \tag{63}$$

The actual fluid quality was formulated as

$$x = kN(x_E)x_E , \tag{64}$$

where $N(x_E)$ is a nonequilibrium parameter and x_E is the equilibrium quality given by Eq. 38 for the assumed isentropic expansion. A knowledge of $N(x_E)$

at the throat describes the nonequilibrium mass-transfer process at that location. Noting the no-slip condition at the throat, Eq. 64 is differentiated to produce

$$\left(\frac{dx}{dP}\right)_t = N\left(\frac{dx_E}{dP}\right)_t, \tag{65}$$

where $(dN/dP)_t$ has been shown to be negligible[8] for constant-area ducts and is also assumed to be negligible for nozzle flows.

Differentiating Eq. 38 and substituting into Eq. 65 yield

$$\left(\frac{dx}{dP}\right)_t = -\frac{N}{s_{VL_{E_t}}}\left[x_i\frac{ds_{V_E}}{dP} + (1 - x_i)\frac{ds_{L_E}}{dP}\right]_t. \tag{66}$$

The factor $(ds_{V_E}/dP)_t$ is determined by combining the reversible First Law for the vapor phase (Eq. 42), the equation of state of the vapor phase treated as an ideal gas, the polytropic expansion relation for the vapor phase (Eq. 60), the definition of the constant-pressure specific heat capacity of the vapor phase, the ratio of specific heat capacities of the vapor phase, and the relation between the gas constant and the specific heat capacities of the vapor phase treated as an ideal gas. This yields

$$\left(\frac{ds_{V_E}}{dP}\right)_t = -\frac{c_{p_V}}{P_t}\left(\frac{1}{n} - \frac{1}{\gamma}\right). \tag{67}$$

When Eq. 67 is substituted into Eq. 66, and Eq. 66 into Eq. 63, the relation for the critical flow rate becomes

$$G_c = \left\{\frac{x_i v_V}{nP} + \frac{(v_V - v_{L_i})}{s_{VL_E}}\left[(1 - x_i)N\frac{ds_{L_E}}{dP} - \frac{x_i c_{p_V}}{P}\left(\frac{1}{n} - \frac{1}{\gamma}\right)\right]\right\}_t^{-1/2}. \tag{68}$$

The parameter $N(x_{E_t})$ is of primary importance in the low-quality regime. It was evaluated by noting the throat equilibrium quality at the point where the measured critical flow rates[15,16] started to significantly increase above the homogeneous-equilibrium-calculated critical flow rate. The nonequilibrium parameter is thus of significance for throat qualities less than the value at which the measured flow rates are greater than the equilibrium-calculated flow rates. Based on these observations, the nonequilibrium parameter is formulated as

$$N(x_{E_t}) = \begin{cases} x_{E_t}/0.14, & x_{E_t} < 0.14 \\ 1, & x_{E_t} \geq 0.14. \end{cases} \tag{69}$$

The relation for the critical flow rate (Eq. 68) is then coupled with the overall two-phase momentum equation to obtain a solution based only on upstream stagnation conditions:

$$-\left[v_V x_i + v_{L_i}(1 - x_i)\right] dP = d\left(\tfrac{1}{2}u^2\right). \tag{46}$$

Using the assumption of a polytropic expansion of the vapor phase permits Eq. 46 to be integrated from the upstream location to the throat location under the assumptions listed above, and it can be rearranged to produce

$$(1 - x_i)v_{L_i}P_{i_0}(1 - \eta) + \frac{\gamma x_i P_{i_0}}{\gamma - 1}\left(v_{V_i} - \eta v_{V_t}\right) = \tfrac{1}{2}G_c^2\left[x_i v_{V_t} + v_{L_i}(1 - x_i)\right]^2. \tag{70}$$

The relation for the critical flow rate (Eq. 68) is substituted into Eq. 70 and rearranged to yield

$$\eta = \left[\frac{\dfrac{1 - \alpha_i}{\alpha_i}(1 - \eta) + \dfrac{\gamma}{\gamma - 1}}{\dfrac{1}{2\beta\alpha_t^2} + \dfrac{\gamma}{\gamma - 1}}\right]^{\gamma/(\gamma - 1)}, \tag{71}$$

where

$$v_{V_t} = v_{V_i}\eta^{-1/\gamma}, \tag{72}$$

$$\alpha_i = \frac{v_{V_i}x_i}{v_{V_i}x_i + v_{L_i}(1 - x_i)}, \tag{73}$$

$$\alpha_t = \frac{v_{V_t}x_i}{v_{V_t}x_i + v_{L_i}(1 - x_i)}, \tag{74}$$

and

$$\beta = \frac{1}{n} + \left(1 - \frac{v_{L_i}}{v_{V_t}}\right)\left[\frac{(1 - x_i)NP_t}{x_i s_{VLE_t}}\frac{ds_{LE}}{dP} - \frac{c_{p_V}}{s_{VL_i}}\left(\frac{1}{n} - \frac{1}{\gamma}\right)\right]. \tag{75}$$

The transcendental relation for the critical pressure ratio (Eq. 71) is solved by iteration, and the resulting critical pressure ratio is used in Eq. 68 to determine the critical flow rate. Thus, unique solutions for the critical flow rate and critical pressure ratio are obtained for given upstream stagnation conditions.

When x_i goes to unity, i.e., when the upstream fluid becomes completely saturated vapor, Eq. 71 reduces to

$$\eta = \left(\frac{2}{\gamma + 1}\right)^{\gamma/(\gamma-1)} \tag{76}$$

and Eq. 68 is simplified to

$$G_c = \left(\frac{v_V}{\gamma P}\right)_t^{-1/2} . \tag{77}$$

Equations 76 and 77 are precisely the formulations for the critical flow rate (Eq. 17) and the critical pressure ratio (Eq. 19) derived in a single-phase system for an ideal gas expanding isentropically.

The foregoing formulation for the critical flow rate and critical pressure ratio has been based on a uniformly distributed flow with a nonzero entrance quality through an ideal nozzle. For entrance geometries that depart from an ideal nozzle, a two-phase compressible discharge coefficient, essentially the same as the single-phase compressible discharge coefficient,[93-95] can be used, and Eq. 71 is altered in the term $(\frac{1}{2}C_d^2\beta\alpha_t^2)$.

This model can also be applied to saturated and slightly subcooled liquid entrance conditions. For this case, $x_i \leq 0$, and the critical flow relation in Eq. 68 reduced to

$$G_c = \left[(v_V - v_{L_i})\frac{N}{s_{VL_E}}\frac{ds_{L_E}}{dP}\right]_t^{-1/2} . \tag{78}$$

The same relation for the nonequilibrium parameter (Eq. 69) is used in Eq. 78. One additional assumption must be made regarding the thermodynamic state of the vapor at the throat. It is assumed that the vapor is saturated at the throat pressure. The zero-inlet-quality condition reduced the critical-pressure-ratio relation (Eq. 70) to

$$\eta = 1 - \frac{G_c^2 v_{L_i}}{2P_{i_0}}. \tag{79}$$

The critical flow rate in Eq. 78 is substituted into Eq. 79, and the resulting transcendental relation is solved for the critical pressure ratio and subsequently for the critical flow rate. Thus, both the critical flow rate and critical pressure ratio are also determined for saturated and slightly subcooled liquid inlet conditions.

This identifies one of the significant features of this model; namely, it can predict both the critical flow rate and critical pressure ratio for saturated and slightly subcooled liquid, two-phase mixtures, as well as saturated and superheated vapor entrance fluid conditions. This capability makes this model a versatile and useful analytical tool.

c. Specific Initially Subcooled and Saturated Liquid Analytical Model. The following initially subcooled and saturated liquid critical-flow model is reviewed in this section because it will be used in the following subcooled blowdown model (Sec. III.C).

(1) Henry Model. Henry[96] proposed a model to predict the critical flow rate and critical pressure ratio for initially subcooled and saturated liquid flowing through constant-area ducts with sharp and well-rounded entrances and $L/D \geq 0$. The assumptions in the model are:

(a) The flow is one-dimensional.

(b) It is frictionless and adiabatic.

(c) It is homogeneous: $k = 1$.

(d) The liquid phase is incompressible.

(e) The rate of mass transfer at the choking location is finite (not frozen), but less than equilibrium.

The foregoing assumptions reduce Eq. 35 to

$$\frac{1}{G_c^2} = -\left[x\frac{dv_V}{dP} + (v_V - v_L)\frac{dx}{dP}\right]_e . \tag{80}$$

For constant-area, sharp-entrance ducts of $0 \leq L/D < 3$, the flow regime is a superheated liquid jet surrounded by a two-phase annulus. For $3 < L/D \leq 12$, the superheated liquid jet breaks up and vapor is formed within it. It is assumed that the fluid is completely disbursed at 12D, and the axial pressure distribution is constant until the breakup is complete. The pressure drop from upstream to $L = 12D$ in a sharp-entrance tube is then geometry-induced, and it can be written as

$$\eta = 1 - \frac{G_c^2 v_{L_i}}{2C_d^2 P_{i_0}}, \tag{81}$$

where the orifice discharge coefficient $C_d = 0.61$ is used. The fluid quality is assumed to be zero at 12D, but the rate of mass transfer, $(dx/dP)_e$, is considered to be finite. The exit quality is formulated as in Eq. 64 with $k = 1$, and the exit equilibrium quality is that in Eq. 38. The nonequilibrium parameter N, given by

$$N = \begin{cases} 20x_{E_e}, & x_{E_e} < 0.05 \\ 1, & x_{E_e} \geq 0.05, \end{cases} \tag{82}$$

was developed for exit pressures up to 300 psia, and it was assumed to be valid at 12D. From Eqs. 38 and 64, the factor $(dx/dP)_e$ in Eq. 80 then becomes

$$\left(\frac{dx}{dP}\right)_e = N\left(\frac{dx_E}{dP}\right)_e = \frac{-N}{s_{VL_e}}\left[x_E\frac{ds_V}{dP} + (1 - x_E)\frac{ds_L}{dP}\right]_e. \tag{83}$$

This simplifies Eq. 80 to

$$\frac{1}{G_c^2} = \left[-(v_V - v_{L_i})N\frac{dx_E}{dP}\right]_e, \tag{84}$$

where the vapor phase is assumed to be saturated at the exit pressure. Equations 84 and 81 are similar to those derived by Henry and Fauske[1] in Eqs. 78 and 79 for nozzle flow, except for the differences of the discharge coefficient and the exit equilibrium quality. Equations 81 and 84 are then solved simultaneously while satisfying the critical-flow criterion, Eq. 13, for the critical flow rate and critical pressure ratio based only on the upstream stagnation pressure and temperature. Even though this model is derived for L/D = 12, it has been shown to be accurate to at least L/D = 5.[9]

The foregoing model can be extended to consider sharp-entrance, constant-area ducts of L > 12D. In this case, the total pressure drop is the entrance pressure drop, Eq. 81, plus a momentum flashing pressure drop given by

$$\Delta P_M = G_c^2 x_e(v_{V_e} - v_{L_i}). \tag{85}$$

The overall pressure drop is then the sum of Eqs. 81 and 85, which yields

$$\eta = 1 - \frac{G_c^2}{P_{i_0}}\left[\frac{v_{L_i}}{2C_d^2} + x_e(v_{V_e} - v_{L_i})\right]. \tag{86}$$

The nonequilibrium parameter N in Eq. 82 is assumed to be applicable for L/D > 12, and the exit quality is considered to be finite. The vapor phase is considered to expand isothermally; when this assumption is combined with Eq. 83, Eq. 80 becomes

$$\frac{1}{G_c^2} = \left[\frac{xv_V}{P} - (v_V - v_{L_i})N\frac{dx_E}{dP}\right]_e. \tag{87}$$

For sharp-entrance tubes, the exit quality is assumed to increase and approach the long-tube exit quality x_{LT} (Eq. 64) in an exponential manner as given by

$$x_e = x_{LT}\left(1 - \exp\left\{-B[(L/D) - 12]\right\}\right), \tag{88}$$

where B = 0.0523. Equations 86, 87, 88, and 64 are then solved simultaneously while satisfying the critical-flow criterion (Eq. 13) for the critical flow rate and critical pressure ratio based only on the upstream stagnation pressure and temperature.

The model can also be extended to consider ducts of $L/D \geq 0$ with a smooth entrance for which $C_d = 1$. The quality is assumed to be zero at $L/D = 0$, and the entrance pressure drop is given by Eq. 81 with $C_d = 1$. Equation 86 for $C_d = 1$ is considered to describe the total pressure drop, and the critical flow rate is assumed to be represented by Eq. 87. The exit quality for a smooth-entrance duct is given by

$$x_e = x_{LT}\left\{1 - \exp\left[-B(L/D)\right]\right\}, \tag{89}$$

where x_{LT} is formulated in Eq. 64 and B is again 0.0523.

C. Subcooled-blowdown Model

The initial period of blowdown in which the fluid in a system is initially subcooled or saturated liquid is analyzed in this section. It is assumed that a system that initially contains a fluid at an elevated subcooled-liquid thermodynamic state is instantaneously opened to ambient conditions. The flow from the system through the constant-area exhaust duct is considered to be one-dimensional and choked at the discharge-duct exit for most of the subcooled period of decompression. The elasticity of the vessel material is considered, and the volume of the exhaust duct is assumed to be constant.

The period at the start of subcooled blowdown in which the flow rate increases from zero to a quasi-steady choked value is normally relatively short. This interval is also typically of the same order as the time required to exhaust the original fluid mass contained within the discharge duct. This can be shown by applying the momentum equation to the fluid in a smooth-entrance, frictionless exhaust duct as

$$(P_{i_0} - P_a)A_e = \rho_\ell A_e L_{ED}\frac{du}{dt}. \tag{90}$$

Equation 90 yields a constant fluid acceleration in the ideal discharge duct as given by

$$\frac{dG}{dt} = \rho_\ell\frac{du}{dt} = \frac{1}{L_{ED}}(P_{i_0} - P_a). \tag{91}$$

Equation 91 can be integrated for an arbitrary entrance to the exhaust duct to determine the time required for the flow rate to increase to a given value as

$$t_G = \frac{GL_{ED}}{C_d(P_{i_0} - P_a)}. \tag{92}$$

The required time to exhaust the original fluid mass in the discharge duct can be evaluated from

$$m_{ED} = \rho_\ell A_e L_{ED} = \int_0^{t_{EM}} GA_e\, dt = \int_0^{t_{EM}} \frac{C_d}{L_{ED}} A_e(P_{i_0} - P_a)t\, dt, \tag{93}$$

which yields

$$t_{EM} = L_{ED}\left[\frac{2\rho_\ell}{C_d(P_{i_0} - P_a)}\right]^{1/2}. \tag{94}$$

Thus, for any flow rate less than

$$G = \left[2C_d\rho_\ell(P_{i_0} - P_a)\right]^{1/2}, \tag{95}$$

and in particular for the critical flow rate, Eqs. 92 and 94 indicate that $t_{G_c} < t_{EM}$. For Test 2 in this study, which was initiated at 402-psia saturated-water conditions, the length of the exhaust duct was about 13 in., the discharge coefficient was virtually unity as ascertained in the calibration test, and the initial critical flow rate was about 6100 lbm/sec-ft^2. This test is used for illustration, even though it was an initially saturated-liquid run. The time required for the flow rate to increase to 6100 lbm/sec-ft^2 was about 4 msec; the required time to empty the original fluid mass in the discharge duct was about 9 msec. This shows that the accelerating flow period at the start of blowdown is small compared to the overall subcooled decompression period during most of which time the flow is choked.

The transient, unchoked flow rate at the start of subcooled blowdown can be determined from Eq. 92 while accounting for the instantaneous internal vessel pressure. When the flow rate in Eq. 92 increases to the critical flow rate, the flow becomes choked at the exit of the exhaust duct. The critical flow rate and the critical pressure ratio can be independently determined from an initially subcooled- and saturated-liquid critical-flow model, such as that of Henry,[96] evaluated at the instantaneous internal vessel conditions. After the increasing transient flow rate equals the critical flow rate, the flow is then choked, and the exit pressure is assumed to increase instantaneously to the critical exit pressure and remain at such a value for the remainder of subcooled decompression.

The continuity equation for flow from the system is

$$\frac{dm_\ell}{dt} = -GA_e, \tag{96}$$

and this relation with the unchoked flow rate from Eq. 92, or the critical flow rate, whichever is pertinent, can be integrated to determine the instantaneous fluid mass remaining within the system. The specific volume of the remaining liquid within the system is then determined from

$$v_\ell = \frac{V_T}{m_\ell}. \tag{97}$$

The effect of the elasticity of the vessel material on the subcooled blowdown can be accounted for by considering the hoop stress in a thin-walled vessel,[97] $\delta/D_i \leq 0.1$, as given by

$$\sigma = \frac{1}{2\delta}\left[P_0 D_i - P_a(D_i + 2\delta)\right]. \tag{98}$$

The strain ε produced by a normal stress σ in a vessel that obeys Hooke's law in the elastic range of the vessel material is

$$\varepsilon = \frac{\sigma}{E_{ves}}, \tag{99}$$

where the strain is defined as

$$\varepsilon = \frac{dr}{r}. \tag{100}$$

For a cylindrical vessel, the internal volume is given by

$$V_T = \pi r_i^2 L, \tag{101}$$

and differentiating Eq. 101 produces

$$dV_T = 2V_T\frac{dr_i}{r_i}. \tag{102}$$

The strain (Eq. 100) can be substituted directly into Eq. 102 to determine the change in the original, unstressed vessel volume by the initial difference in pressure imposed across the vessel wall (Eq. 98).

Equation 97 can be differentiated to produce

$$\frac{dv_\ell}{dt} = \frac{1}{m_\ell}\frac{dV_T}{dt} - \frac{V_T}{m_\ell^2}\frac{dm_\ell}{dt}, \tag{103}$$

where dm_ℓ/dt is evaluated from Eq. 96, and dV_T/dt is evaluated by determining the change in the volume of the vessel caused by the internal vessel pressure decreasing from the initial stagnation pressure.

The rate of pressure decrease within the system is also controlled by the elasticity of the liquid as given by

$$\frac{dP}{dt} = -\frac{E_\ell}{v_\ell}\frac{dv_\ell}{dt}, \tag{104}$$

where dv_ℓ/dt is determined from Eq. 103. Equations 98-104 can then be combined to determine the pressure in the vessel at a given time during depressurization after acoustic relief. This analysis then predicts the subcooled decompression characteristics of a system while considering the elasticity of both the vessel material and the contained liquid, unchoked flow at the start of the blowdown, and critical flow during the major portion of subcooled decompression.

D. Bubble-growth Blowdown Model

The pressure-recovery phenomenon during the early stage of blowdown after the system pressure has dropped below the local saturation pressure is analyzed in this section. It is postulated that the volume-producing mechanism within the system after the end of subcooled depressurization is that of inertially and thermally dominated vapor-bubble growth. The internal volume of the system is considered constant, so that

$$V_T = V_V + V_L = m_V v_V + m_L v_L. \tag{105}$$

Equation 105 can be differentiated to produce

$$\frac{dv_V}{dt} = \frac{-1}{m_V}\left(v_L\frac{dm_L}{dt} + v_V\frac{dm_V}{dt} + m_L\frac{dv_L}{dt}\right). \tag{106}$$

We can determine dv_L/dt from the elasticity of the liquid phase as

$$\frac{dv_L}{dt} = \frac{-1}{E_L v_L}\frac{dP}{dt}. \tag{107}$$

If the vapor phase is assumed to expand along the saturated-vapor boundary, which is essentially an isothermal expansion, the left side of Eq. 106 can be approximated as

$$\frac{dv_V}{dt} = -\frac{v_V}{P}\frac{dP}{dt}. \tag{108}$$

Substituting Eqs. 107 and 108 into Eq. 106 produces the following relation for the time rate of change of the system pressure:

$$\frac{dP}{dt} = \frac{PE_L}{m_V v_V E_L + V_L P}\left(v_L \frac{dm_L}{dt} + v_V \frac{dm_V}{dt}\right). \tag{109}$$

The total mass flow rate from the system is given by

$$\frac{dm}{dt} = -GA_e. \tag{110}$$

For homogeneous, incompressible flow, which is a good approximation during the early, low-void-fraction period of the blowdown,

$$G = \rho u = \left[2\rho(1 - \eta)P_{i_0}\right]^{1/2}, \tag{111}$$

where η is the saturated-liquid critical-exit-pressure ratio, and the fluid density is given by

$$\rho = \rho_V\alpha + \rho_L(1 - \alpha). \tag{112}$$

Equation 111 can be rearranged as

$$u = \left[\frac{2(1 - \eta)P_{i_0}}{\rho_V\alpha + \rho_L(1 - \alpha)}\right]^{1/2}. \tag{113}$$

The mass flow rate of the liquid phase from the system is then

$$\frac{dm_L}{dt} = -\rho_L A_e(1 - \alpha)\left[\frac{2(1 - \eta)P_{i_0}}{\rho_V\alpha + \rho_L(1 - \alpha)}\right]^{1/2}, \tag{114}$$

and the mass flow rate of the vapor phase from the system is

$$\frac{dm_{V_e}}{dt} = -\rho_V A_e\alpha\left[\frac{2(1 - \eta)P_{i_0}}{\rho_V\alpha + \rho_L(1 - \alpha)}\right]^{1/2}. \tag{115}$$

Equation 114 for the rate of liquid mass escaping from the system can be substituted directly into Eq. 109. The change in the mass of the vapor phase within the system in Eq. 109 is the net result of the production rate of vapor mass by bubble growth within the system and the rate of vapor mass exhausted from the system.

The inertially dominated bubble-growth period[98] given by

$$r = \left[\tfrac{2}{3} v_\ell (P_{sat} - P_\ell)\right]^{1/2} t \tag{116}$$

is very short for most fluids, and it was approximately 10^{-8} sec in the tests reported in this study. Thus, the bubble growth is assumed to be primarily thermally controlled,[99,100] as given by

$$r = \left[\frac{12}{\pi}\alpha_\ell \mathrm{Ja}^2\right]^{1/2} t^{1/2}, \tag{117}$$

where the Jakob number Ja is

$$\mathrm{Ja} = \frac{c_{p_L} \rho_L (T - T_{sat})}{\rho_V h_{VL}}. \tag{118}$$

This is ascertained by equating Eqs. 116 and 117 to determine the period of inertially dominated bubble growth. This time interval serves as the minimum time increment for calculating bubble growth if only the thermally dominated regime is considered. However, the inertially controlled period should always be determined and considered if it is significant.

The volume of an individual spherical bubble growing in a thermally dominated manner, Eq. 117, is given by

$$V_b = \tfrac{4}{3}\pi \left(\frac{12}{\pi}\alpha_\ell \mathrm{Ja}^2\right)^{3/2} t^{3/2}, \tag{119}$$

where t is the time from inception.

The departure diameter of steam bubbles growing from a surface in pool-boiling conditions has been correlated by Cole and Rohsenow[101] and is given by

$$D_d = 1.5 \times 10^{-4} \left[\frac{\sigma}{g(\rho_L - \rho_V)}\right]^{1/2} \left(\frac{c_{p_L} \rho_L T_{sat}}{\rho_V h_{VL}}\right)^{5/4}. \tag{120}$$

The departure diameter can then be used in Eq. 117 to determine when a bubble will separate from the surface. By knowing the departure-bubble diameter and the total amount of internal surface area within the system, and considering that the bubbles on the wall at departure are spherical in shape and arranged in a typical triangular array, we can determine the maximum number of nucleation sites by assuming the bubbles touch at departure as

$$N_{MAX} = \frac{2}{\sqrt{3}} \frac{S_T}{D_d^2}. \tag{121}$$

The period of growth of a given generation of bubbles from the surface can be broken down into time increments less than the time of departure of the bubbles in order to analyze their differential growth. For a time greater than the inertially controlled period and less than the departure time of a bubble from the surface, the increasing diameter of a bubble can be determined from Eq. 117. Equation 119 can be differentiated to determine the incremental increase in the volume of a given generation of bubbles as

$$\Delta V_{V_{\tau,g}} = \frac{3}{2} V_{V_{\tau-1,g}} \frac{\Delta t_\tau}{t} + 3V_{V_{\tau-1,g}} \frac{\Delta Ja_\tau}{Ja_\tau}, \tag{122}$$

where $V_{V_{\tau-1,g}}$ is the total volume of vapor in the generation of bubbles at time step $\tau - 1$. When the diameter of the growing bubbles on the surface reach the departure diameter given in Eq. 120, another generation of bubbles leaves the surface and continues to grow in the bulk liquid. The net increase in vapor volume of all previous generations in the free stream during a given time interval is

$$\Delta V_{V_{\infty_\tau}} = \sum_{g=1}^{G-1} \left(\frac{3}{2} V_{V_{\infty_{\tau-1,g}}} \frac{\Delta t_\tau}{t} + 3V_{V_{\infty_{\tau-1,g}}} \frac{\Delta Ja_\tau}{Ja_\tau} \right) + v_{V_\tau} \Delta m_{V_{e_\tau}}, \tag{123}$$

where Δm_{V_e} is given in Eq. 115. The total vapor volume of all previous generations in the free stream up to the present time is then

$$V_{V_\infty} = \sum_{\tau=1}^{T} \Delta V_{V_{\infty_\tau}}. \tag{124}$$

The total vapor volume in all generations of bubbles up to the present time is

$$V_V = V_{V_\infty} + V_{V_w}, \tag{125}$$

where

$$V_{V_w} = \sum_{\tau'=1}^{\tau'} \Delta V_{V_{w_{\tau'}}} = \sum_{\tau'=1}^{\tau'} \left(\frac{3}{2} V_{V_{w_{\tau'-1}}} \frac{\Delta t_{\tau'}}{t} + 3 V_{V_{w_{\tau'-1}}} \frac{\Delta Ja_{\tau'}}{Ja_{\tau'}} \right). \tag{126}$$

Time in Eq. 126 is measured from the start of the current generation of bubbles growing from the solid surface. The void fraction in a given section, i, of the system can be determined by knowing the current total volume of vapor in that sector as

$$V_{V_i} = \sum_{g=1}^{G} V_{b_{g_i}} N_{g_i}, \tag{127}$$

and the current total vapor volume in the entire system as

$$V_{V_T} = \sum_{g=1}^{G} V_{b_{g_T}} N_{g_T}, \tag{128}$$

where the volume of a bubble in a given generation is stated in Eq. 119. If the pressure is nearly uniform in the system, so that the bubble size growing from the surface and the number of existing bubble generations are approximately the same in all regions of the system, then

$$V_{V_i} \Big/ V_{V_T} = \sum_{g=1}^{G} N_{g_i} \Big/ \sum_{g=1}^{G} N_{g_T}. \tag{129}$$

Using Eq. 121 reduces Eq. 129 to

$$\frac{V_{V_i}}{V_{V_T}} = \frac{S_i}{S_T}. \tag{130}$$

Since the void fraction in a given sector of the system is defined as

$$\alpha_i \equiv \frac{V_{V_i}}{V_i}, \tag{131}$$

use of Eq. 130 produces

$$\alpha_i = \frac{S_i}{S_T V_i} V_{V_T}. \tag{132}$$

The value of the void fraction in the region nearest the break in the system is then used in Eqs. 114 and 115 to determine the amount of the liquid and vapor phases exhausted from the system per unit time. The total vapor volume produced in the system at a given time is the sum of the increase in volume of the vapor bubbles in the free stream and those growing from the solid surface, as given by

$$\Delta V_{V_\tau} = \Delta V_{V_{\infty_\tau}} + \Delta V_{V_{w_\tau}'}, \tag{133}$$

where the two terms on the right side of Eq. 133 are given in Eqs. 123 and 126. The incremental mass of vapor produced within the system can be approximated as

$$\Delta m_{V_{P_\tau}} = \rho_{V_\tau} \Delta V_{V_\tau}. \tag{134}$$

The net change in the mass of the vapor phase within the system is then

$$\Delta m_{V_\tau} = \Delta m_{V_{P_\tau}} + \Delta m_{V_{e_\tau}}. \tag{135}$$

This net change in the mass of the vapor within the system, given by Eq. 135, is then used in Eq. 109, and the current total mass of the vapor phase contained within the system is

$$m_V = \sum_{\tau=1}^{\underline{\tau}-1} \Delta m_{V_\tau} + \Delta m_{V_{\underline{\tau}}}. \tag{136}$$

If the diameter of the bubbles in the present generation growing from the surface has not yet reached the departure diameter, they and the free stream bubbles continue to grow at a rate determined by the instantaneous Jakob number (see Eq. 122). However, if the diameter of the growing bubbles in the present generation has reached the departure diameter, this generation of bubbles separates from the surface, and the current internal vessel pressure determines a new departure-bubble diameter from Eq. 120. This then determines, from Eq. 121, a new value of the number of vapor bubbles growing from the surface in the next generation. This analysis then applies to the period of blowdown in which the fluid configuration remains to be that of bubbles growing in a superheated liquid.

E. Dispersed Blowdown Model

The period of blowdown in which the fluid configuration changes from vapor bubbles growing in a superheated liquid toward a dispersed liquid-vapor mixture that approaches thermodynamic equilibrium is considered in this section. If the transition from a bubbly to dispersed fluid configuration is assumed to occur at a characteristic value of the void fraction α_i, such as about 0.3, and the remaining fluid is assumed to expand isentropically, the pressure P_i and fluid quality x_i at this condition would then determine the initial specific entropy s_i from which the fluid would expand in the dispersed regime of blowdown as given by

$$s_i = s_V(P_i)x_i + s_L(P_i)(1 - x_i). \tag{137}$$

For a homogeneous fluid, the quality at the fluid-configuration transition in Eq. 137 can be determined from

$$x_i = \frac{v_L(P_i)\alpha_i}{v_L(P_i)\alpha_i + v_V(P_i)(1 - \alpha_i)}. \tag{138}$$

The continuity equation for flow from the system is given by

$$\frac{dm}{dt} = -G_c A_e, \tag{139}$$

which can be integrated to determine the instantaneous fluid mass remaining within the system. The two-phase critical flow rate in Eq. 139 is determined from the Henry-Fauske[1] critical-flow model. The instantaneous specific volume of the remaining mixture is determined from $v = V/m$, and this specific volume can then be used to determine the homogeneous-fluid quality from

$$x = \frac{\frac{V}{m} - v_L(P)}{v_{VL}(P)}. \tag{140}$$

If the remaining homogeneous mixture is assumed to expand isentropically so that

$$s_i = s_V(P)x + s_L(P)(1 - x) = \text{constant}, \tag{141}$$

where the fluid quality in Eq. 141 is that from Eq. 140, then Eqs. 137-141 can be combined to determine the pressure history in a system during the homogeneously dispersed regime of blowdown.

IV. EXPERIMENTAL APPARATUS

A. Description of Experimental Apparatus

Figure 4 is a schematic diagram of the blowdown vessel, its internals, and its supporting mechanisms. The method in which the vessel was mounted and the associated hardware is illustrated in Figs. 5 and 6, and the pertinent dimensions of the vessel and the internals are shown in Fig. 7.

The purpose of the internals was to simulate a similar hydraulic configuration in the experimental blowdown vessel as in a full-size reactor vessel, particularly in the downcomer annulus region. The flow areas in the downcomer annulus were scaled by the ratio of the exhaust-duct flow area in the experimental vessel to the inlet-duct flow area in a full-size vessel. During the blowdown, the internal vessel geometry forced the fluid to descend to the bottom of the internal skirt before it ascended the downcomer annulus.

1. Blowdown Vessel and Internal Geometry

The blowdown vessel was a Type 304L stainless steel cylinder with $17\frac{5}{16}$-in. ID and a 7/16-in.-thick wall. It had a Type 304L stainless steel dome end cap on the bottom, and a Type 304L stainless steel dome end cap and flange connection on the top. When the vessel was completely assembled with all its internals and the extension spool on the exhaust port, the internal volume was 5.40 ft^3 up to the location of the inner rupture disk.

The internal skirt consisted of an upper flange of 1/4-in.-thick, $22\frac{1}{8}$-in.-OD, 14-in.-ID Type 304 stainless steel plate, a section of 14-in., 15-in.-long Type 304 stainless steel pipe, a rim of 3/8-in.-thick, $15\frac{1}{2}$-in.-OD, $13\frac{7}{16}$-in.-ID Type 304 stainless steel plate, and a section of 18.038-in.-long, 16-in. Type 304 stainless steel pipe. These pieces were welded together to make the internal skirt. Spacers of 5/16-in. diameter and 9/16 in. long were welded around the outside diameter of the lower portion of the skirt to maintain a uniform annular spacing between the outside of the skirt and the inside of the pressure vessel, as shown in Fig. 8. Figure 9 is an assembly drawing of the blowdown vessel and its internals.

The portion of the vessel below the dome flange was wrapped with shielded, Nichrome, resistance trace-heater wire as shown in Fig. 10. The total heating power of the trace heaters was about 2 kW. In addition, three U-shaped immersion heaters (of 4-kW power each) were installed in the vessel through the upper flange, as shown in Fig. 11. One cylindrical immersion heater (of 6-kW power) was also installed in the vessel through the bottom flange. This provided a total electrical heating power of about 20 kW.

The entire vessel and exhaust duct were then covered with about 1 in. of felt insulation. A coating of muslin was applied over the insulation.

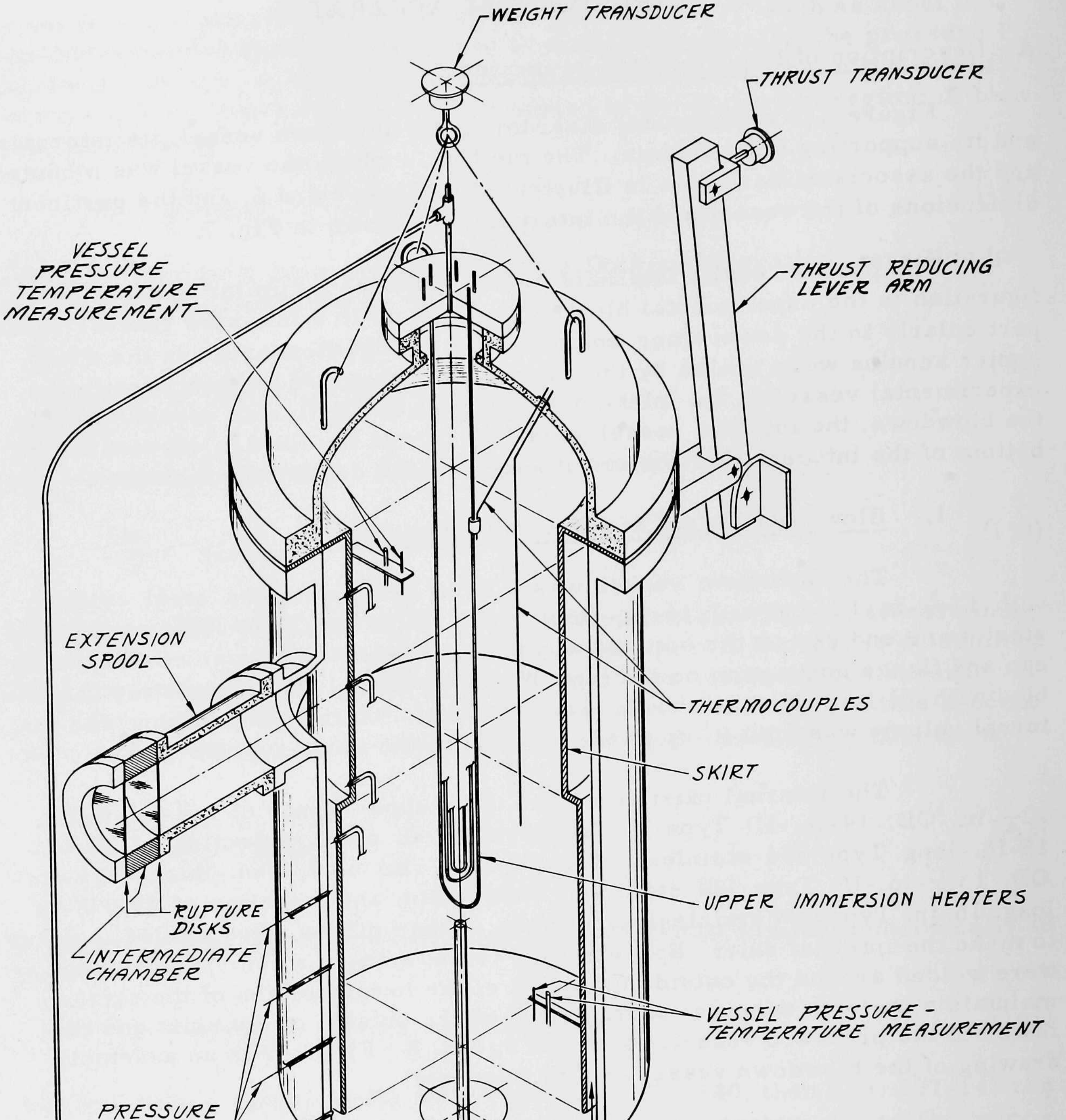
WEIGHT TRANSDUCER
THRUST TRANSDUCER
VESSEL PRESSURE TEMPERATURE MEASUREMENT
THRUST REDUCING LEVER ARM
EXTENSION SPOOL
THERMOCOUPLES
SKIRT
UPPER IMMERSION HEATERS
RUPTURE DISKS
INTERMEDIATE CHAMBER
VESSEL PRESSURE-TEMPERATURE MEASUREMENT
PRESSURE TAPS
DOWNCOMER ANNULUS
LOWER IMMERSION HEATER
VESSEL DIFFERENTIAL PRESSURE TRANSDUCER

Fig. 4. Schematic of Blowdown Vessel and Internals. ANL Neg. No. 900-3186.

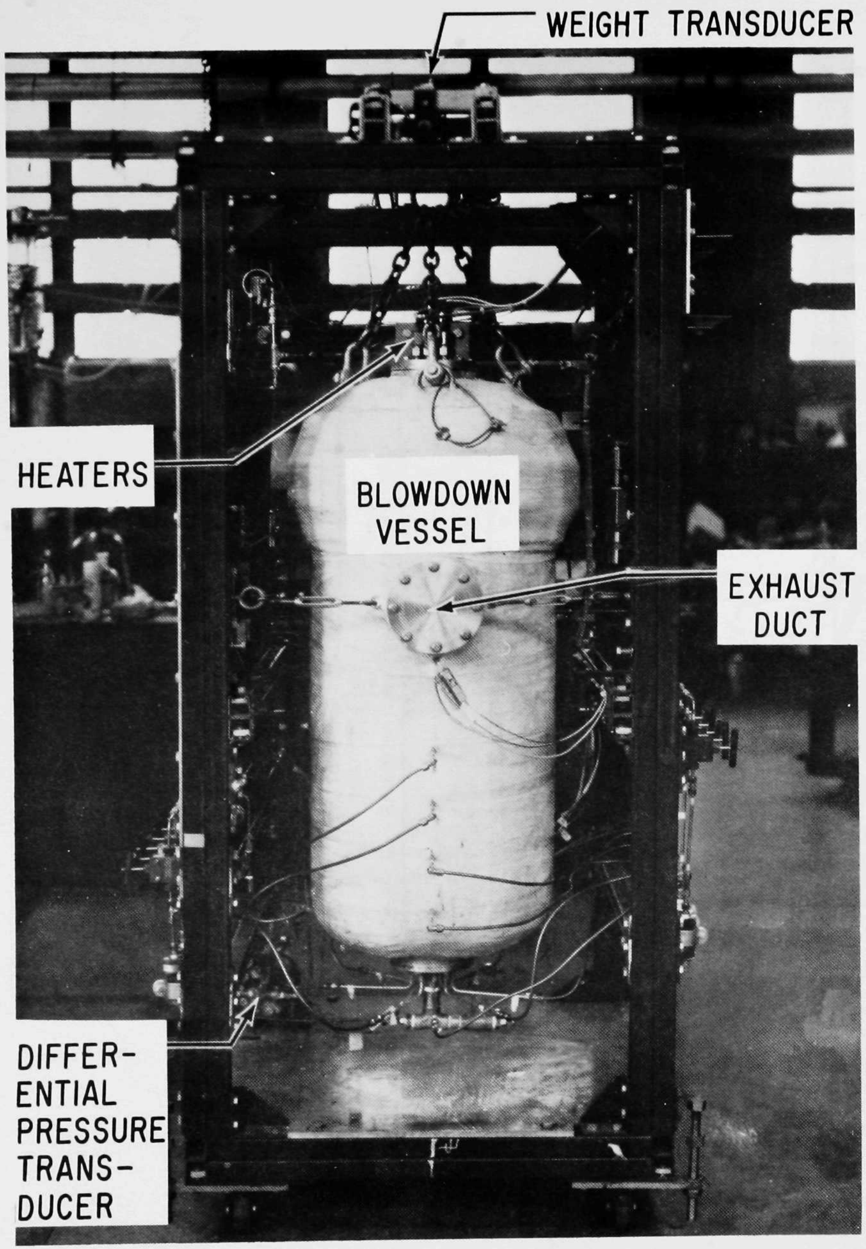
WEIGHT TRANSDUCER
HEATERS
BLOWDOWN VESSEL
EXHAUST DUCT
DIFFERENTIAL PRESSURE TRANSDUCER

Fig. 5. Front View of Blowdown Apparatus.
ANL Neg. No. 900-5146A Rev. 1.

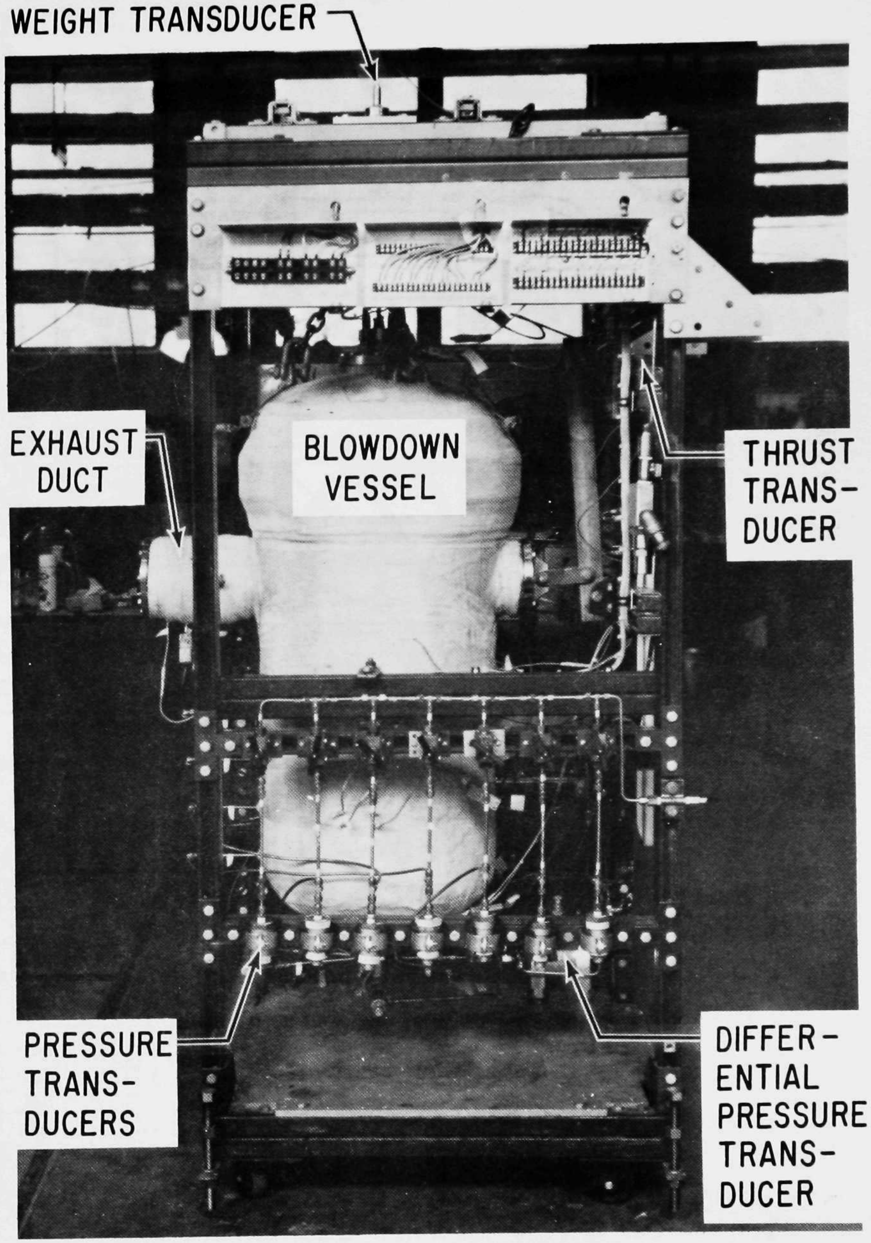
WEIGHT TRANSDUCER
EXHAUST DUCT
BLOWDOWN VESSEL
THRUST TRANSDUCER
PRESSURE TRANSDUCERS
DIFFERENTIAL PRESSURE TRANSDUCER

Fig. 6. Side View of Blowdown Apparatus.
ANL Neg. No. 900-5145A Rev. 1.

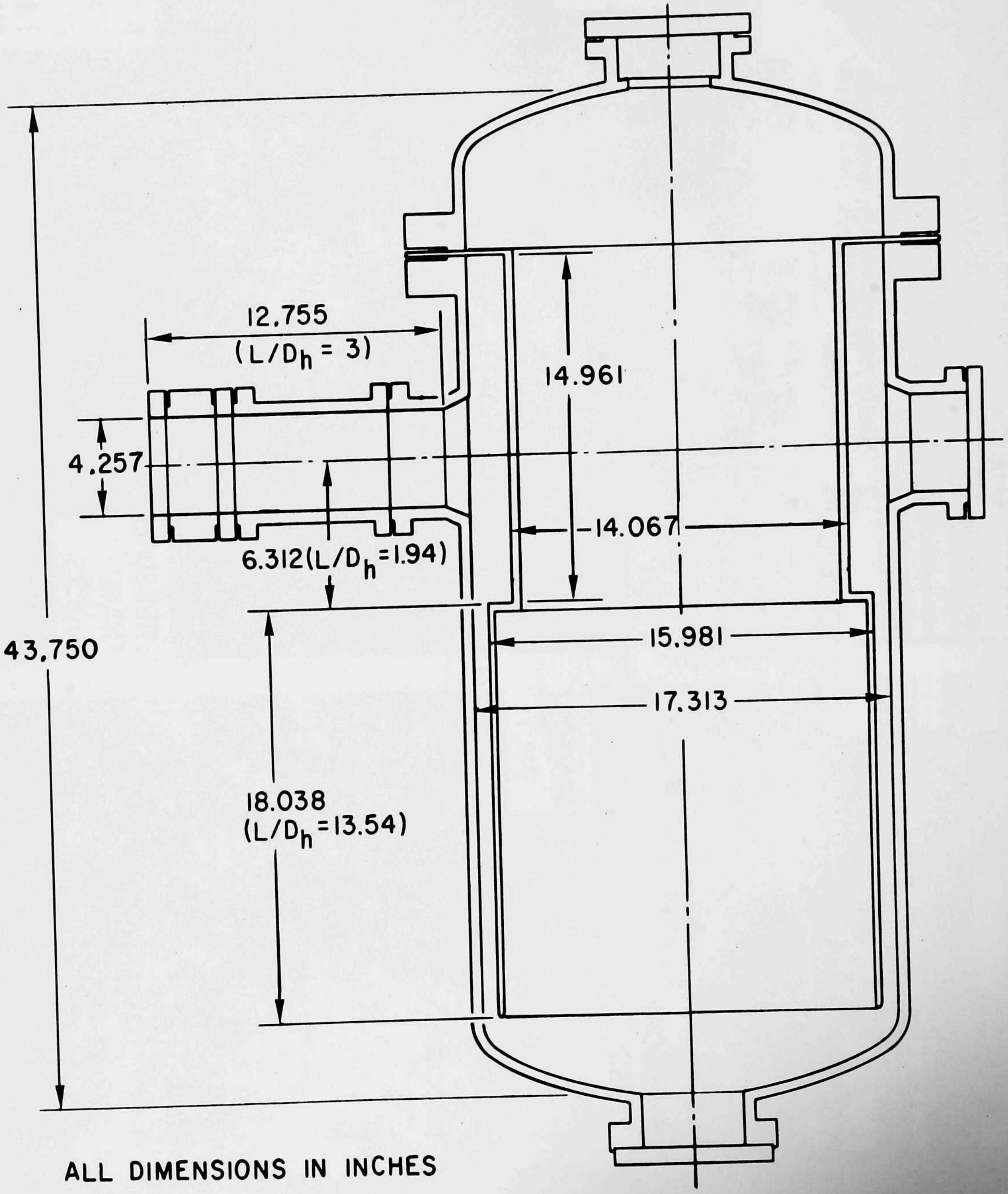
12.755
(L/D_h = 3)
14.961
4.257
14.067
6.312(L/D_h=1.94)
43.750
15.981
17.313
18.038
(L/D_h=13.54)
ALL DIMENSIONS IN INCHES

Fig. 7. Small-size Blowdown Vessel and Internals. ANL Neg. No. 900-4070A Rev. 1.

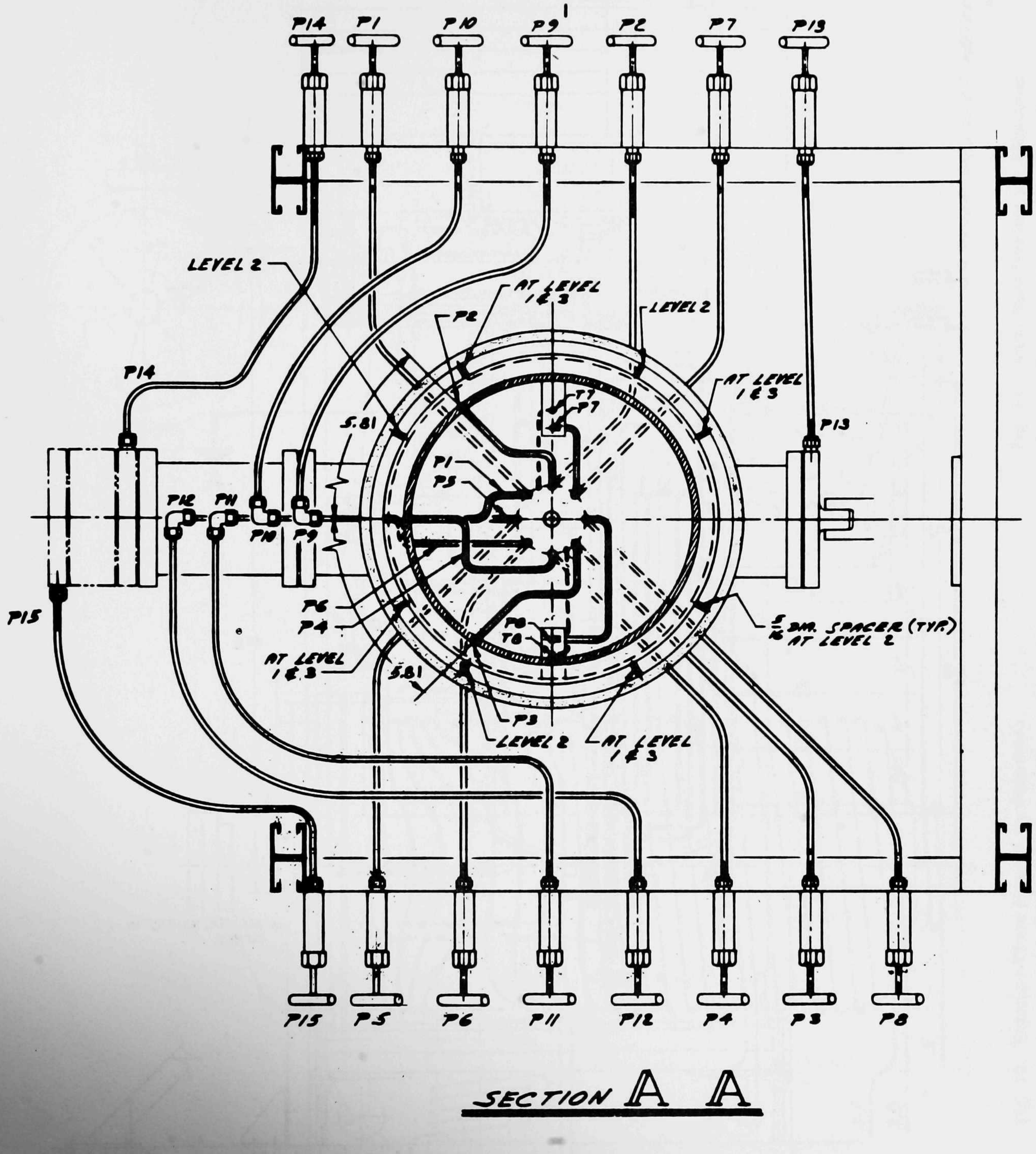
P14
P1
P10
P9
P2
P7
P13
LEVEL 2
AT LEVEL 1 & 3
P2
LEVEL 2
P14
AT LEVEL 1 & 3
T7
P7
5.81
P13
P1
P5
P12
P11
P10
P9
P15
P6
P4
P8
T8
AT LEVEL 1 & 3
5.81
5/16 DIA. SPACER (TYP.) AT LEVEL 2
P3
LEVEL 2
AT LEVEL 1 & 3
P15
P5
P6
P11
P12
P4
P3
P8
SECTION A A

Fig. 8. Top View of Internal Geometry of Blowdown Vessel. (All dimensions in inches.) ANL Neg. No. 900-4319B.

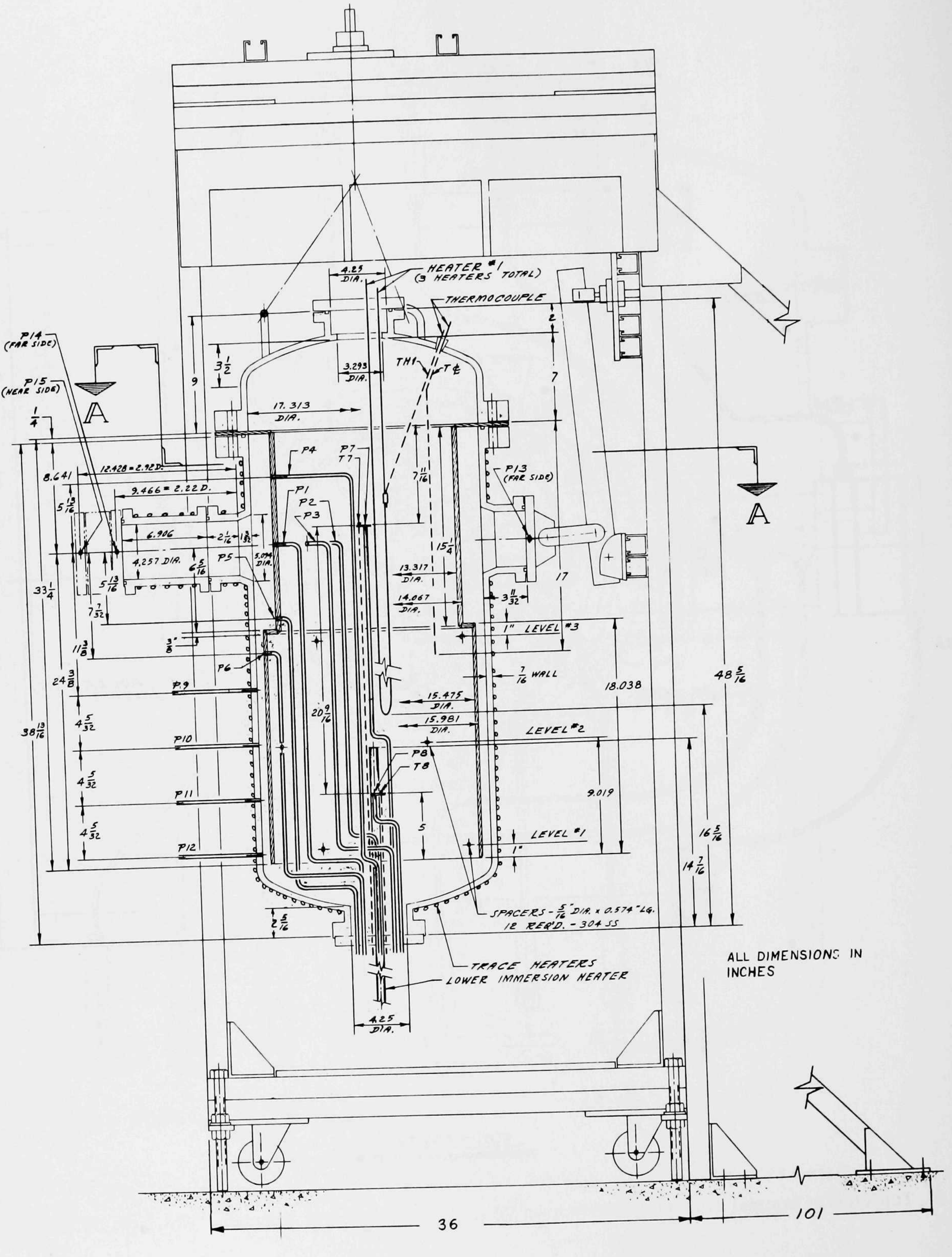
HEATER #1 (3 HEATERS TOTAL)
4.25 DIA.
THERMOCOUPLE
P14 (FAR SIDE)
P15 (NEAR SIDE)
A
A
3 1/2
9
2
7
3.293 DIA.
TH1
T ℄
17.313 DIA.
1/4
8.641
12.428 = 2.92 D.
9.466 = 2.22 D.
5 13/16
6.906
2 1/16
1 3/32
4.257 DIA.
6 5/16
5 13/16
P5
5.094 DIA.
P4
P7
T7
P1
P2
P3
7 11/16
15 1/4
P13 (FAR SIDE)
13.317 DIA.
14.067 DIA.
3 11/32
17
33 1/4
7 7/32
11 3/8
3"/8
1" LEVEL #3
P6
7/16 WALL
24 3/8
18.038
48 5/16
P9
15.475 DIA.
15.981 DIA.
20 9/16
LEVEL #2
38 13/16
4 5/32
P10
P8
T8
9.019
4 5/32
P11
5
16 5/16
LEVEL #1
4 5/32
P12
1"
14 7/16
SPACERS - 5/16" DIA. x 0.574" LG. 12 REQ'D. - 304 SS
2 5/16
TRACE HEATERS
LOWER IMMERSION HEATER
ALL DIMENSIONS IN INCHES
4.25 DIA.
36
101

Fig. 9. Internal Geometry and Mounting of Blowdown Vessel. ANL Neg. No. 900-4319 Rev. 2.
]

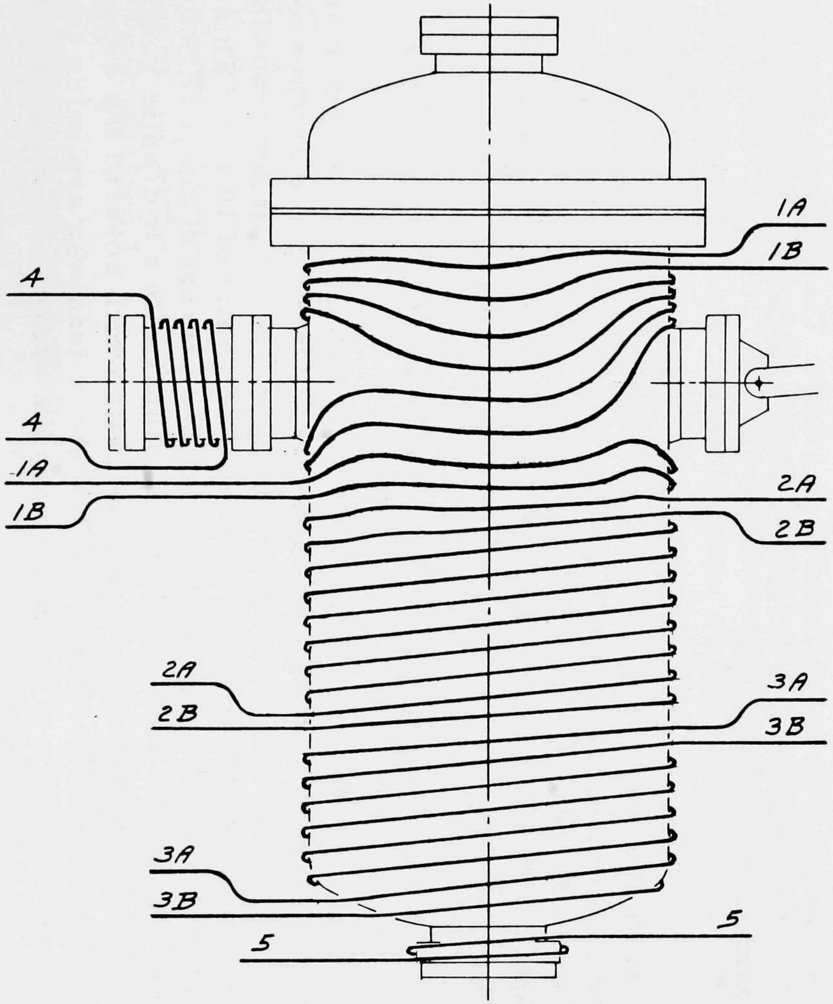
1A
1B
4
4
1A
1B
2A
2B
2A
2B
3A
3B
3A
3B
5
5

Fig. 10. External Trace Heaters for Blowdown Vessel. ANL Neg. No. 900-4321.

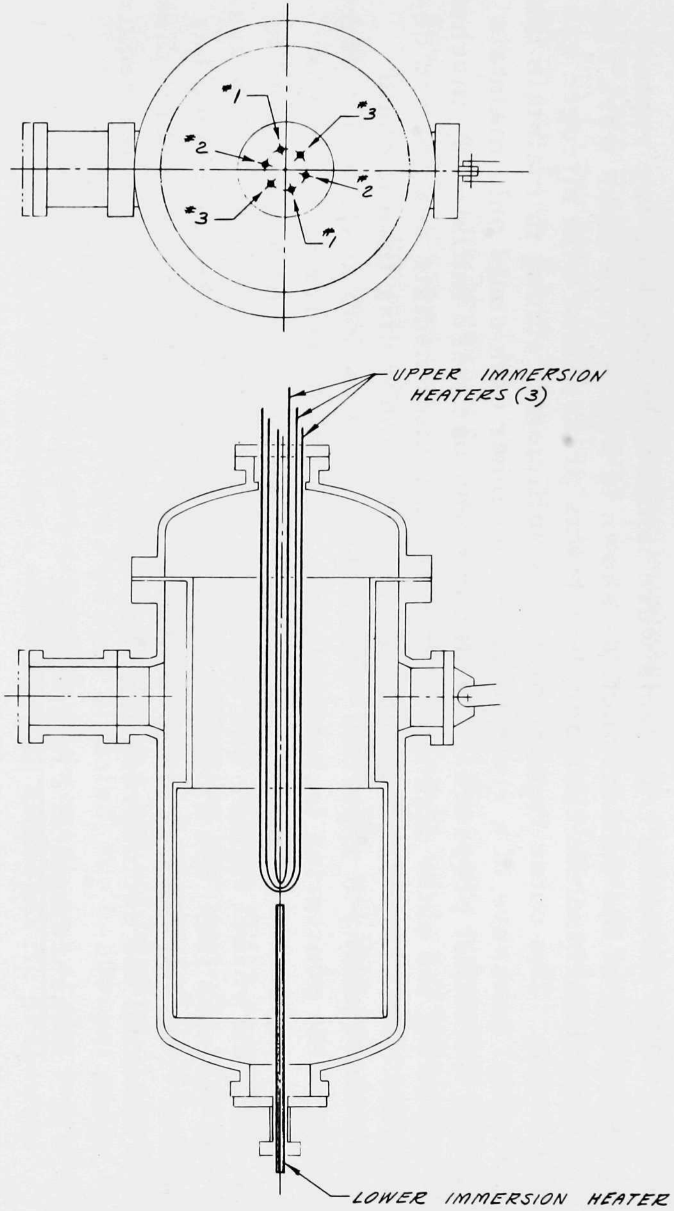
#1
#3
#2
#2
#3
#1
UPPER IMMERSION HEATERS (3)
LOWER IMMERSION HEATER

Fig. 11. Immersion Heaters for Blowdown Vessel. ANL Neg. No. 900-4322.

2. Rupture-disk Assembly

The blowdown transients were initiated by breaking two rupture disks on the end of the exhaust duct, as shown in Fig. 4. The disks were separated by an intermediate chamber, which was pressurized with nitrogen gas during heatup. The outer rupture disk was sufficiently strong to maintain the entire initial pressure of a given test, but the inner disk could only maintain about half the initial pressure. The decompressions were initiated by mechanically rupturing the outer disk and permitting the intermediate chamber to depressurize. This imposed a greater force on the inner disk than it could sustain; consequently it ruptured. There was also a backup system to rupture the disks if the puncturing technique failed. A high-pressure nitrogen-gas source was connected to the blowdown vessel, which could have been used to pressurize the vessel further and eventually fail the rupture disks. This system was isolated from the blowdown vessel with a valve to keep nitrogen gas separated from the working fluid. Mechanically failing the outer rupture disk always initiated the decompressions, and the backup system was never required.

3. Measurement of Fluid Weight

As can be seen in Fig. 4, the vessel and its contents were suspended from a weight transducer, which was a Statham, UC3, unbonded-type strain-gauge, Universal Transducing Cell. The cell was mounted in a Statham, UL4, 1000-lb_f load-cell accessory head, which permitted the cell to detect a maximum load of 1250 lb_f.

The weight transducer was statically precalibrated by filling and emptying the vessel with cold water. During the test, the initial weight of the nearly saturated water within the vessel was known from the internal vessel volume and the measured initial stagnation temperature of the fluid. This, coupled with a posttest determination of the remaining water in the vessel, also permitted an accurate, hot weight calibration.

4. Thrust Measurement

As shown in Fig. 4, the thrust that was produced during the blowdown was transmitted through a reducing lever arm to another force transducer, which was the same type instrument as the weight transducer. The thrust-reducing lever arm had a reduction ratio of 10 to 1. This combination permitted the measurement at a maximum thrust of about 12,500 lb_f. The thrust transducer was statically calibrated with a hydraulic jack, and the static load was applied directly to a blank plate which covered the exhaust port during the calibration (Figs. 5 and 6). The static load was applied in this manner to simulate the action of the thrust upon the vessel and instrumentation during the actual decompression.

5. Pressure Measurement

All the pressure measurements were made with strain-gauge pressure transducers. Figure 12 is a schematic diagram showing the location of the 15 pressure taps. More detailed locations of the pressure taps are also shown in Figs. 8 and 9.

The pressure transducers were all Statham, unbonded, strain-gauge transducers, and their ranges varied from 0-500 to 0-2500 psig, the more sensitive ones being located at the positions of greatest importance. The response of each transducer was about 3250 Hz, and this was considerably faster than the blowdown event.

All the pressure transducers in the system were calibrated cold by filling the system with water and then imposing nitrogen-gas pressure over the water. The gas pressure was monitored with a calibrated 0-500-psi bourbon-tube pressure gauge. There was also a hot calibration of the pressure transducers. Just before a test was initiated, the 0-500-psi gauge indicated the initial stagnation pressure within the vessel, and at the end of the decompression, all the pressures were down to atmospheric pressure.

6. Measurement of Void Fraction

An attempt was made to measure the bulk void fraction of the fluid remaining in the vessel during the blowdown with a differential pressure transducer. The instrument used was a Statham, ±5 psi, 5000-psig-maximum, PM-80-type, unbonded strain-gauge transducer. Its position and the location of its connections to the vessel are indicated in Fig. 4.

The differential pressure transducer was calibrated cold by filling and emptying the vessel with water. A hot calibration of the transducer was also possible. Just before a test was started, the vessel was full of nearly saturated water and the transducer indicated a full condition. When the decompression was completed, the transducer registered an empty condition plus the remaining liquid that was accounted for.

The differential pressure transducer did not perform precisely as desired in these tests. The transducer recording system either did not respond, or it responded in a manner that saturated the recording system. The saturation effect was probably due to the diaphragm in this transducer hitting its mechanical stops. Thus, reliable measurements of the bulk void fraction were not obtained.

7. Temperature Measurement

The temperatures of the fluid and the vessel were monitored with 14 Chromel-Alumel thermocouples as shown in Fig. 13. Eight thermocouples

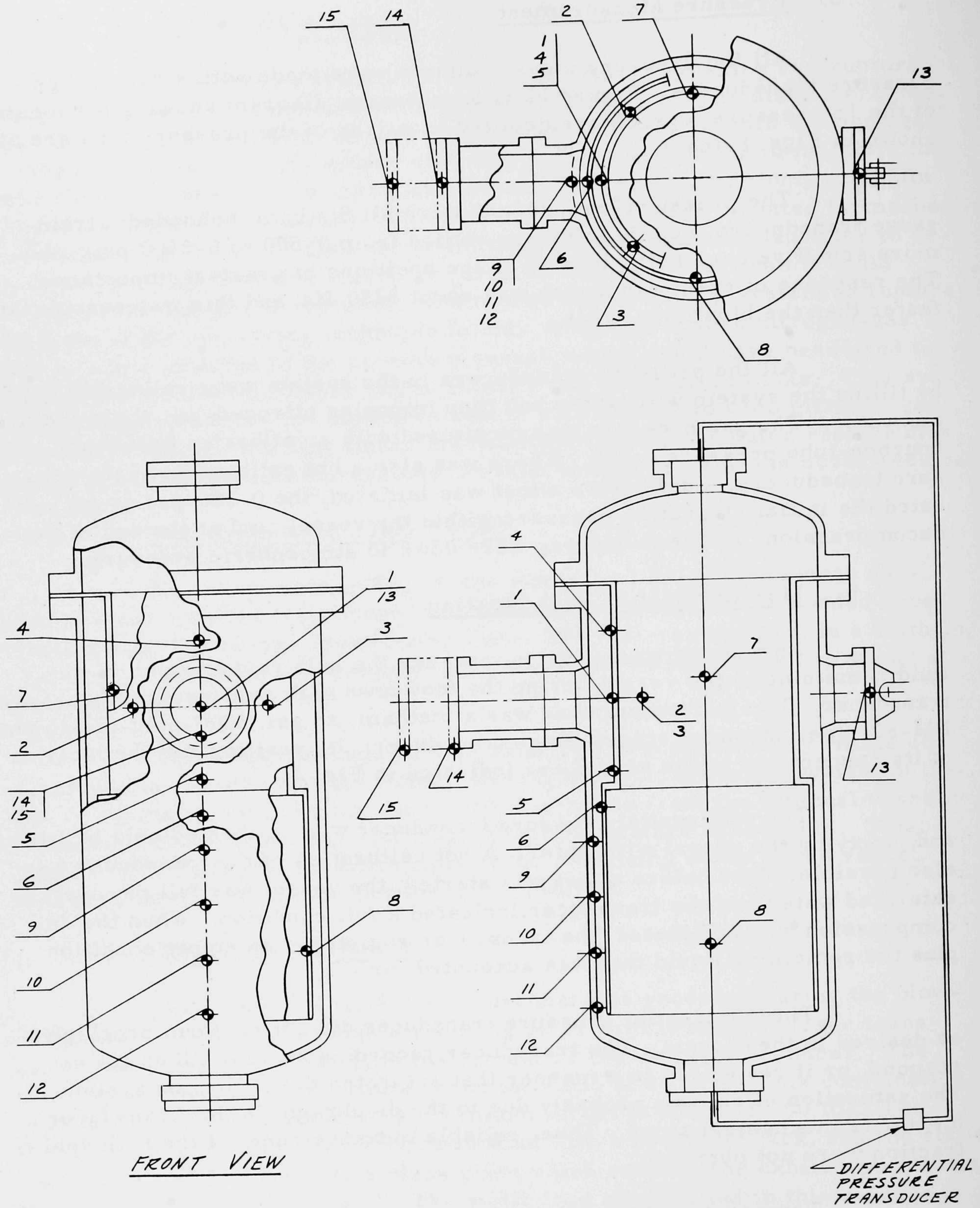
15
14
1
4
5
2
7
13
6
9
10
11
12
3
8
4
1
13
3
7
2
14
15
5
6
9
10
11
8
12
FRONT VIEW
4
1
7
2
3
14
15
13
5
6
9
10
8
11
12
DIFFERENTIAL
PRESSURE
TRANSDUCER

Fig. 12. Pressure-tap Locations. ANL Neg. No. 900-4323.

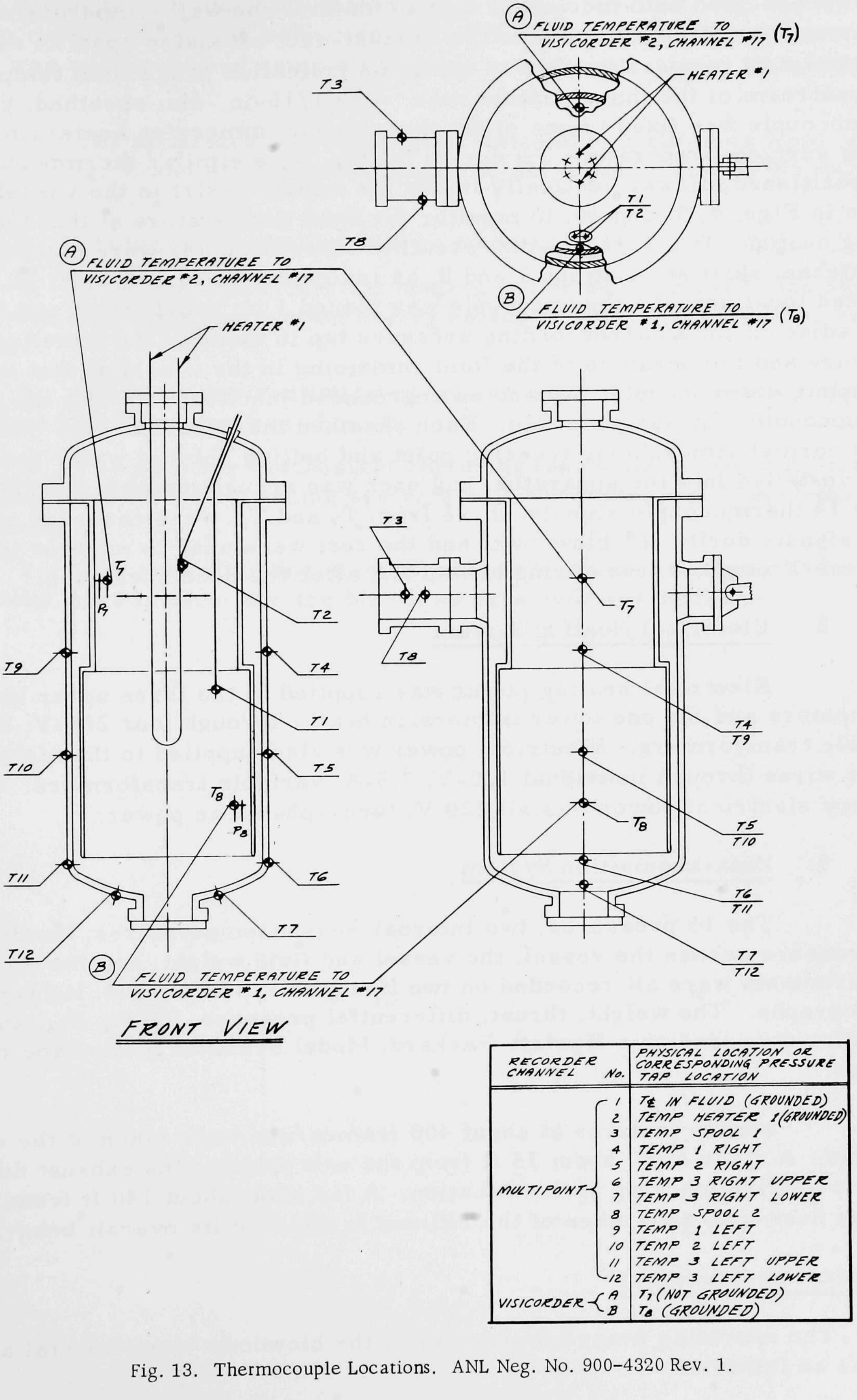
(A) FLUID TEMPERATURE TO VISICORDER #2, CHANNEL #17 (T_7)
HEATER #1
T3
T1
T2
T8
(B) FLUID TEMPERATURE TO VISICORDER #1, CHANNEL #17 (T_8)
(A) FLUID TEMPERATURE TO VISICORDER #2, CHANNEL #17
HEATER #1
T_7
P_7
T2
T9
T4
T1
T10
T5
T_8
P_8
T11
T6
T12
T7
(B) FLUID TEMPERATURE TO VISICORDER #1, CHANNEL #17
FRONT VIEW
T3
T8
T_7
T4
T9
T5
T10
T_8
T6
T11
T7
T12

RECORDER CHANNEL	No.	PHYSICAL LOCATION OR CORRESPONDING PRESSURE TAP LOCATION
MULTIPOINT	1	T℄ IN FLUID (GROUNDED)
	2	TEMP HEATER 1 (GROUNDED)
	3	TEMP SPOOL 1
	4	TEMP 1 RIGHT
	5	TEMP 2 RIGHT
	6	TEMP 3 RIGHT UPPER
	7	TEMP 3 RIGHT LOWER
	8	TEMP SPOOL 2
	9	TEMP 1 LEFT
	10	TEMP 2 LEFT
	11	TEMP 3 LEFT UPPER
	12	TEMP 3 LEFT LOWER
VISICORDER	A	T_7 (NOT GROUNDED)
	B	T_8 (GROUNDED)

Fig. 13. Thermocouple Locations. ANL Neg. No. 900-4320 Rev. 1.

were spot-welded onto the vessel wall to monitor the wall temperature. Two thermocouples were welded onto the exhaust-duct extension spool to measure the spool wall temperature and to obtain an indication of the fluid temperature just upstream of the inner rupture disk. One 1/16-in.-dia, sheathed, grounded thermocouple was fixed to one of the three upper immersion heaters to monitor its surface temperature T_H during heatup. One similar thermocouple, $T_{\mathbb{C}}$, was positioned midway vertically inside the internal skirt in the vessel, as shown in Figs. 4, 9, and 10, to monitor the fluid temperature at that location during heatup. Two 1/16-in.-dia, sheathed thermocouples were placed inside the internal skirt at locations 7 and 8, as indicated in Figs. 4, 8, 9, 12, and 13. At these locations, the thermocouple was placed 1 in. apart from, and immediately adjacent to, a corresponding pressure tap to monitor the simultaneous pressure and temperature of the fluid remaining in the vessel at that location. The upper thermocouple, T_7, was an ungrounded junction, whereas the lower thermocouple, T_8, was grounded. Each sheathed thermocouple was checked at the normal atmospheric freezing point and boiling point of water before being installed into the apparatus, and each was accurate within ±0.5°F. Two of the 14 thermocouple signals, those from T_7 and T_8, were recorded as transient signals during the blowdown, and the rest were used to monitor the fluid and vessel temperatures during heatup and after the decompression.

8. Electrical Heating System

Electrical heating power was supplied to the three upper immersion heaters and the one lower immersion heater through four 280-V, 28-A, variable transformers. Electrical power was also supplied to the eight trace heater wires through individual 120-V, 7.5-A, variable transformers. The primary electrical power was all 220 V, three-phase, ac power.

9. Data-acquisition System

The 15 pressures, two internal-vessel temperatures, the differential pressure across the vessel, the vessel and fluid weight, and the thrust measurements were all recorded on two Honeywell, Model 1508, light-pen oscillographs. The weight, thrust, differential pressure, P_1, P_8, P_{14}, and T_8 were also recorded on a Hewlett-Packard, Model 3955, magnetic-tape recording unit.

Motion pictures at about 400 frames/sec were taken of the exhausting fluid. A close shot, about 15 ft from the exit plane of the exhaust duct, was taken to confirm choking at that location. A far shot, about 140 ft from the exhaust duct, was also taken of the effluent to observe its overall behavior.

B. Operating Procedure

The operating procedure for use of the blowdown experimental apparatus was as follows:

1. After all the instrumentation in the system had been calibrated and two rupture disks had been installed at the exit of the exhaust duct, the vessel was evacuated and completely filled with demineralized water under vacuum.

2. The apparatus was thoroughly fastened to a concrete floor, as indicated in Fig. 9, and all the instrumentation and power connections were made to the apparatus.

3. Photographic equipment was made ready.

4. Twenty kW of electrical heating power was applied to the system. Liquid was bled from the system during heatup to control the internal vessel pressure.

5. When the desired initial operating conditions were reached, the electrical heating power was shut off.

6. The primary mechanical rupturing mechanisms, the auxiliary rupturing system, the recording systems, and the photographic systems were made ready.

7. The recording and photographic systems were actuated, the rupture disks were broken, and the blowdown transient was initiated.

V. CALIBRATION TEST OF EXPERIMENTAL APPARATUS

To demonstrate that the system instrumentation and hardware would respond properly during the two-phase blowdown tests, a calibration decompression was performed with room-temperature water and a pressurized gas volume.

The system configuration for the calibration run is shown in Fig. 14. Rupture disks were installed at the exit of the exhaust port, and the vessel was evacuated and then filled with a known mass of room-temperature (68°F) demineralized water of 8 Mohm-cm resistivity under vacuum. Care was taken to eliminate any remaining gas in the annular spacing between the internal skirt and the vessel wall. All the pressure lines were bled to ensure that the annulus and the pressure lines were completely filled with liquid. The amount of water bled from the pressure lines was subtracted from the initial water inventory put into the vessel in order to determine the final mass and volume of water contained within the vessel. The remaining volume in the interior of the internal skirt and at the top of the vessel was filled and pressurized with nitrogen gas, as shown in Fig. 14. After the blowdown was initiated, the gas expanded against the relatively incompressible piston (that is, the water) until most of the water was exhausted.

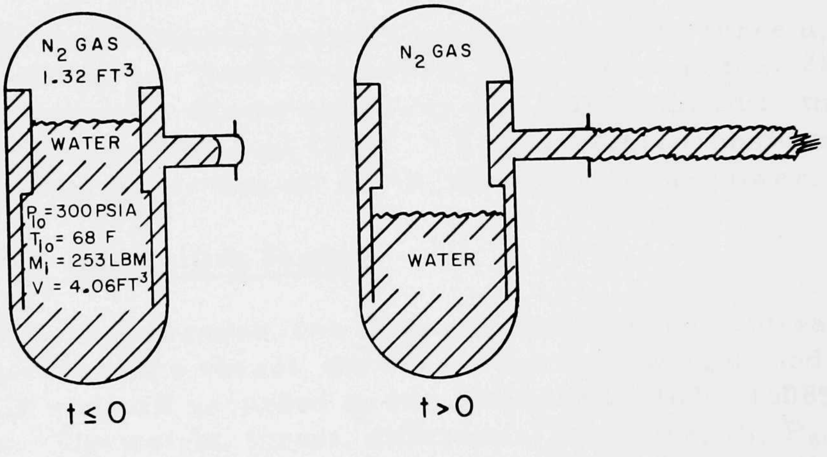

Fig. 14. System Configuration for the Calibration Run. ANL Neg. No. 900-4951.

The primary measurements were the remaining mass and the thrust; these data are shown in Figs. 15 and 16. The flow-rate history derived from the remaining-mass history in Fig. 15 is shown in Fig. 17. The concern for making certain the weight transducer responded properly was due to the large thrust load exerted on the vessel compared to the weight of the vessel and contents during the blowdown. Also, the thrust transducer signal was suspect because of possible mechanical coupling effects due to potential vessel movement and misalignment. The intent was to show that the effect of mechanical coupling of the weight and thrust transducers via the vessel had been minimized, indicating that the two instruments were virtually isolated from each other.

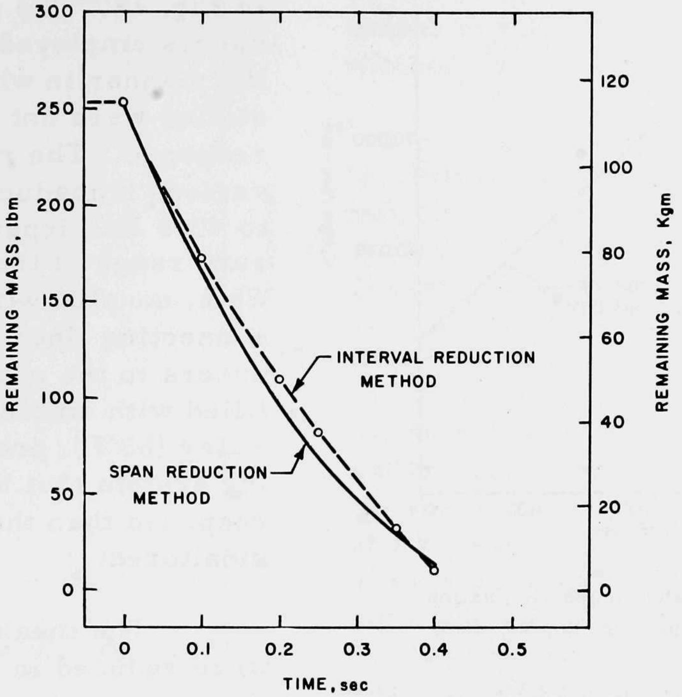

Fig. 15. Remaining Mass in the Calibration Run. ANL Neg. No. 900-4953.

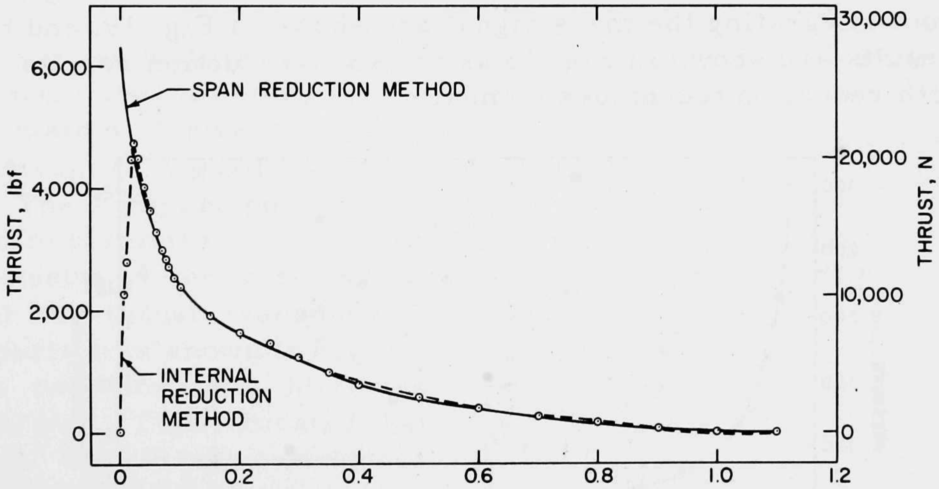

Fig. 16. Thrust Developed in the Calibration Run. ANL Neg. No. 900-4960.

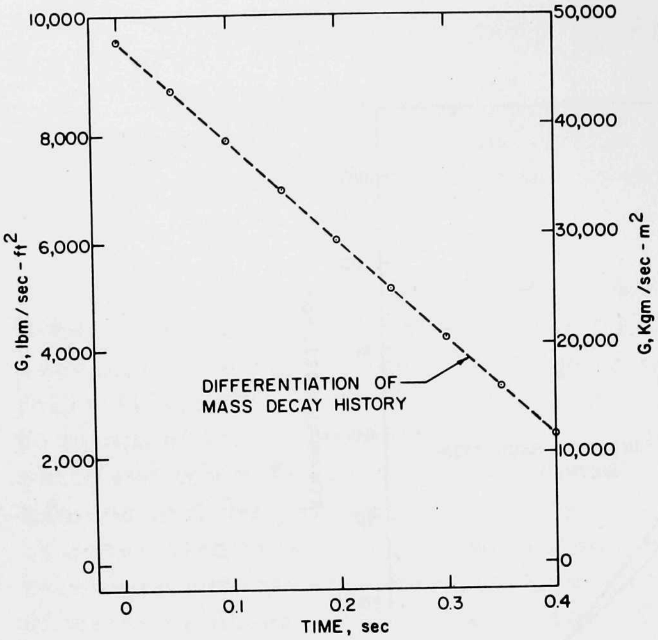

Fig. 17. Flow Rates in the Calibration Run. ANL Neg. No. 900-4965.

The measured internal pressure history in the vessel is shown in Fig. 18. The pressure transducers employed in the system and the manner in which they were installed were not suspect as to their response. The response of the various transducers was from 2500 to 4000 Hz, depending upon the pressure range of the individual sensor. This, coupled with the fact that the connecting lines from the transducers to the pressure taps were filled with ambient-temperature water (68°F), presented a measuring system that had a much faster response than the event being monitored.

The measured mass data were reduced in two ways. The first method was to determine the integrated average value of the analog mass signal at desired points in time. This was done at all desired times to produce the interval-reduction mass history in Fig. 15. The second technique was to integrate the analog mass signal (see Fig. C.1) over the entire time of the decompression, and then smooth and differentiate the integrated signal. The results from integrating the mass signal are shown in Fig. 19, and the differentiated results are shown in Fig. 15 as the span-reduction results. The results of both reduction techniques compare very well.

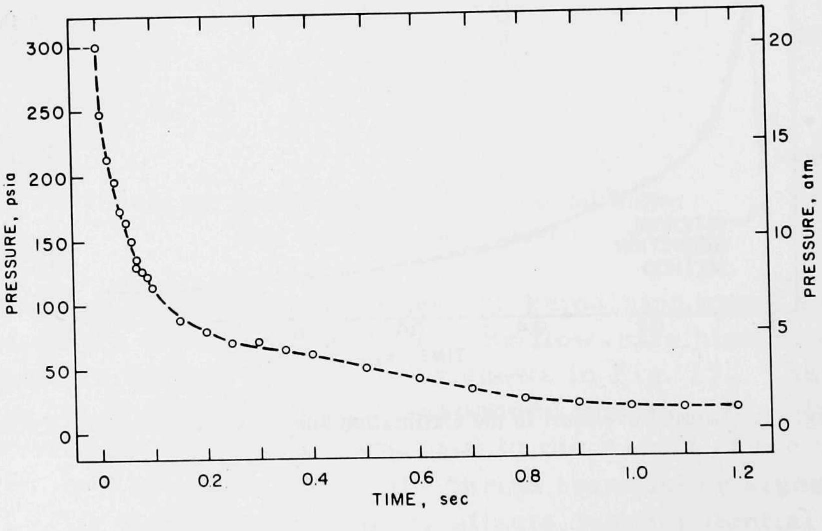

Fig. 18. Internal Vessel Pressure in the Calibration Run. ANL Neg. No. 900-5069 Rev. 2.

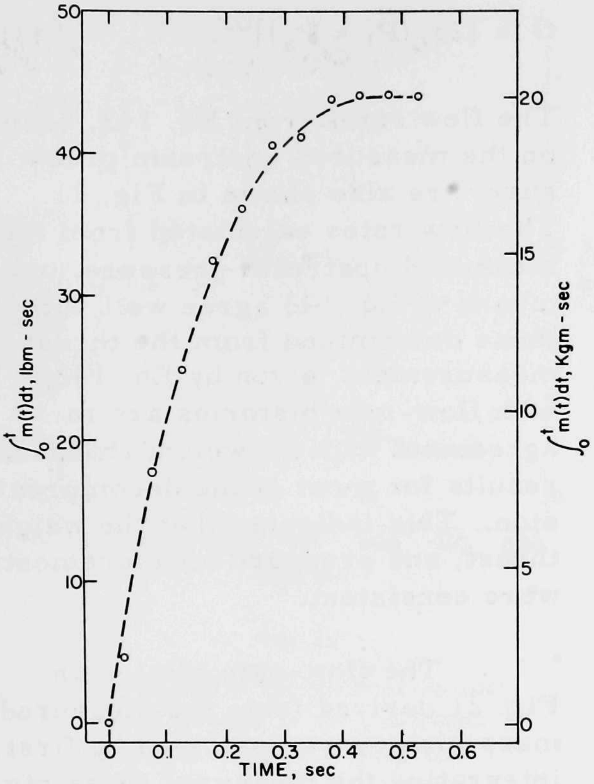

Fig. 19

Span-reduction Method of the Remaining Mass in the Calibration Run. ANL Neg. No. 900-4946.

The same procedure was employed in reducing the thrust data as seen in Figs. C.4, 16, and 20. The thrust results from both reduction methods also compare very well.

The consistency of the system-instrumentation response was determined by comparing various independent evaluations of the flow rate from the vessel. As previously noted, the measurements of primary interest were the weight and thrust signals. Since the exhausting fluid was all liquid, this permitted a check on the weight, thrust, and pressure measurements. By knowing the density of the exhausting fluid and knowing that the exit pressure was always equal to the downstream pressure (namely, the atmospheric pressure), the flow rate per unit area from the vessel could be evaluated from the measured thrust by

$$G = \left(\frac{F\rho_\ell}{A_e}\right)^{1/2}. \tag{142}$$

The mass history in Fig. 15 can be differentiated to determine the flow-rate history derived from the weight-transducer signal, given in Fig. 17. The comparison of these two flow-rate histories is a check on the consistency of the response of the weight and thrust transducers. This comparison is shown in Fig. 21, where the two flow-rate histories correspond well. This indicated that the weight- and thrust-transducer signals were consistent, and it also established confidence in their response.

The consistency of the weight and pressure measurements can also be examined. For the same assumptions used in Eq. 142, the flow rate per unit area from the vessel can be evaluated from

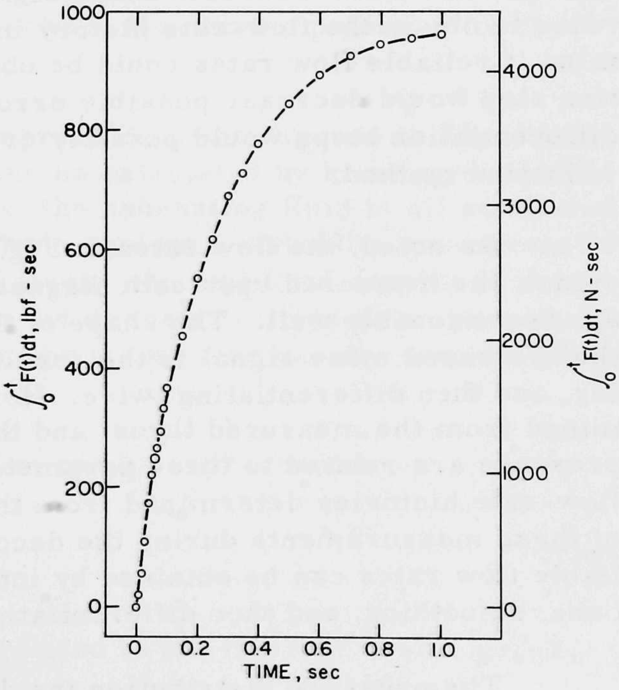

Fig. 20. Span-reduction Method of the Thrust in the Calibration Run. ANL Neg. No. 900-4947.

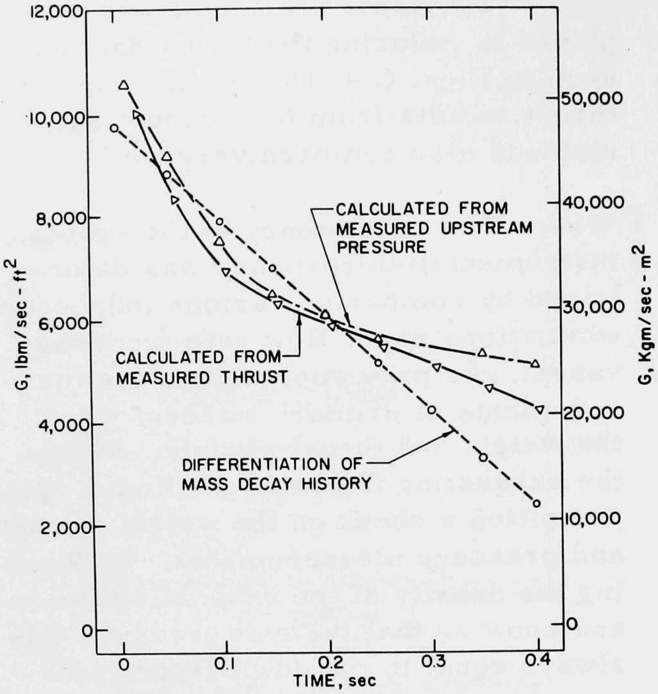

Fig. 21. Comparison of the Mass Flow Rates Determined from the Mass Decay Signal and Those from the Thrust and Upstream Pressure Signals in the Calibration Run. ANL Neg. No. 900-4948.

$$G = [2\rho_\ell(P_1 - P_a)]^{1/2}. \qquad (143)$$

The flow rates from Eq. 143, based on the measured upstream pressure, are also shown in Fig. 21. The flow rates calculated from the measured upstream pressure, by means of Eq. 143 agree well with those determined from the thrust measurement, given by Eq. 142; both flow-rate histories are in agreement with the weight-transducer results for most of the decompression. This indicates that the weight, thrust, and pressure measurements were consistent.

The flow-rate history in Fig. 21 derived from the measured mass history was obtained by first integrating the measured mass signal (see Fig. C.1), the results of which are indicated in Fig. 19, then by differentiating the smoothed curve in Fig. 19 to obtain the mass history in Fig. 15, and then by differentiating the mass history in Fig. 15 to obtain the flow-rate history in Figs. 17 and 21. Since the measured mass signal was integrated once and differentiated twice to obtain the flow-rate history in Fig. 21, this was a good test to determine if reliable flow rates could be obtained in this manner. The one integration step would decrease possible error in reducing the signal, but the two differentiation steps would possibly create potential errors in the data-reduction method.

As noted, the flow rates in Fig. 21 determined from the measured mass signal, the measured upstream stagnation pressure, and the measured thrust agree reasonably well. The shape of the flow-rate history determined from the measured mass signal is the result of integrating the signal once, smoothing, and then differentiating twice. However, the flow-rate histories determined from the measured thrust and the measured upstream stagnation pressure are related to these parameters by Eqs. 142 and 143. Thus, the flow-rate histories determined from these parameters would follow the trend of these measurements during the decompression. Figure 21 shows that reliable flow rates can be obtained by integrating the measured mass signal once, smoothing, and then differentiating twice.

The pressure distribution inside the vessel during the calibration test was considered. Figure 22 shows the differences between the average internal

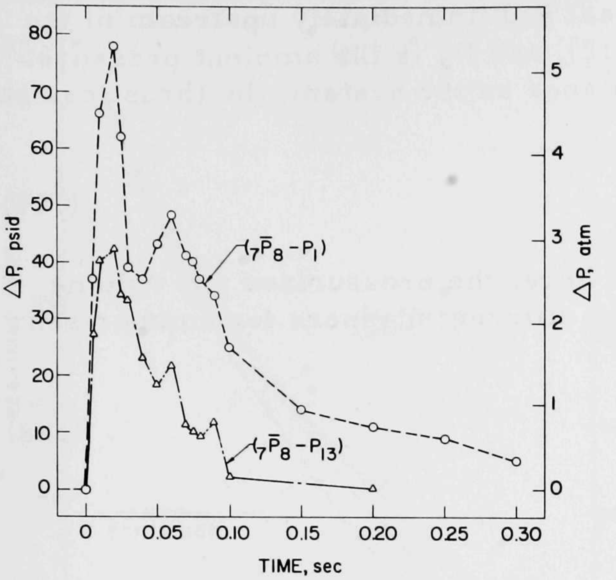

Fig. 22

Comparison of the Measured Internal Vessel Pressures in the Calibration Run. ANL Neg. No. 900-5046 Rev. 1.

vessel pressure, ${}_7\bar{P}_8$, the exhaust-duct inlet pressure, P_1, and the pressure on the opposite side of the internal skirt from the exhaust duct, P_{13}. This figure demonstrates that the differential pressure on the exhaust-port side of the internal skirt was about twice that on the side of the internal skirt away from the exhaust duct during the decompression. This indicated that there was about twice the driving potential for flow up the downcomer annulus on the exhaust-port side of the internal skirt as opposed to the side of the internal skirt away from the exhaust duct. When the flow-rate history of Fig. 21 and the differential pressure history at the exhaust-duct inlet, given in Fig. 22, were used, the equivalent flow area inside the downcomer annulus could be determined from

$$\dot{m} = A[2\rho_\ell({}_7\bar{P}_8 - P_1)]^{1/2}. \tag{144}$$

This resulted in a flow area about 84% of the total cross-sectional flow area of the lower-downcomer annulus. This suggests the existence of a two-dimensional flow distribution in the downcomer annulus, most of the flow being up the exhaust-port side of the annulus, where the driving potential for flow was the greatest.

The system response to a decompression as configured in Fig. 14 can be readily determined. The response can be calculated by knowing the initial stagnation conditions and by knowing that the exhausting fluid is all subcooled liquid, so that the pressurizing gas expands against a virtually incompressible piston. Since the exhausting fluid is all liquid, the exit fluid density is known, and the exit pressure is always equal to the downstream pressure, namely, the atmospheric pressure. In this case, the thrust then results strictly from momentum flow.

The loss of mass from the system can be expressed as

$$\frac{dm}{dt} = -GA_e, \tag{145}$$

and the instantaneous flow rate can be related to the internal vessel pressure by

$$G = [2\rho_\ell(P_1 - P_a)]^{1/2}, \tag{146}$$

where P_1 is the pressure inside the vessel and immediately upstream of the exhaust-duct entrance (see Figs. 9 and 12), and P_a is the ambient pressure. By performing an overall momentum balance on the system, the thrust can be related to the flow rate by

$$F = G^2 A_e v_\ell . \tag{147}$$

For the short blowdown time considered here, the pressurized gas volume (see Fig. 14) is assumed to expand in two different manners for comparison: isentropically,

$$PV_g^\gamma = \text{Constant}, \tag{148}$$

and isothermally,

$$PV_g = \text{Constant}. \tag{149}$$

Since the exhausting fluid is all liquid,

$$\frac{dV_\ell}{dt} = v_\ell \frac{dm}{dt} = -\frac{dV_g}{dt}. \tag{150}$$

The system response for an isentropic expansion of the gas can then be determined from

$$\frac{dP}{dt} + \frac{\gamma G A_e}{\rho_\ell V_g} P = 0 \tag{151}$$

and for an isothermal expansion from

$$\frac{dP}{dt} + \frac{G A_e}{\rho_\ell V_g} P = 0. \tag{152}$$

This formulation permits the calculation of the m(t), G(t), F(t), and P(t) of the decompression.

Figure 23 compares the measured and calculated remaining mass. The isentropic prediction was essentially coincident with the measurements to about 150 msec. At that time, the measurements started to drop below the isentropic prediction and assume a decay slope similar to the isothermal prediction. The isentropic calculation implicitly assumes no heat exchange, whereas the isothermal prediction assumes complete and instantaneous heat transfer in order to keep the gas temperature constant. The transition of the measured remaining-mass history from the isentropic prediction to assuming a decay slope similar to the isothermal prediction at about 150 msec indicates that the gas expanded nearly isentropically from the start of the blowdown to about 150 msec, and then changed to expanding in a nearly isothermal manner from about 150 msec to the end of the decompression. The gas could have conceivably gained considerable thermal energy by 150 msec into the decompression, because if it was assumed to expand isentropically from the initiation of the blowdown to this time, when the internal vessel pressure was about 88 psia (see Fig. 18), the volume occupied by the gas would have increased to about 3.17 ft^3 and the gas temperature would have decreased to about -88°F. The gas-volume increase to about 3.17 ft^3 would indicate that the liquid level was then about 6.75 in. above the bottom of the internal skirt. This is consistent with the volume of remaining liquid indicated in Fig. 15 at this time.

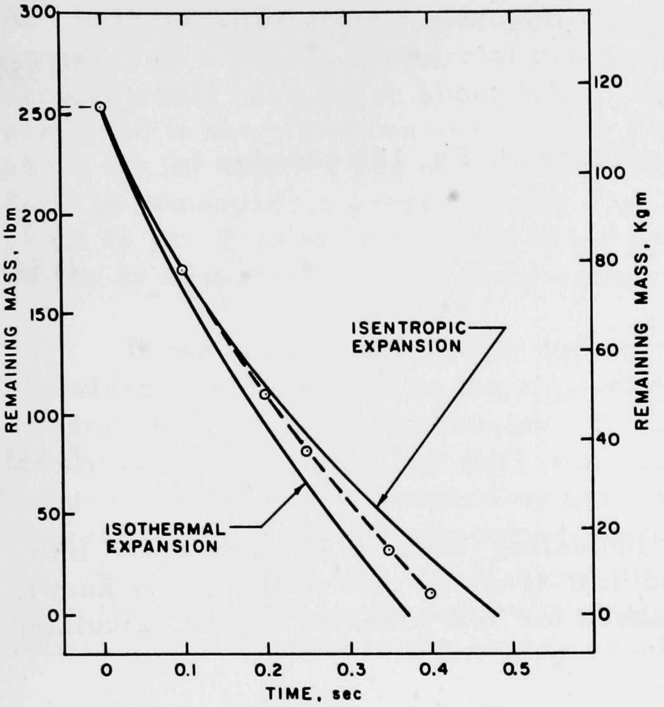

Fig. 23

Comparison of the Measured and Calculated Remaining Mass in the Calibration Run. ANL Neg. No. 900-4962.

Since the liquid was exhausted so rapidly, the liquid level on the inside of the internal skirt was accelerated downward so quickly that fragmentation of the liquid surface could have occurred and produced a fine mixture of liquid droplets entrained in the expanding gas. Since the volumetric heat capacity of the nitrogen gas was insignificant compared to that of the water, the bulk-water temperature remained nearly constant during the decompression. With a temperature difference between the expanding gas and the water and vessel wall of about 150°F at this time, there could have been considerable heat exchange if the heat-transfer surface area was sufficient. If water was dispersed in the gas as small droplets, the interfacial surface area for heat transfer would have been much larger than the exposed wall-surface area, and with the large temperature difference between the gas and the water, considerable heat would have been transferred to the expanding gas.

If the nitrogen gas were considered to have expanded isothermally from 150 msec on, the heat-transfer rate necessary to maintain the gas at a constant temperature can be readily determined. For an isothermal process,

$$PV_g = \text{Constant.} \tag{149}$$

The energy equation governing the expansion process is given by

$$\frac{dq}{dt} + v_g \frac{dP}{dt} = c_{p_g} \frac{dT_g}{dt}. \tag{153}$$

Since the process is assumed to be isothermal, Eq. 153 reduces to

$$\frac{dq}{dt} = -\frac{V_g}{m_g} \frac{dP}{dt}. \tag{154}$$

Using Eqs. 152 and 154 produces

$$\frac{dQ}{dt} = GA_e P v_\ell. \tag{155}$$

The right side of Eq. 155 is positive, indicating that heat is transferred into the expanding gas. Since the required heat-transfer rate to the gas is known from Eq. 155, the interfacial surface area for heat transfer can be calculated from

$$\frac{dQ}{dt} = hS(T_{water} - T_g) \tag{156}$$

if an appropriate heat-transfer coefficient is assumed. If the gas started to expand isothermally at 150 msec, the flow rate from the system at this time was about 7000 $lb_m/sec\text{-}ft^2$ (see Fig. 21), the internal vessel pressure was about 88 psia (see Fig. 18), and the gas temperature was about -88°F after the initial isentropic expansion. From Eq. 155, the heat-transfer rate to the gas to maintain it at -88°F would have been about 181 Btu/sec. If a heat-transfer coefficient of 50 $Btu/hr\text{-}ft^2\text{-}°F$ is assumed, the required heat-transfer surface area from Eq. 156 is about 84 ft^2. As previously noted, if the liquid level was assumed to fall as a plane surface, the level at 150 msec would be about 6.75 in. above the bottom of the internal skirt. This would expose a total wall-surface area of about 13.8 ft^2, which is only about one-sixth of the required 84 ft^2 of surface area. If a characteristic spherical-liquid-droplet size such as 100 μm is assumed, the required mass of suspended water in the nitrogen gas to provide the necessary heat-transfer surface area can be determined from the difference between the required heat-transfer surface area from Eq. 156 (84 ft^2) and the available wall-surface area (13.8 ft^2) at this time. The resulting mass of suspended 100-μm-dia liquid droplets would have to be about 0.24 lb_m, and the volumetric density of these size droplets would be about 37,900 droplets/$in.^3$ This is a reasonable mass of water to be suspended in the gas.

It can be shown that the assumed 100-μm-dia water droplets would stay in suspension during the decompression in order to serve as a heat source for the expanding gas. A 100-μm-dia sphere of water falling in nitrogen gas would reach a terminal speed of about 1 ft/sec at about 140 msec after start of fall.

At 150 msec after start of descent, which is when the expansion appeared to progress in a nearly isothermal manner (see Fig. 23), an individual liquid droplet would have fallen about 1.5 in. At 400 msec, when virtually no mass remained in the blowdown vessel (see Fig. 23), a droplet would have fallen about 4.5 in. After 1 sec of fall, when the internal vessel pressure was nearly down to atmospheric pressure (see Fig. 18), a droplet would have only fallen about 12 in. This indicates that liquid droplets of 100-μm diameter would have stayed in suspension during the decompression.

It can also be shown that sufficient heat could be transferred from the entrained liquid droplets to the expanding gas in order for the gas to approach an isothermal-expansion behavior. By using Eqs. 145 and 150 together with the measured mass history m(t) (see Fig. 15), we can determine the increasing volume occupied by the expanding gas. The initial decrease in the internal vessel pressure and the gas temperature can be evaluated isentropically from Eq. 148. Following this initial expansion, the heat-transfer rate to the gas from the entrained liquid can be evaluated from Eq. 156. This heat-transfer rate can then be used in the energy equation

$$\frac{dQ}{dt} - P\frac{dV_g}{dt} = c_{v_g} m_g \frac{dT_g}{dt} \tag{157}$$

to evaluate the gas temperature. If the expanding gas behaves ideally:

$$PV_g = m_g R T_g, \tag{158}$$

the internal vessel pressure can be estimated. Use of the heat-transfer rate from Eq. 156 in

$$\frac{dQ}{dt} = c_\ell m_\ell \frac{dT_\ell}{dt} \tag{159}$$

permits the required drop in the temperature of the entrained liquid to be determined. It is assumed that the entrained liquid does not freeze during the expansion. This technique permits the calculation of the internal vessel pressure, the expanding-gas temperature, and the entrained-liquid temperature during the decompression, all based on the measured remaining mass history (see Fig. 15). The results are shown in Fig. 24. The same calculation can also be performed by using a flow-rate relation rather than the measured mass history as in this case.

For the assumed 100-μm-dia water droplets at these temperatures, the Biot number (that is, the ratio of the internal thermal resistance to the surface thermal resistance) hL/k is less than 0.1, indicating that the temperature distribution is nearly uniform at all times in a liquid-droplet sphere of this size during a temperature transient. When the above analysis is performed,

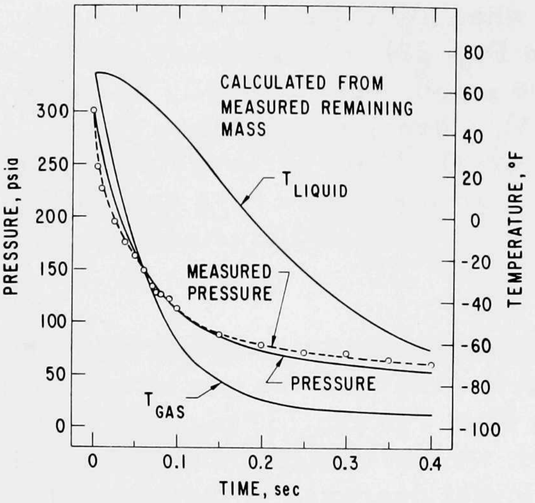

Fig. 24. Comparison of the Measured Internal Vessel Pressure and That Calculated from the Measured Mass Decay History, Considering Heat Transfer from the Entrained Liquid to the Expanding Gas in the Calibration Run. ANL Neg. No. 900-5159.

the temperature of the entrained liquid, which is assumed to remain in the liquid state during the decompression, decreases to about -60°F (see Fig. 24) at the time when most of the fluid had been exhausted from the vessel, namely, 0.4 sec in Fig. 15. The calculated history of internal vessel pressure from this analysis based on the measured remaining mass history compares very well with the measured history of internal vessel pressure, as seen in Fig. 24. This comparison indicates that the required heat transfer to the expanding gas for it to approach an isothermal behavior later in the blowdown can be supplied from the entrained liquid. The approach of the expanding gas to an isothermal behavior is illustrated in Fig. 24.

Figure 15 compares the flow rates determined from the measured mass history, and Fig. 25 shows the isentropic and isothermal calculated flow rates. The calculated flow rates agree well with the trend of the measurements. Figure 25 also shows the flow rates that were evaluated from the thrust and entrance pressure measurements (see Eqs. 142 and 143). The isentropic and isothermal predictions bracket the measured and inferred flow rates for most of the decompression. The flow-rate histories that were calculated from the thrust and entrance pressure measurements have a decay slope similar to the isentropic prediction early in the decompression, but the slope changes to nearly correspond to the isothermal prediction later in the blowdown. This transition occurs at about 150 msec. The favorable flow-rate comparisons in Fig. 25 indicate that the instrumentation in question responded properly.

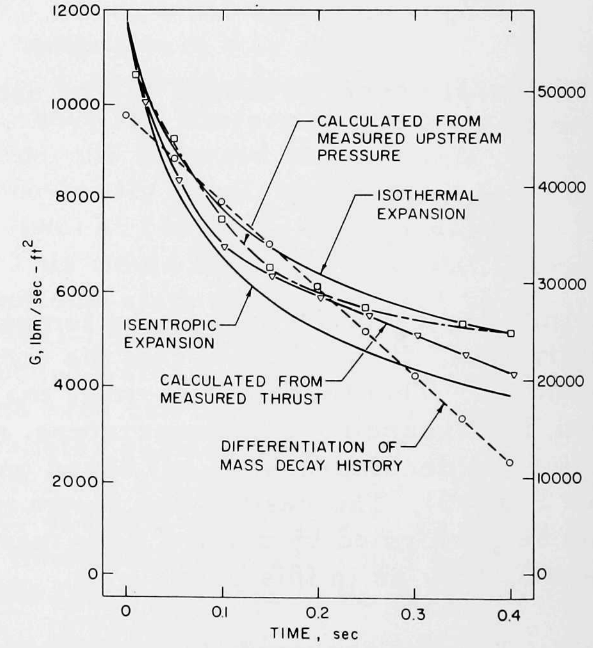

Fig. 25. Comparison of the Mass Flow Rates Determined from the Experimental Measurements and the Calculated Mass Flow Rates in the Calibration Run. ANL Neg. No. 900-5074.

Figure 26 compares the measured and calculated thrust. The isentropic calculation predicts the measured thrust well to about 100 msec, after which the slope of the measured-thrust history becomes similar to the isothermal prediction. The time of transition of the agreement of the measured-thrust history from the isentropic prediction to the isothermal prediction is similar to that of the remaining-mass history in Fig. 23, the flow-rate history in Fig. 25, and the history of internal vessel pressure in Fig. 27. Here again the expansion process was nearly isentropic to about 100 msec, after which it approached an isothermal behavior for the rest of the decompression. The heat-transfer prediction, also shown in Fig. 26, is in accord with the measured

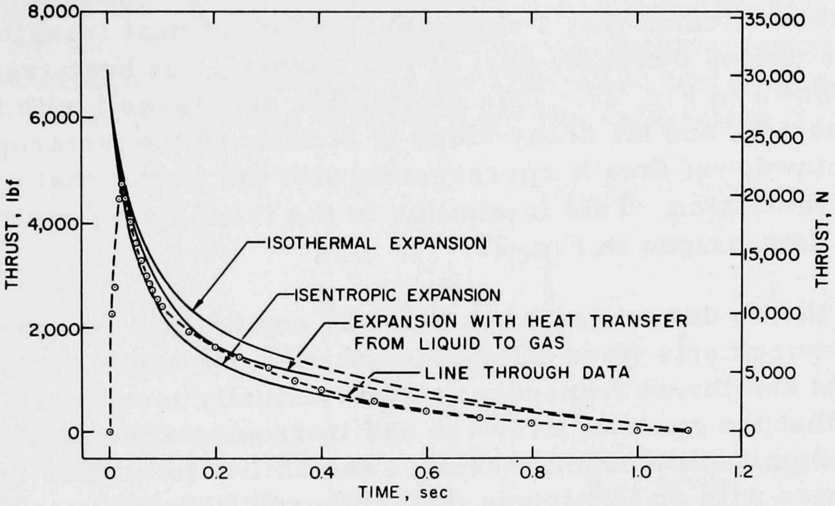

Fig. 26. Comparison of the Measured and Calculated Thrust in the Calibration Run. ANL Neg. No. 900-4996 Rev. 1.

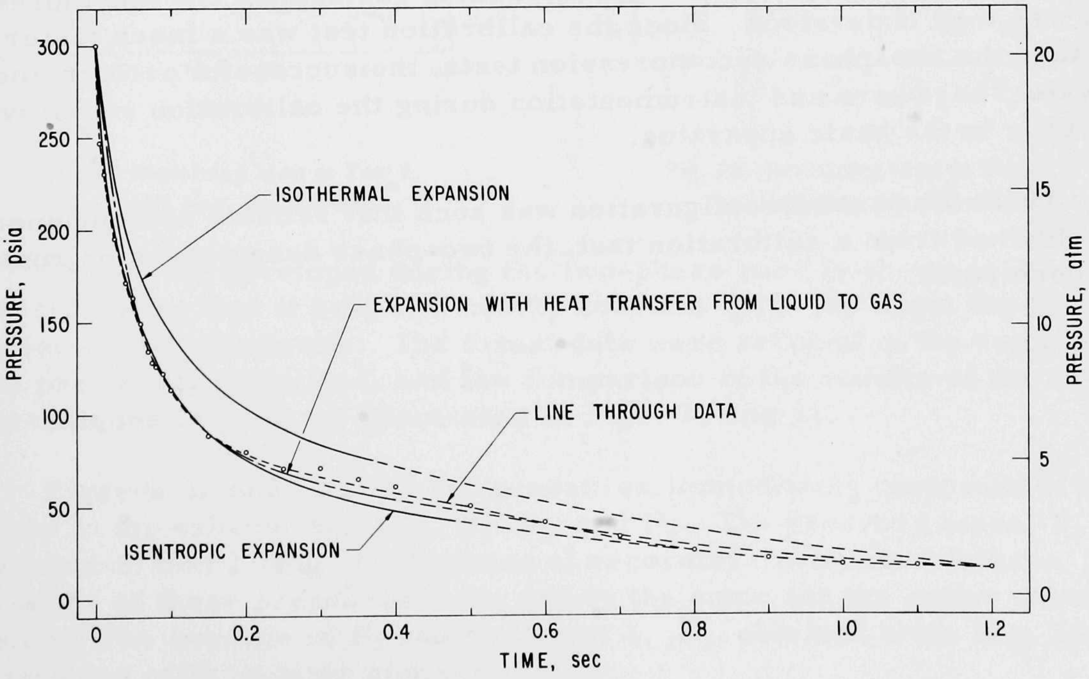

Fig. 27. Comparison of the Measured and Calculated Internal Vessel Pressure in the Calibration Run. ANL Neg. No. 900-4976 Rev. 4.

thrust during the blowdown. The slope of the heat-transfer prediction is similar to the isentropic calculation early in the decompression, after which it assumes a decay slope similar to the isothermal prediction.

Figure 27 compares the histories of the measured and calculated internal vessel pressures. The measurements and the isentropic prediction were almost coincident to about 150 msec, and then the measurements assumed a decay slope similar to the isothermal prediction. The coincidence of the measurement of the internal vessel pressure and the isentropic prediction to about 150 msec indicates that a negligible amount of heat transferred to the expanding gas during the early part of this period. The heat-transfer prediction is also shown in Fig. 27. This calculation agrees well with the data during the decompression, and its decay slope is similar to the isentropic prediction early in the blowdown; then it corresponds with the isothermal prediction later in the depressurization. This is similar to the trend in the measured and predicted thrust comparison in Fig. 26.

Since it was demonstrated in Figs. 21 and 25 that the mass, thrust, and pressure measurements were all consistent with one another, this indicates that the weight and thrust transducers were virtually isolated from each other. This showed that the system hardware and instrumentation would respond properly during a rapid decompression. The ability to further bracket the system response with an isentropic and isothermal expansion of the pressurizing gas, and also to predict the measured history of internal vessel pressure and indicate the approach of the expanding gas to an isothermal behavior, all based upon the measured remaining-mass history, indicates that the nature of the decompression process of the expanding gas against the incompressible liquid was well understood. Since the calibration test was a much faster blowdown than the two-phase decompression tests, the successful performance of the system hardware and instrumentation during the calibration run provided confidence in the basic apparatus.

Once the system configuration was such that reliable measurements were obtained from a calibration test, the two-phase decompression runs were performed.

VI. EXPERIMENTAL RESULTS FOR TWO-PHASE BLOWDOWN

The data from two two-phase decompression tests are reported in this study. The initial stagnation conditions of the two runs were 290- and 402-psia saturated water, and the fluid weight, thrust, pressure, and temperature measurements from these tests are indicated in this chapter. The original analog data signals are presented in Appendix C.

The mass of the remaining fluid in the blowdown vessel is shown in Figs. 28 and 29. These figures indicate that the initial flow rates were relatively large, but they rapidly decreased as the decompression progressed. The measured remaining-mass data in the two-phase tests were reduced in the same manner as previously described for the calibration test.

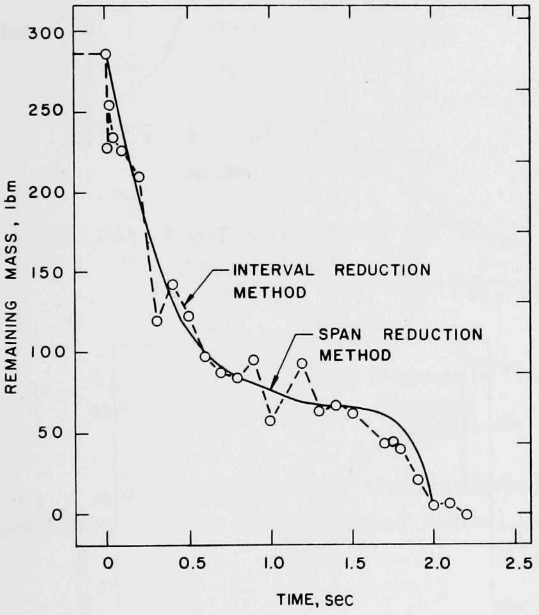

Fig. 28. Remaining Mass in Test 1.
ANL Neg. No. 900-5055.

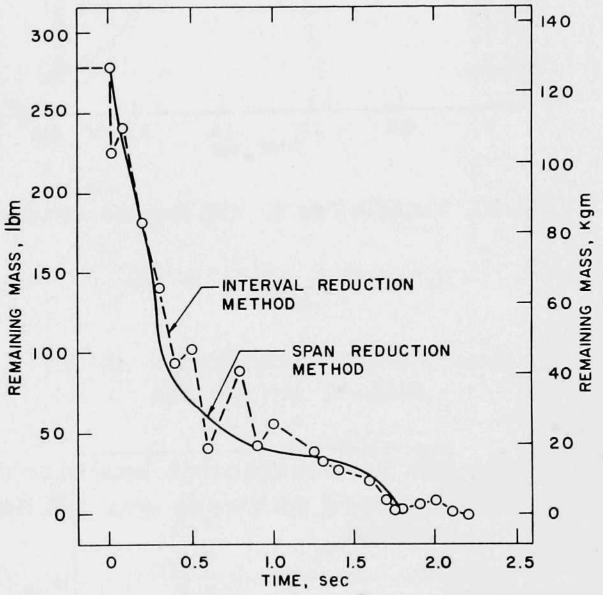

Fig. 29. Remaining Mass in Test 2.
ANL Neg. No. 900-5090.

The thrust developed during the two-phase runs is shown in Figs. 30 and 31 indicating that it held at a nearly constant value for about the first 500 msec of the blowdowns. The thrust data were reduced in the same manner as previously described, and the comparison of the results of the reduction techniques is good, as illustrated in Figs. 30 and 31.

Figures 32 and 33 show the pressures immediately upstream of the entrance to the exhaust duct, P_1, P_2, P_3, and P_4. The pressure signal P_1 was unavailable in test 1 (Fig. 32) because of recording-instrument failure. The magnitudes of these pressures were nearly the same for the entire decompression. The average of P_2 and P_3 in test 1, ${}_2\overline{P}_3$, obtained from Fig. 32, was used in place of P_1 in later comparisons.

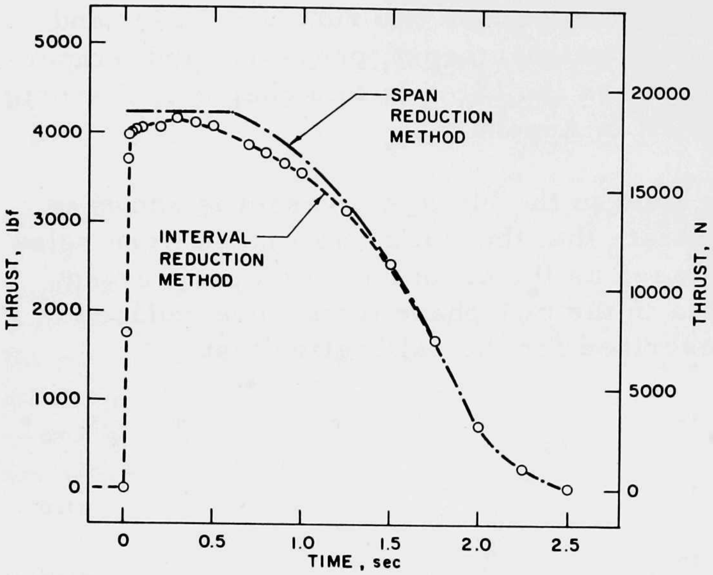

Fig. 30. Thrust in Test 1. ANL Neg. No. 900-5131.

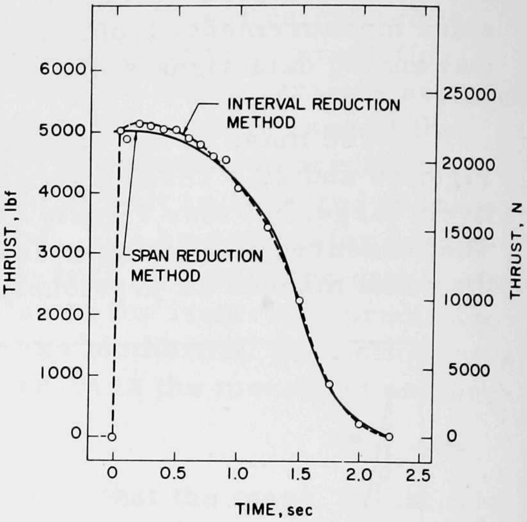

Fig. 31. Thrust in Test 2. ANL Neg. No. 900-5047.

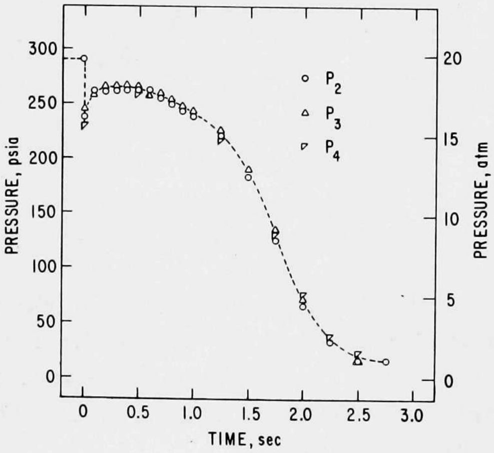

Fig. 32. Pressures Upstream of the Entrance to the Exhaust Duct in Test 1. ANL Neg. No. 900-5142.

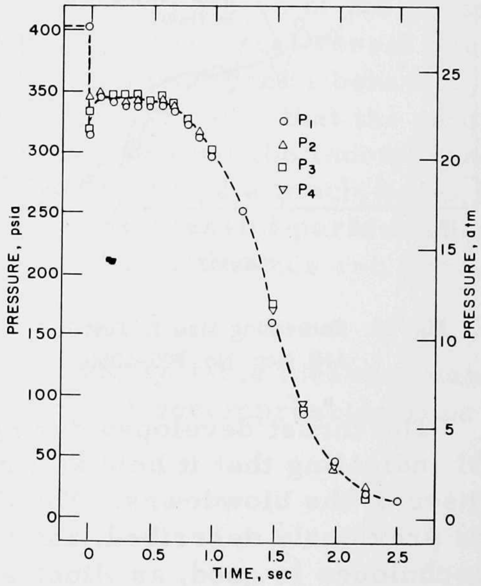

Fig. 33. Pressures Upstream of the Entrance to the Exhaust Duct in Test 2. ANL Neg. No. 900-4975.

The pressures inside the internal skirt, P_7 and P_8, are shown in Figs. 34 and 35. Pressure tap P_7 was located in the upper part of the internal skirt, and pressure tap P_8 was located in the lower region of the internal skirt, as shown in Figs. 8, 9, and 12. These two pressures were nearly the same for the entire blowdown. The average of P_7 and P_8, namely, ${}_7\overline{P}_8$, was also used in later comparisons.

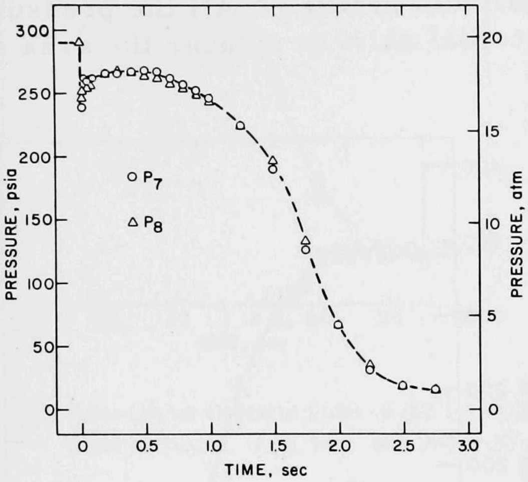

Fig. 34. Internal Vessel Pressures in Test 1. ANL Neg. No. 900-5097.

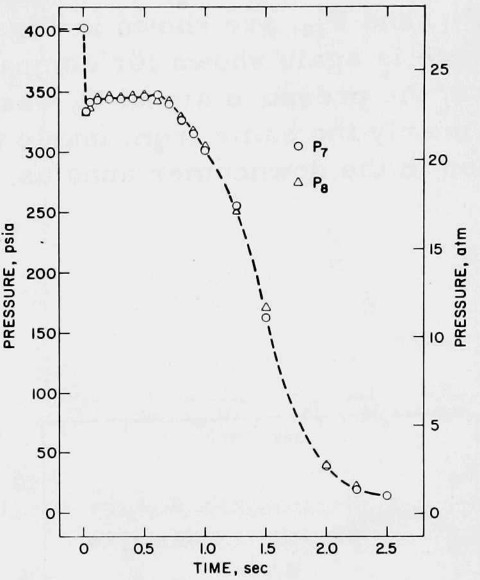

Fig. 35. Internal Vessel Pressures in Test 2. ANL Neg. No. 900-5099.

The pressures immediately upstream and downstream of the area expansion in the downcomer annulus, P_5 and P_6, are shown in Figs. 36 and 37.

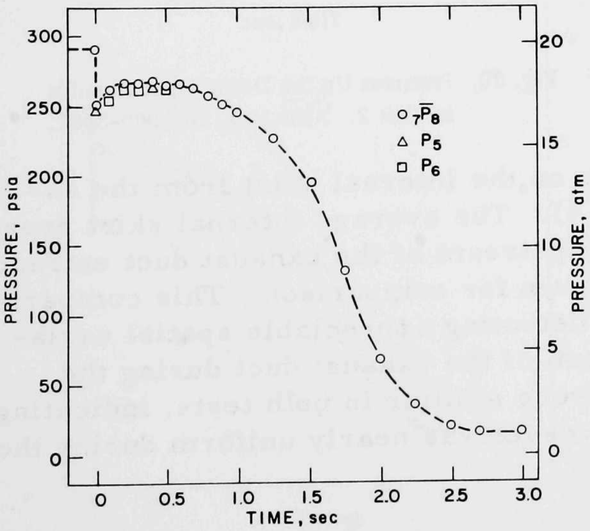

Fig. 36. Pressures Upstream and Downstream of the Area Expansion in the Annulus in Test 1. ANL Neg. No. 900-5088.

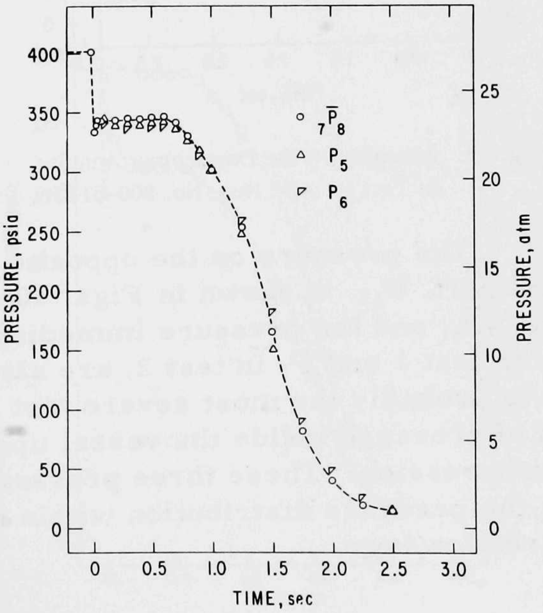

Fig. 37. Pressures Upstream and Downstream of the Area Expansion in the Annulus in Test 2. ANL Neg. No. 900-5144.

The average internal skirt pressure, ${}_7\overline{P}_8$, is also shown for comparison. Because of recording-instrument failure, Fig. 36 contains no data for P_5 and P_6 beyond 600 msec. There was very little difference among the pressures upstream and downstream of the area expansion and inside the internal skirt during the decompressions.

The pressures up the downcomer annulus before the area expansion, P_9, P_{10}, P_{11}, and P_{12}, are shown in Figs. 38 and 39. The average internal skirt pressure is again shown for comparison. Because of recording-instrument failure, the pressure signal P_9 was unavailable in test 1. All the pressures were nearly the same from inside the internal skirt to up near the area expansion in the downcomer annulus.

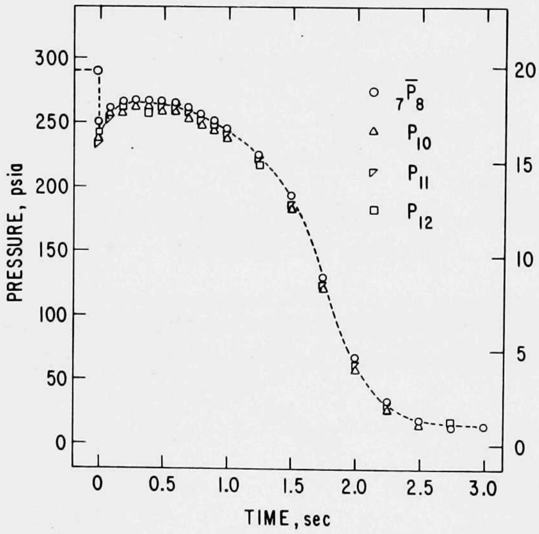

Fig. 38. Pressures Up the Downcomer Annulus in Test 1. ANL Neg. No. 900-5143.

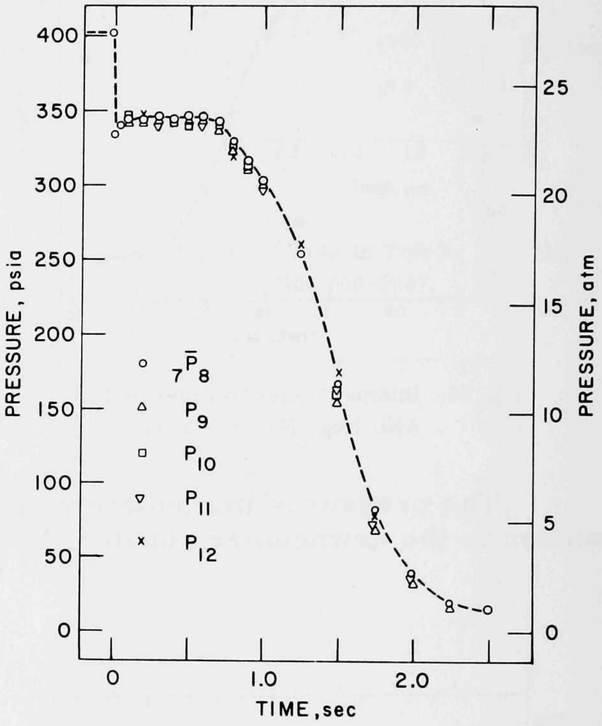

Fig. 39. Pressures Up the Downcomer Annulus in Test 2. ANL Neg. No. 900-5087.

The pressure on the opposite side on the internal skirt from the exhaust port, P_{13}, is shown in Figs. 40 and 41. The average internal skirt pressure, ${}_7\overline{P}_8$, and the pressure immediately upstream of the exhaust duct entrance, ${}_2\overline{P}_3$, in test 1 and P_1 in test 2, are also shown for comparison. This comparison is probably the most severe test for detecting appreciable spatial variation of pressure inside the vessel upstream of the exhaust duct during the decompression. These three pressures were similar in both tests, indicating that the pressure distribution within the vessel was nearly uniform during the entire blowdown.

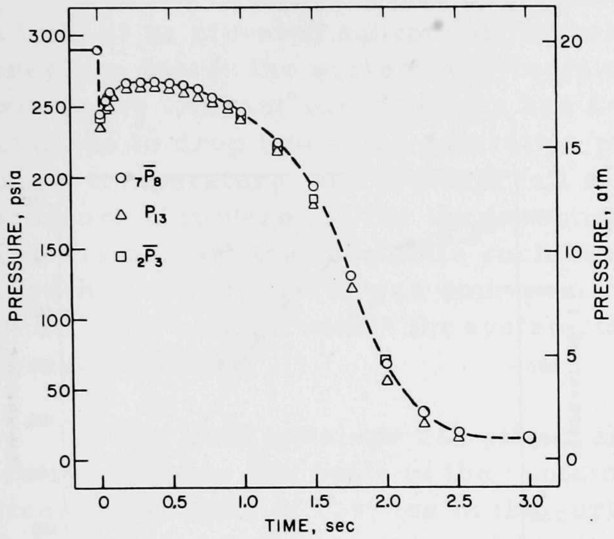

Fig. 40. Pressures on Opposite Sides of the Internal Skirt in Test 1. ANL Neg. No. 900-5082.

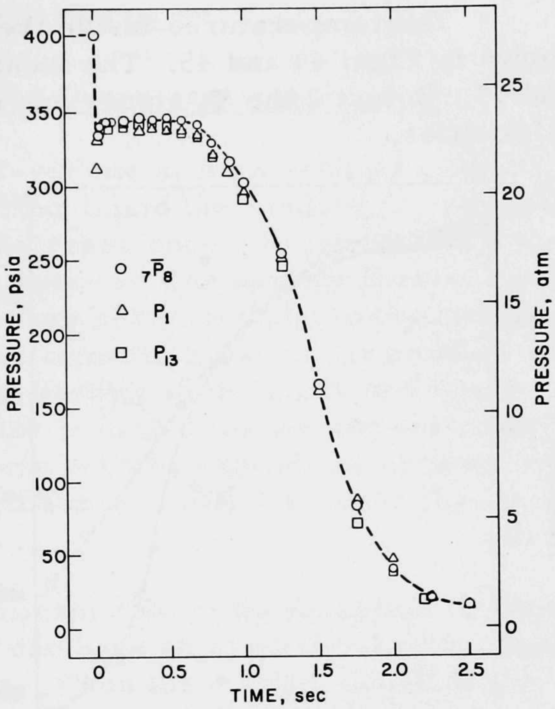

Fig. 41. Pressures on Opposite Sides of the Internal Skirt in Test 2. ANL Neg. No. 900-5091.

Figures 42 and 43 show the pressures immediately upstream of the exhaust-duct entrance, $_2\overline{P}_3$ in test 1 and P_1 in test 2, and the pressure near the end of the exhaust duct, P_{14}. The ratio of these two pressures, P_e/P_{i_0}, is the critical exit-pressure ratio during the critical flow period of the decompression.

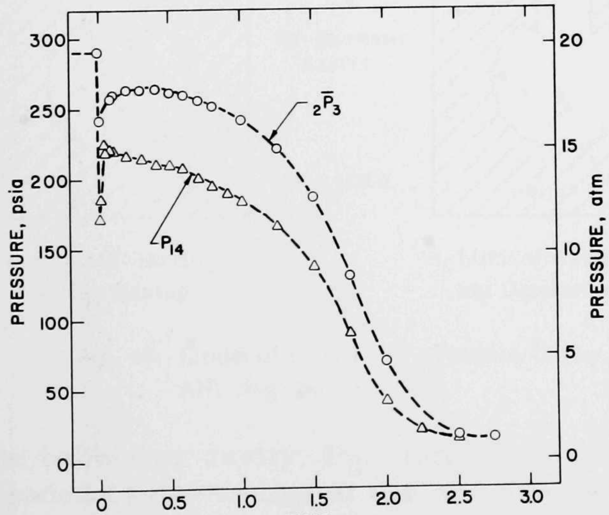

Fig. 42. Pressures Upstream and Near the Exit of the Exhaust Duct in Test 1. ANL Neg. No. 900-5094.

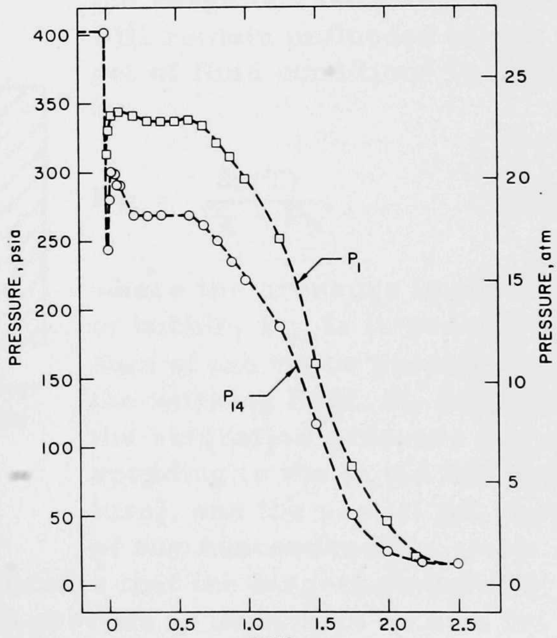

Fig. 43. Pressures Upstream and Near the Exit of the Exhaust Duct in Test 2. ANL Neg. No. 900-5051.

The temperatures inside the internal skirt region, T_7 and T_8, are shown in Figs. 44 and 45. The locations of T_7 and T_8 are indicated in Figs. 8 and 13. In test 2 the T_8 signal was not recorded because of instrument difficulties.

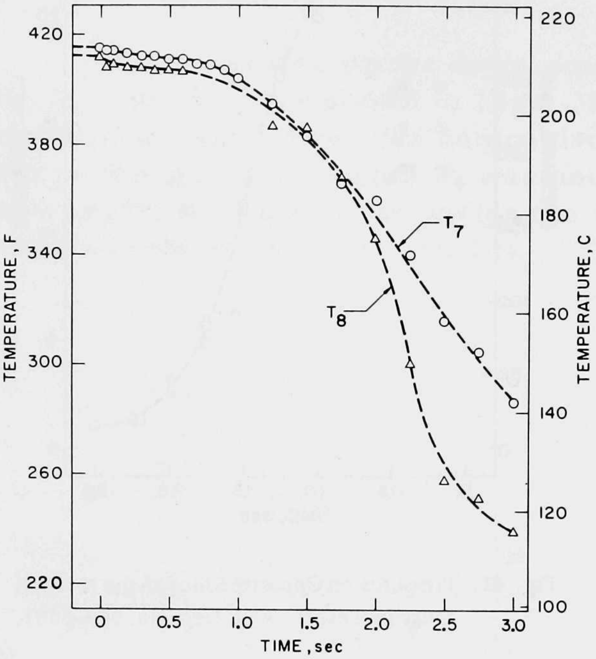

Fig. 44. Internal Vessel Temperatures in Test 1. ANL Neg. No. 900-5092.

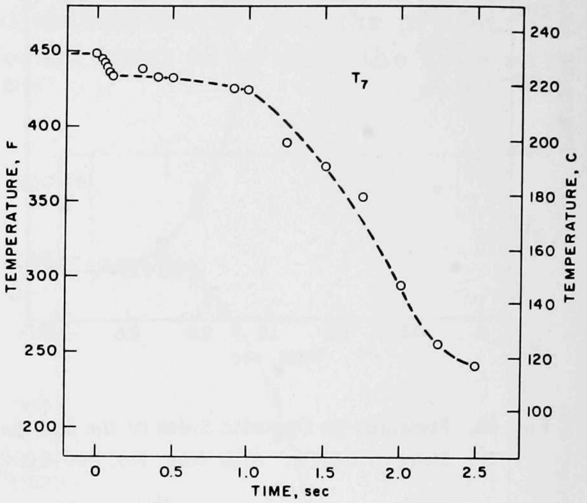

Fig. 45. Internal Vessel Temperatures in Test 2. ANL Neg. No. 900-5108.

VII. DISCUSSION OF RESULTS

A. The Role of Incipient Vaporization in the Decompression Process

In the decompression of a constant-volume system initially containing a fluid at an elevated subcooled- or saturated-liquid thermodynamic state, the pressure inside the system will begin to decrease once a break from the system to the ambient surroundings has been opened. The system pressure will continue to drop below the saturation pressure corresponding to the initial liquid temperature, and it would fall all the remaining way to the ambient pressure if it were not for the inception of flashing of the contained liquid. The mechanism that prohibits such behavior is the activation and unstable growth of vapor and/or gas embryos. These bubbles expand and produce additional fluid volume within the system, which subsequently increases the internal vessel pressure.

The fluid envelope can play a significant role in the inception of vaporization because the walls of the container can have an assortment of various sizes and shapes of cavities in the surface. When the system, which is the fluid envelope and everything within it, is initially filled with liquid, some of the cavities may be flooded immediately, but there will be some that will resist flooding because of surface-tension effects. These remaining unflooded surface cavities can play a principal role in the incipient vaporization process.

The manner in which the pressure and temperature of the contained fluid are increased during heatup has also been shown[102] to effect the initiation of vaporization. If a typical surface cavity can be idealized as a reentrant cavity, as illustrated in Fig. 46, the range of cavity radii that will remain unflooded at any set of fluid conditions is bounded by

$$R_E = \frac{2\sigma(T)}{P_\ell - P_b}, \qquad (160)$$

where the pressure in the cavity of bubble, P_b, is in general the sum of the vapor pressure of the working fluid, P_v (which is the saturation pressure corresponding to the liquid temperature), and the partial pressure of any noncondensible gases in the bubble or cavity, P_g. Equation 160 indicates that the largest remaining unflooded cavity radius at the end of a heatup process is dependent on how the pressure and temperature of the working fluid are controlled during the heatup.

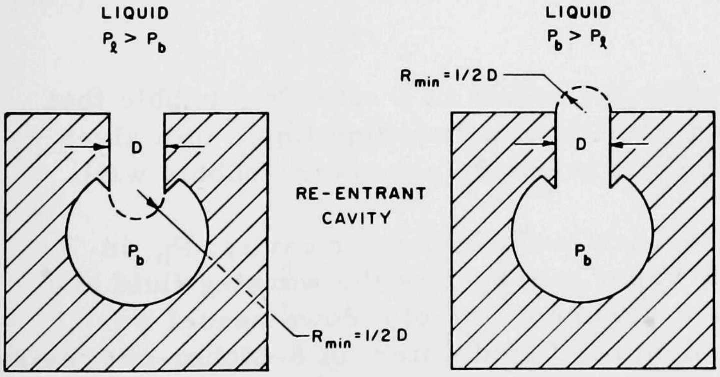

a. Limit of Stability during Heatup

b. Limit of Stability during Depressurization

Fig. 46. Limits of Stability of a Surface Cavity. ANL Neg. No. 900-5132.

Consider a surface cavity as a reentrant cavity, as shown in Fig. 46. The discontinuity of the cavity neck at the wall surface and also inside the cavity indicates that the minimum equilibrium radius of curvature of the meniscus is that of a hemisphere at these two locations.[103] During a heatup process, the free-stream liquid will not penetrate into the cavity any further that that shown in Fig. 46a unless the pressure difference $P_\ell - P_b$ exceeds the surface-tension limit of $2\sigma/R_{min}$. Thus, the schematic in Fig. 46a indicates the limit of mechanical stability of the meniscus so that the cavity will not flood during heatup. Likewise, during a depressurization, the bubble will not grow into the liquid any farther than that shown in Fig. 46b unless $P_b - P_\ell$ exceeds the surface-tension limit. Similarly, the meniscus position in Fig. 46b represents the limit of mechanical stability of the liquid-vapor interface during the decompression.

The surface tension of a liquid can be represented as

$$\sigma(T) = \sigma_0\left(1 - \frac{T}{T_c}\right)^n. \tag{161}$$

For water, the thermodynamic critical temperature T_c is 705°F, σ_0 is a constant equal to 0.01156 lb_f/ft, and n is also a constant equal to 1.22. Equation 161 can be used in Eq. 160 to yield the equilibrium spherical radius of a bubble as

$$R_E = \frac{2\sigma_0\left(1 - \frac{T}{T_c}\right)^n}{P_V + P_g - P_\ell}. \tag{162}$$

Equation 162 can be used to determine the radius of a spherical bubble that will remain in mechanical equilibrium with a surrounding liquid of a given temperature and at a given difference in pressure across the bubble wall.

As previously noted, the pressure in the bubble or cavity, P_b, in Eq. 160 is generally the sum of the vapor pressure of the working fluid and any gas partial pressures. In this experiment, the blowdown vessel was evacuated and then was filled with demineralized water, of 8-Mohm-cm resistivity, under vacuum. This procedure should have removed almost all the vapors and gases from the vessel before filling. However, the water that was put into the blowdown vessel did have dissolved gas within it. If there was some gas, primarily air, in the surface cavities, once the vessel was completely filled with water, as the temperature of the mixture was increased, the partial pressure of the air in solution would have increased. This can be shown by considering Henry's Law for the equilibrium soluble concentration of a solute:

$$C(P, T) = K(T)P_g. \tag{163}$$

For conditions at 14.5 psia and 67°F, the water would have contained a maximum concentration of about 0.00146 lb_m of air per ft^3 of water[104] as shown in Fig. 47. Since the water was put into the blowdown vessel at this pressure and temperature and was heated from this state in an all-liquid condition, it was unable to dissolve more air or gas from the external environment as it was heated. Consequently, the concentration of the air in the mixture was constant, and Eq. 163 can be rewritten as

$$K(T_2)P_{g_2} = K(T_1)P_{g_1}, \tag{164}$$

where state 2 is an elevated thermodynamic state and state 1 is some reference state. If atmospheric conditions are taken as the reference state, then the equilibrium partial pressure of air in the mixture at an elevated thermodynamic state is given by

$$P_{g_2} = P_{g_{atm}} \frac{K(T_{atm})}{K(T_2)}. \tag{165}$$

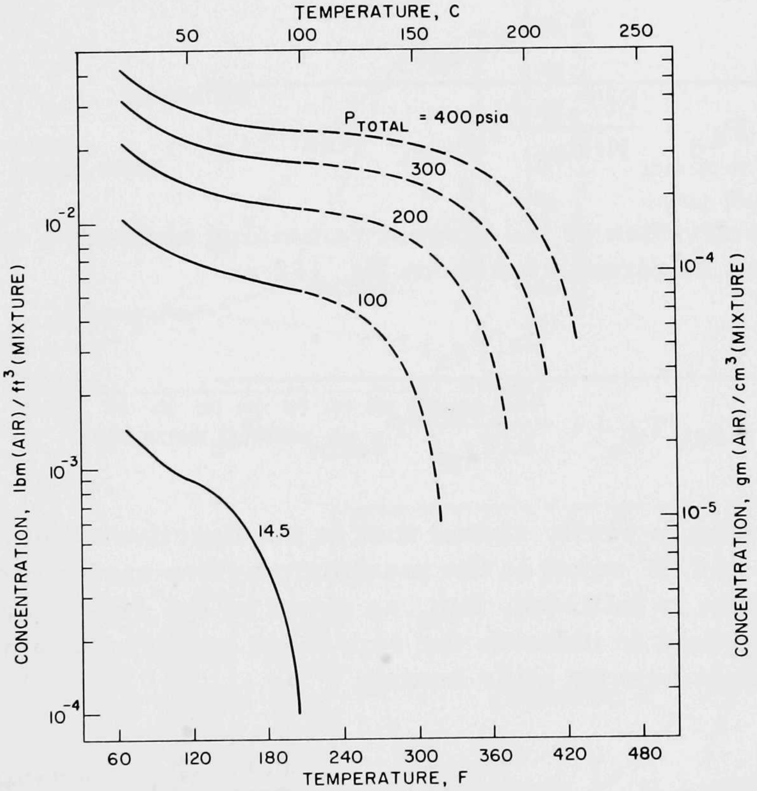

Fig. 47. Equilibrium Concentration of Air in Water.
ANL Neg. No. 900-5174 Rev. 2.

Since the concentration coefficient K(T) for air in water decreases with increasing temperature,[104] the partial pressure of the air in the mixture would have increased as the temperature of the mixture increased. The partial pressure of air in water at 67°F and a total pressure of 14.5 psia is about

14.2 psia. With a knowledge of how the pressure and temperature of the working fluid were increased during heatup, the history of the largest remaining unflooded cavity size during the heatup can be determined. If it is assumed that the noncondensible gases in the system play a role in the deactivation and activation sequences of a cavity, Eqs. 160 and 165 can be combined to yield

$$R_E = \frac{2\sigma_0\left(1 - \frac{T_\ell}{T_c}\right)^n}{P_\ell - \frac{K(T_{atm})}{K(T_\ell)} P_{g_{atm}} - P_{sat}(T_\ell)} . \tag{166}$$

Once the heatup process has been completed, and the largest remaining unflooded cavity size and the thermodynamic state at which it occurred during heatup have been determined, Eq. 166, and then Eqs. 162 and 165, can be used to estimate the superheat required to activate the largest remaining unflooded cavity. This superheat can also be determined directly. The largest remaining unflooded cavity size during deactivation can be determined from Eq. 166 as

$$R_{E_d} = \frac{2\sigma(T_{\ell_d})}{P_{\ell_d} - \frac{K(T_{atm})}{K(T_{\ell_d})} P_{g_{atm}} - P_{sat}(T_{\ell_d})} . \tag{167}$$

At the time of activation of the largest remaining unflooded cavity, its mechanical stability can be formulated from Eq. 162 as

$$R_{E_a} = \frac{2\sigma(T_{\ell_a})}{P_{sat}(T_{\ell_a}) + \frac{K(T_{atm})}{K(T_{\ell_a})} P_{g_{atm}} - P_{\ell_a}} . \tag{168}$$

The maximum cavity radius that is not deactivated during heatup, R_{E_d} as given in Eq. 168, is equal to the maximum active cavity radius just before the decompression is initiated, R_{E_a} as given in Eq. 168. These two relations can then be combined to indicate the superheat required to activate the largest remaining unflooded cavity after heatup:

$$\left[P_{sat}(T_{\ell_a}) - P_{\ell_a}\right] = \frac{\sigma(T_{\ell_a})}{\sigma(T_{\ell_d})}\left[P_{\ell_d} - \frac{K(T_{atm})}{K(T_{\ell_d})} P_{g_{atm}} - P_{sat}(T_{\ell_d})\right]$$

$$- \frac{K(T_{atm})}{K(T_{\ell_a})} P_{g_{atm}} . \tag{169}$$

Equations 162 and 169 should produce the same result for the pressure at which unstable bubble growth would begin once the minimum deactivated cavity radius has been determined from Eq. 166. This is, then, the general criterion for how far the system pressure will drop below the saturation pressure corresponding to the initial liquid temperature before unstable bubble growth will start. This is the initiation of the volume-producing mechanism within the system in which the activation of the available surface cavities for bubble nucleation start the production of the vapor phase.

During the heatup process in these tests, the pressure and temperature of the liquid were increased simultaneously, and for each incremental increase in the pressure and temperature, successively smaller remaining surface cavities were flooded as dictated by Eq. 160. The internal vessel pressure was normally maintained about 50 psi greater than the saturation pressure corresponding to the instantaneous liquid temperature during the heatup process. This is shown in Figs. 48 and 49, where the histories of the internal vessel pressure and the liquid temperature are shown for time before the

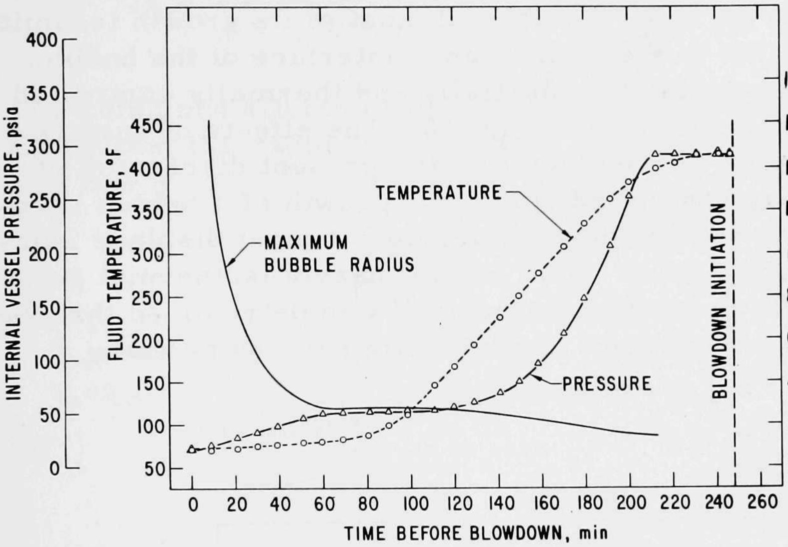

Fig. 48

Maximum Stable Cavity Radius during Heatup in Test 1. ANL Neg. No. 900-5171 Rev. 3.

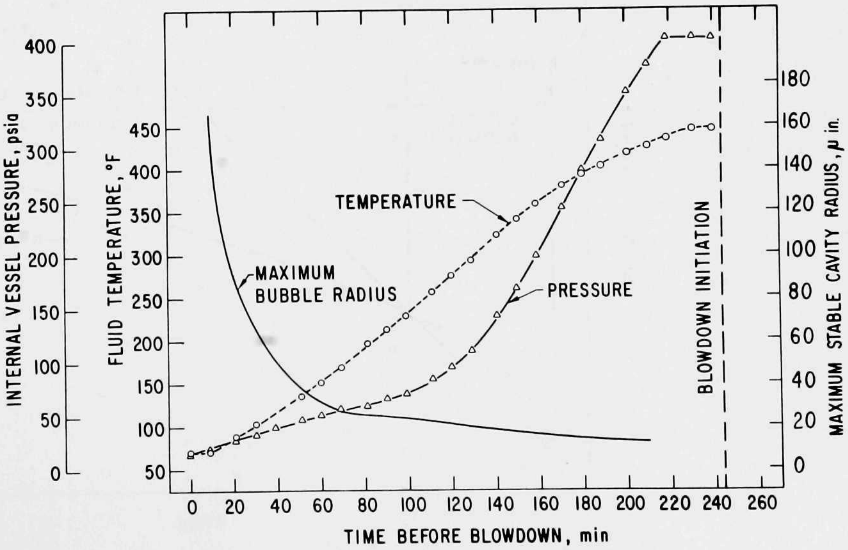

Fig. 49

Maximum Stable Cavity Radius during Heatup in Test 2. ANL Neg. No. 900-5170 Rev. 3.

decompressions were initiated. If the 50-psi differential-pressure criterion is used in Eq. 166, which assumes that whatever gas was in the system played a role in the deactivation process of a surface cavity, the history of the largest remaining, equilibrium, unflooded cavity size during heatup can be determined, and this is also shown in Figs. 48 and 49. As a result, in the largest remaining unflooded cavity size before decompression initiation is about 13.763 μin. in test 1 and 12.359 μin. in test 2. When these values are used in Eq. 168, the calculated system pressure for cavity stability limits are 286 psia in test 1 and 399 psia in test 2. These values are the same as those calculated from Eq. 169. The intent in these tests was to generate an initially saturated liquid state from which to start the decompressions. Figures 48 and 49 show that the largest remaining unflooded cavity size was established just before the nearly saturated liquid state was reached.

The unstable growth of a bubble resulting from a nucleation site is initially limited by inertial and surface-tension constraints; however, this period of bubble growth is very short for most fluids, and most of its growth is limited by the rate of thermal conduction to the liquid-vapor interface of the bubble. The radius of a growing bubble during the inertially and thermally controlled periods of growth is shown schematically in Fig. 50. The effects of surface tension and noncondensible gases are neglected in the present discussion of bubble growth. In the inertially controlled stage, the growth of a bubble is influenced by the presence of the surrounding liquid; i.e., it must displace adjacent liquid in order to continue to grow. This initial, nearly isothermal period of bubble growth was originally treated by Rayleigh,[98] who determined that the radius of a bubble during this period grew linearly with time as given by

$$r(t) = \left[\frac{2}{3}v_\ell(P_b - P_\ell)\right]^{1/2}t. \tag{170}$$

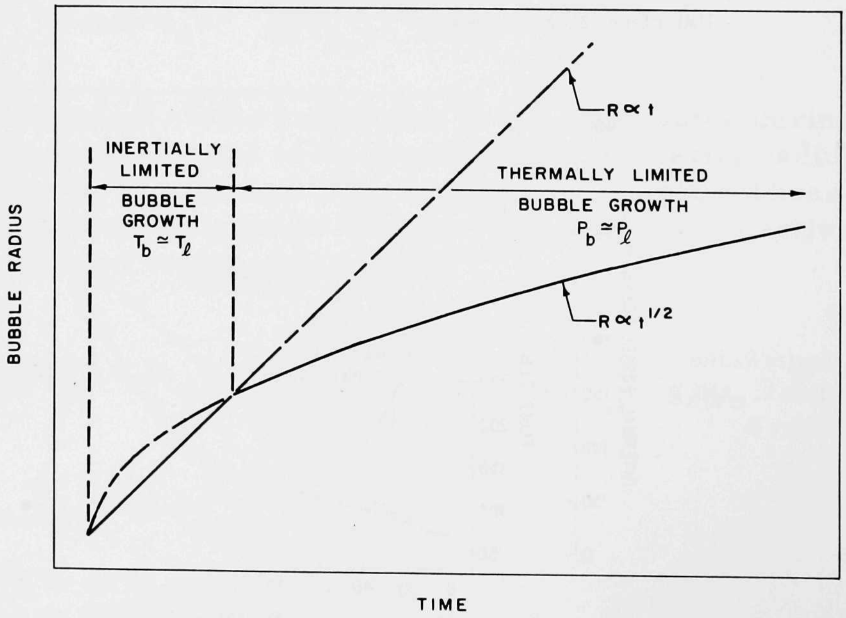

Fig. 50. Growth Characteristics of Vapor Bubble during the Inertially and Thermally Controlled Growth Periods. ANL Neg. No. 900-5175 Rev. 1.

Sufficient superheat is available in the inertial-growth period for the bubble to grow potentially to the size indicated by the heat-transfer-controlled mechanism (see Fig. 50), but the inertia of the surrounding liquid prohibits the growth of the bubble to this size. The growth of the bubble during the thermally controlled stage is shown schematically in Figs. 50 and 51. During this period, the pressure in the bubble and the liquid are nearly uniform. The radius of a growing bubble during this period increases as the square root of time:[99,100]

$$r(t) = \left(\frac{12}{\pi}\alpha_{\ell}\mathrm{Ja}^2\right)^{1/2} t^{1/2}, \tag{171}$$

where the Jakob number Ja is formulated as

$$\mathrm{Ja} = \frac{c_{p_L}\rho_L(T_w - T_{sat})}{\rho_V h_{VL}}. \tag{172}$$

The combined effects of inertially and thermally controlled bubble growth indicate that the radius of a growing bubble would approximately follow the solid line in Fig. 50.

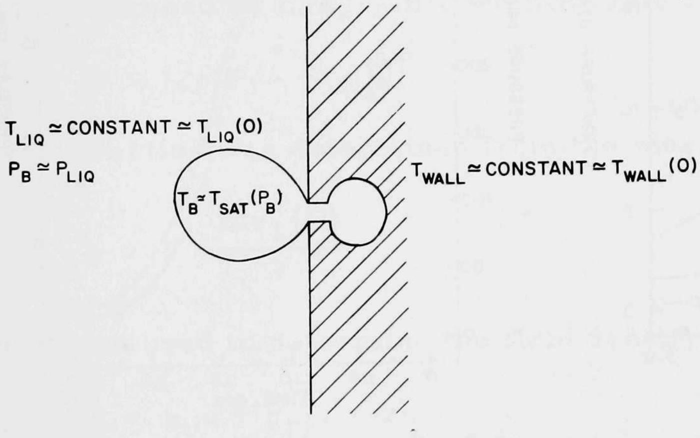
$T_{LIQ} \simeq$ CONSTANT $\simeq T_{LIQ}(O)$
$P_B \simeq P_{LIQ}$
$T_B \simeq T_{SAT}(P_B)$
$T_{WALL} \simeq$ CONSTANT $\simeq T_{WALL}(O)$

Fig. 51

Unstable Thermal Growth of a Bubble Resulting from a Surface Cavity. ANL Neg. No. 900-5114 Rev. 1.

B. Thermodynamics of the Vaporization Process

In the period immediately following the initiation of the decompression in tests 1 and 2, the saturation pressures corresponding to the measured internal vessel temperatures were greater than the measured internal vessel pressures, as seen in Figs. 52 and 53. Two thermocouples measured the internal transient temperatures. The upper thermocouple inside the internal skirt, T_7, was a sheathed, ungrounded thermocouple, with a measured response time of about 340 msec. The lower thermocouple inside the internal skirt, T_8, was a sheathed, grounded thermocouple, with a measured response time of about 100 msec. The locations of the P_7-T_7 and P_8-T_8 pairs are shown in Figs. 4, 8, 9, 12, and 13. These response times are of about the same magnitude as the time that the saturation pressures corresponding to the measured internal vessel temperatures were initially greater than the measured pressures.

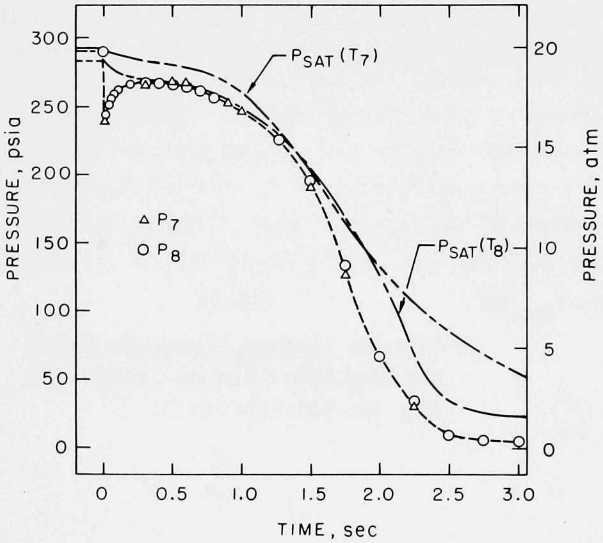

Fig. 52. Comparison of the Measured Pressures and the Saturation Pressures Corresponding to the Measured Temperatures in Test 1. ANL Neg. No. 900-4983 Rev. 1.

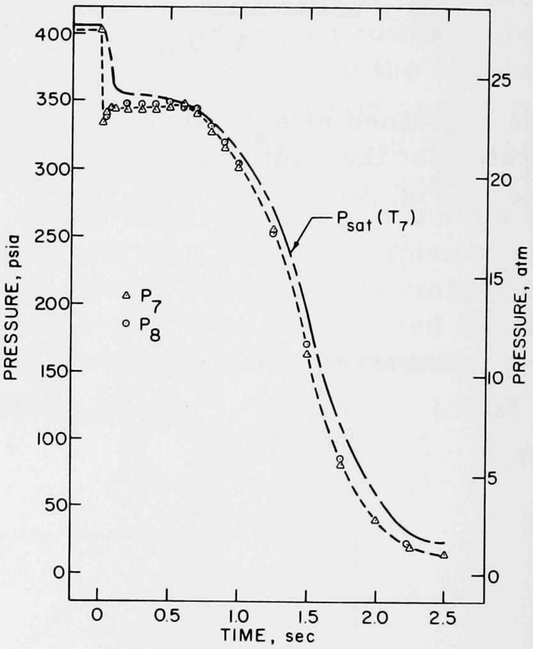

Fig. 53. Comparison of the Measured Pressures and the Saturation Pressure Corresponding to the Measured Temperature in Test 2. ANL Neg. No. 900-4964 Rev. 1.

In test 1, the saturation pressure corresponding to the measured internal vessel temperature began to lag the measured pressure at about 1.5 sec, as seen in Fig. 52. At this time there was only about 40 lb_m of fluid remaining within the vessel, as seen in Fig. 54. This left very poor cooling capability inside the vessel; therefore the thermocouples began to lag the fluid temperature because of their own thermal inertia and also because of the hot structural supports near them. The same trend was true in test 2, as seen in Fig. 53, but the severity was not as marked or as strong a function of the remaining mass (see Fig. 55).

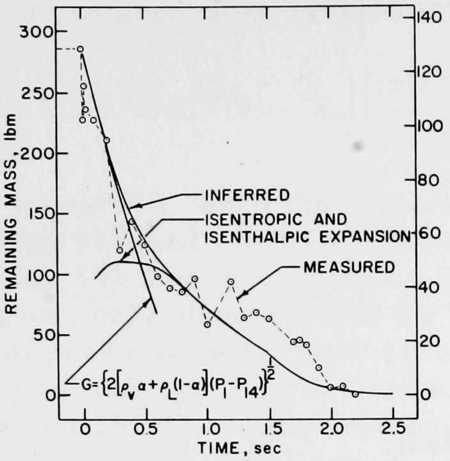

Fig. 54. Comparison of the Measured and Inferred Remaining Mass in Test 1. ANL Neg. No. 900-4995 Rev. 1.

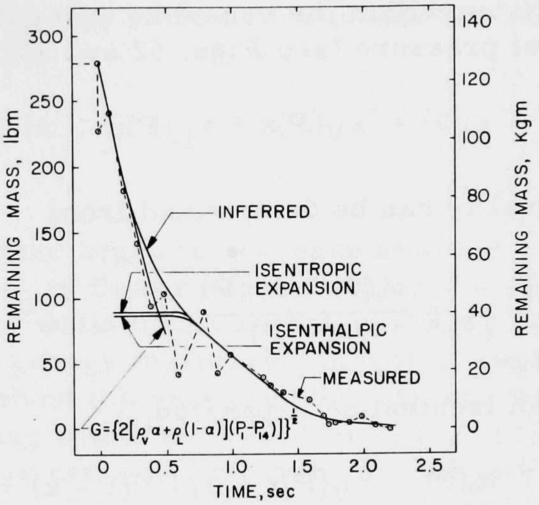

Fig. 55. Comparison of the Measured and Inferred Remaining Mass in Test 2. ANL Neg. No. 900-4973.

It was most important to have reliable mass-history data in this experiment in order to also have a good knowledge of the critical flow rate during the blowdown. The inferred mass-decay history early in the decompression was determined by integrating the flow-rate relation

$$G = [2\rho(P_1 - P_{14})]^{1/2}. \tag{173}$$

A void fraction was determined from the measured results as

$$\alpha = 1 - \frac{mv_L(P)}{V}, \tag{174}$$

and it was used to determine the fluid density from

$$\rho = \rho_V\alpha + \rho_L(1 - \alpha). \tag{175}$$

The simultaneously measured upstream stagnation pressure, ${}_2\overline{P}_3$ in test 1 and P_1 in test 2, and the exit pressure, P_{14}, were used to determine the instantaneous flow rate from Eq. 173. The flow rate was then integrated:

$$\dot{m}(\tau) = m(0) - A_e \int_0^T G(t)dt, \tag{176}$$

to determine the remaining fluid mass based on the measured results in the early period of the decompression.

The remaining mass history during the latter portion of the depressurization could be bracketed with an isentropic and isenthalpic equilibrium expansion within the vessel by using the history of the measured internal vessel pressure (see Figs. 52 and 53). For an isentropic expansion,

$$s_0(0) = s_V(P)x + s_L(P)(1 - x) = \text{constant}; \tag{177}$$

the quality can be determined from

$$x_s = \frac{s_0(0) - s_L(P)}{s_{VL}(P)}. \tag{178}$$

For an isenthalpic expansion,

$$h_0(0) = h_V(P)x + h_L(P)(1 - x) = \text{constant}; \tag{179}$$

the quality becomes

$$x_h = \frac{h_0(0) - h_L(P)}{h_{VL}(P)}. \tag{180}$$

The equilibrium quality is then used to determine the specific volume of the remaining mixture as

$$v = \frac{V}{m} = v_V(P)x + v_L(P)(1 - x), \tag{181}$$

from which the remaining fluid mass can be evaluated. The volume used in Eq. 181 was that within the internal-skirt region, which was 78.5% of the total internal vessel volume. This was done because most of the fluid mass resided inside the internal-skirt region in the latter portion of the decompression. This procedure led to a determination of the remaining fluid mass based on the history of the high-resolution, measured, internal vessel pressure. The resulting remaining masses determined in this manner are shown in Figs. 54 and 55. The remaining mass calculated by the two equilibrium expansion paths was essentially the same in test 1, but the remaining mass calculated from the isentropic expansion was slightly greater than that calculated from the isenthalpic expansion in test 2. This is reasonable, since the expansion started from a higher pressure-temperature state in test 2 than in test 1.

The isentropic and isenthalpic internal vessel expansions were evaluated as to which would best describe the actual physical process. For the time scale of these blowdowns, an insignificant amount of heat was transferred from the internal solid surfaces of the vessel to the remaining fluid. This can be shown by considering the walls of the vessel to be semi-infinite slabs with a large Biot number, i.e., a large ratio of internal, conductive, thermal resistance to surface, convective, thermal resistance, and also for the condition that

$\delta/2\sqrt{\alpha t} > 1/2$. The amount of thermal energy extracted from the surface under these conditions is given by

$$\Delta Q = 2kS\left[T(0) - T_{\infty}\right]\left[\frac{\Delta t}{\pi\alpha_{w}}\right]^{1/2}. \tag{182}$$

In test 1, when the system pressure began to decrease at about 1 sec (see Fig. 52), and when only about 73 lb_m of fluid remained within the vessel (see Fig. 54), the heat removed from the walls of the vessel was about 200 Btu, which was only about 0.2% of the initial energy inventory. In test 2, when the system pressure began to decrease at about 0.6 sec (see Fig. 53), and when there was about 96 lb_m of fluid remaining within the vessel (see Fig. 55), only about 250 Btu of thermal energy was extracted from the vessel walls, or about 0.2% of the initial energy inventory. Since a negligible amount of heat was transferred to the remaining fluid from the vessel structure during this period of the decompression, the expansion was essentially an isentropic process.

The initial, inferred mass-decay history, obtained from Eqs. 173-176, was then used in conjunction with the isentropic-expansion results later in the blowdown, given by Eqs. 178 and 181, to indicate the remaining mass history for the entire decompression. The combined results for the inferred mass decay history based on the measurements are shown in Figs. 54 and 55.

Figures 54 and 55 show that the thermodynamic equilibrium calculation of the remaining mass agreed with the measurements only after about 700 msec into the decompression, which is also when the system pressure started to decrease significantly (see Figs. 52 and 53). This is when the void fraction of the remaining fluid within the internal-skirt region had increased to about 0.5, as seen in Figs. 56 and 57. This shows that the behavior of most of the remaining fluid inside the internal-skirt region before about 700 msec was not that of thermodynamic equilibrium. We will show later that the activation of the available surface cavities was the mechanism for maintaining the system pressure during this early period of the decompression. The constant internal vessel pressure demonstrated itself as a constant remaining mass in the thermodynamic equilibrium calculations shown in Figs. 54-57.

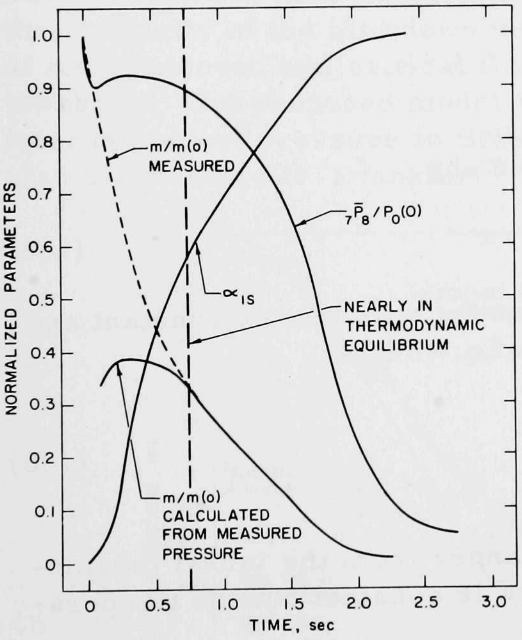

Fig. 56. An Indication of When Thermodynamic Equilibrium of the Remaining Fluid in the Internal-skirt Region Was Reached in Test 1. ANL Neg. No. 900-5160 Rev. 1.

Figures 54 and 55 also show that the inferred remaining mass compared well with the measurements for most of the blowdown.

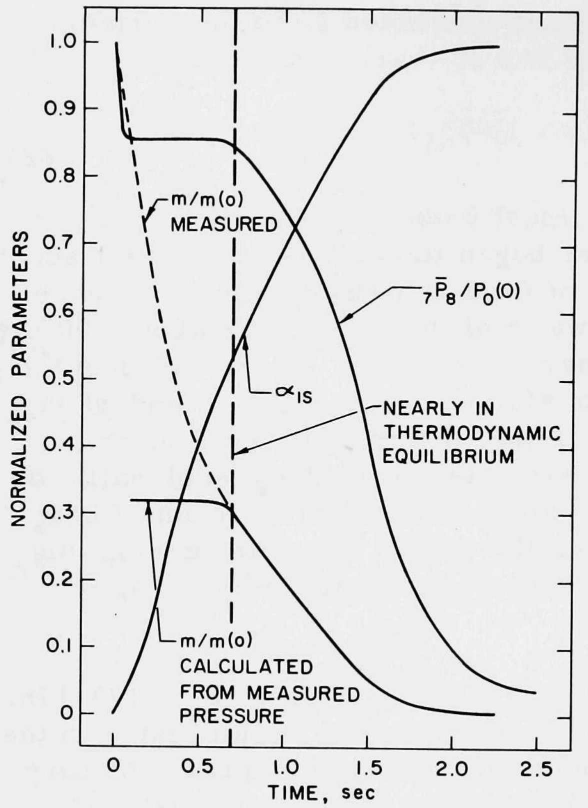

Fig. 57. An Indication of When Thermodynamic Equilibrium of the Remaining Fluid in the Internal-skirt Region Was Reached in Test 2. ANL Neg. No. 900-5161 Rev. 1.

The only period of slight disagreement was in test 1 (see Fig. 54) from about 1.2 to 2.0 sec, when the measurements were somewhat greater than the inferred remaining mass. The pressure data in this experiment provided the greatest resolution of the measurements for this flow configuration. The inferred remaining-mass results in Figs. 54 and 55 based on these pressure data are therefore considered to be the most accurate representations of the remaining fluid mass in the system during the decompression.

To demonstrate that the fluid quality would increase and the remaining mass would decrease while the pressure is nearly constant and the temperature decreases, as in Figs. 56 and 57, the following nonequilibrium analysis is considered.

The volume of the system is constant and equal to

$$V = mv = \text{constant}. \tag{183}$$

Differentiating Eq. 183 produces

$$m\,dv + v\,dm = 0, \tag{184}$$

where the homogeneous specific volume is given by

$$v = v_V(P)x + v_L(P)(1 - x). \tag{185}$$

By differentiating Eq. 185 and by assuming that the pressure is constant and the liquid phase incompressible, we can write Eq. 184 as

$$\left(\frac{dm}{m}\right)_P = \frac{-v_{VL}(P)}{v_V(P)x + v_L(P)(1 - x)}dx. \tag{186}$$

Evaluating the fluid quality in an isentropic manner from the initial thermodynamic state to the region where the pressure is constant but the temperature is variable produces

$$x = \frac{s_0(0) - s_\ell(T)}{s_V(P) - s_\ell(T)}. \tag{187}$$

Use of this equation reduces Eq. 186 to

$$\left(\frac{dm}{m}\right)_P = \frac{v_{VL}(P)(1 - x)}{[s_V(P) - s_\ell(T)][v_V(P)x + v_L(P)(1 - x)]} ds_\ell(T). \tag{188}$$

From the combined First and Second Laws of Thermodynamics, the constant-pressure condition indicates that

$$ds_\ell(T) = c_{p_\ell} \frac{dT_\ell}{T_\ell}, \tag{189}$$

and Eq. 188 becomes

$$\left(\frac{dm}{m}\right)_P = \frac{v_{VL}(P)c_{p_\ell}(1 - x)}{[s_V(P) - s_\ell(T)][v_V(P)x + v_L(P)(1 - x)]} \frac{dT_\ell}{T_\ell}. \tag{190}$$

Equation 190 shows that, at constant pressure, a temperature decrease will increase the fluid quality (Eqs. 187 and 189) and, hence, decrease the remaining mass. The pressure did remain nearly constant for about 0.5 sec in both tests, as seen in Figs. 56 and 57, and the remaining mass did decay considerably during this period, also shown in Figs. 56 and 57.

Although the decompressions reported in this study were initiated from a nearly saturated liquid state, there was no subcooled blowdown period as such; a simple subcooled blowdown model was formulated (see Sec. III.C), and it is compared to some available data. The proposed model incorporates the elasticity of the blowdown vessel, unchoked flow during the initial period of the blowdown, and critical flow during the later stage of subcooled decompression. The proposed model is compared to the histories of the measured internal vessel pressure in BNWL[79] runs 25 and 52 in Figs. 58 and 59, and also in the Battelle-Frankfurt[77] run 13 in Fig. 60. The model compares well

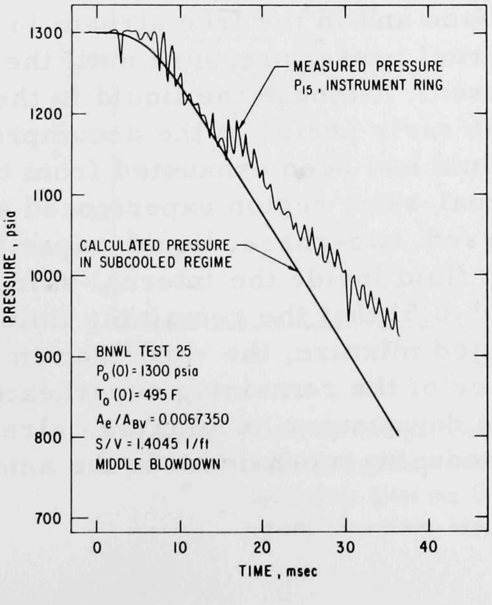

Fig. 58

Comparison of the Subcooled Blowdown Model to the Data of BNWL Run 25.[79]
ANL Neg. No. 900-75-96.

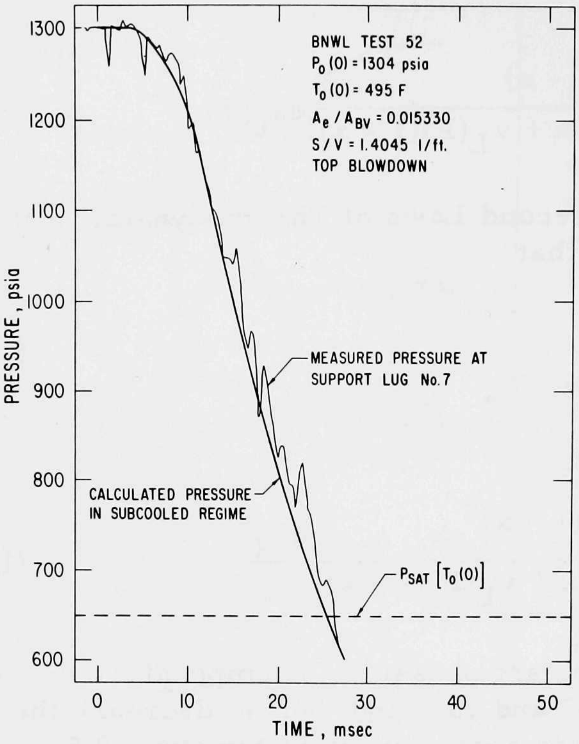

Fig. 59. Comparison of the Subcooled Blowdown Model to the Data of BNWL Run 52.[79] ANL Neg. No. 900-75-95.

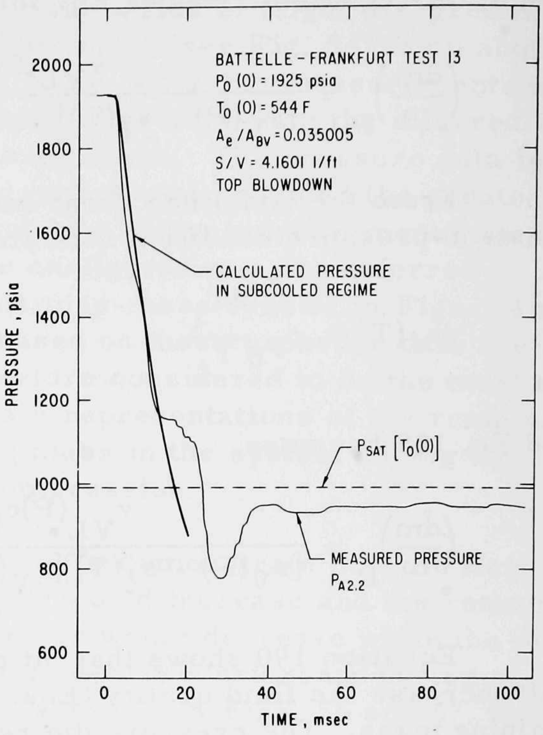

Fig. 60. Comparison of the Subcooled Blowdown Model to the Data of Battelle-Frankfurt Run 13.[77] ANL Neg. No. 900-75-98.

with the measured pressure in Fig. 58 to about 16 msec, after which the data rise slightly above the prediction. There was dissolved nitrogen gas in the water during these tests, and the rise in the measured pressure above the calculation is attributed to gas coming out of solution in this run. The model and the data compare well in Figs. 59 and 60. The departure of the measured pressure from the calculated pressure at about 13 msec in Fig. 60 is also attributed to dissolved gas coming out of solution.

The activation of the available surface cavities plus the growth of the bubbles already detached from the surface and in the free stream in each sector of the system sustained the internal vessel pressure until the remaining fluid became relatively well dispersed. Although the liquid in the internal-skirt region was superheated during the early period of the decompression (see Figs. 54 and 55), once sufficient fluid had been exhausted from the vessel the remaining fluid inside the internal-skirt region experienced a flow-regime transition toward a well-dispersed, two-phase, liquid-vapor mixture. Once the void fraction of the remaining fluid inside the internal-skirt region had increased to such a value (about 0.3-0.5) that the remaining fluid in this region approached a uniformly distributed mixture, the vaporization was controlled by heat transfer from the surface of the remaining superheated liquid droplets. The fluid configuration in the downcomer annulus was already well dispersed at this time, so the vapor-producing mechanism in the annulus was already that of vaporization from superheated liquid surfaces. Hence, the remaining fluid inside the internal skirt approached thermodynamic equilibrium conditions in the latter part of the decompression when the fluid configuration in that sector of the system became well dispersed. This is shown in Figs. 56 and 57 when the thermodynamic equilibrium prediction of the remaining mass based on the measured internal vessel pressure came into agreement with the measured remaining mass.

At the start of the decompressions, the system pressure dropped below the saturation pressure and activated the largest remaining unflooded surface cavities still existing after heatup, as indicated in Sec. VII.A. The vapor bubbles originating from these cavities expanded and went through the inertially controlled bubble-growth period in about 10^{-8} sec in these tests, and then they continued to grow while being limited by thermal conduction to the liquid-vapor interface of the bubble. The inertially controlled bubble-growth period in these runs was determined by equating the bubble radius during inertially dominated growth (Eq. 170) to the bubble radius during thermally dominated growth (Eq. 171). This is indicated by the intersection of the two growth characteristics in Fig. 50, and it establishes the transition from inertially to thermally dominated bubble growth. The bubbles then continued to expand and pressurize the system. The effect of the volume-production rate within the system and the rate of volume escape from the system is then the controlling mechanism of the system pressure history while the fluid configuration is one of vapor bubbles growing in a superheated liquid. The proposed bubble-growth blowdown model of Sec. III.D is based on this concept, and it is illustrated in more detail as follows.

The prediction of the system pressure history in the bubble-growth regime of blowdown as a function of initial liquid superheat is shown in Fig. 61.

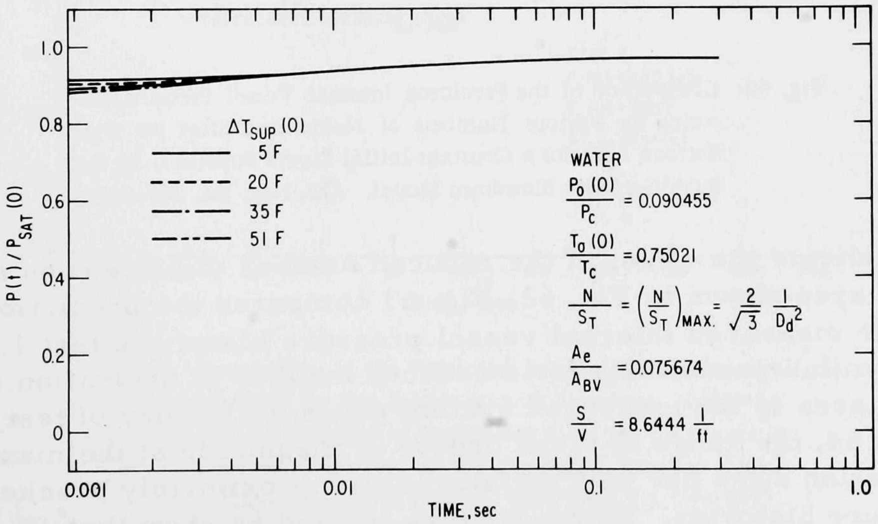

Fig. 61. Predicted Internal Vessel Pressure Histories for Various Initial Liquid Superheats for the Maximum Number of Nucleation Sites per Unit Surface Area by the Bubble-growth Blowdown Model. ANL Neg. No. 900-5523.

In this figure, the initial superheat of the liquid at the start of the bubble-growth period of depressurization is varied from 5 to 51°F for a decompression that started at 290 psia and 414°F. In Fig. 61 all the pressure histories, regardless of the initial liquid superheat, are essentially coincident for time greater than about 4 msec. This indicates that the system pressure history in the bubble-growth regime of blowdown is nearly independent of the initial liquid superheat at the beginning of this period of decompression for a given system geometry.

In view of the foregoing point, we shall consider the effect of the number of potential nucleation sites per unit surface area on the system pressure history for a given initial liquid superheat. Figure 62 shows this effect for an initial superheat of 16°F, and the number of nucleation sites per unit surface area from its maximum value for a given departure diameter to 0.001 of its maximum number. Decreasing the number of nucleation sites decreases the predicted pressure history.

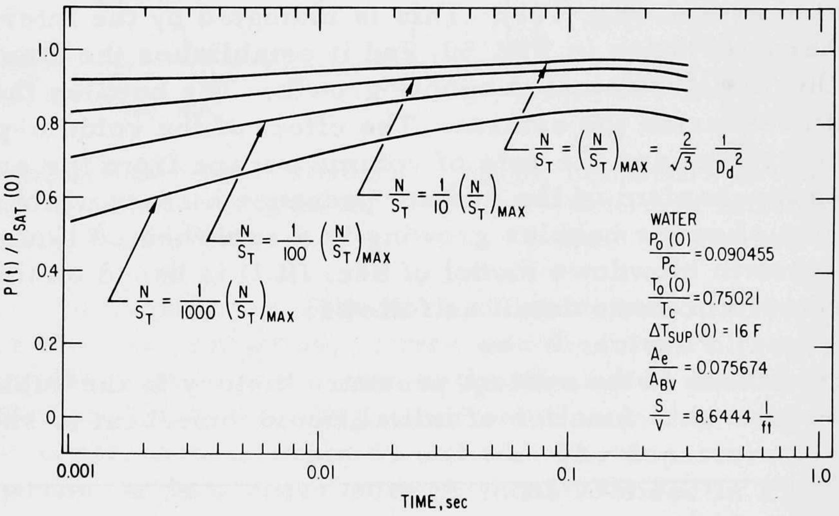

Fig. 62. Comparison of the Predicted Internal Vessel Pressure Histories for Various Numbers of Nucleation Sites per Unit Surface Area for a Constant Initial Liquid Superheat by the Bubble-growth Blowdown Model. ANL Neg. No. 900-5520.

To indicate the effect of the reduced number of nucleation sites per unit surface area shown in Fig. 62, Fig. 63 compares the predictions in Fig. 62 to the measured internal vessel pressure history in test 1. Figure 64 compares similar predictions for a reduced number of nucleation sites per unit surface area to the measured system pressure history of test 2. In both Figs. 63 and 64, the range of three orders of magnitude of the maximum number of nucleation sites per unit surface area approximately brackets the measured pressure histories. However, Figs. 63 and 64 show that 1% of the maximum number of nucleation sites per unit surface area appear to best predict the measured system pressure histories.

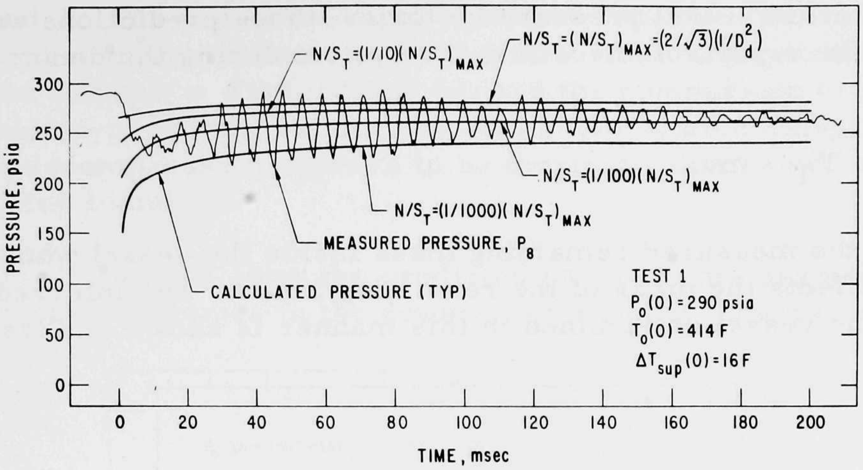

Fig. 63. Comparison of the Predicted Internal Vessel Pressure Histories by the Bubble-growth Blowdown Model for Various Numbers of Nucleation Sites per Unit Surface Area as Compared to the Measured Internal Vessel Pressure History in Test 1. ANL Neg. No. 900-5524.

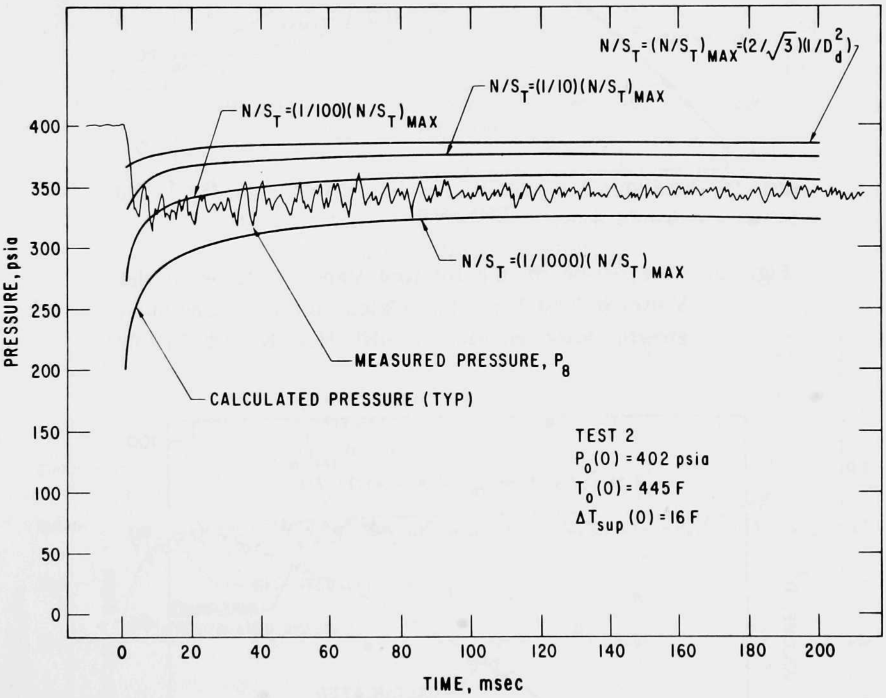

Fig. 64. Comparison of the Predicted Internal Vessel Pressure Histories by the Bubble-growth Blowdown Model for Various Numbers of Nucleation Sites per Unit Surface Area as Compared to the Measured Internal Vessel Pressure History in Test 2. ANL Neg. No. 900-5521.

Since the predicted pressure histories in Figs. 63 and 64 for 1% of the maximum number of nucleation sites per unit surface area agree best with the measured internal vessel pressure histories, those predictions are further examined. The vapor volume within the system during the decompression is given by

$$V_V = V_T - mv_L, \tag{191}$$

where m is the measured remaining mass inside the vessel whose magnitude primarily reflects the mass of the remaining liquid. The inferred vapor volume within the vessel determined in this manner is shown in Figs. 65 and 66

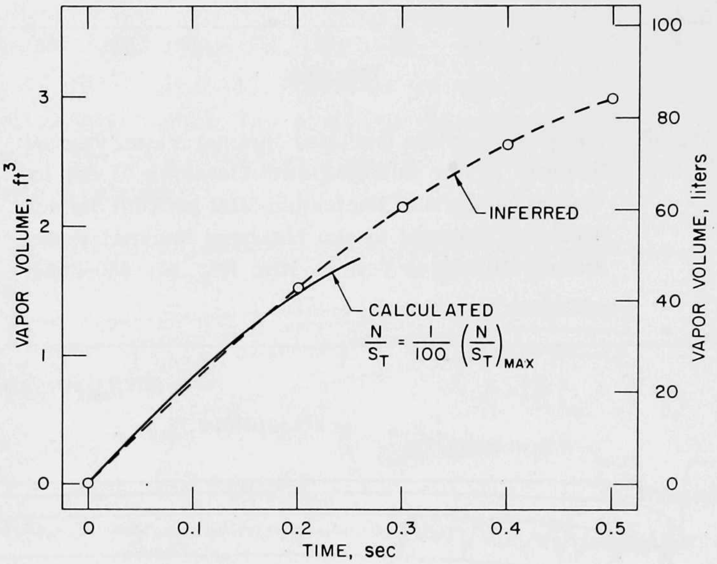

Fig. 65. Comparison of the Inferred Vapor Volume in the Vessel in Test 1 and that Calculated by the Bubble-growth Blowdown Model. ANL Neg. No. 900-5770.

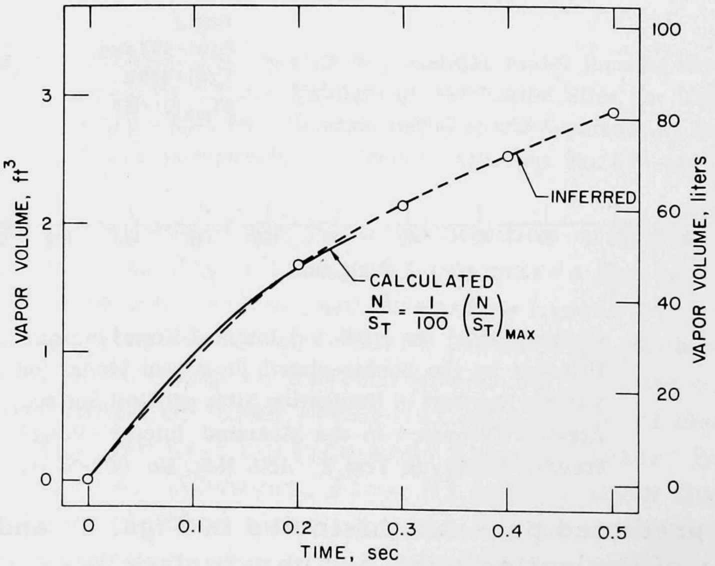

Fig. 66. Comparison of the Inferred Vapor Volume in the Vessel in Test 2 and that Calculated by the Bubble-growth Blowdown Model. ANL Neg. No. 900-5771.

for tests 1 and 2. The predicted vapor volume within the system for 1% of the maximum number of nucleation sites per unit surface area is compared to the inferred vapor volume in Figs. 65 and 66, and the comparison is good. Thus, the vapor-volume-producing mechanism within the system during the early period of the decompression appears to be thermally dominated bubble growth in a superheated liquid.

Figures 67 and 68 show the predicted pressure history and the calculated void-fraction histories in the downcomer annulus, internal skirt, and the

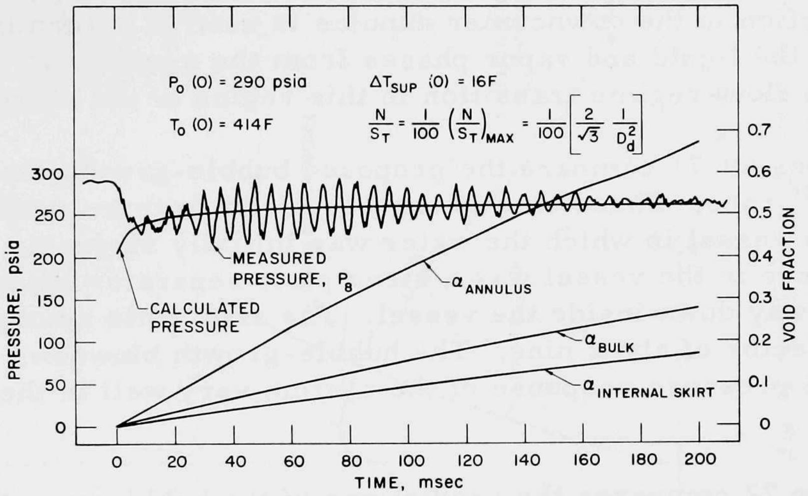

Fig. 67. Comparison of the Measured and Calculated Internal Vessel Pressure by the Bubble-growth Blowdown Model in Test 1. ANL Neg. No. 900-5507.

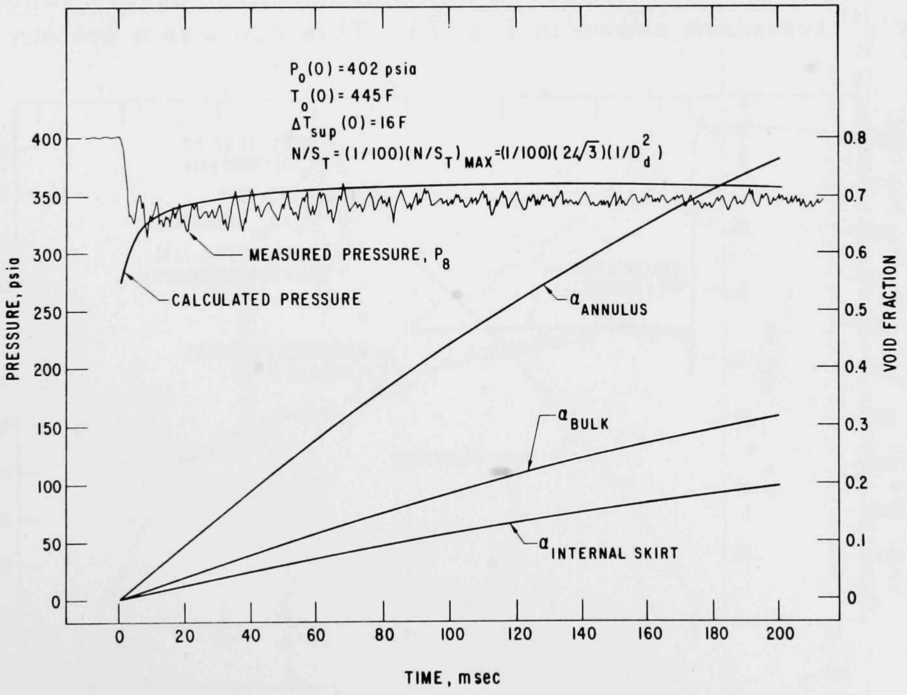

Fig. 68. Comparison of the Measured and Calculated Internal Vessel Pressure by the Bubble-growth Blowdown Model in Test 2. ANL Neg. No. 900-5538.

bulk void fraction in the vessel for tests 1 and 2 for 1% of the maximum number of nucleation sites per unit surface area. Since this analysis only considers bubble growth in a superheated liquid, it applies only during the period of time that this fluid configuration exists during the decompression. Although the maximum void fraction in a bubbly fluid configuration without bubble coalescence is about 0.7, in practice[105-107] the bubbly fluid configuration is not sustained beyond a void fraction of about 0.3-0.4. Hence, the predictions in Figs. 67 and 68 are applicable primarily in the range of the void fraction in the downcomer annulus from zero to about 0.3. These predictions compare well with the measured internal vessel pressure histories in this experiment. The void fraction in the downcomer annulus is used in determining the mass flow rates of the liquid and vapor phases from the system, so it is the best indicator of a flow-regime transition in this region of the system.

Figures 69-71 compare the proposed bubble-growth blowdown model to three CSE[79] runs. These blowdowns were from bottom, middle, and top locations of a vessel in which the water was initially stagnant. The only internal structure in the vessel was a sieve plate separator located about two-thirds of the way down inside the vessel. The area ratio among these runs ranged by a factor of about nine. The bubble-growth blowdown model predicts the measured pressure response of the system very well in the range of its applicability.

Figure 72 compares the predictions of the bubble-growth model to the measured internal vessel pressure history of Battelle-Frankfurt[77] run 13. This was an upper middle blowdown, and the predictions agree well with the measured system pressure in the applicable range of the model.

The predicted and measured internal vessel pressure histories in one of Ungerer's[67] tests are shown in Fig. 73. This run was a bottom blowdown,

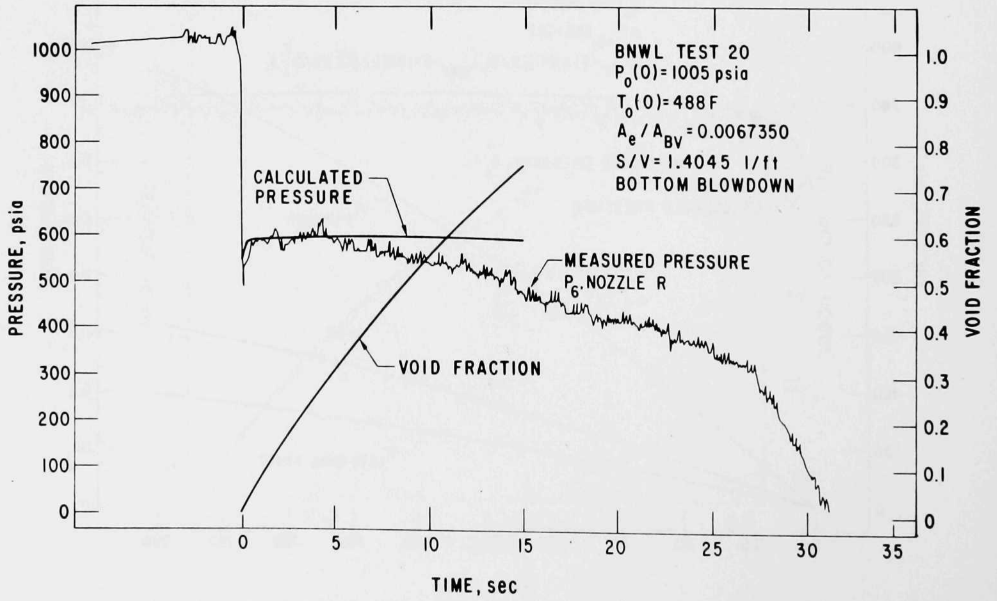

Fig. 69. Comparison of the Measured and Predicted Pressure Histories by the Bubble-growth Blowdown Model in BNWL Run 20.[79] ANL Neg. No. 900-5541.

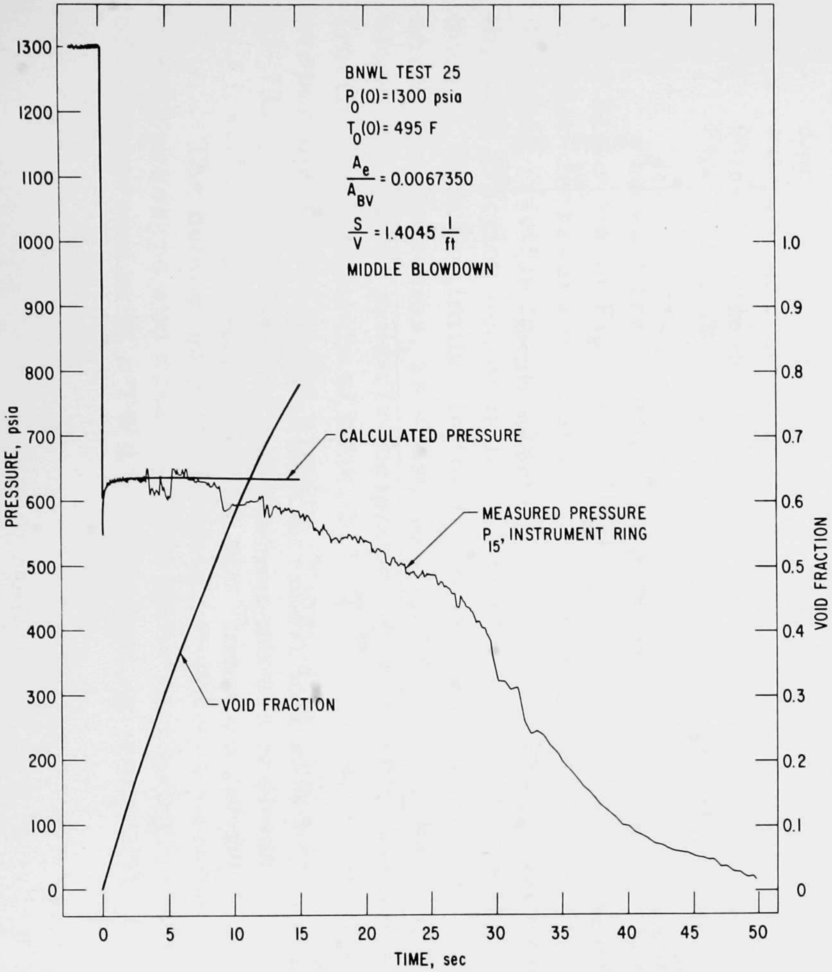

Fig. 70. Comparison of the Measured and Predicted Pressure Histories by the Bubble-growth Blowdown Model in BNWL Run 25.[79] ANL Neg. No. 900-5518.

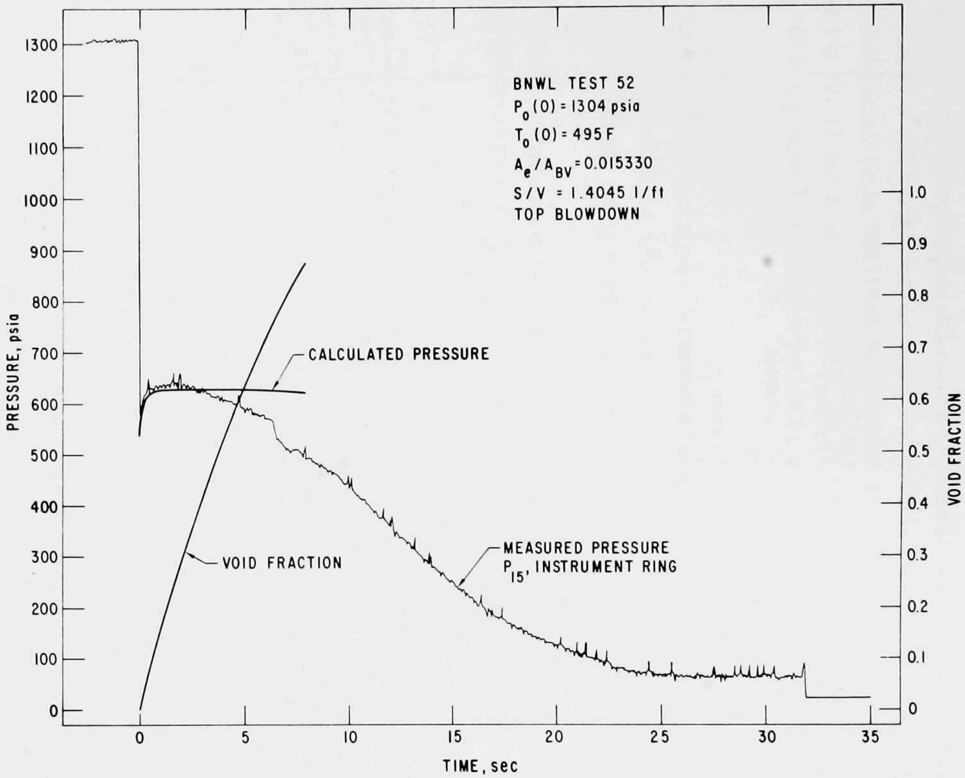

Fig. 71. Comparison of the Measured and Predicted Pressure Histories by the Bubble-growth Blowdown Model in BNWL Run 52.[79] ANL Neg. No. 900-5540.

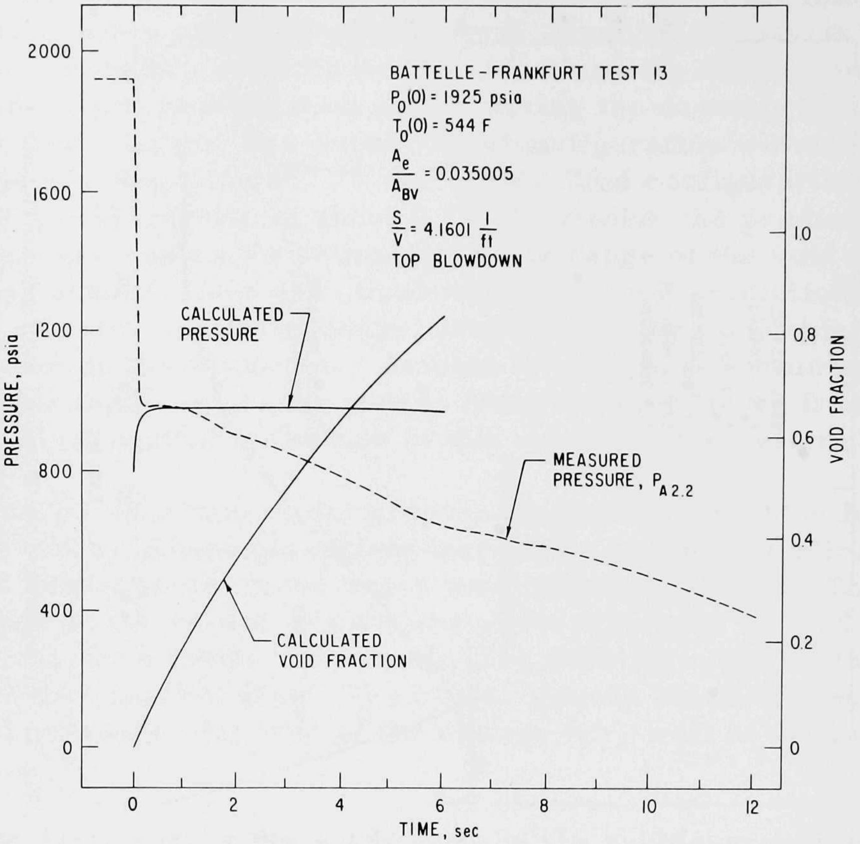

Fig. 72. Comparison of the Measured and Predicted Pressure Histories by the Bubble-growth Blowdown Model in the Battelle-Frankfurt Run 13.[77] ANL Neg. No. 900-5527.

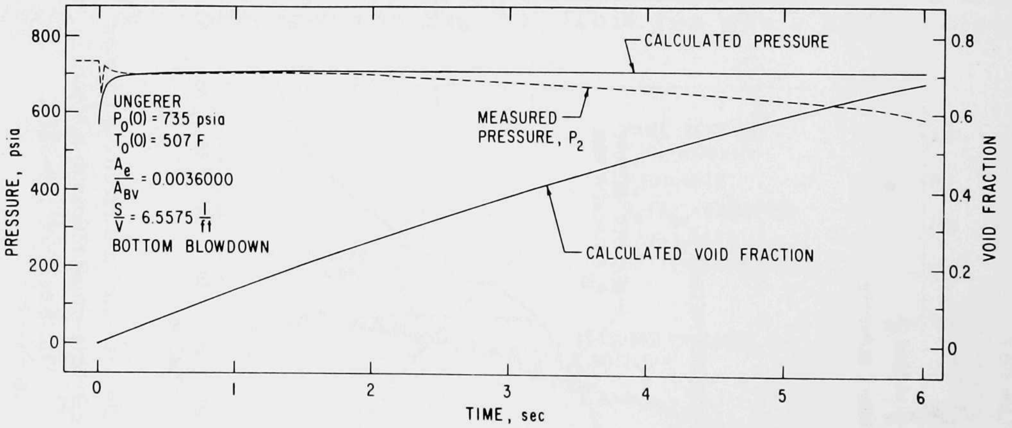

Fig. 73. Comparison of the Measured and Predicted Pressure Histories by the Bubble-growth Blowdown Model in Ungerer's Experiment.[67] ANL Neg. No. 900-5525.

and there was no structure inside the vessel. The measured and calculated pressure histories during the bubble-growth regime of decompression are essentially identical to a calculated void fraction of about 0.2, and the pressures compare well to a calculated void fraction of about 0.3, which is approximately the upper limit of applicability of the bubble-growth blowdown model.

The foregoing comparisons indicate that the proposed bubble-growth blowdown model predicts the system pressure history during decompression well in the applicable range of the model.

The system pressure history during the period of decompression when the pressure is maintained by bubble growth is dependent upon the amount of internal surface area and also upon the size of the exit from the system. Figure 74 shows that the system pressure is greater for reduced area ratios, the ratio of the exit flow area to the internal vessel flow area, for a given ratio of internal vessel surface area to internal vessel volume (S/V). The volume of the vessel employed in this study is used for illustration. The system pressure is also greater for increased S/V at a given area ratio. The system pressure is more sensitive to S/V as the area ratio is increased, and the pressure also recovers slower as the area ratio is increased and S/V is decreased. The system pressure is typically more sensitive to S/V than it is to the area ratio. These trends are what would be intuitively expected.

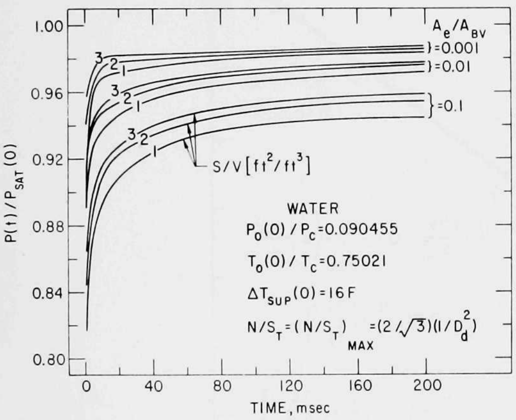

Fig. 74. Prediction of the Pressure History during the Initial Stage of Decompression for the Proposed Bubble-growth Blowdown Model. ANL Neg. No. 900-5506.

The void fraction within the system associated with the predicted pressure histories in Fig. 74 is illustrated in Fig. 75, which shows that the void fraction decreases dramatically as the area ratio is reduced for a given S/V. The void fraction increases as S/V is increased for a given area ratio, but the void fraction becomes less dependent upon S/V as the area ratio is reduced. This is similar to the trend in the predicted system pressure at smaller area ratios, as shown in Fig. 74. Thus, the proposed bubble-growth blowdown model predicts the proper trends in the system pressure and void fraction as a function of time, S/V, and area ratio, and it also predicts the proper magnitude of the system pressure, as illustrated in Figs. 63, 64, and 67-73.

The bubble-growth blowdown model was used to predict the internal vessel pressure and void-fraction histories during the bubble-growth regime of decompression of a PWR vessel starting from 2250 psia and 575°F. The break was considered to be an instantaneous, double-ended, guillotine rupture in an inlet coolant line of 27.5-in. inside diameter. The internal vessel pressure in this regime of blowdown was essentially independent of the initial liquid superheat, as shown in Fig. 61. It has also been shown in Figs. 63 and 64 that the pressure history that best predicts the measurements in this study is the one in which 1% of the maximum number of nucleation sites per unit surface area are considered to be active. This is assumed to also be characteristic of a PWR-vessel blowdown.

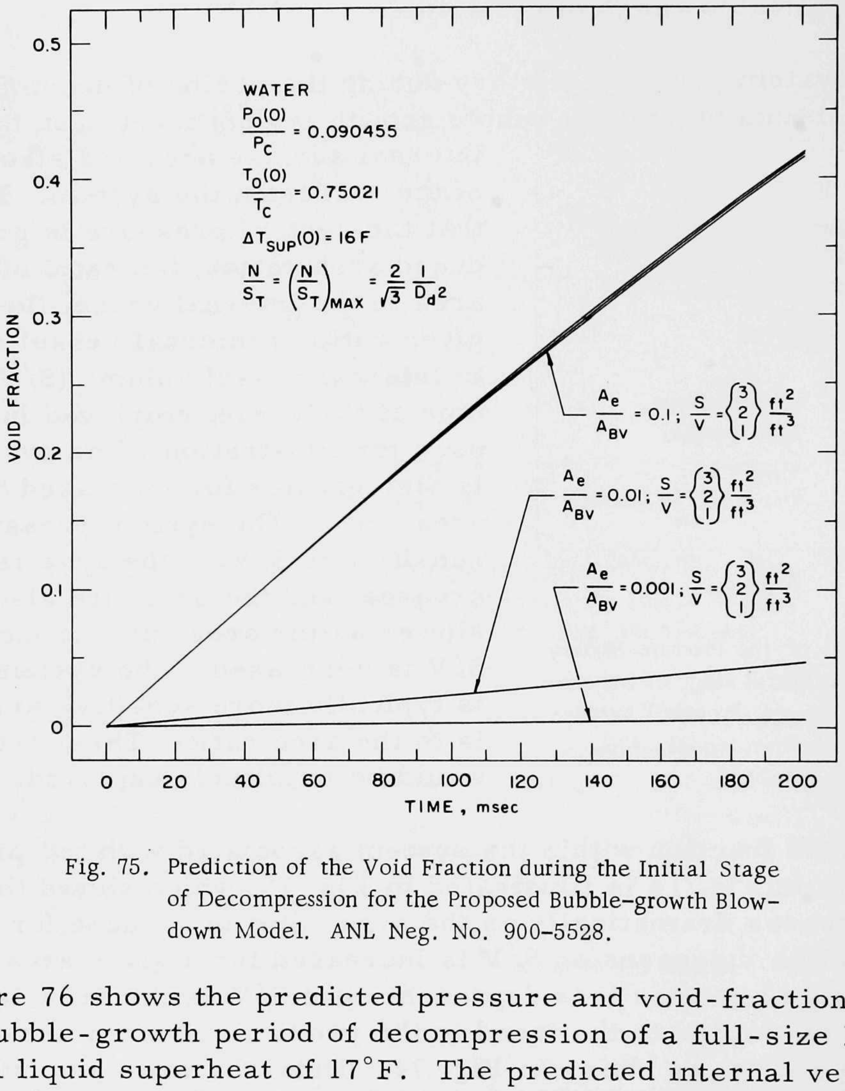

Fig. 75. Prediction of the Void Fraction during the Initial Stage of Decompression for the Proposed Bubble-growth Blowdown Model. ANL Neg. No. 900-5528.

Figure 76 shows the predicted pressure and void-fraction histories during the bubble-growth period of decompression of a full-size PWR vessel for an initial liquid superheat of 17°F. The predicted internal vessel pressure initially decreases because more volume is escaping from the system than is being produced within the system. The system pressure continues to decrease until sufficient liquid superheat is generated so that the rate of vapor-volume production within the system becomes equal to the escape rate of fluid volume from the system. The internal vessel pressure then reaches a relative minimum, and it subsequently increases because more vapor volume is being generated within the system than there is fluid volume escaping from the system. The internal vessel pressure during this period of blowdown then increases at a decreasing rate because the liquid superheat decreases as the system pressure approaches the saturation pressure. The time required for the internal vessel pressure to recover is more sensitive to S/V than it is to the area ratio, as shown in Fig. 74. The void fraction in the region of the PWR vessel inside the core barrel is the greatest, as seen in Fig. 76. Thus, a PWR system will probably not experience a nonuniform flow regime inside the vessel during blowdown as was the case in this investigation; rather, the fluid in the vessel will probably depressurize in a nearly homogeneous manner.

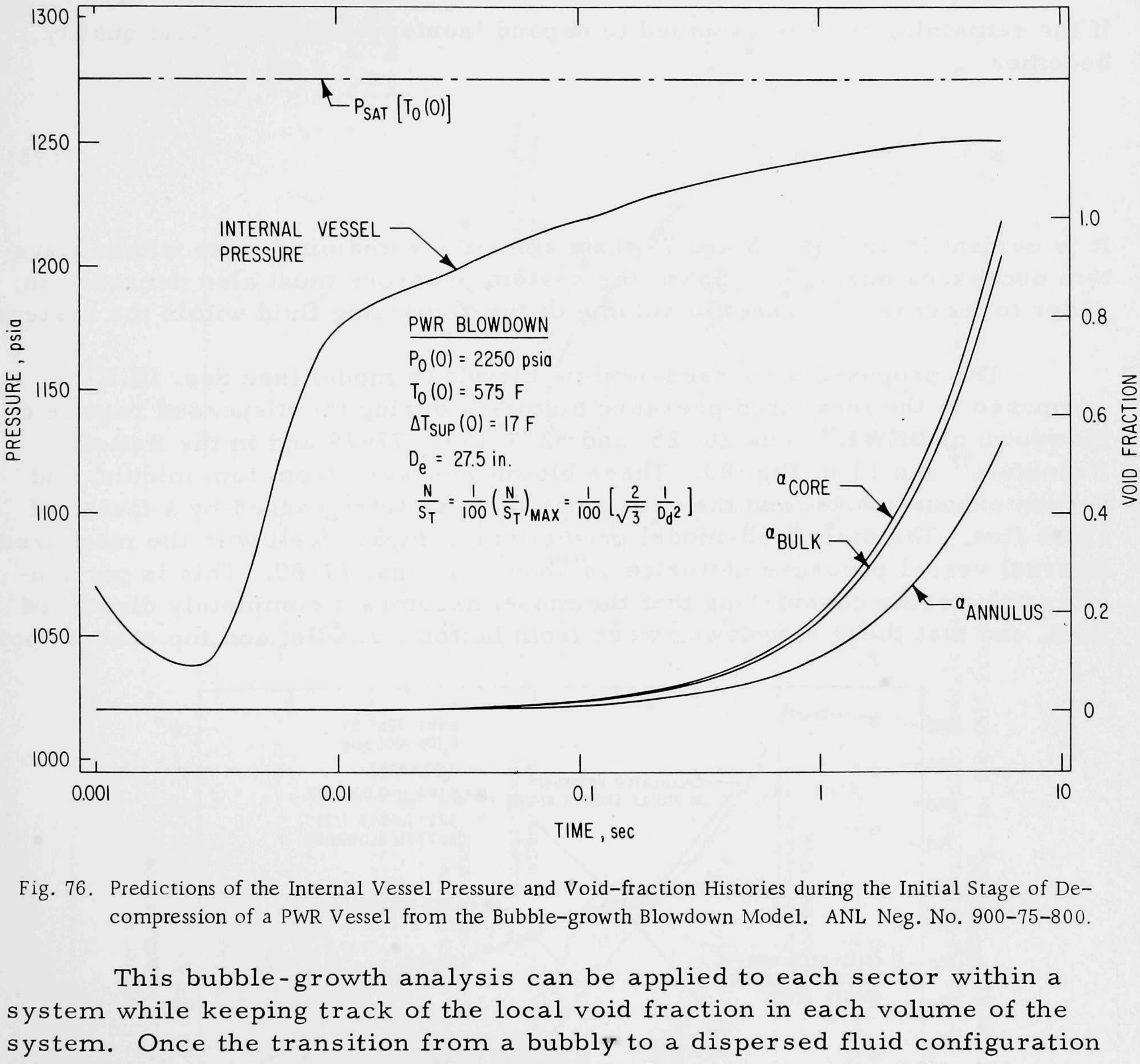

Fig. 76. Predictions of the Internal Vessel Pressure and Void-fraction Histories during the Initial Stage of Decompression of a PWR Vessel from the Bubble-growth Blowdown Model. ANL Neg. No. 900-75-800.

This bubble-growth analysis can be applied to each sector within a system while keeping track of the local void fraction in each volume of the system. Once the transition from a bubbly to a dispersed fluid configuration takes place in a given sector of the system, the vaporization of the superheated liquid droplets would then be the only remaining mechanism to sustain the pressure in that volume of the system. This bubble-growth blowdown model can also be used to predict the decompression characteristics in the bubble-growth regime of depressurization in an initially nonisothermal system as well as in an initially isothermal system.

When the fluid configuration in a given volume of a system changes from bubbles expanding in a superheated liquid toward that of dispersed superheated liquid droplets entrained in the vapor phase, thermodynamic equilibrium is closely approached, and a decrease in pressure is required to supply additional fluid volume to the system. This can be shown by considering the specific volume of the remaining fluid:

$$v = \frac{V}{m} = v_V(P)x + v_L(P)(1 - x). \tag{192}$$

If the remaining fluid is assumed to expand isentropically, the fluid quality becomes

$$x = \frac{s_i - s_L(P)}{s_{VL}(P)}. \tag{193}$$

It is evident from Eqs. 78 and 79 that, since the remaining mass within a system decreases during blowdown, the system pressure must also decrease in order to increase the specific volume of the remaining fluid within the system.

The proposed dispersed-regime blowdown model (see Sec. III.E) is compared to the measured pressure histories during the dispersed regime of blowdown of BNWL[79] runs 20, 25, and 52 in Figs. 77-79 and in the Battelle-Frankfurt[77] run 13 in Fig. 80. These blowdowns were from top, middle, and bottom exhaust ports, and the area ratio in these tests ranged by a factor of about five. The dispersed-model predictions compare well with the measured internal vessel pressure histories as shown in Figs. 77-80. This is particularly noteworthy considering that the model assumes a completely dispersed fluid, and that these blowdowns were from bottom, middle, and top exhaust ports

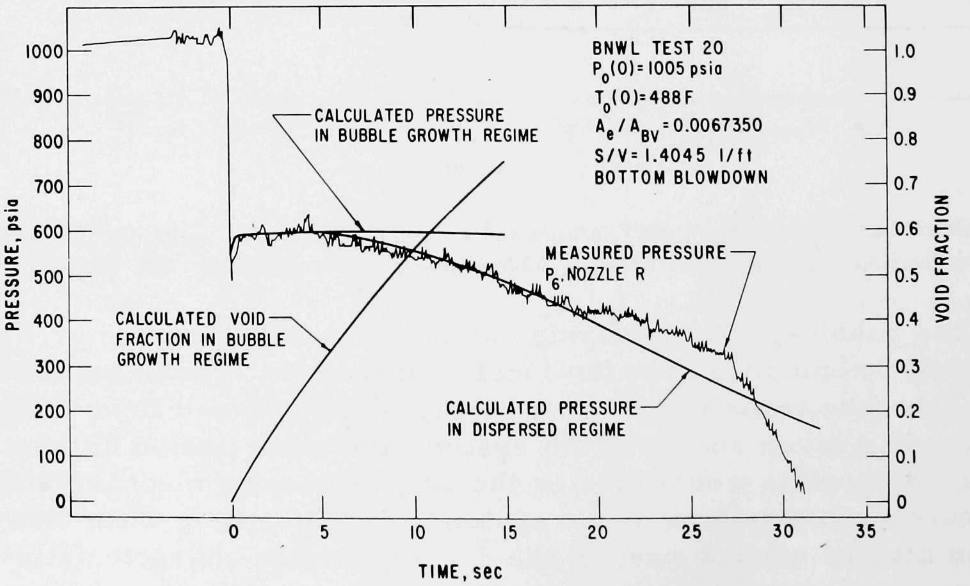

Fig. 77. Comparison of the Dispersed-regime Blowdown Model to the Data of BNWL Run 20.[79] ANL Neg. No. 900-5541 Rev. 1.

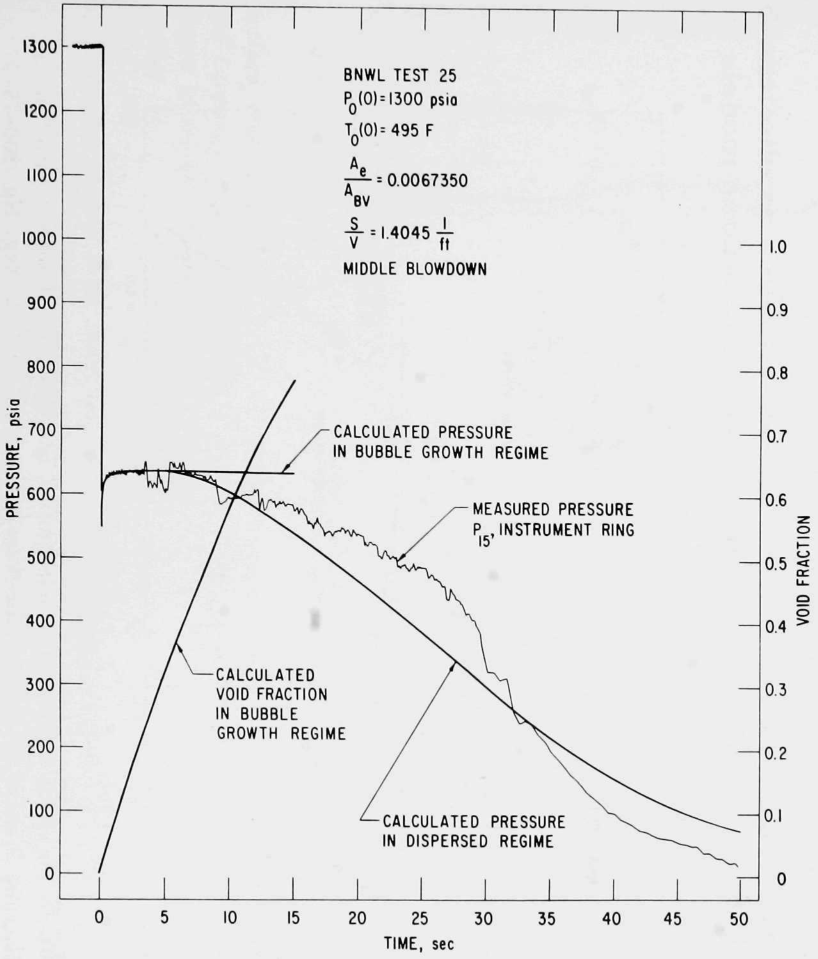

Fig. 78. Comparison of the Dispersed-regime Blowdown Model to the Data of BNWL Run 25.[79] ANL Neg. No. 900-5518 Rev. 1.

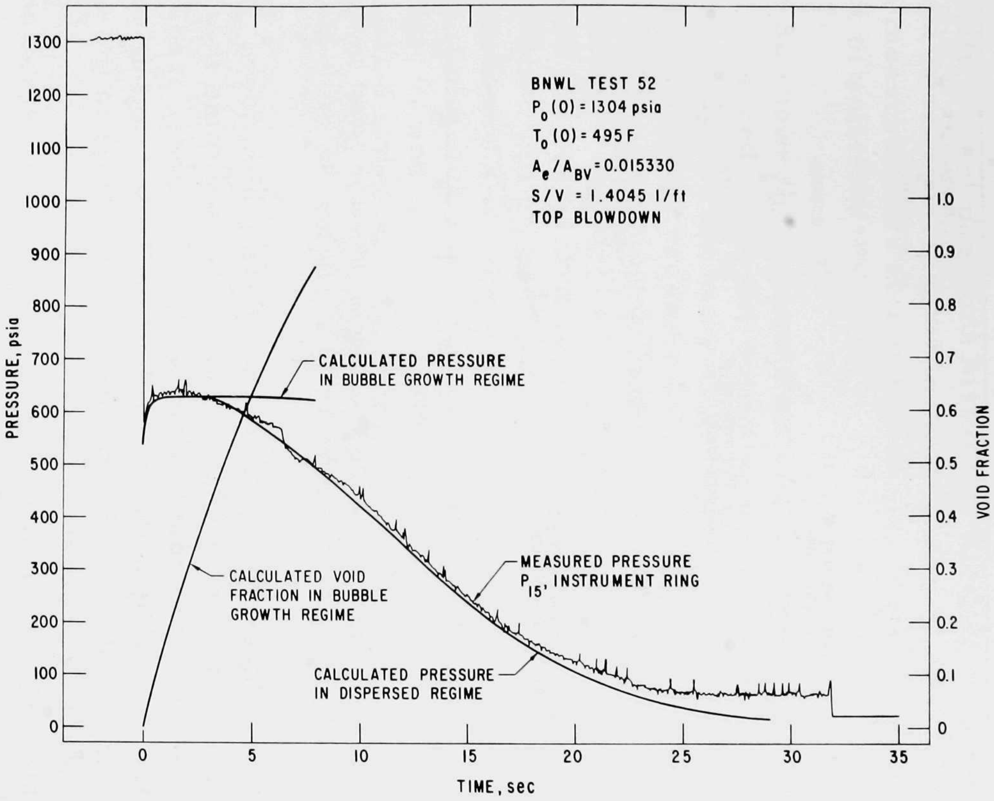

Fig. 79. Comparison of the Dispersed-regime Blowdown Model to the Data of BNWL Run 52.[79] ANL Neg. No. 900-5540 Rev. 1.

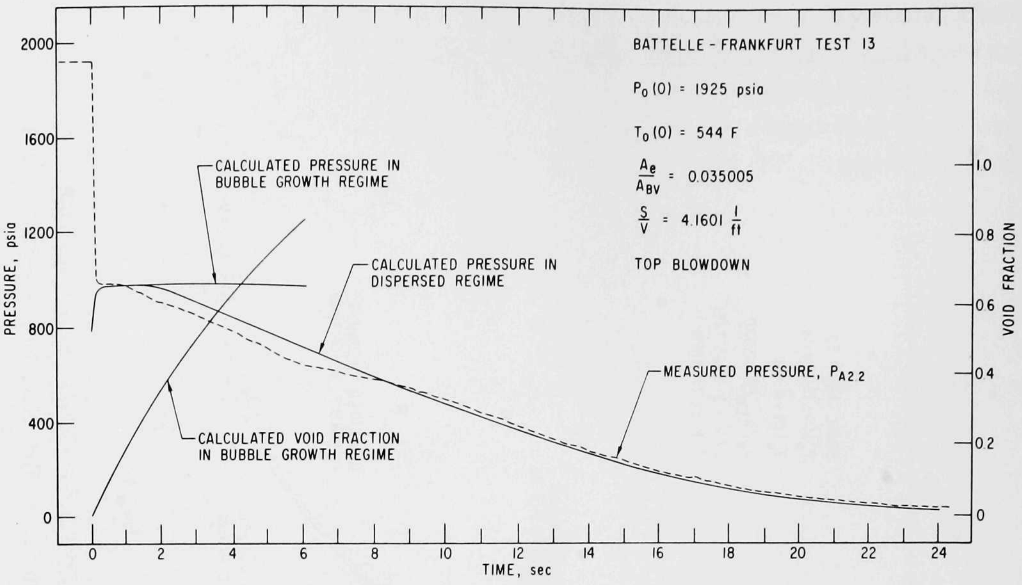

Fig. 80. Comparison of the Dispersed-regime Blowdown Model to the Data of Battelle-Frankfurt Run 13.[77] ANL Neg. No. 900-75-262.

of a vessel that influences phase separation during blowdown. Also, the dispersed-regime blowdown model is based only on simple thermodynamics, and it predicts the measurements fairly well. The model predicts the top blowdown results somewhat better than the middle and bottom decompression data (see Figs. 79 and 80), which indicates that the fluid in the vessel was probably more nearly a homogeneous equilibrium mixture in the top blowdown case. This is physically reasonable based on visual observations of blowdown in glass vessels.[72,73]

Figure 81 compares the combined pressure-history predictions from the subcooled, bubble-growth, and dispersed-regime blowdown models to the

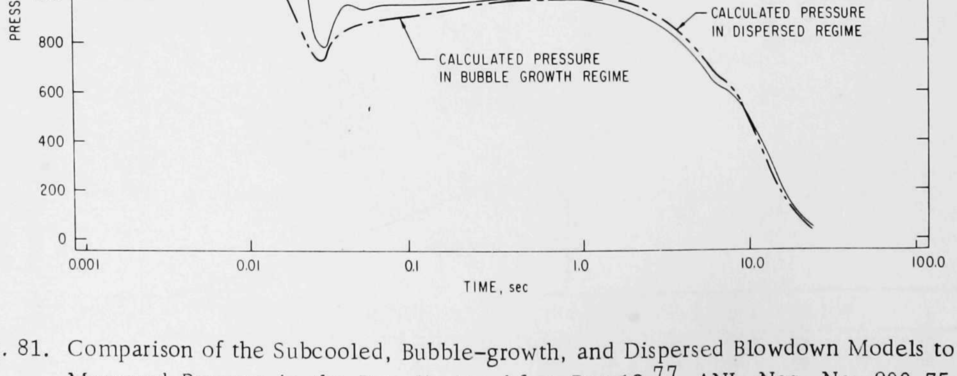

Fig. 81. Comparison of the Subcooled, Bubble-growth, and Dispersed Blowdown Models to the Measured Pressure in the Battelle-Frankfurt Run 13.[77] ANL Neg. No. 900-75-97.

measured internal vessel pressure history of Battelle-Frankfurt[77] run 13. The comparison is reasonably good, even though the predictions deviate somewhat from the measurements at about 25 msec. This is attributed to dissolved gas coming out of solution.

Figure 82 shows the proposed manner in which the liquid and vapor phases were configured inside the blowdown vessel during the decompressions reported in this study. In the early stage of the blowdown, $0 < t \le 100$ msec, the decrease in the system pressure below the initial saturation pressure activated the largest remaining unflooded surface cavities. Since there were potentially many more surface cavities per unit volume in the downcomer annulus region of the vessel than anywhere else in the system, most of the excess vapor volume initially generated within the vessel was in this region. The bubble-growth analysis supports this, as indicated by the void fraction in the downcomer annulus as compared to the void fraction in the internal skirt as shown in Figs. 67 and 68. The bubbles originating from these cavities expanded and supplied additional vapor volume to the system, which forced the internal vessel pressure to partially recover (see Figs. 67 and 68); however, many of these expanding bubbles were swept out of the vessel with the initial fluid exhausted from the downcomer annulus. The fluid configuration in the downcomer annulus changed from bubbly to nearly dispersed by about 100 msec, and this then only left the growing bubbles on the inside of the internal skirt wall to maintain the system pressure. Once the downcomer annulus was initially nearly voided, the vapor layer on the inside wall of the skirt could have been swept into the downcomer annulus along with dispersed liquid from the interior of the internal skirt region.

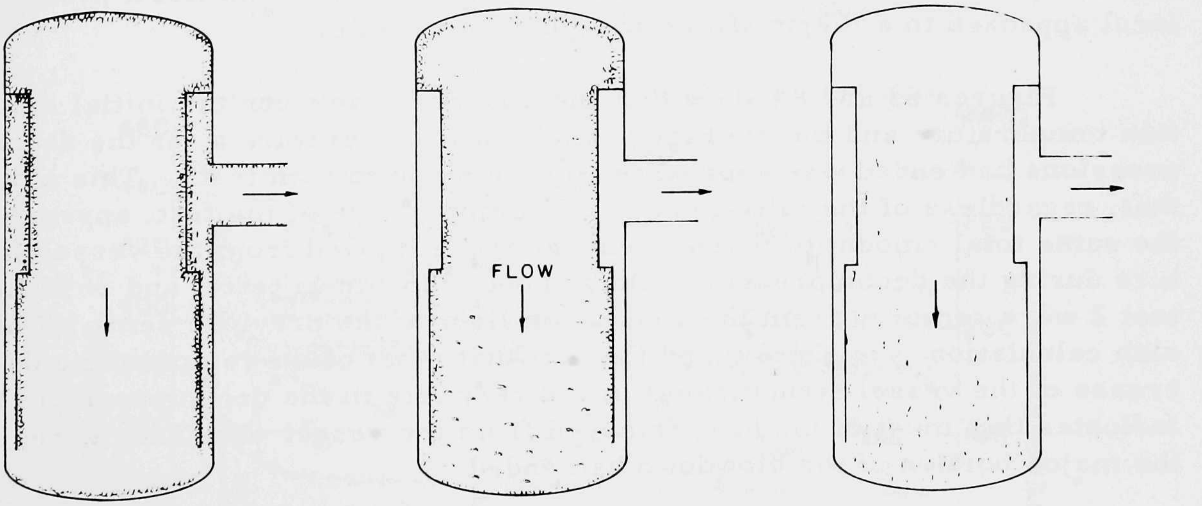

$0 < t \le 100$ msec

Surface Voids Activated and Growing, Superheated Liquid Internally, Annulus Voided

$100 \le t \le 600$ msec

Bubbles Expanding into Bulk of Superheated Liquid

$0.6 \le t \le 2.0$ sec

Dispersed Two Phase, Liquid-Vapor Mixture

Fig. 82. Cross Section of the Blowdown Vessel Illustrating the Proposed Flow Regimes inside the Vessel during the Various Stages of Decompression in These Tests. ANL Neg. No. 900-5110 Rev. 1.

Figures 52 and 53 show that the internal vessel pressure did not immediately decrease once the downcomer annulus had initially been voided; rather, the pressure remained nearly constant for about $100 \leq t \leq 600$ msec. During this period, the smaller number of vapor bubbles per unit volume inside the internal skirt were growing by conduction-controlled energy transfer from the superheated liquid in that region, providing additional vapor volume to the system to maintain the pressure. By about 600 msec, the fluid inside the internal skirt region probably approached a dispersed mixture of liquid and vapor, as indicated in Figs. 56 and 57. This is also indicated by the bubble-growth analysis. When the predictions shown in Figs. 67 and 68 are continued to when the fluid configuration in the internal skirt changes from bubbly to dispersed (i.e., at a void fraction of about 0.4), this transition occurs at 500-700 msec. Once the remaining fluid within the internal skirt had become a dispersed, two-phase, liquid-vapor mixture (at $0.6 \leq t \leq 2.0$ sec), the system pressure began to decrease in a nearly thermodynamic equilibrium manner (see Figs. 56 and 57).

The nearly thermodynamic equilibrium conditions for the pressure and temperature of the remaining fluid, shown in Figs. 52 and 53, were recorded near the inside wall of the skirt, as shown in Figs. 4, 8, 9, 12, and 13. Local thermodynamic equilibrium conditions could nearly have existed near the walls where the vapor phase was being generated, which is also where the instrumentation was located, while the bulk of the interior of the internal skirt would have remained as superheated liquid. The thermocouples themselves probably behaved as nucleation surfaces and, hence, promoted the formation of the vapor phase from their surfaces. This is why it is so difficult to ascertain a superheated liquid state with a thermocouple that can itself promote the local approach to a thermodynamic equilibrium state.

Figures 83 and 84 show that the difference between the initial stagnation temperature and the average vessel-wall temperature after the decompressions had ended was approximately the same in both tests. This indicates that, regardless of the initial stagnation temperature of the test, approximately the same total amount of thermal energy was removed from the vessel structure during the decompression. Only about 3385 Btu in test 1 and 3690 Btu in test 2 were removed from the vessel. In light of the previous semi-infinite-slab calculation (see Eq. 68) and the fact that most of the temperature decrease of the vessel structure occurred very late in the decompression, this indicates that most of the heat removed from the vessel was transferred after the major portion of the blowdown had ended.

The foregoing bubble-growth analysis has shown that the remaining fluid within a system will select a superheat to maintain the system pressure nearly constant during the initial period of a decompression when vapor bubbles are expanding in a superheated liquid. The size of a growing spherical bubble in the thermally dominated growth regime is given by Eq. 171. The more potentially active the nucleation sites available, the smaller would be the required

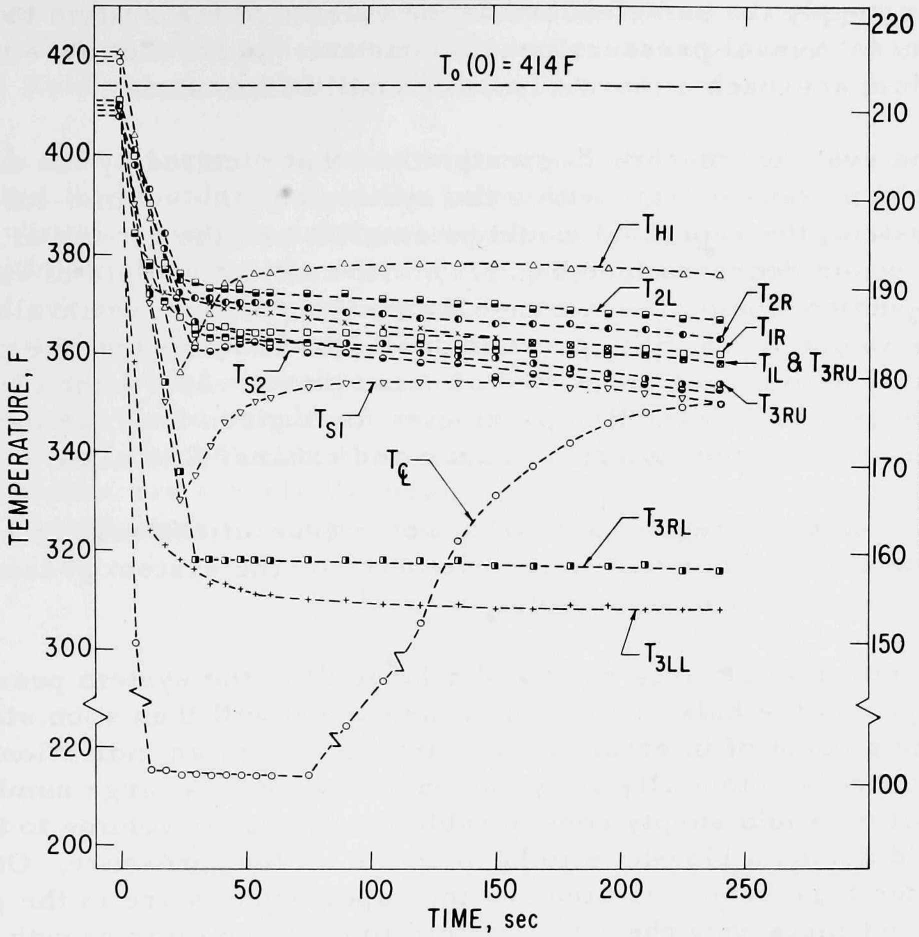

Fig. 83. Temperature of the Vessel Structure after Blowdown in Test 1. ANL Neg. No. 900-5010.

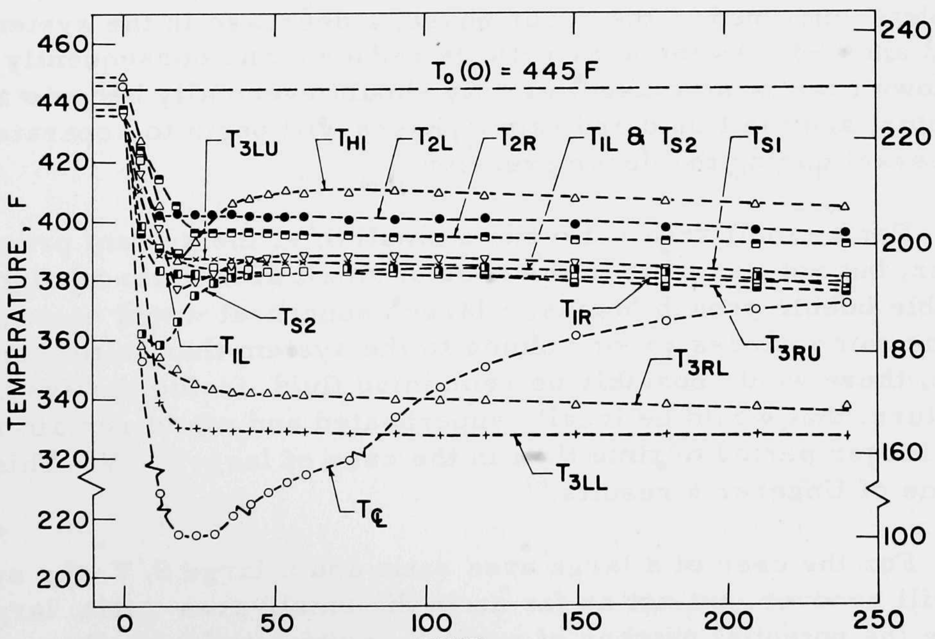

Fig. 84. Temperature of the Vessel Structure after Blowdown in Test 2. ANL Neg. No. 900-5007.

superheat to supply the same excess vapor volume to the system to maintain the internal vessel pressure nearly constant; hence, the more nearly would the fluid approach a thermodynamic equilibrium state.

If the system pressure is greater than that dictated by the net effect of the volume-production rate within the system and the volume-loss rate from the system, the superheat would be smaller and the growth of the existing bubbles would decrease (see Eq. 171). Therefore, the rate of vapor-volume production would decrease, and the system pressure would also decrease. The inverse would occur if the pressure were too low. Hence, the pressure history in a system during the period of expansion of vapor bubbles in a superheated liquid is a self-regulating parameter for a given internal nucleation-site surface area per unit internal volume and exhaust flow area.

Based on the foregoing remarks, some generalizations can be made as to the effect of the internal vessel geometry on the system pressure history during the bubble-growth regime of blowdown.

(1) For a small area ratio and a large S/V, the system pressure will recover to nearly the bulk saturation pressure and will then soon start to decrease. The amount of internal vessel surface area is an indication of the number of initially potentially active surface cavities. A large number of surface cavities would supply considerable excess vapor volume to the remaining fluid during a blowdown to keep up the system pressure. Once most of the cavities have been activated and the vapor bubbles are in the process of growing, not much superheat is required to continue their growth, and the remaining fluid near the surface approaches local thermodynamic equilibrium conditions. When the fluid configuration inside the system changes from bubbles expanding in a superheated liquid toward that of dispersed superheated liquid droplets entrained in the vapor phase, a decrease in the system pres- by Eqs. 192 and 193. As the area ratio is reduced, and consequently the total blowdown time is increased, gravity should eventually become a significant factor, and the liquid and vapor phases will begin to separate in the blowdown vessel during the decompression.

(2) For a small area ratio and a small S/V, the system pressure will recover, but not as far as in the case of small area ratio and large S/V. Once unstable bubble growth begins, a larger superheat would be required to supply the same excess vapor volume to the system than in the foregoing case. Also, there would possibly be remaining fluid, inside the system away from structure, that would be locally superheated and would remain in this state for a longer period of time than in the case of larger S/V. This is the case in some of Ungerer's results.[67]

(3) For the case of a large area ratio and a large S/V, the system pressure will recover, but not as far as in the small-area-ratio, large-S/V case. Since the potential number of surface cavities is large, thermodynamic

equilibrium will probably nearly exist once the initial pressure recovery occurs, and the system pressure will soon decrease in order to produce additional fluid volume within the system.

(4) For a large area ratio and a small S/V, the system pressure will recover to a lower value than in the large-area-ratio, large-S/V case. This situation will also require a larger superheat to supply the same excess vapor volume within the system than in the large-S/V case. The smaller potential number of surface cavities will probably leave local sectors of superheated liquid existing in the system for a longer time than in the large-S/V case. This is the case in the experimental results from this investigation, and it is also the case in the results of some of the CSE tests,[70,79] Ungerer's tests,[67] the Rosa tests,[81] the Battelle-Frankfurt tests,[80] and the Japanese tests.[65] The foregoing trends are clearly illustrated in Fig. 74. Hence, the system geometry does significantly effect the system pressure history during decompression.

C. Effect of the Internal Vessel Geometry on the Blowdown

1. Detection of Internal Choking

An evaluation of compressible flow inside the blowdown vessel was made by comparing the observed pressures P_5, P_6, and P_8 at locations given in Figs. 8, 9, and 12. If internal choking had occurred at the area enlargement in the downcomer annulus, P_6 would have only been about 75% of P_8 because of the required fluid acceleration in the approach to the choking location. In addition, if the flow was choked at the area enlargement, P_5 may not necessarily have been less than P_6. This would have depended upon the back pressure to the area enlargement, P_1, which was the entrance pressure to the exhaust duct. Hence, the pressures P_6 and P_8 provided the most sensitive and reliable assessment of potential choking at the area enlargement, and if P_5 was significantly less than P_6, this would simply verify that the flow was choked at this location. Since only a small pressure drop was detected from locations 8 to 6, it was concluded that internal choking did not occur at the area enlargement in the downcomer annulus between locations 6 and 5. This is indicated in Figs. 85 and 86, where P_5 and P_6 are compared to the lower internal skirt pressure P_8. From a one-dimensional viewpoint, this is not surprising, since the minimum flow area in the vessel was in the exhaust duct. The flow area in the downcomer annulus was about 2.5 times as large as the exhaust-duct flow area. In Fig. 85, P_5 and P_6 data are not presented past 600 msec because of recording-instrument failure.

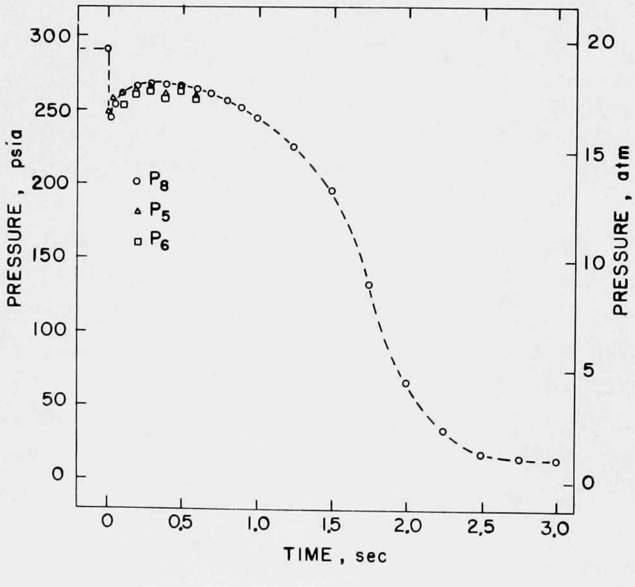

Fig. 85. Pressures Upstream and Downstream of the Area Expansion in Test 1. ANL Neg. No. 900-4984.

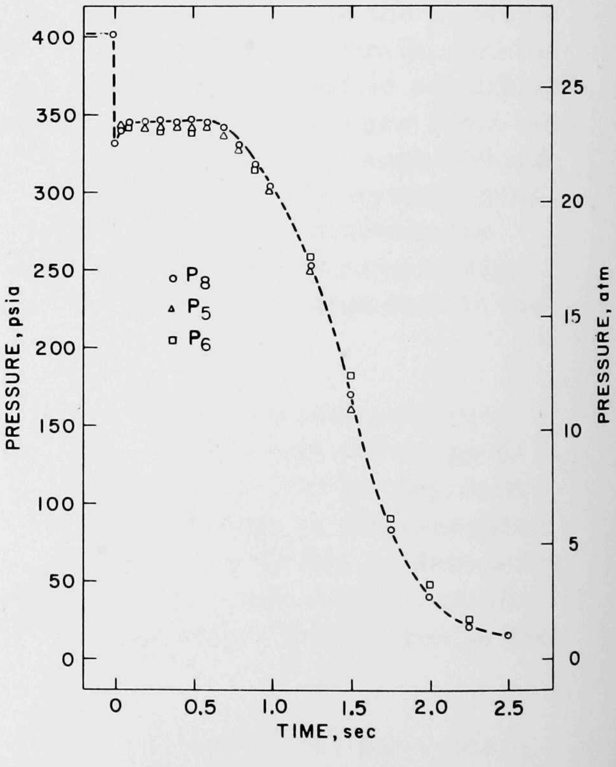

Fig. 86. Pressures Upstream and Downstream of the Area Expansion in Test 2. ANL Neg. No. 900-4979.

Figures 87 and 88 show that, consistent with the no-choking observation at the internal flow-area enlargement, there was only a small pressure gradient up the downcomer annulus in the approach to the flow-area enlargement. In these figures, P_9-P_{12} are compared to the average internal skirt pressure ${}_7\overline{P}_8$. All pressure-tap locations are defined in Figs. 8, 9, and 12. This showed that the fluid was not appreciably compressible at the flow-area enlargement nor up the downcomer annulus in the approach to the area enlargement.

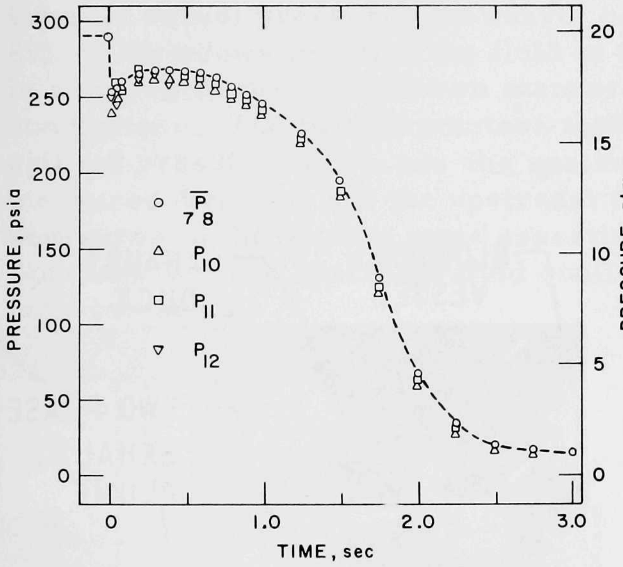

Fig. 87. Pressures up the Downcomer Annulus in Test 1. ANL Neg. No. 900-4974.

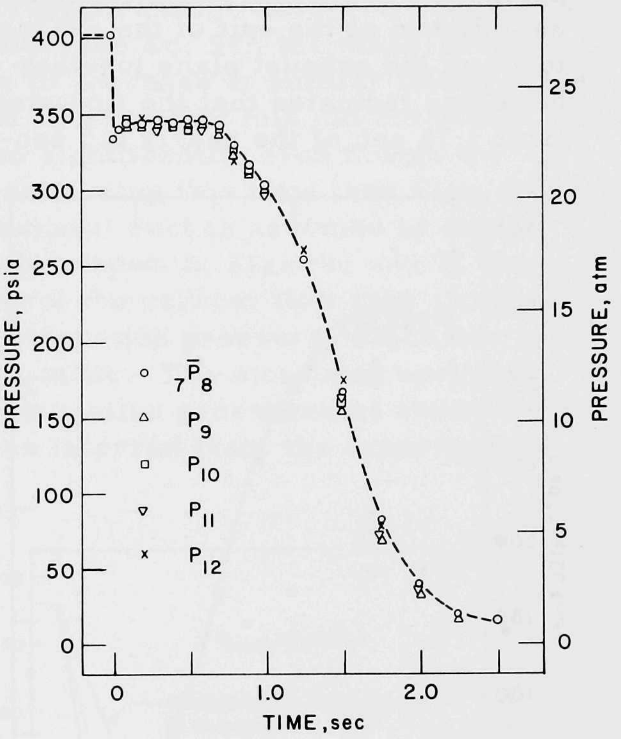

Fig. 88. Pressures up the Downcomer Annulus in Test 2. ANL Neg. No. 900-5087.

The observation of small pressure differences inside the vessel noted in Figs. 85-88 was common throughout the system. An overall demonstration of the effect the internal vessel geometry had on the pressure distribution inside the vessel during the decompression is shown in Fig. 89, which compares the pressure immediately upstream and on the centerline of the exhaust duct, P_1, with the average internal skirt pressure ${}_7\overline{P}_8$ in test 2. In test 1, the pressure signal P_1 was unavailable. This comparison indicates that all the remaining fluid within the vessel experienced nearly the same instantaneous pressure during the blowdown. This is consistent with the experimental observations indicated in Ref. 81.

2. External Choking

Although the flow was not choked internally, it was definitely choked at the exit plane of the exhaust duct. Figure 90 shows a side view of the exhaust plane in test 2 very early in the decompression. Test 2 was started at 402 psia and 445°F, and the initially contained fluid mass was 279 lb_m. This photograph was taken about 25 msec after the start of the depressurization, at which time the upstream pressure had decreased to about 320 psia, the exit pressure was about 260 psia, and the upstream isentropic fluid quality was about 0.031. To indicate size in Fig. 90, the outside diameter of the uninsulated portion of the exhaust duct is 6.69 in., and the inside diameter is 4.257 in. The very rapid expansion at the exhaust plane, which is characteristic of choking at that location, can certainly be seen in the figure. Motion pictures of the exit plane during the depressurization indicated that fully developed critical flow was established at the exit of the exhaust duct in about 25 msec. The motion pictures of the exhaust plane together with the measured critical-pressure-ratio histories indicated that the flow was choked at the exit plane for at least the first 1.75 sec of the nearly 2.5 sec-decompressions.

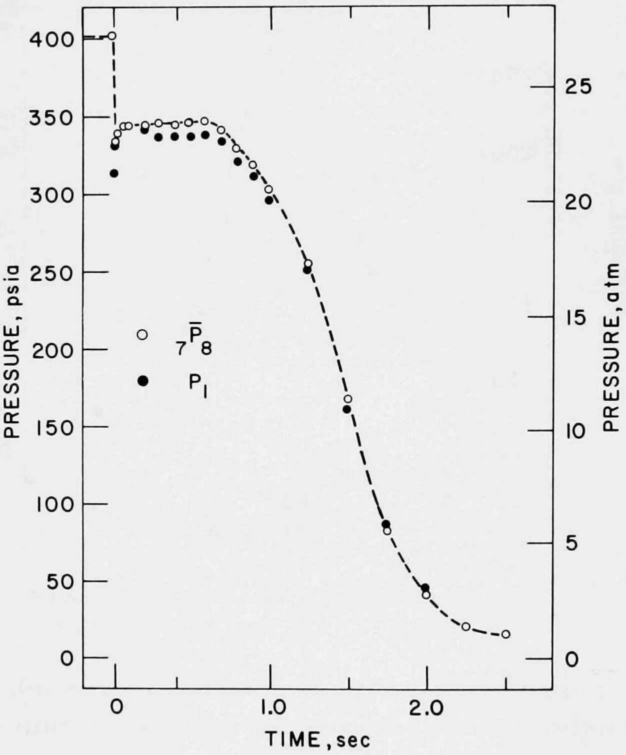

Fig. 89. Comparison between the Pressure Upstream of the Exhaust Duct and the Average Internal Skirt Pressure in Test 2. ANL Neg. No. 900–4978.

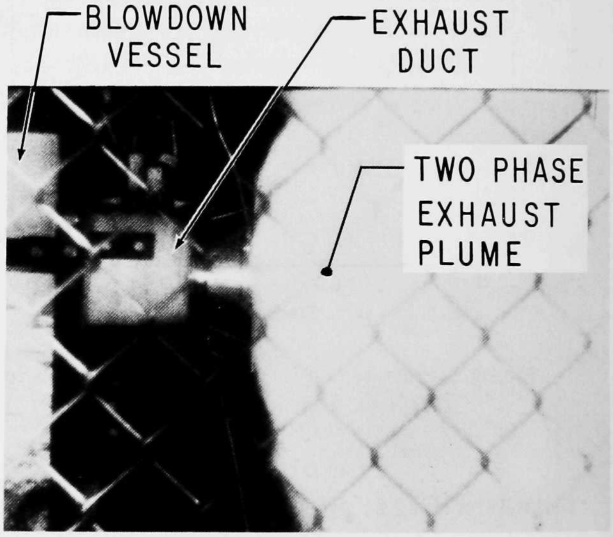

Fig. 90. Choking at the Exhaust Plane in Test 2. ANL Neg. No. 900–4586A.

3. Internal Flow Regimes

The internal vessel geometry did significantly affect the flow regimes generated inside the vessel during the decompression (see Fig. 82). The first indication of this was observed in the mass-decay histories in Figs. 54 and 55. Early in the depressurization, the slope of the mass-decay history was relatively steep, but it decreased significantly with increasing time.

If (1) the fluid remaining within the vessel was assumed to always be uniformly distributed, (2) the measured upstream pressure history, ${}_2\overline{P}_3$ in test 1 and P_1 in test 2, was used, (3) the contents remaining within the vessel were assumed to expand in an isentropic manner:

$$x_i = \frac{s_L[T_0(0)] - s_L(P)}{s_{VL}(P)}, \tag{194}$$

and (4) an insignificant or frozen amount of phase change occurred as the mixture exhausted out of the choked exhaust duct (see Eq. 54), the mass-decay histories in Figs. 54 and 55 would continue to decrease at similar initial rates, as seen in Figs. 91 and 92. Figures 91 and 92 show that this did not occur; instead, the measured flow rates decreased significantly, even though the internal vessel pressure was nearly constant during this time (see Figs. 85-89). A blowdown in which the fluid in the exhaust duct is assumed to expand in a homogeneous-equilibrium manner is also shown in Figs. 91 and 92 for comparison. The two parameters that control the critical flow rate and the critical pressure ratio are the upstream stagnation pressure, which was measured directly, and the upstream fluid quality. The measured upstream pressures in these tests were essentially stagnation pressures as shown in Appendix B. The upstream fluid quality was inferred from the experimental measurements.

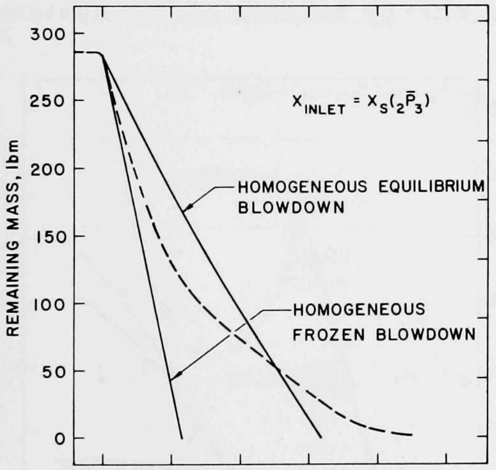

Fig. 91

Comparison of Predictions of the Homogeneous-Equilibrium and Homogeneous-frozen Critical-flow Models for the Remaining Mass for the Internal Vessel Quality Being the Isentropic Quality Corresponding to the Measured Pressure in Test 1. ANL Neg. No. 900-4957 Rev. 1.

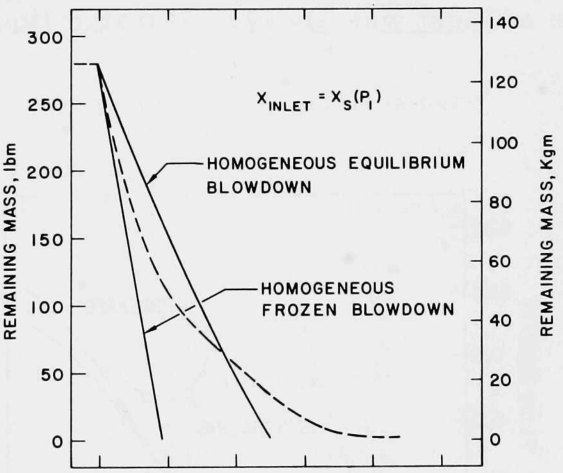

Fig. 92

Comparison of Predictions of the Homogeneous-Equilibrium and Homogeneous-frozen Critical-flow Models for the Remaining Mass for the Internal Vessel Quality Being the Isentropic Quality Corresponding to the Measured Pressure in Test 2. ANL Neg. No. 900-4958 Rev. 1.

4. Upstream Fluid Quality

Four techniques for estimating the fluid quality at the entrance to the exhaust duct were investigated, and the methods were evaluated by using each in determining the integrated energy lost from the system during the blowdown.

The first two techniques were to assume that the remaining fluid inside the vessel was always uniformly dispersed, and that this fluid expanded in an isentropic and isenthalpic equilibrium manner as dictated by Eqs. 177 and 179. The isentropic and isenthalpic equilibrium qualities of the remaining fluid based on the measured internal vessel pressure are shown in Figs. 93 and 94. Figures 91 and 92 show that the assumption of an isentropic expansion of the remaining fluid within the vessel did not adequately predict the measured mass-decay histories. An energy balance on the system, given by Eq. 12, using the isentropic upstream quality from Eq. 194 and the measured critical flow rates indicated that only about 92% of the initial energy contained within the vessel had been exhausted, as seen in Tables II and III. When the maximum equilibrium upstream fluid quality (the isenthalpic quality given by Eq. 180) was used with the measured critical flow rates, it also indicated that only about 93% of the initial energy inventory within the vessel had been exhausted.

The third method was to assume the blowdown was stratified; i.e., the effluent was always saturated liquid. An energy balance on the system

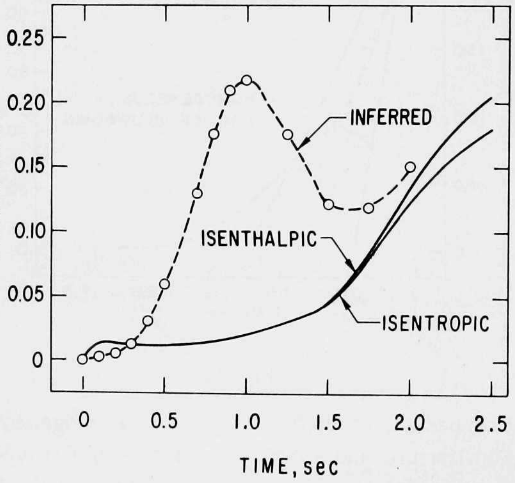

Fig. 93. Comparison of the Inferred Fluid Quality and the Inlet Isentropic and Isenthalpic Qualities at the Inlet Based on the Measured Pressure in Test 1. ANL Neg. No. 900-4980 Rev. 1.

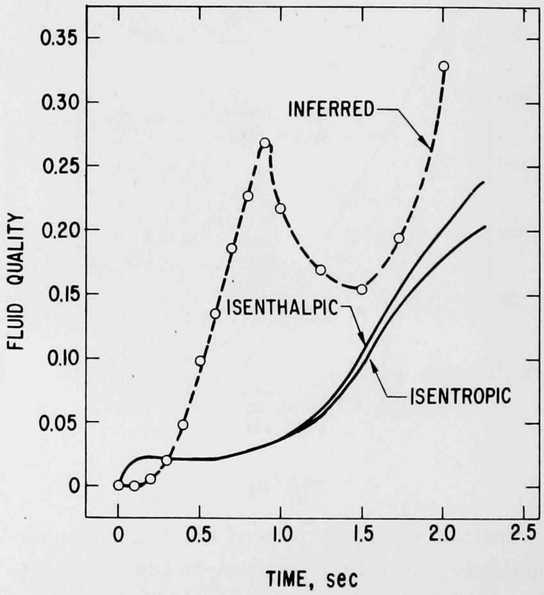

Fig. 94. Comparison of the Inferred Fluid Quality and the Inlet Isentropic and Isenthalpic Qualities at the Inlet Based on the Measured Pressure in Test 2. ANL Neg. No. 900-4981 Rev. 1.

TABLE II. Comparison of Energy Remaining in Vessel with Upstream Fluid Quality in Test 1
(ANL Neg. No. 900-75-329)

t sec	ENERGY REMAINING, Btu x_{inferred}	 $x_{\text{isentropic}}$	 $x_{\text{isenthalpic}}$	 $x=0_{\text{stratified}}$
0	112103	112103	112103	112103
0.1	97688	97457	97259	97721
0.2	84004	83455	83101	84156
0.3	71929	71283	70793	72339
0.4	62112	61665	61067	63003
0.5	54397	54454	53791	56020
0.6	48112	48803	48063	50548
0.7	42762	44303	43512	46212
0.8	37748	40481	39647	42539
0.9	33182	37211	36347	39419
1.0	28745	34132	33233	36496
1.2	20286	28122	27153	30862
1.4	12834	22390	21354	25613
1.6	6164	16712	15595	20623
1.8	1335	12017	10797	16776
2.0	-851	9475	8177	14923
2.2	-1576	8422	7076	14258
	1% too much exhausted	8% too little exhausted	6% too little exhausted	13% too little exhausted
ΔQ_{wall} ($0 \leq t \leq 2.0$ sec)	1959 0.3% too little exhausted	1959 9% too little exhausted	1959 8% too little exhausted	1959 14% too little exhausted

TABLE III. Comparison of Energy Remaining in Vessel with Upstream Fluid Quality in Test 2
(ANL Neg. No. 900-75-328)

t sec	ENERGY REMAINING, Btu x_{inferred}	 $x_{\text{isentropic}}$	 $x_{\text{isenthalpic}}$	 $x=0_{\text{stratified}}$
0	118789	118789	118789	118789
0.1	101601	101208	101172	101601
0.2	84873	83809	83738	84973
0.3	71145	69766	69695	71616
0.4	61133	59956	59865	62285
0.5	53213	52751	52631	55432
0.6	46579	47166	47023	50119
0.7	40671	42544	42382	45724
0.8	35078	38458	38279	41865
0.9	29682	34727	34532	38381
1.0	24572	31149	30939	35079
1.2	15653	24344	24106	28946
1.4	7714	17785	17547	23337
1.6	2171	12898	12596	19509
1.8	-147	10840	10480	18091
2.0	-1105	10050	9654	17177
2.2	-1502	9863	9454	17079
	1% too much exhausted	8% too little exhausted	8% too little exhausted	14% too little exhausted
ΔQ_{wall} ($0 \leq t \leq 1.5$ sec)	1919 0.4% too little exhausted	1919 10% too little exhausted	1919 10% too little exhausted	1919 16% too little exhausted

assuming the upstream quality was always zero, however, indicated that only about 86% of the initial energy inventory had been exhausted. None of these results were in agreement with the experimental data. Hence, it was concluded that the fluid quality at the entrance to the exhaust duct was neither zero nor the uniformly dispersed values assumed in the foregoing calculations.

The remaining technique of evaluating the upstream fluid quality to the exhaust duct used many of the various measurements. With the measured mass, thrust, and entrance and exit pressure histories, the specific volume at the exit of the exhaust duct could be evaluated from the momentum equation as

$$v_e = \frac{1}{G_c^2}\left(\frac{F}{A_e} + P_a - P_e\right). \qquad (195)$$

If it is assumed that the flow in the exhaust duct was homogeneous, $k = 1$, the exit specific volume is given by Eq. 185. Since the exhaust duct was only three diameters (3D) long, it is considered that there was a negligible amount of phase change in this short length. This meant that the fluid quality is assumed constant from the upstream location to where $L = 3D$, or at the exit of the exhaust duct. In general, it was considered that

$$x_1 \simeq x_{14} \simeq x_e = \frac{v_e - v_L(P_e)}{v_V(P_e) - v_L(P_e)}. \qquad (196)$$

If the vapor phase is assumed to expand isentropically from the upstream location to the exit:

$$v_{V_e} = v_{V_i}\left(\frac{P_e}{P_{i_0}}\right)^{-1/\gamma} \qquad (197)$$

and the specific volume of the liquid phase is considered to be constant from the upstream to exit locations, Eq. 196 can be recast as

$$x_i \simeq \frac{v_e - v_L(P_{i_0})}{v_{V_i}\eta^{-1/\gamma} - v_L(P_{i_0})}, \qquad (198)$$

where η is the critical pressure ratio. The inlet stagnation pressure, ${}_2\bar{P}_3$ in test 1 and P_1 in test 2, and the exit pressure, P_{14}, were used in Eq. 198. The locations of these pressure measurements are shown in Figs. 8, 9, and 12.

The foregoing formulation for the inlet fluid quality is for homogeneous flow in the exhaust duct. For nonhomogeneous flow, $k > 1$, combination of the continuity equation

$$\rho A u = \rho_V A_V u_V + \rho_L A_L u_L \qquad (199)$$

and a summation of the momentum flow rates of each phase

$$\dot{m}u = \dot{m}_V u_V + \dot{m}_L u_L \tag{200}$$

yield a relation for the nonhomogeneous fluid quality as a function of the velocity ratio, $k = u_V/u_L$, as given by

$$x = \frac{-\left[\frac{v_V}{k} + v_L(k-2)\right] + \left\{\left[\frac{v_V}{k} + v_L(k-2)\right]^2 + 4(v - v_L)\left[v_V\frac{k-1}{k} - v_L(k-1)\right]\right\}^{1/2}}{2\left[v_V\frac{k-1}{k} - v_L(k-1)\right]}. \tag{201}$$

The assumptions in Eqs. 196 and 197 can be used in Eq. 201 to determine the upstream fluid quality for the nonhomogeneous case. Tables IV and V demonstrate that the nonhomogeneous quality increases with increased velocity ratio.

For tests 1 and 2, the upstream fluid quality determined from Eqs. 196-198 are shown in Figs. 93 and 94, and also in Tables IV and V. An energy balance on the system using Eq. 12 and the homogeneous inferred upstream quality, (see Eq. 198) indicates an energy balance within 1% of the initial energy inventory in both tests 1 and 2, as seen in Tables II and III. When the nonhomogeneous upstream fluid qualities were used with the measured critical flow rates in an energy balance on the system, given by Eq. 12, they indicated that considerably more energy had been exhausted from the system than initially was contained within the system (see Tables IV and V). The fact that there was good agreement, with only about 1% more energy exhausted

TABLE IV. Comparison of Inferred Upstream Fluid Quality with Velocity Ratio in Test 1
(ANL Neg. No. 900-75-287)

t sec	x_{inferred} Velocity Ratio					
	1.0	1.5	2.0	3.0	4.0	5.0
0	0	0	0	0	0	0
0.10	0.002	0.003	0.004	0.006	0.007	0.009
0.20	0.006	0.008	0.011	0.016	0.020	0.023
0.30	0.013	0.020	0.026	0.036	0.044	0.050
0.40	0.031	0.045	0.058	0.078	0.092	0.102
0.50	0.059	0.084	0.106	0.136	0.154	0.166
0.60	0.068	0.097	0.121	0.153	0.173	0.185
0.70	0.130	0.179	0.214	0.255	0.277	0.290
0.80	0.176	0.236	0.275	0.319	0.341	0.353
0.90	0.210	0.276	0.317	0.361	0.383	0.395
1.00	0.217	0.285	0.326	0.370	0.392	0.404
1.25	0.176	0.236	0.276	0.319	0.342	0.355
1.50	0.122	0.169	0.203	0.244	0.267	0.280
1.75	0.120	0.165	0.199	0.240	0.264	0.278
2.00	0.151	0.205	0.243	0.287	0.311	0.325
2.25	0.576	0.652	0.684	0.712	0.725	0.732
ENERGY EXHAUSTED	0.3% too little	7% too much	10% too much	16% too much	18% too much	20% too much

TABLE V. Comparison of Inferred Upstream Fluid Quality with Velocity Ratio in Test 2
(ANL Neg. No. 900-75-288)

t sec	x_{inferred} Velocity Ratio					
	1.0	1.5	2.0	3.0	4.0	5.0
0	0	0	0	0	0	0
0.10	-	-	-	-	-	-
0.20	0.006	0.008	0.011	0.016	0.020	0.022
0.30	0.020	0.030	0.039	0.053	0.063	0.070
0.40	0.048	0.069	0.087	0.114	0.130	0.140
0.50	0.098	0.137	0.166	0.203	0.223	0.235
0.60	0.135	0.185	0.220	0.261	0.282	0.294
0.70	0.186	0.247	0.287	0.330	0.351	0.362
0.80	0.227	0.296	0.338	0.381	0.402	0.413
0.90	0.268	0.343	0.386	0.429	0.449	0.460
1.00	0.217	0.284	0.326	0.369	0.390	0.402
1.25	0.169	0.227	0.266	0.309	0.331	0.344
1.50	0.155	0.210	0.248	0.292	0.315	0.328
1.75	0.194	0.258	0.299	0.344	0.367	0.381
2.00	0.331	0.412	0.455	0.497	0.518	0.529
2.25	0.666	0.731	0.758	0.780	0.790	0.796
ENERGY EXHAUSTED	0.4% too little	6% too much	10% too much	14% too much	16% too much	18% too much

from the system than initially contained when the homogeneous upstream quality was used, indicates that the exhausting flow was nearly homogeneous. Hence, this good agreement in energy balance indicates that the deviation of the actual exhausting mixture from a homogeneous mixture was small. Once the upstream fluid quality was established, it and the measured upstream stagnation pressure completely define the required parameters for calculating the critical flow rate and the critical exit-pressure ratio from analytical models.

The energy balances in Tables II and III consider no heat addition to the fluid from the solid surfaces inside the vessel, as deduced from Eq. 182, during the time when most of the fluid remained within the vessel. If the maximum possible heat extracted from the walls is calculated from Eq. 182 over the time period from the beginning of the decompression to when the internal vessel pressure was nearly down to atmospheric pressure, this would show that about 1959 Btu in test 1 and 1919 Btu in test 2 could have been extracted from the vessel walls. If this energy content is accounted for in Tables II and III, this would indicate a slightly better energy balance when employing the homogeneous upstream inferred fluid quality, and slightly more disagreement in the energy balances when employing the isentropic and isenthalpic upstream qualities, and also the saturated-liquid inlet condition. The energy values in Tables IV and V account for the energy removed from the vessel walls.

Figures 93 and 94 indicate that; in both tests, the inferred upstream fluid quality started to depart significantly from the equilibrium upstream qualities at about 300 msec. This was after the annulus had initially been nearly voided, as seen in Figs. 54 and 55; at this time the voids near the inside wall of the lower internal skirt may have been swept into the downcomer annulus along with dispersed liquid from the interior of the internal-skirt region. It was also at about this same time that the flow rates started to decrease significantly from the initial values as shown in Figs. 54 and 55. This is consistent, since the critical flow rate has been experimentally demonstrated to decrease significantly for small increases in the upstream quality in the very low quality range.[15, 16]

5. Interpretation of the Internal Flow Regime

A nonuniformity of fluid density appeared to exist within the vessel during these two-phase tests, starting at about 300 msec into the decompressions. At this early time into the depressurization, when about three-fifths of the initial fluid mass remained within the vessel (see Figs. 95 and 96), the flow-regime transition from bubbly to dispersed in the downcomer annulus was nearly complete (see Figs. 67 and 68). At about this same time, some of the vapor phase adjacent to the inner wall of the lower internal skirt may have been swept up the downcomer annulus along with dispersed liquid from the interior of the internal skirt toward the entrance to the exhaust duct. Figures 56, 57, 95, and 96 also indicate that when the measured remaining mass decreased to about one-fourth or one-third of the initial inventory, it corresponded with the thermodynamic-equilibrium-calculated value of the remaining mass as based on the measured internal vessel pressure. At about the same time, the upstream fluid quality reached its maximum value, and the internal vessel pressure and the thrust began to decrease from their nearly constant values. This indicated that thermodynamic equilibrium was closely approached.

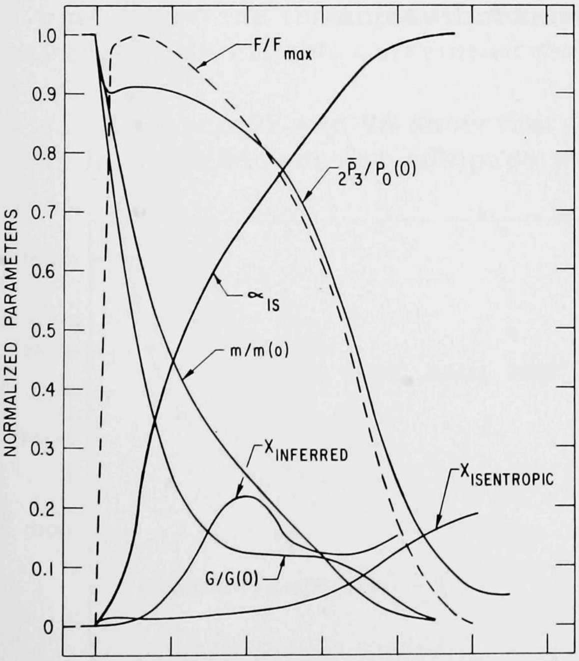

Fig. 95. Normalized Blowdown Characteristics in Test 1. ANL Neg. No. 900-5112 Rev. 1.

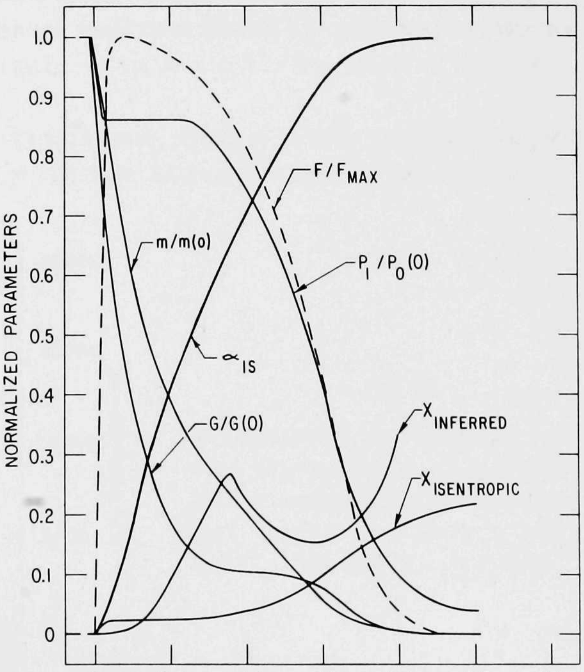

Fig. 96. Normalized Blowdown Characteristics in Test 2. ANL Neg. No. 900-5113 Rev. 1.

The relative coincidence of the mass decaying to about three-fifths of its initial inventory (which was approximately the total initial mass minus the mass originally contained within the downcomer annulus), the inferred upstream quality starting its rapid increase above the average bulk quality of the fluid inside the internal skirt, the isentropic quality, and the significant decrease in the critical flow rate contributed to indicating that there was a nonuniform distribution of fluid density within the vessel. The preferential transport of the vapor phase into the upper annulus region, which probably produced the large inlet qualities experienced in these tests, was brought about by the effect of the downcomer-annulus geometry. The effect of the downcomer geometry was to force the fluid down the inside of the internal skirt and up the annulus to reach the exhaust location. Once the downcomer annulus was initially nearly voided, this geometry promoted the lighter phase that was being generated on the inside wall of the internal skirt to entrain liquid from within the internal-skirt region and ascend the downcomer annulus. Consequently, the mixture quality that reached the upper annulus region was considerably greater than the average vessel quality (the isentropic quality), which was essentially the condition of the mixture in the interior of the internal skirt.

The decreasing portion of the inferred quality curves in Figs. 93 and 94 did not have a significant effect upon the overall energy balance on the system. Figures 95 and 96 indicate that, when the inferred quality was at its maximum value, the mass inventory had already decreased to about one-fourth of its initial value, and the flow rates had decreased to about one-eighth of their original magnitude in both tests. Therefore, the region to the right of the maximum in the inferred-entrance-quality curves contributed very little to the overall energy balance. Hence, that portion of the curve was insignificant compared to the region of the curve left of the maximum when the flow rate was considerably greater earlier in the decompression.

D. Comparison of Our Transient, Large-duct, Critical-flow Data with Steady-state, Small-duct, Critical-flow Data

Two important questions yet unanswered concerning the maximum compressible discharge phenomenon during a LOCA are (1) whether the two-phase critical-flow phenomenon is different in the transient case than in the steady-state case, and (2) whether the size of the discharge duct has any effect upon the phenomenon. These questions are particularly important from the physical standpoint and also from the modeling viewpoint of understanding the phenomenon. If the two-phase critical-flow phenomenon is the same in the transient, large-duct case as in the steady-state, small-duct case, then the best presently available analytical techniques that have been verified against the high-resolution, steady-state, small-duct experimental data can then be used to model the two-phase critical-flow phenomenon in the transient, large-duct case.

In this study, the critical flow rate was determined from the measured mass-decay histories as illustrated in Figs. 54 and 55. The resulting critical flow rates, together with the inferred upstream qualities determined from Eqs. 195-198, were then compared to Neusen[15] and Maneely's[16] steady-state, small-duct, critical-flow rate data. The critical pressure ratios from these decompressions were also compared to Neusen and Maneely's critical-pressure-ratio data. The steam-water experimental results of Refs. 15 and 16 were for upstream stagnation pressures from 100 to 950 psia, and for upstream qualities from 0.010 to 0.2275. Neusen and Maneely's geometries were convergent-divergent, axisymmetric nozzles with 0.253- and 0.438-in. throat diameters. The steam-water critical-pressure-ratio data of Deich et al.[18] were also used for comparison. The inlet stagnation pressure in Ref. 18 was 17.6 psia, and the inlet qualities were from 0.2 to 1.0. The geometry was a convergent-divergent, axisymmetric nozzle with a 1.281-in. throat diameter.

Figures 97 and 98 show that the transient, large-duct, critical-flow rates in these blowdowns compare well with the steady-state, small-duct,

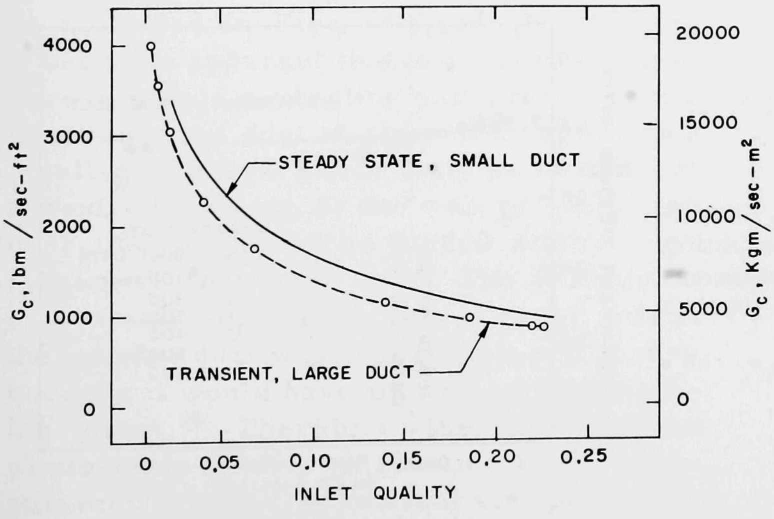

Fig. 97

Comparison of the Transient, Large-duct, Critical-flow Rates in Test 1 and the Corresponding Steady-state, Small-duct, Critical-flow Rates in Refs. 15 and 16. ANL Neg. No. 900-5059.

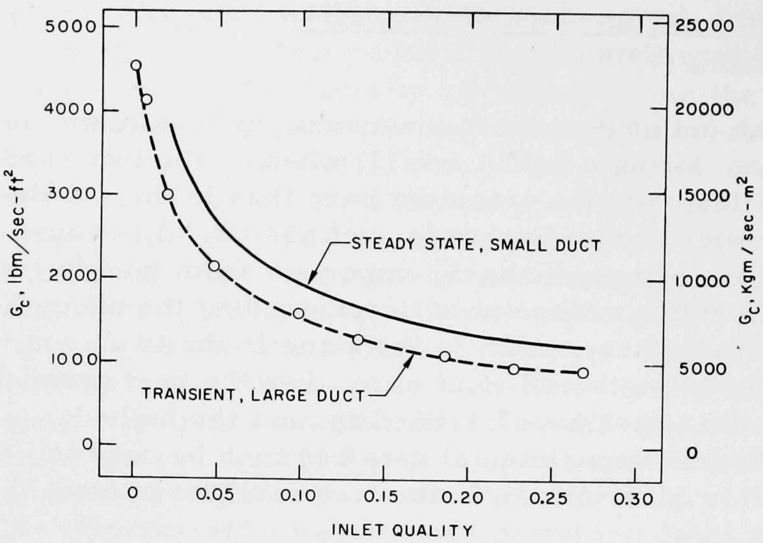

Fig. 98

Comparison of the Transient, Large-duct, Critical-flow Rates in Test 2 and the Corresponding Steady-state, Small-duct, Critical-flow Rates in Refs. 15 and 16. ANL Neg. No. 900-5096.

critical-flow rates. The average difference between the measured transient, large-duct, critical-flow rates and the steady-state, small-duct, critical-flow rates is about 19%. The salient fact to be recognized from Figs. 97 and 98 is that the two-phase critical-flow rate in the transient, large-duct case appears to be similar to that in the steady-state, small-duct case.

To demonstrate good correlation between any two sets of two-phase critical-flow results, whether experimental and/or analytical, good correspondence must be shown between the critical throat-pressure ratio in addition to the critical flow rate. Figures 99 and 100 compare the transient, large-duct, critical-exit-pressure ratios from these decompressions with the steady-state small-duct, critical-pressure-ratio data of Neusen,[15] Maneely,[16] and Deich et al.[18] These figures show that the transient, large-duct, critical-pressure-ratio data from these tests also compare very well with the steady-state, small-duct data to an upstream quality of about 0.06. At this value of the upstream quality, the transient, large-duct results from these tests begin to rise slightly above the general trend of the steady-state, small-duct data. A possible explanation for this behavior is that the location at which the exit pressure

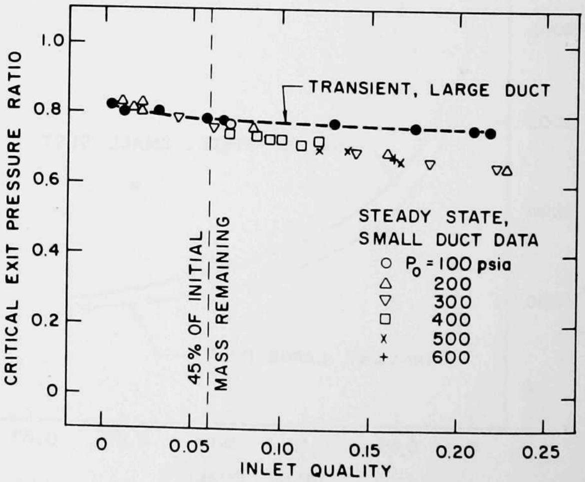

Fig. 99

Comparison of the Transient, Large-duct, Critical-exit-pressure Ratio in Test 1 and the Corresponding Steady-state, Small-duct, Critical-throat-pressure Ratio of Refs. 15 and 16. ANL Neg. No. 900-5077 Rev. 1.

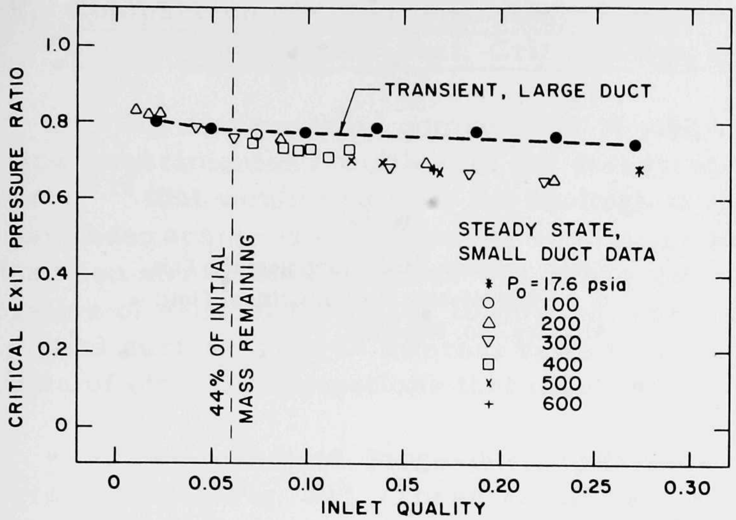

Fig. 100

Comparison of the Transient, Large-duct, Critical-exit-pressure Ratio in Test 2 and the Corresponding Steady-state, Small-duct, Critical-throat-pressure Ratio of Refs. 15, 16, and 18. ANL Neg. No. 900-5078 Rev. 1.

was measured in these decompressions was pressure tap 14, which was 0.78 of a diameter (0.78D) upstream of the actual exit plane of the constant-area exhaust duct, as seen in Figs. 8, 9, and 12. The location of pressure tap 14 was an effort to obtain a pressure more indicative of the true, one-dimensional, centerline, critical exit pressure of the flow. The choice 0.78D upstream was not unique, but was thought to be sufficient to avoid most of the effect of the steep-wall pressure gradient near the exit plane of the constant-area duct, as indicated schematically in Fig. 101. It has been shown[8,9,108] that the attachment of a small-angle divergence to the exit of a constant-area duct, rather than a rapid divergence, permits a much better measurement of the one-dimensional, centerline, critical exit pressure with a wall pressure tap. This presents the effect of a diverging nozzle. If the axial and radial pressure distributions in the near vicinity of the exit of a constant-area duct at critical flow were investigated, they would appear as indicated in Figs. 101 and 102. Hence, it becomes apparent that to accurately measure the true centerline exit pressure in a constant-area duct at critical flow, either a small-angle divergence must be attached to the exit of the duct, or the wall pressure tap near the exit must be moved slightly upstream of the actual exit. The attachment of a small-angle divergence at the exit of the exhaust duct was undesirable in this case because it would have increased the resulting thrust.[86] Therefore, the latter method was used in an effort to obtain a better measurement of the true critical exit pressure.

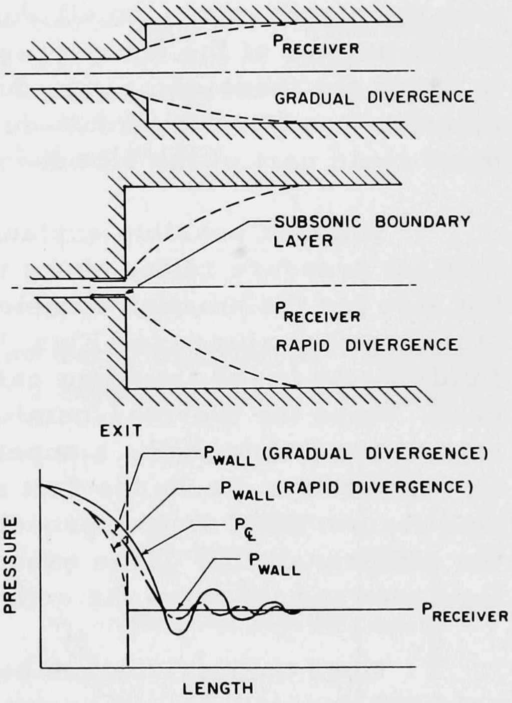

Fig. 101. Axial Pressure Distribution at Critical Flow near the Exit of a Constant-area Duct Having a Gradual and Rapid Divergence Downstream of the Exit. ANL Neg. No. 900-5085.

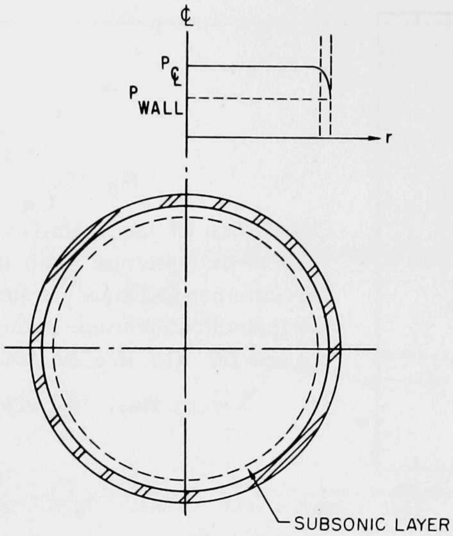

Fig. 102

Radial Pressure Distribution near the Exit of a Constant-area Duct at Critical Flow. ANL Neg. No. 900-5048.

Figures 99 and 100 show that the time period in which the transient, large-duct, critical pressure ratios agreed well with the steady-state, small-duct, critical-pressure-ratio data was the time span in which the major portion of the decompression occurred. In other words, for time greater than when the inferred inlet quality was about 0.06, the critical flow rate had already decreased to less than about 2000 $lb_m/sec\text{-}ft^2$ (see Figs. 97 and 98), and only about 44% of the initial fluid mass remained within the system. This indicates that these transient, large-duct, critical pressure ratios did agree very well with the steady-state, small-duct, critical-pressure-ratio data during the major portion of the decompression. The latter period of the depressurization in which the transient, large-duct, critical pressure ratios were slightly greater than the steady-state, small-duct, critical-pressure-ratio data was after the most rapid part of the blowdown had occurred.

Another possible explanation not only for the increase in the transient critical pressure ratios above the steady-state values at higher inlet qualities, but also for the smaller transient critical flow rates than the corresponding steady-state values (see Figs. 97 and 98), is the potential nonequilibrium inlet-fluid effects in the transient case that probably did not exist in the steady-state case. Since the thermodynamic state of the fluid within the vessel during the decompression includes a superheated liquid phase, the fluid upstream of the entrance to the discharge duct may be in the process of relaxing toward an equilibrium state as it approaches the exhaust location. This would increase the compressibility of the exhausting mixture, which would reduce the critical flow rate and increase the critical pressure ratio.

Good comparison has been demonstrated between both the critical flow rate and the critical exit pressure ratio for these transient, large-duct experimental results and the steady-state, small-duct data.

E. Comparison of Other Transient, Large-duct, Critical-flow Data with the Steady-state, Small-duct, Critical-flow Data

To make a valid comparison of other transient, large-duct, critical-flow experimental results with the steady-state, small-duct, critical-flow data[15,16] that would relate to the findings in this investigation, the data should have been acquired under conditions similar to those in the present study. Comparison should only be made with other data that were acquired with similar ratios of exhaust flow area to internal vessel flow area, A_e/A_{bv}, and internal vessel surface area to internal vessel volume, S/V. The transient, large-duct data of other investigations that meet these criteria are considered below.

The transient, large-duct, critical-flow rates in one of Ungerer's[67] tests are shown in Fig. 103. These results are for a bottom blowdown through a convergent-divergent nozzle in which A_e/A_{bv} was 0.025 and S/V of the internal vessel was about 1 ft^2/ft^3. The initial stagnation condition of the fluid was nearly saturated water at 750 psia. These transient, large-duct, critical-flow rates are in general agreement with the steady-state, small-duct, critical-flow rates.

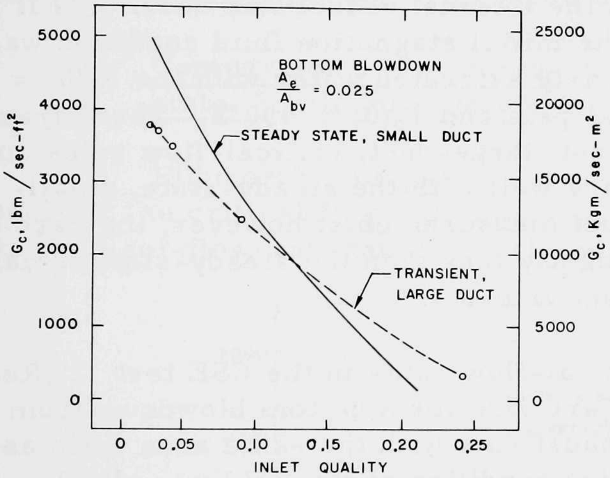

Fig. 103

Comparison of Ungerer's[67] Transient, Large-duct, Critical-flow Rates for A_e/A_{bv} = 0.025 and the Corresponding Steady-state, Small-duct, Critical-flow Rates in Refs. 15 and 16. ANL Neg. No. 900-5058.

Other transient, large-duct, critical-flow rates of Ungerer[67] are presented in Fig. 104. These results are also for a bottom blowdown through a

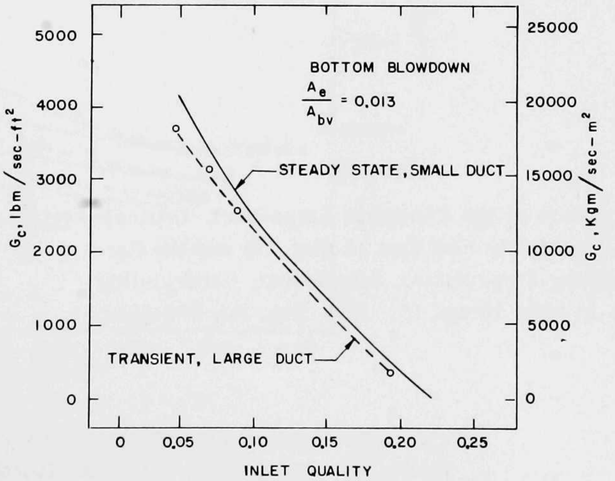

Fig. 104

Comparison of Ungerer's[67] Transient, Large-duct, Critical-flow Rates for A_e/A_{bv} = 0.013 and the Corresponding Steady-state, Small-duct, Critical-flow Rates in Refs. 15 and 16. ANL Neg. No. 900-5060.

convergent-divergent nozzle, but with $A_e/A_{bv} = 0.013$. The S/V of the internal vessel was the same in this run as in the previous test, and the initial stagnation fluid conditions were also the same. These transient, large-duct, critical-flow rates also compare well with the steady-state, small-duct, critical-flow-rate data. The transient, large-duct, critical-flow rates were slightly less than the steady-state, small-duct values in Fig. 104, as they were for part of the decompression in Fig. 103. This is the trend observed in the present study (see Figs. 97 and 98).

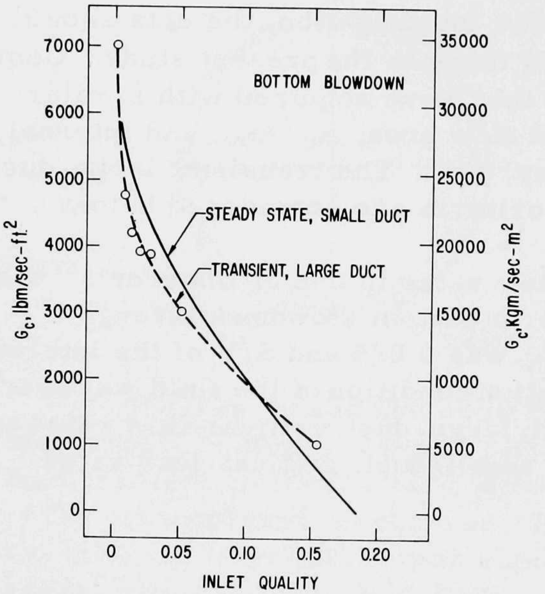

Fig. 105. Comparison of the Transient, Large-duct, Critical-flow Rates in the CSE Test 7 (Ref. 70) and the Corresponding Steady-state, Small-duct, Critical-flow Rates in Refs. 15 and 16. ANL Neg. No. 900-5045.

The transient, large-duct, critical-flow rates in the CSE test 7 (Ref. 70) are shown in Fig. 105. These results are for a bottom blowdown through a constant-area pipe in which $A_e/A_{bv} \simeq 0.007$. The L/D of the exhaust duct was about 8, and the S/V of the internal vessel was about 1.24 ft^2/ft^3. The initial stagnation fluid condition was nearly saturated water with the $P_0(0) = 671$ psia and $T_0(0) = 490$°F. These transient, large-duct, critical-flow rates compare well with the steady-state, small-duct measurements; however, they are also slightly less than the steady-state, small-duct values.

The transient, large-duct, critical-flow rates in the CSE test 11 (Ref. 70) are shown in Fig. 106. These results are also for a bottom blowdown from the same vessel and through the same exhaust duct with the same area ratio as in the foregoing run. The initial stagnation condition of the fluid was nearly saturated water at $P_0(0) = 1450$ psia and $T_0(0) = 575$°F. These transient, large-duct, critical-flow rates are also in good agreement with the steady-state, small-duct data.

Fig. 106

Comparison of the Transient, Large-duct, Critical-flow Rates in the CSE Test 11 (Ref. 70) and the Corresponding Steady-state, Small-duct, Critical-flow Rates in Refs. 15 and 16. ANL Neg. No. 900-5052.

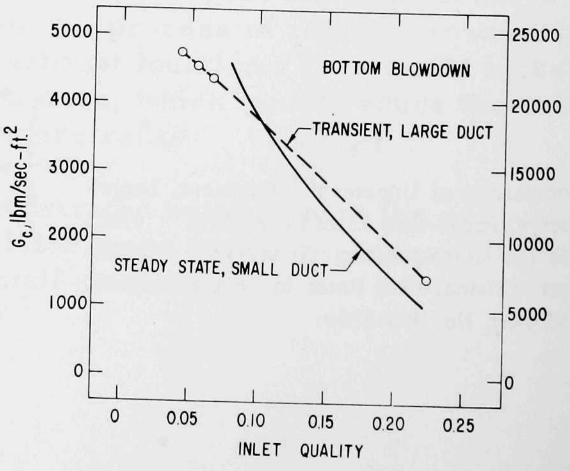

The important point to be realized from these comparisons of other transient, large-duct, critical-flow-rate results to the steady-state, small-duct, critical-flow-rate data, and also in the comparisons of the transient, large-duct, critical-flow data from the present investigation to the steady-state, small-duct, critical-flow results, is that the two-phase critical-flow phenomenon appears to be essentially the same in the transient, large-duct case as in the steady-state, small-duct case. The implication of this finding is that the best presently available two-phase critical-flow analytical models that have been verified against the high-resolution, steady-state, small-duct, critical-flow data can then be validly employed to model the two-phase critical-flow phenomenon in the transient, large-duct case.

F. Comparison of Predictions to the Steady-state, Small-duct, Critical-flow Data from Various Critical-flow Analytical Models

Before the various predictions from the two-phase critical-flow model are compared to the transient, large-duct, critical-flow data of this and other studies, it is instructive first to compare them to the available high-resolution, steady-state, small-duct, critical-flow data.

1. Comparison of the Homogeneous-equilibrium Model to the Steady-state, Small-duct Data

Figure 107 compares the prediction of the homogeneous-equilibrium model for the critical flow rate [see Sec. III.B.2.b(1)] to the steady-state, small-duct, critical-flow-rate data.[15,16] The experimental data of Refs. 15, 16, and 18

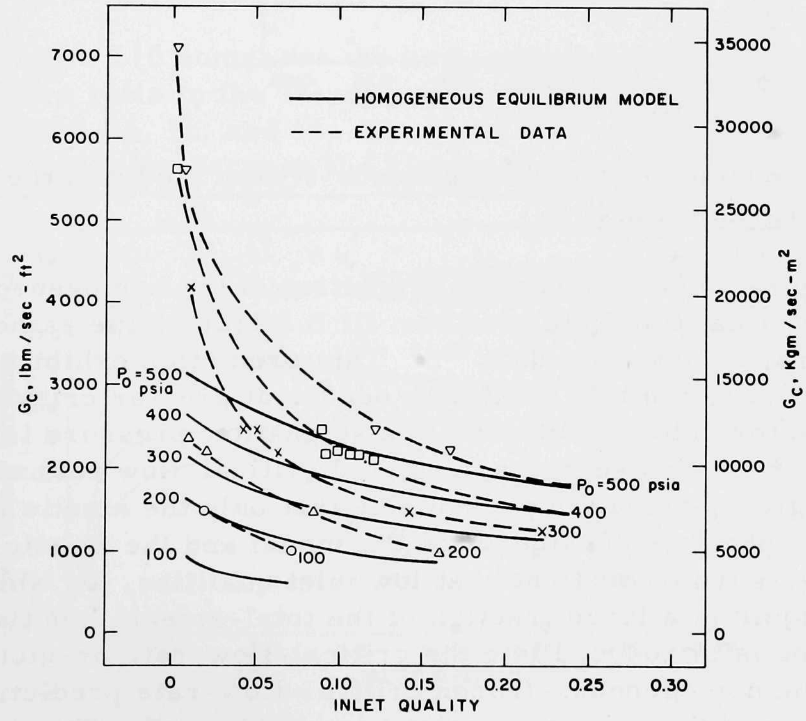

Fig. 107. Comparison of the Homogeneous-equilibrium Critical-flow Model to the Steam-Water Critical-flow-rate Data of Refs. 15 and 16. ANL Neg. No. 900-5064 Rev. 1.

were for steam-water mixtures. The homogeneous-equilibrium model underpredicts the critical flow rate at low qualities, but it comes into better agreement with the measured critical flow rates at higher qualities. The homogeneous-equilibrium critical flow rate approaches the measured critical flow rate at successively greater qualities as the stagnation pressure is increased. The underprediction of the critical flow rate at low qualities is due to the thermodynamic equilibrium assumption in the model, which breaks down due to nonequilibrium effects. Figure 108 compares the homogeneous-equilibrium critical-pressure-ratio prediction to the critical-pressure-ratio data of Refs. 15, 16, and 18. The measured critical pressure ratio is essentially independent of the stagnation pressure and is also a very weak function of the fluid quality. The homogeneous-equilibrium critical-pressure-ratio prediction shown in Fig. 108 covers the stagnation pressure range of the data, from 100 to 600 psia, and the prediction is also essentially independent of the stagnation pressure. The homogeneous-equilibrium critical-pressure-ratio prediction is slightly low in the low-quality range, but it matches the data better in the higher-quality range.

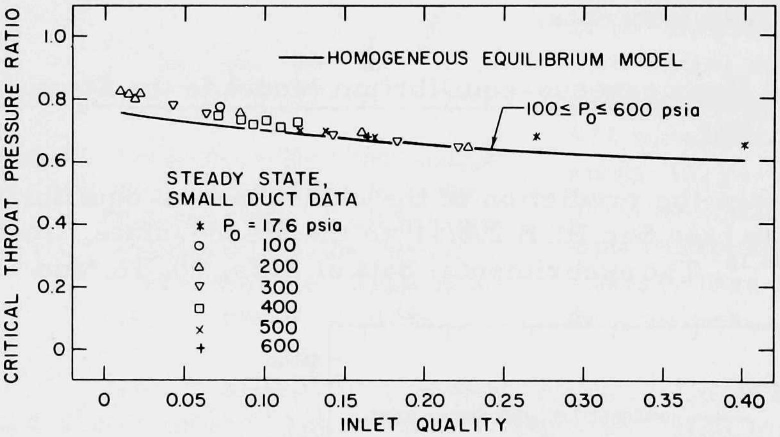

Fig. 108

Comparison of the Homogeneous-equilibrium Critical-flow Model to the Steam-Water Critical-pressure-ratio Data of Refs. 15, 16, and 18. ANL Neg. No. 900-5066 Rev. 1.

2. Comparison of the Homogeneous-frozen Model to the Steady-state, Small-duct Data

Figure 109 compares the prediction of the homogeneous-frozen model for the critical flow rate [see Sec. III.B.2.b(2)] to the same steady-state small-duct, critical-flow-rate data.[15,16] This prediction exhibits a maximum at low inlet qualities, and this maximum occurs at greater critical flow rates and also at greater inlet qualities as the stagnation pressure is increased. The reason for the decrease in the predicted critical flow rate at small inlet qualities for a given stagnation pressure is that only the kinetic energy of the expanding vapor phase is considered in the model and the kinetic energy of the liquid phase is ignored. Hence, at low inlet qualities, for which the kinetic energy of the liquid is a large fraction of the total-stream kinetic energy, a significant error is introduced into the critical-flow-rate prediction, as shown in Fig. 109. The homogeneous-frozen critical-flow-rate prediction agrees with the data beyond the maximum point reasonably well. This indicates that the critical flow rate for upstream qualities beyond the nonequilibrium inlet range, $0 < x_i \leq 0.10$, does not depart far from the homogeneous-frozen critical flow rate.[1,15,16]

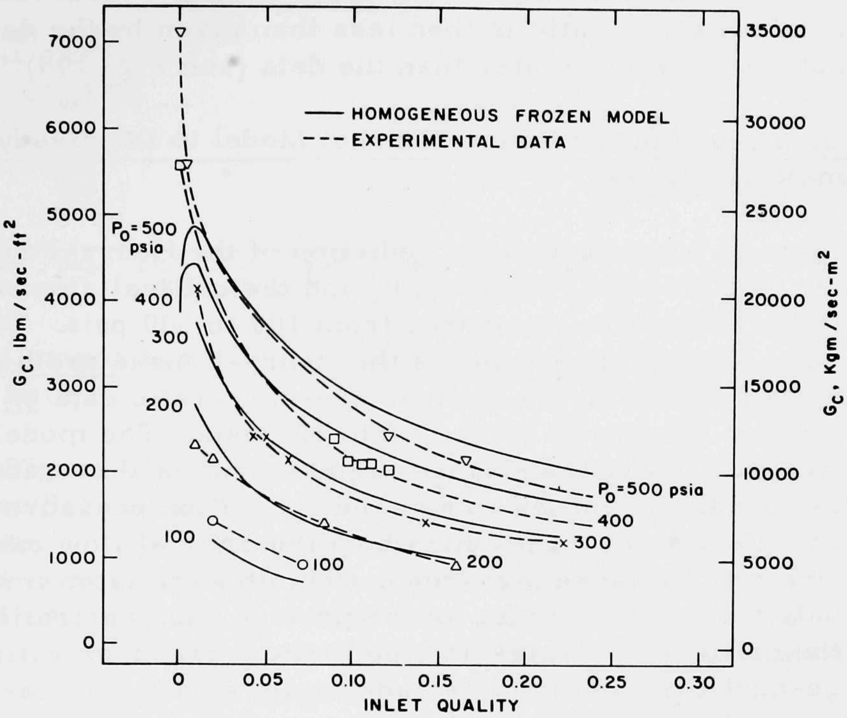

Fig. 109. Comparison of the Homogeneous-frozen Critical-flow Model to the Steam-Water Critical-flow-rate Data of Refs. 15 and 16. ANL Neg. No. 900-5539.

Figure 110 compares the homogeneous-frozen prediction for the critical pressure ratio to the steady-state, small-duct, critical-pressure-ratio data of Refs. 15, 16, and 18. The predicted critical pressure ratio decreases at low qualities because the kinetic energy of the liquid is neglected.

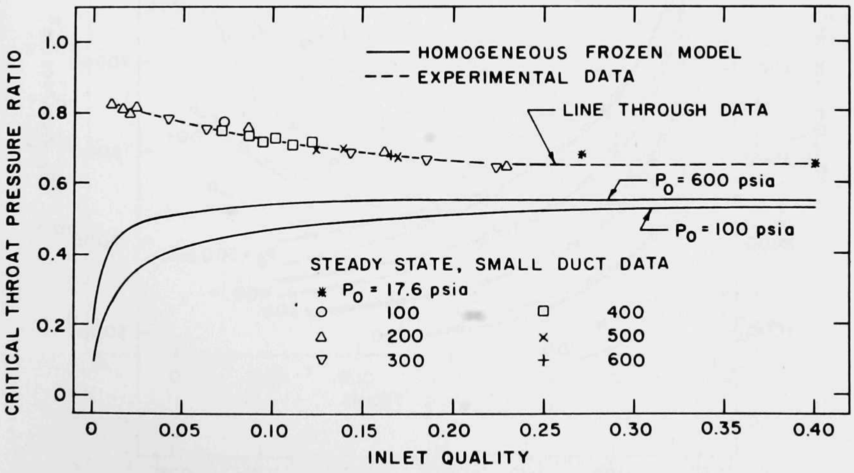

Fig. 110. Comparison of the Homogeneous-frozen Critical-flow Model to the Steam-Water Critical-pressure-ratio Data of Refs. 15, 16, and 18. ANL Neg. No. 900-5526.

The prediction for the critical pressure ratio does not rise as high as the measured critical pressure ratio, even at larger inlet qualities, because there is assumed to be no flashing in the duct. Therefore, the fluid is not as compressible as it actually would be with mass transfer occurring, and the predicted critical pressure ratio is then less than given by the data, and the critical flow rate is slightly greater than the data (see Fig. 109).

3. Comparison of the Henry-Fauske[1] Model to the Steady-state, Small-duct Data

Figure 111 compares the prediction of the Henry-Fauske model for critical flow rate [see Sec. III.B.2.b(d)] and the critical-flow-rate data of Refs. 15 and 16 for stagnation pressures from 100 to 500 psia. The comparison is quite good. Figure 112 compares the Henry-Fauske prediction for the critical exit pressure ratio to the critical-pressure-ratio data of Refs. 15, 16, and 18 for stagnation pressures from 17.6 to 600 psia. The model prediction is essentially independent of the stagnation pressure, as illustrated in Fig. 112, where the single prediction shown covers the stagnation pressure range of the data. The Henry-Fauske model predicts both the critical flow rate and the critical pressure ratio of these high-resolution, steady-state, small-duct, critical-flow data very well. In view of the previous demonstration of the similarity of the critical flow rates and the critical pressure ratios in the transient, large-duct case and in the steady-state, small-duct case, the Henry-Fauske model should also predict the transient, large-duct, critical flow rates and critical pressure ratios quite well.

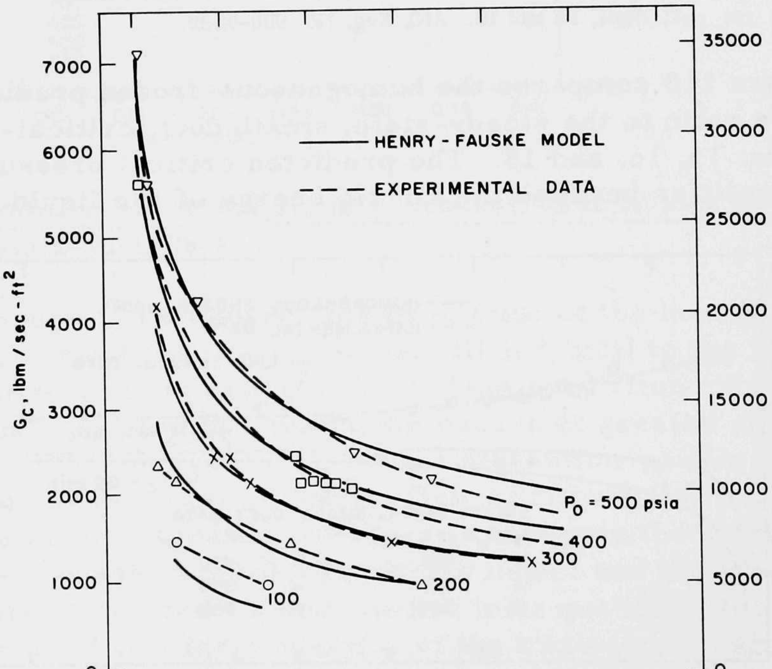

Fig. 111. Comparison of the Henry-Fauske[1] Critical-flow Model to the Steam-Water Critical-flow-rate Data of Refs. 15 and 16. ANL Neg. No. 900-5068 Rev. 1.

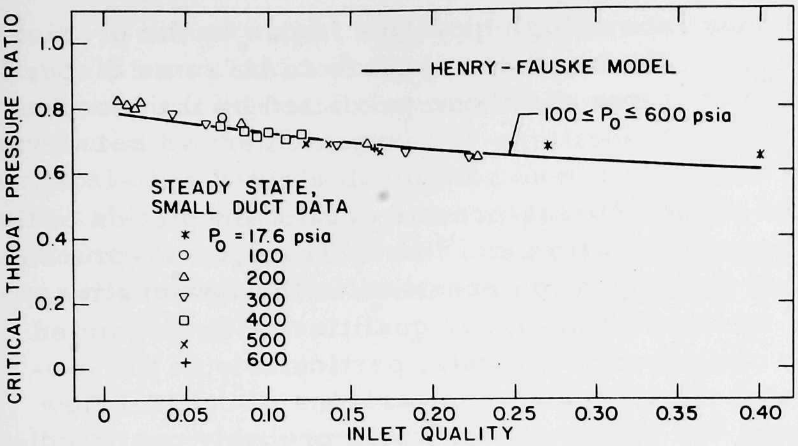

Fig. 112

Comparison of the Henry-Fauske[1] Critical-flow Model to the Steam-Water Critical-pressure-ratio Data of Refs. 15, 16, and 18. ANL Neg. No. 900-5075 Rev. 1.

4. Comparison of the Moody[2] Model to the Steady-state, Small-duct Data

Figure 113 compares the prediction of the Moody model for critical flow rate [see Sec. III.B.2.b(3)] to the same steady-state, small-duct, critical-flow-rate data.[15,16] The Moody prediction underestimates the measured critical flow rates at low qualities and overpredicts the measured critical flow rates at higher qualities. The underprediction of the critical flow rate at low qualities is due to the thermodynamic equilibrium assumption in this model, and the

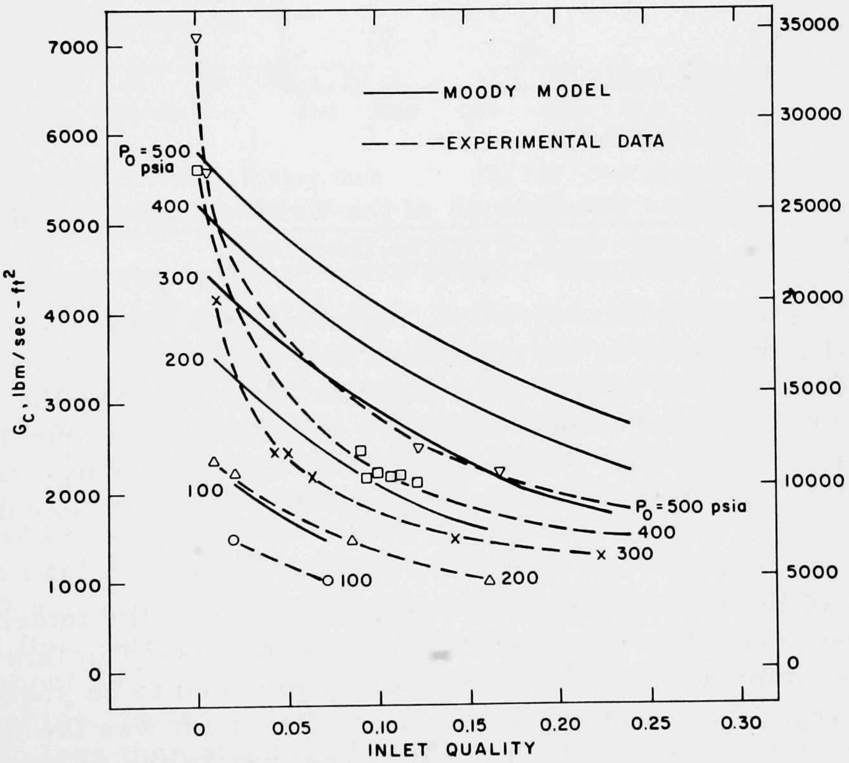

Fig. 113. Comparison of the Moody[2] Critical-flow Model to the Steam-Water Critical-flow-rate Data of Refs. 15 and 16. ANL Neg. No. 900-5065 Rev. 1.

overprediction of the critical flow rate at high qualities is due to the predicted high velocity ratio $k = (v_V/v_L)^{1/3}$. Hence, there appears to be some disparity between the measured critical flow rates and those predicted by the Moody model.

Figure 114 compares the critical-pressure-ratio prediction of the Moody model to the critical-pressure-ratio data.[15,16,18] The critical-pressure-ratio prediction is a function of the stagnation pressure in the low-quality range, but this dependence is diminished at higher qualities. The predicted critical pressure ratio is low compared to the data, particularly in the low-quality range. Hence, in view of the foregoing comparisons of critical flow rate and critical pressure ratio, the Moody model would probably overpredict the critical flow rate and underpredict the critical pressure ratio over much of the range of most transient, critical-flow data.

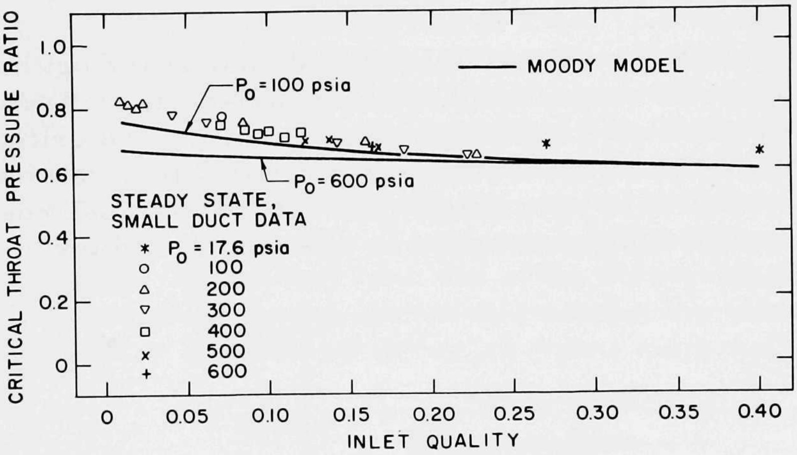

Fig. 114

Comparison of the Moody[2] Critical-flow Model to the Steam-Water Critical-pressure-ratio Data of Refs. 15, 16, and 18. ANL Neg. No. 900-5111 Rev. 2.

G. Comparison of Various Predictions of the Critical-flow Analytical Model to Our Transient, Large-duct, Critical-flow Data

As experimentally demonstrated, the two-phase critical-flow phenomenon is essentially the same in the transient, large-duct case as in the steady-state, small-duct case. It is therefore instructive to compare the predictions of the various critical-flow models that have been developed principally for steady-state critical flow and verified primarily against steady-state, small-duct, critical-flow data to the transient, large-duct, critical-flow data from this investigation.

In light of the nonuniformity of the fluid quality in the internal-skirt and the downcomer-annulus regions of the vessel witnessed in this system during these decompressions, the depressurizations had to be analyzed in primarily two separate regions of the system. The first was the fluid action inside the blowdown vessel in which the flow regimes in the various sectors of the system were developed and the entrance conditions to the exhaust duct were established. The second was the fluid behavior in the choked exhaust duct.

The upstream stagnation-pressure histories in tests 1 and 2 shown in Figs. 115 and 116, and the upstream fluid-quality histories in Figs. 93 and 94, were used to evaluate the critical flow rates and the critical pressure ratios predicted by the homogeneous-equilibrium, Moody,[2] and Henry-Fauske[1] critical-flow models during the decompression. The homogeneous-frozen critical-flow model was not compared to these transient, large-duct, critical-flow data because the prediction of the critical pressure ratio by this model does not compare well with experimental data (see Fig. 110).

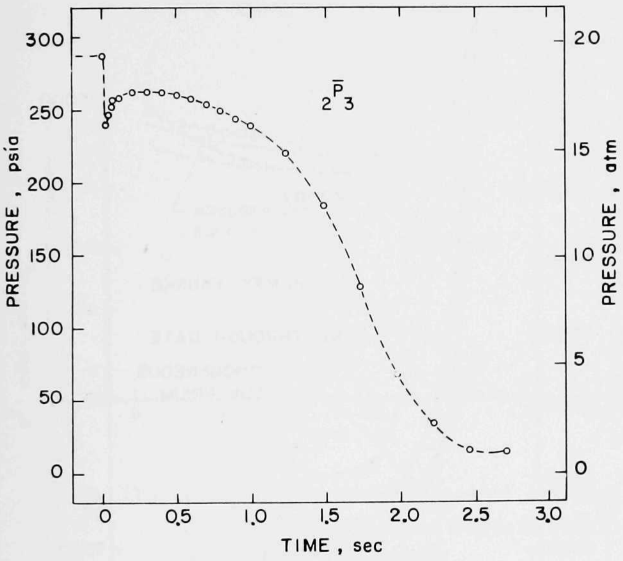

Fig. 115. Pressures Upstream of the Exhaust Duct in Test 1. ANL Neg. No. 900-4982.

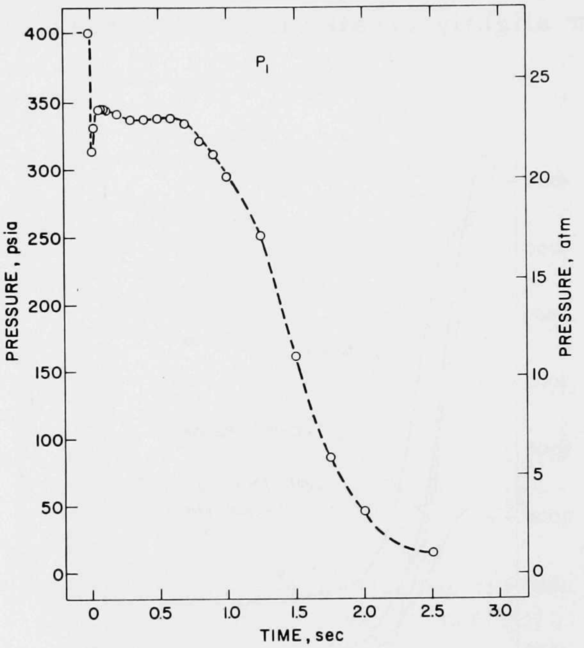

Fig. 116. Pressure Upstream of the Exhaust Duct in Test 2. ANL Neg. No. 900-5049 Rev. 1.

The measured and calculated critical flow rates in tests 1 and 2 are compared in Figs. 117 and 118. In both figures, the homogeneous-equilibrium model best predicted the measured critical flow rates after the initial, low-quality period of the decompression. In the early portion of the blowdown, the homogeneous-equilibrium model underpredicted the critical flow rate. This is because the model assumes equilibrium phase change, but there was a period at the start of the decompression when the inlet fluid quality was small ($x_i < 0.10$) and nonequilibrium effects prevailed. Hence, the actual critical flow rate is greater than that predicted by any equilibrium calculation. Note in Figs. 117 and 118 that, when the homogeneous-equilibrium prediction for the critical flow rate did come into agreement with the measured critical flow rate, only about 40% of the initial fluid mass remained within the blowdown vessel (see Figs. 54 and 55), and the measured critical flow rate had already decreased to less than about 1800 $lb_m/sec\text{-}ft^2$. Hence, as far as the critical flow rate is concerned, most of the decompression had already been completed by the time the homogeneous-equilibrium prediction for the critical flow rate agreed with the measured critical flow rate. The internal vessel pressure (see Figs. 115 and 116) started to decrease from its nearly constant value at about the same time when the homogeneous-equilibrium critical flow rate agreed with the measured critical flow rate. This is consistent with the apparent occurrence of thermodynamic equilibrium of the remaining fluid (see Figs. 56 and 57). The Moody[2] model significantly overpredicts the measured critical flow rates for the entire blowdown in both tests. The Henry-Fauske[1] prediction for the critical flow rate agrees well with the trend of the data while only being slightly greater than the measurements for most of the decompression. The Henry-Fauske prediction for critical flow rate was always equal to or slightly greater than the measurements for the entire depressurization.

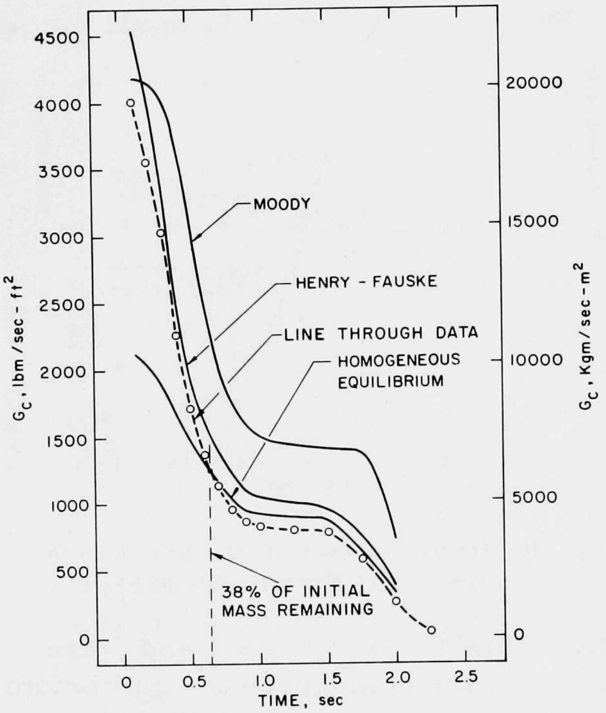

Fig. 117. Comparison of the Measured and Predicted Critical Flow Rates in Test 1. ANL Neg. No. 900-5126 Rev. 1.

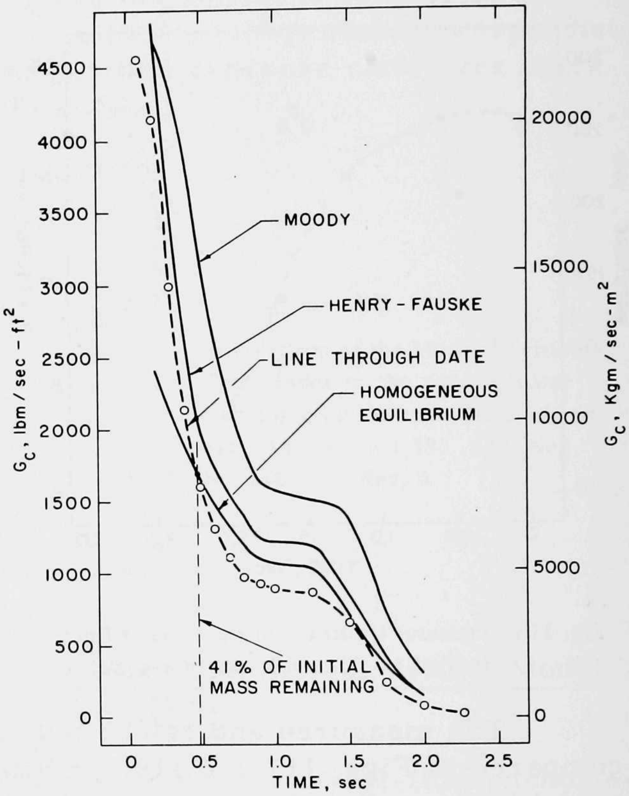

Fig. 118. Comparison of the Measured and Predicted Critical Flow Rates in Test 2. ANL Neg. No. 900-5128 Rev. 1.

The measured and calculated critical exit pressure ratios in tests 1 and 2 are compared in Figs. 119 and 120. The Henry-Fauske prediction of the overall critical-pressure-ratio history is best, with both the homogeneous-equilibrium and Moody predictions underestimating the data.

The measured and calculated remaining fluid mass within the blowdown vessel is shown in Figs. 121 and 122. The Moody[2] prediction of the remaining fluid mass decreased very rapidly below the experimental results of both tests because of the excessively high predicted critical flow rates, as seen in Figs. 117 and 118. The Henry-Fauske[1] prediction of the remaining fluid mass followed the trend of the data in test 1 (see Fig. 121) reasonably well, and it slightly underpredicted the measurements in test 2 (see Fig. 122). The reason for the underprediction in test 1 is because of the conservative prediction for critical flow rate past 600 msec, as shown in Fig. 117. The same reason applies to the results in test 2, except that the flow-rate prediction was more conservative in this case (see Fig. 118). The homogeneous-equilibrium predictions of the remaining fluid mass in both tests 1 and 2 were considerably greater than given by the data. This is because of the underprediction of the critical flow rate early in the blowdown in both tests, as shown in Figs. 117 and 118.

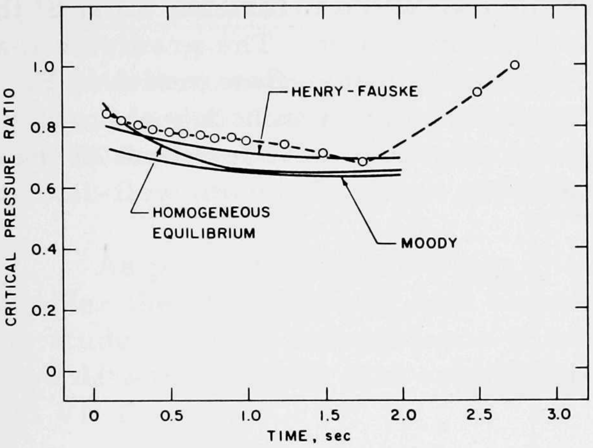

Fig. 119. Comparison of the Measured and Predicted Critical Pressure Ratios in Test 1. ANL Neg. No. 900-5127.

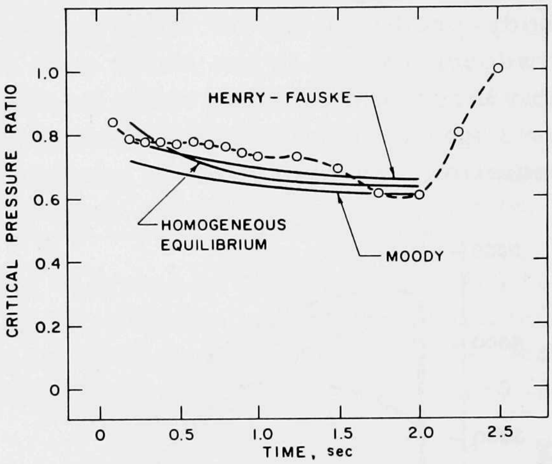

Fig. 120. Comparison of the Measured and Predicted Critical Pressure Ratios in Test 2. ANL Neg. No. 900-5125.

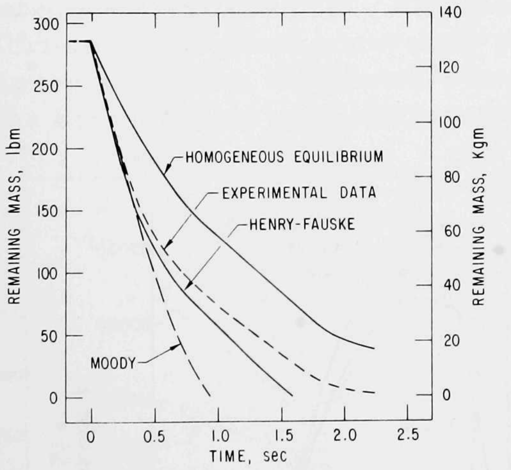

Fig. 121. Comparison of the Measured and Predicted Remaining Mass in Test 1. ANL Neg. No. 900-5095 Rev. 1.

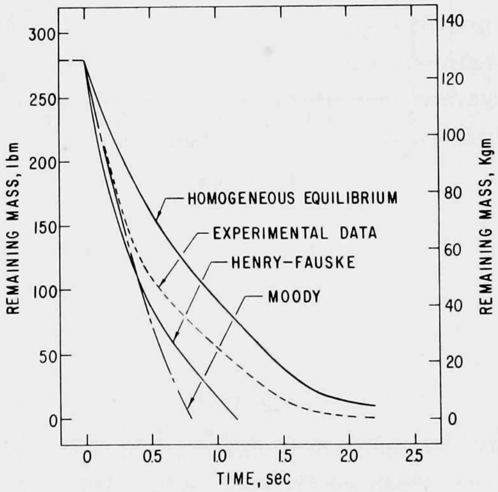

Fig. 122. Comparison of the Measured and Predicted Remaining Mass in Test 2. ANL Neg. No. 900-5100 Rev. 1.

The measured and calculated thrust histories in tests 1 and 2 are compared in Figs. 123 and 124. The predicted thrust history obtained by employing the homogeneous-equilibrium critical-flow model in Eq. 195 agrees with the data relatively well in the latter part of the decompression, but the maximum in the predicted thrust history is later in time than the measurements indicated. This is due to the underpredicted critical flow rate early in the depressurization, as seen in Figs. 117 and 118. The homogeneous-equilibrium-predicted thrust increased up to this time, even with the underpredicted critical flow rate, because of the increasing fluid quality (see Figs. 93 and 94). The maximum thrust predicted by using the Moody[2] critical-flow model in Eq. 195 was considerably greater than the measured maximum thrust in both tests. The Moody-predicted thrust was greater than the measured thrust for most of the blowdown, except in the latter part of the decompression. The predicted maximum thrust obtained by using the Henry-Fauske[1] critical-flow model in Eq. 195 was slightly greater than the measured maximum thrust in both tests. This prediction was also slightly greater than the measurements for most of the

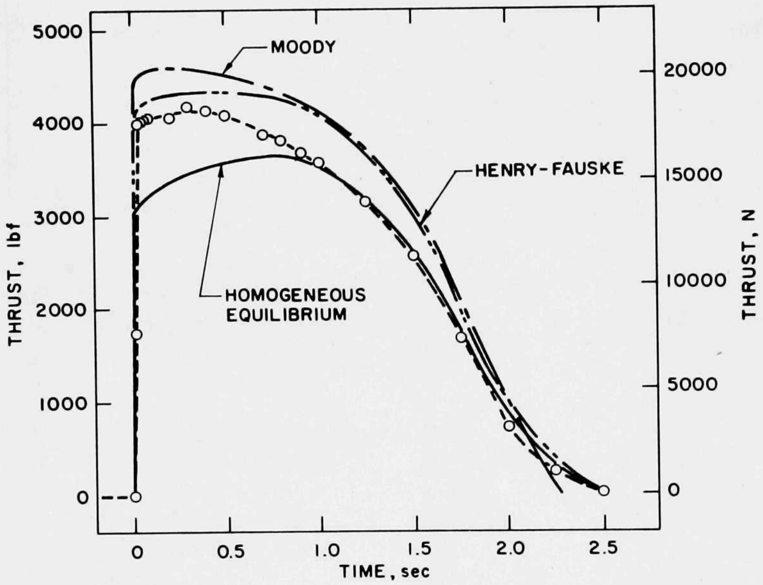

Fig. 123

Comparison of the Measured and Predicted Thrust in Test 1. ANL Neg. No. 900-5133.

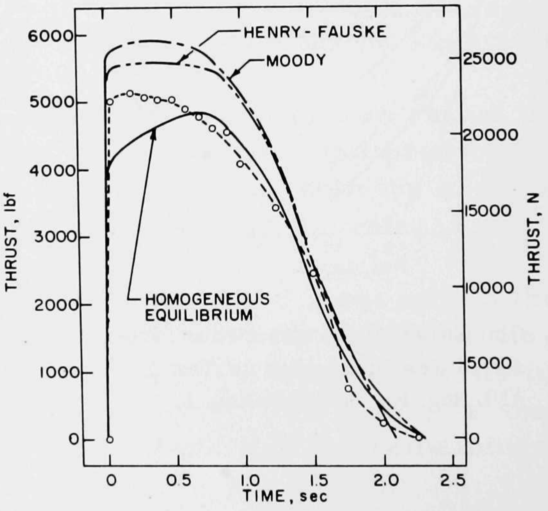

Fig. 124

Comparison of the Measured and Predicted Thrust in Test 2. ANL Neg. No. 900-4994.

blowdown, except in the latter period of the depressurization, but it was less than the Moody prediction over the entire decompression. Of the three cited critical-flow analytical models, the measured thrust histories in these blowdowns are best predicted with the Henry-Fauske[1] critical-flow model.

Based on the foregoing comparisons of the various predictions of the critical-flow analytical models to the experimental data from this investigation, the Henry-Fauske[1] critical-flow model best predicts the overall characteristics of the two-phase-decompression phenomenon.

H. Comparison of Predictions of Various Critical-flow Analytical Models to Other Transient, Large-duct, Critical-flow Data

As demonstrated, the two-phase critical-flow phenomenon is essentially the same in the transient, large-duct case as in the steady-state, small-duct case. It is therefore instructive to also compare the predictions of various critical-flow models to other pertinent transient, large-duct, critical-flow data.

As previously pointed out, it is only relevant to this investigation to consider the experimental data acquired under similar conditions to those in this study. Hence, comparisons of analytical models will only be made with those data that satisfy this criterion, and these data have been presented in Sec. VII.E.

Figure 125 compares the measured transient, large-duct, critical flow rates in one of Ungerer's[67] tests with the corresponding calculated critical flow rates. These data were for a bottom blowdown through a convergent-divergent nozzle in which A_e/A_{bv} was 0.025 and S/V of the internal vessel was about 1 ft^2/ft^3. The initial stagnation condition of the fluid was nearly saturated water at 750 psia. For most of the decompression, the homogeneous-equilibrium model most accurately predicts the critical flow rates. Early in the depressurization, the Henry-Fauske-model prediction is more conservative than the homogeneous-equilibrium prediction, but it predicts critical flow rates

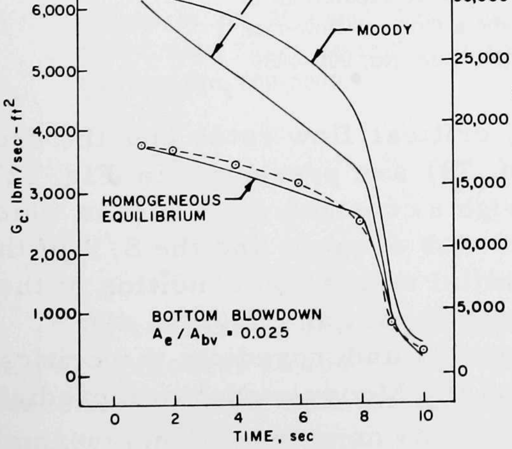

Fig. 125

Comparison of the Critical-flow-model Predictions to Ungerer's[67] Transient, Large-duct, Critical-flow-rate Data for A_e/A_{bv} = 0.025. ANL Neg. No. 900-4997.

that are always somewhat greater than the measured values. For most of the decompression, the Moody model greatly overpredicts the measured critical flow rates.

Figure 126 compares the measured transient, large-duct, critical flow rates of Ungerer[67] the predicted critical flow rates in another bottom blowdown through a convergent-divergent nozzle but with $A_e/A_{bv} = 0.013$. The S/V of the internal vessel was the same in this run as in the test shown in Fig. 125, and the initial stagnation fluid condition was also the same as in the previous run. The same trend in the model predictions is observed in Fig. 126 as in Fig. 125. The homogeneous-equilibrium model most accurately predicts the data for most of the blowdown, and the Moody model significantly overpredicts the measured critical flow rate. The Henry-Fauske model overpredicts the critical flow rates for most of the decompression, but it agrees better with the data toward the end of the blowdown. The predictions of the Henry-Fauske model are always greater than the measured critical flow rates and much less conservative than the Moody-model predictions.

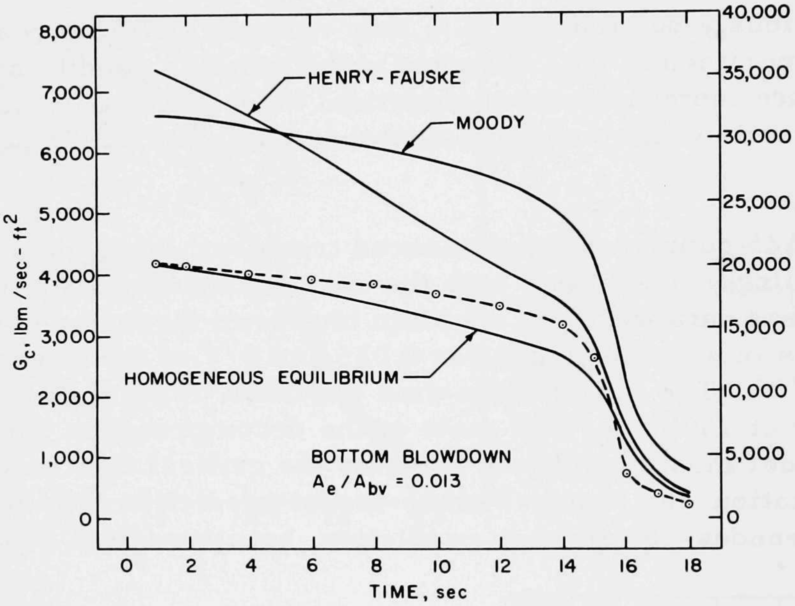

Fig. 126. Comparison of the Critical-flow-model Predictions to Ungerer's[67] Transient, Large-duct, Critical-flow-rate Data for $A_e/A_{bv} = 0.013$. ANL Neg. No. 900-4989.

The measured transient, large-duct, critical flow rates and the predicted critical flow rates in CSE test 7 (Ref. 70) are presented in Fig. 127. These results are for a bottom blowdown through a constant-area duct in which $A_e/A_{bv} \simeq 0.007$. The L/D of the exhaust duct was about 8, and the S/V of the internal vessel was about 1.24 ft^2/ft^3. The initial stagnation condition of the fluid was nearly saturated water with $P_0(0) = 671$ psia and $T_0(0) = 490$°F. The homogeneous-equilibrium model considerably underpredicts the critical flow rates for most of the decompression, and the Moody model overpredicts the critical flow rates by a considerable margin during the blowdown. The Henry-Fauske model overpredicts the critical flow rates early in the decompression, but it corresponds better with the measurements later in the depressurization.

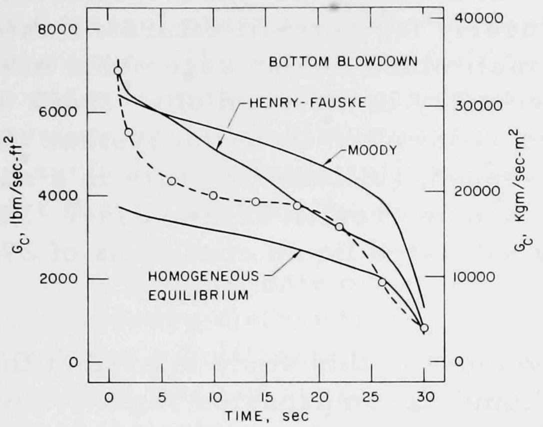

Fig. 127

Comparison of the Critical-flow-model Predictions to the Measured, Transient, Large-duct, Critical Flow Rates in the CSE Test 7.[70] ANL Neg. No. 900-5101.

The measured transient, large-duct, critical flow rates and the calculated critical flow rates in CSE test 11 (Ref. 70) are shown in Fig. 128. These results are also for a bottom blowdown from the same vessel and through the same exhaust duct with the same area ratio as in CSE test 7. The initial stagnation condition of the fluid was again nearly saturated water but with $P_0(0) = 1450$ psia and $T_0(0) = 575°F$. The homogeneous-equilibrium model best predicts the measured critical flow rates for most of the decompression, and the Moody model significantly overpredicts the data during most of the blowdown. The Henry-Fauske model predicts the measurements more conservatively than the homogeneous-equilibrium model early in the decompression, but considerably less conservatively than the Moody model for the bulk of the depressurization.

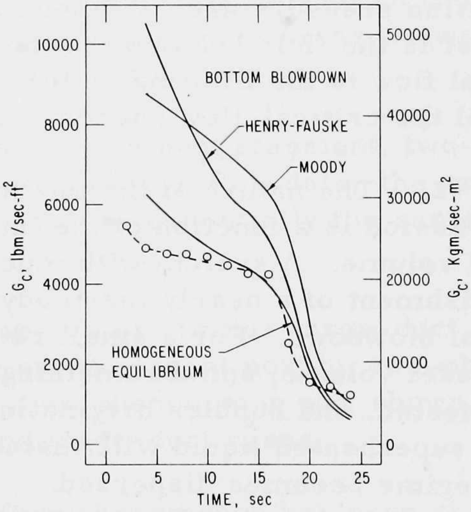

Fig. 128

Comparison of the Critical-flow-model Predictions to the Measured, Transient, Large-duct, Critical Flow Rates in the CSE Test 11.[70] ANL Neg. No. 900-5089.

In evaluating the applicability of the foregoing two-phase critical-flow analytical models to the blowdown transient based upon the previous results, it becomes evident that the Henry-Fauske model[1] best predicts the overall decompression phenomenon once the upstream stagnation fluid conditions are known.

VIII. CONCLUSIONS AND RECOMMENDATIONS

A. Conclusions

Experimental data and comparisons of analytical models have been presented for the blowdown of initially nearly isothermal, saturated water from a small pressure vessel. The vessel, which had an assembled internal volume of 5.40 ft^3, contained internal geometry in the form of a "skirt" that provided a varying flow area to the fluid as it exited from the system. The break in the system simulated a double-ended, guillotine rupture in a short exhaust duct originating from the upper annulus region of the vessel. Experimental decompression data for initially saturated liquid conditions of 290 and 402 psia were presented.

Analytical models have been developed in this study to predict the blowdown characteristics in the subcooled-liquid-decompression regime, the bubble-growth period, and also in the dispersed regime of depressurization. These models exhibit good agreement with the blowdown data of this and other studies.

The following conclusions can be drawn from the results of this investigation concerning the two-phase decompression phenomenon.

1. The two-phase blowdown phenomenon in a pressure vessel should be separated into two related phenomena. The first is the fluid behavior inside the vessel upstream of the entrance to the exhaust duct. The local flow regime, pressure, and fluid quality in each sector of the system contribute to establishing the state of the fluid at the entrance to the exhaust duct. The parameters of primary importance at the inlet to the exhaust duct are the inlet stagnation pressure and the inlet fluid quality. The second phenomenon of interest is the fluid behavior in the choked exhaust duct, where two-phase critical flow is the limiting criterion. The inlet conditions from the vessel control the critical-flow phenomenon in the exhaust duct.

2. The nature of the internal vessel pressure history early in a decompression is a function of the internal vessel surface area and the internal vessel volume. A system with much internal surface area would promote the establishment of a nearly thermodynamic equilibrium state soon after the start of blowdown. For a small ratio of internal vessel surface area to internal vessel volume, some remaining liquid within the system will be locally superheated, and bubbles originating from the solid surfaces and expanding in the superheated liquid will sustain the internal vessel pressure until the flow regime becomes dispersed.

3. The internal vessel pressure history at the beginning of depressurization is also dependent upon the exhaust flow area from the system. For a small exit flow area, the system pressure at the beginning of blowdown will recover to nearly the initial bulk saturation pressure, and then it will be

sustained at approximately this pressure for much of the rest of the decompression. Phase separation within the blowdown vessel will become apparent for smaller exhaust areas. For a large exit flow area, the system pressure history at the beginning of decompression will not recover as far as in the case of a smaller exhaust area for the same surface-to-volume ratio, and the internal vessel pressure will decrease more rapidly during the remainder of the blowdown. The remaining fluid will also depressurize in a more homogeneous manner in the latter period of decompression for a larger exhaust area. The system pressure history at the beginning of blowdown is more sensitive to the surface-to-volume ratio of the interior of the system than it is to the exhaust flow area from the system.

4. Choking only occurred at the exit of the system used in this study, and the pressure distribution inside the vessel was nearly uniform and apparently was not significantly affected by the downcomer geometry. This indicates that the fluid was not appreciably compressible anywhere inside the vessel upstream of the entrance to the exhaust duct.

5. A nonuniform distribution of fluid quality detected in the vessel was promoted by the lack of structural surface area within the internal-skirt region, the downcomer flow geometry, the absence of significant fluid resistance at the bottom of the internal skirt, and the nearly uniform pressure distribution inside the vessel.

6. The liquid inside the vessel at the beginning of these decompressions was superheated, and the liquid remaining within the internal-skirt region remained in this state for most of the time that the internal vessel pressure held at a nearly constant value. Once the remaining fluid inside the internal-skirt region became dispersed, bulk thermodynamic equilibrium was closely approached. This caused the internal vessel pressure to decrease from its previously nearly constant value, and the system pressure was then sustained by vaporization from superheated liquid droplets.

7. By comparison of these and other pertinent transient, two-phase critical-flow data to steady-state, two-phase critical-flow data, the two-phase critical-flow phenomenon was demonstrated to be essentially the same in both the steady state and transient cases.

8. Also by comparison of these and other similar large-duct, two-phase critical-flow data to small, convergent-divergent nozzle, two-phase critical-flow data, the two-phase critical-flow phenomenon was shown to be essentially the same in both the small- and large-duct cases.

9. Since the two-phase critical-flow phenomenon has been shown to be essentially the same in the transient, large-duct case as in the steady-state, small-duct case, the best presently available two-phase critical-flow analytical models that were initially developed for steady-state critical flow can validly be applied in the transient, large-duct, two-phase critical-flow case. Comparison

of the predictions of the available two-phase critical-flow models to these and other similar blowdown data indicate that the Henry-Fauske[1] critical-flow model best predicts the characteristics of the two-phase depressurization phenomenon.

B. Recommendations for Future Work

The results of this and other investigations have promoted questions that should be further investigated in order to gain a clearer understanding of the thermodynamics, heat transfer, and fluid dynamics of the two-phase decompression phenomenon. Some of the key areas that should be investigated are as follows:

1. The location at which the exhaust port exits from the blowdown vessel for a given internal configuration should be further investigated to better understand its effect on the progression of the depressurization process. For example, decompressions from a system similar to that used in this investigation, but with the exhaust duct originating from within the upper internal-skirt region rather than from the upper annulus region, should be performed.

2. For vessel geometries with an internal "skirt," combination of bottom orifice plates and internal-skirt geometry should be studied to investigate the effect of internal vessel surface area and flow resistance upon the flow regimes developed within the vessel during blowdown.

3. Decompressions should be performed in a vessel with various internal geometries to further evaluate the effect of the amount and configuration of internal structural surface area on the flow regimes and pressure-history characteristics in the system during depressurization. Elevated pressure-temperature experiments should also be performed in such a geometry to determine if the nonuniform fluid-quality distribution detected in this experiment at these lower pressures would diminish at higher pressure, and if the upstream fluid quality would approach the equilibrium quality as the initial saturation pressure of the decompression is increased. This would serve as good comparison for the bubble-growth blowdown model proposed in this study.

4. The proposed bubble-growth blowdown model can be used to predict the decompression characteristics of an initially nonisothermal system as well as an initially isothermal system during the bubble-growth regime of depressurization. It is suggested that this model be verified in predicting the initial blowdown characteristics of a system that has a significant initial temperature distribution.

Various combinations of the foregoing suggestions are needed to better understand the effect of the vessel and internal geometry upon the two-phase decompression phenomenon.

APPENDIX A

Data Reduction

In this investigation, the weight and thrust signals were of particular interest. The concern with these two signals was due to the possible mechanical coupling between them via the blowdown vessel. Basically two techniques were used in reducing these two signals. The first method, called the interval technique, was one in which the signal was integrated over a complete cycle of variation from t_1 to t_2, and then divided by the time interval $t_2 - t_1$ to obtain the integrated, mean value of the signal during a given cycle. In this study, the analog signal from the oscillograph and/or the magnetic tape was manually integrated to determine the mean value of the signal over one complete cycle of variation. This was done for the entire lifetime of the signal, thus producing a locus of integrated, mean signal values with time. Typical results derived from this reduction method are presented in Figs. 28 and 29 for the remaining mass, and in Figs. 30 and 31 for the thrust.

The second method, called the span technique, was one in which the harmonic signal was integrated over time for the entire lifetime of the signal, and then the integrated results were smoothed with a third-order least-squares curve fit.

Figures A.1 and A.2 show typical examples of the integrated signal over time and also the smoothed results for the remaining fluid mass in the vessel. Figures A.3 and A.4 show similar results for the thrust. The integrated, smoothed results were then differentiated with respect to time to determine the value of the parameter at various times. This method had the effect of integrating out the high-frequency noise in the signal while still

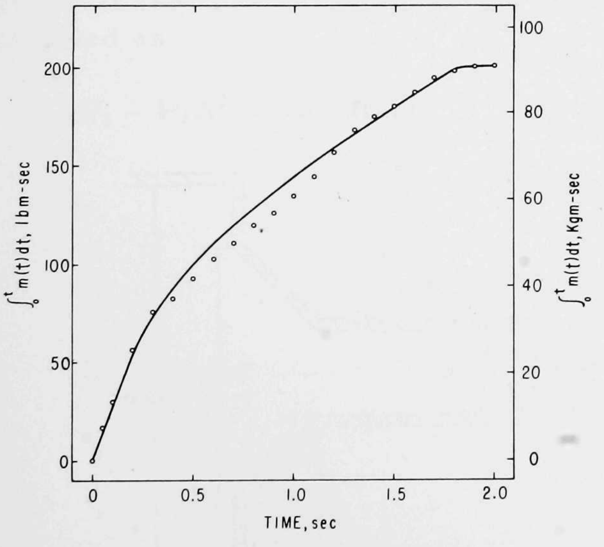

Fig. A.1. The Span-reduction Method of the Remaining Mass in Test 1. ANL Neg. No. 900-4955.

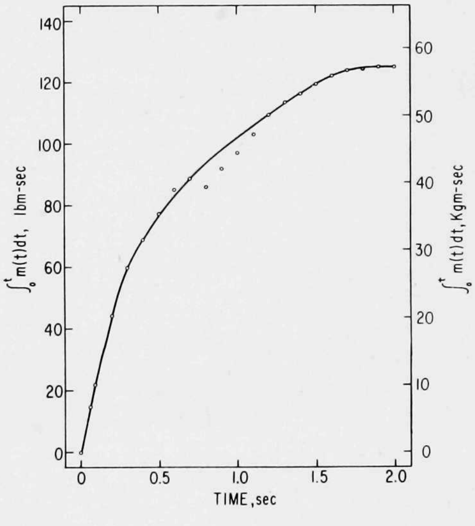

Fig. A.2. The Span-reduction Method of the Remaining Mass in Test 2. ANL Neg. No. 900-4949.

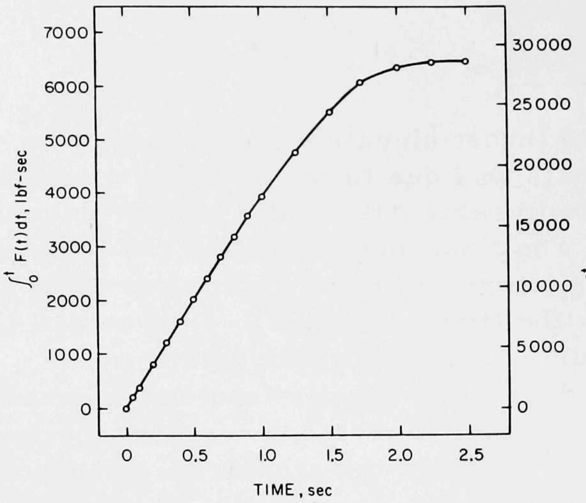

Fig. A.3. The Span-reduction Method of the Thrust in Test 1. ANL Neg. No. 900-4952.

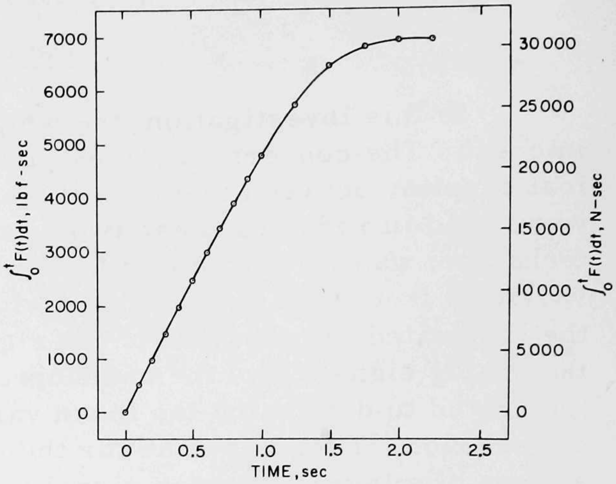

Fig. A.4. The Span-reduction Method of the Thrust in Test 2. ANL Neg. No. 900-4954.

retaining a true representation of the actual signal. This reduction method should produce the same results as the interval technique. The results of data reduction using the span technique are also shown in Figs. 28 and 29 for the remaining mass, and in Figs. 30 and 31 for the thrust. The results of these two data-reduction techniques are indeed very similar.

APPENDIX B

Verification of Internal Vessel Pressures Being Stagnation Pressures

The two-phase critical-flow models[1,2] used to predict the transient critical discharge phenomenon were derived on the basis of an upstream stagnation pressure. Most of the verification experiments for steady-state models have also generated an upstream condition that was essentially stagnant. Since the upstream fluid in these experiments was nearly stagnant, the upstream static and stagnation pressures were essentially equal. It will be shown in this appendix that the measured upstream static pressures in the tests reported in this study were also virtually stagnation pressures.

To illustrate the effect of geometry on the upstream pressure, consider an axisymmetric, convergent nozzle as shown in Fig. B.1. If the flow is assumed to be one-dimensional, steady-state, and incompressible from location 1 to any point in the nozzle, the pressure drop may be written as

$$P_1 - P = \tfrac{1}{2}\rho u^2. \qquad \text{(B.1)}$$

Application of the continuity equation

$$\dot{m} = \rho A u \qquad \text{(B.2)}$$

and substitution for u in Eq. B.1 yield

$$P_1 - P = \frac{\dot{m}}{2\rho A^2}. \qquad \text{(B.3)}$$

Since the mass flow rate $\dot{m}$ and the density ρ are constant, Eq. B.3 can be formulated as

$$(P_1 - P)A^2 = \text{Constant}. \qquad \text{(B.4)}$$

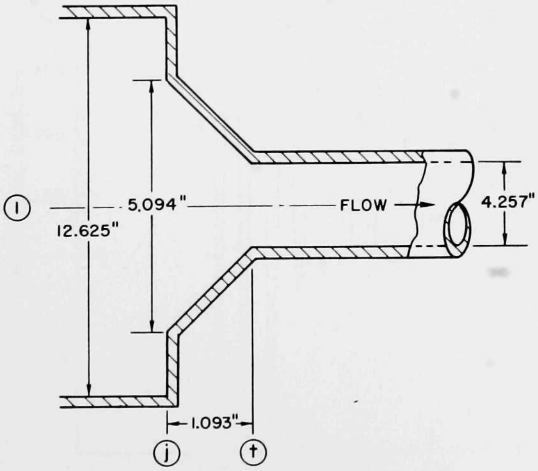

Fig. B.1

Schematic of the Exhaust Geometry.
ANL Neg. No. 900-5076.

In this study, the throat flow area was 14.233 in.^{2} and the flow area from location 1 to location j (see Fig. B.1) was idealized as a circular flow area, the radius of which was the distance from the exhaust-port centerline to the flow-area enlargement in the downcomer annulus, namely, 6.312 in. (see Fig. 7). This produced a flow area of 125 in.^{2} from location 1 to location j. If P_j is considered to be the pressure just inside the convergent nozzle (see Fig. B.1), Eq. B.4 can be written as

$$(P_1 - P_j)A_j^2 = (P_1 - P_t)A_t^2, \tag{B.5}$$

from which we deduce that

$$(P_1 - P_j) = 0.013(P_1 - P_t). \tag{B.6}$$

Thus, in this geometry, only 1.3% of the total pressure drop from upstream to the throat was from location 1 to location j, and 98.7% of the pressure drop was from location j to the throat. Therefore, a pressure measurement at location 1 (see Figs. 8, 9, and 12) was very representative of the upstream stagnation pressure at the exhaust-duct entrance in this system.

APPENDIX C

Experimental Data

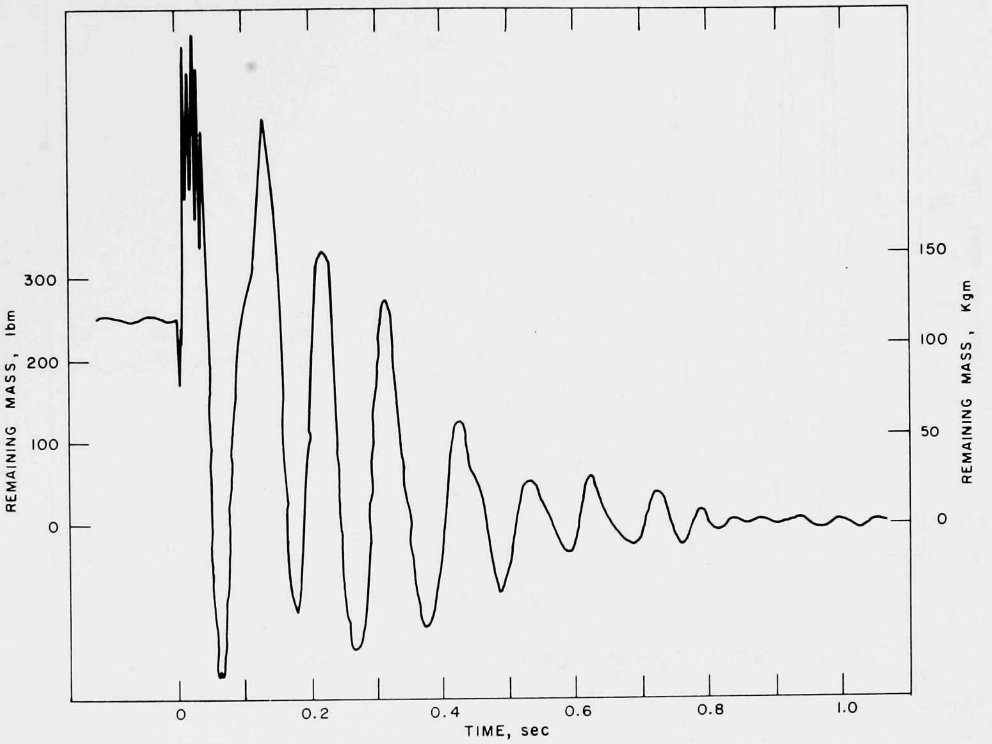

Fig. C.1. Remaining-mass Signal in the Calibration Test.
ANL Neg. No. 900-5070 Rev. 1.

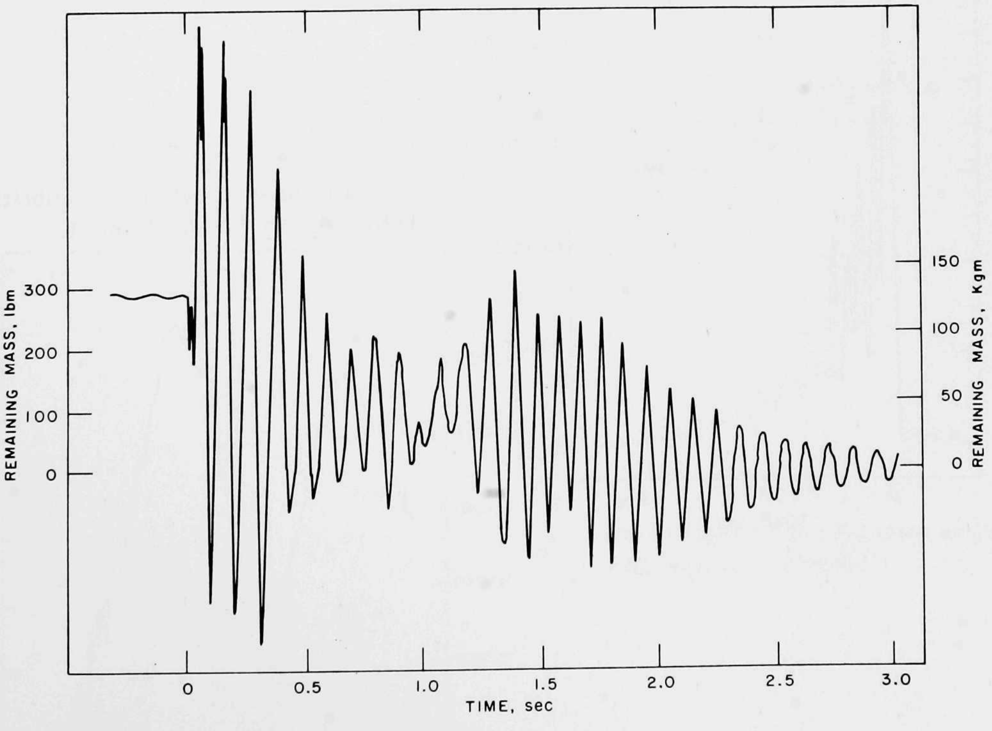

Fig. C.2. Remaining-mass Signal in Test 1. ANL Neg. No. 900-5093 Rev. 1.

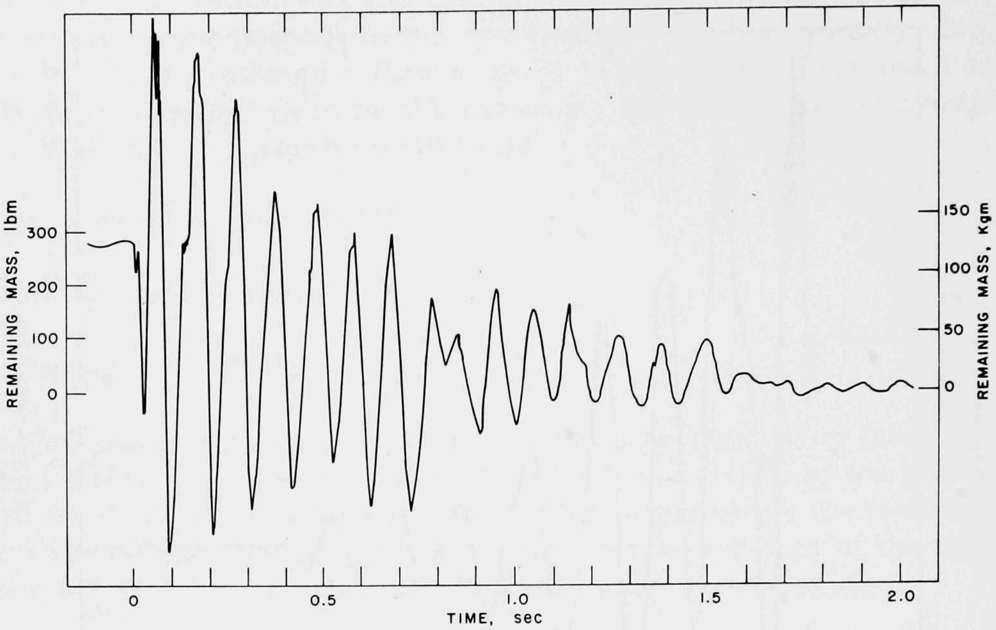

Fig. C.3. Remaining-mass Signal in Test 2. ANL Neg. No. 900-5081.

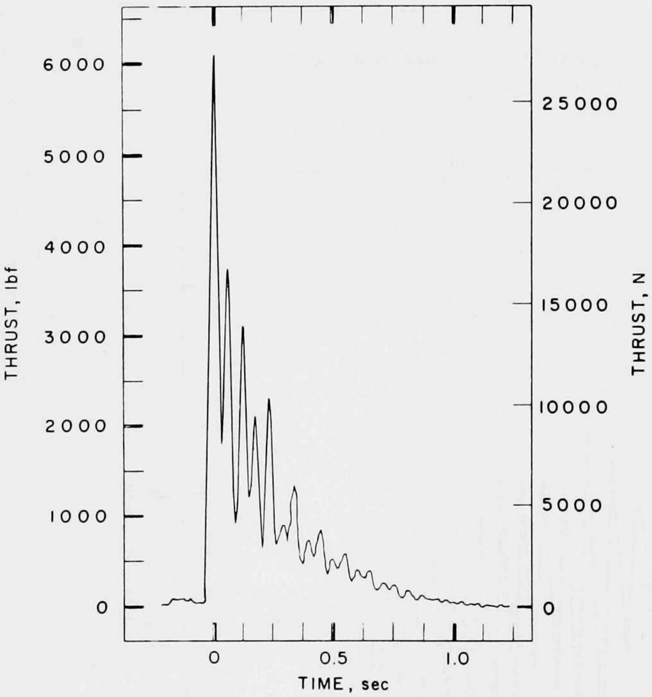

Fig. C.4

Overall Thrust Signal in the Calibration Test. ANL Neg. No. 900-5011 Rev. 1.

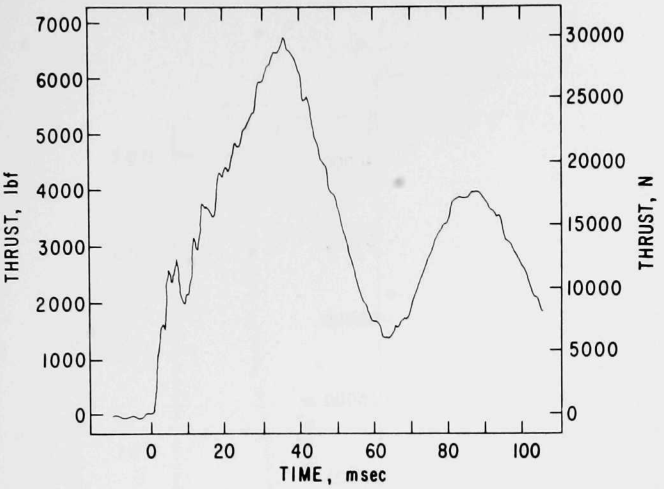

Fig. C.5

Thrust Signal at the Initiation of the Calibration Test. ANL Neg. No. 900-5020.

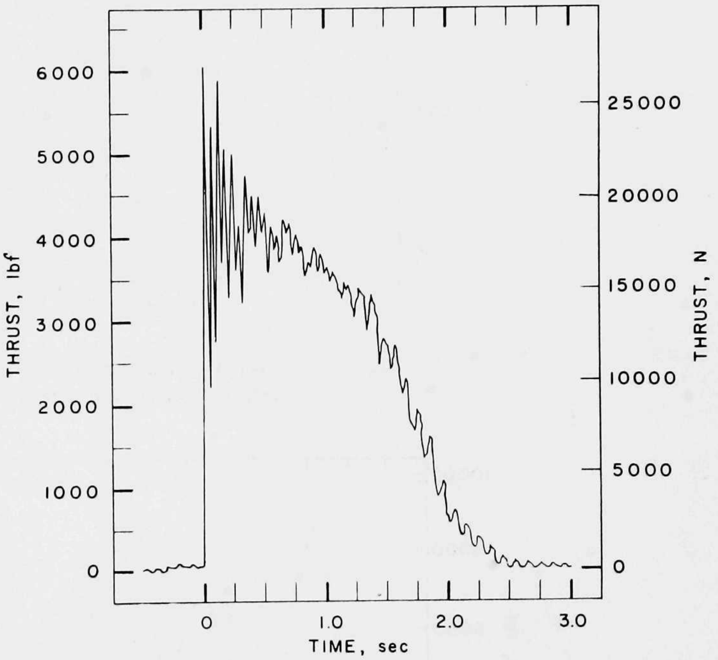

Fig. C.6

Overall Thrust Signal in Test 1. ANL Neg. No. 900-5009 Rev. 1.

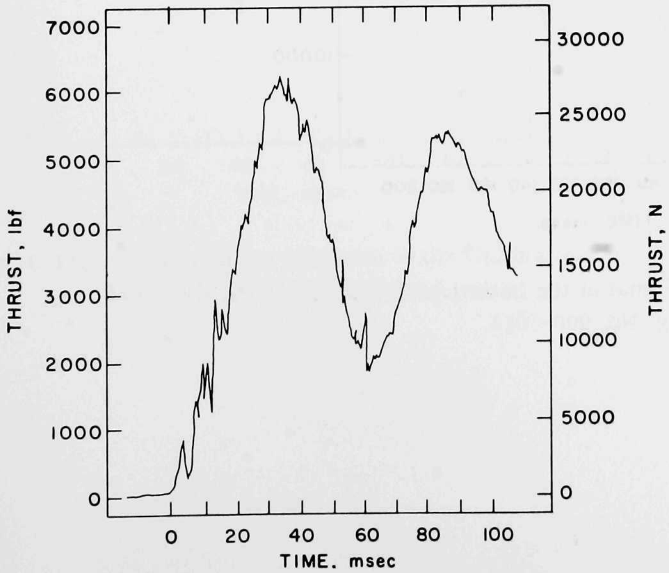

Fig. C.7

Thrust Signal at the Initiation of Test 1. ANL Neg. No. 900-5017.

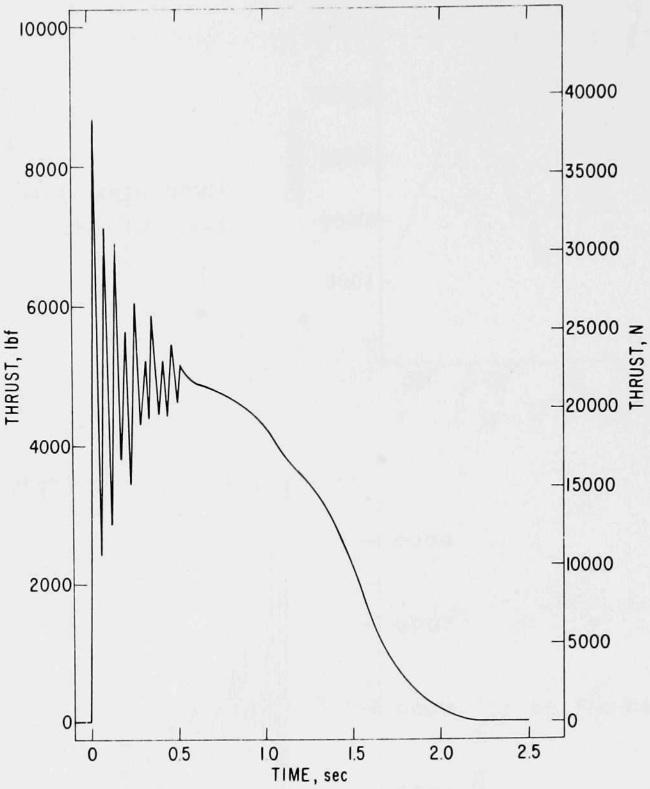

Fig. C.8. Overall Thrust Signal in Test 2.
ANL Neg. No. 900-5001.

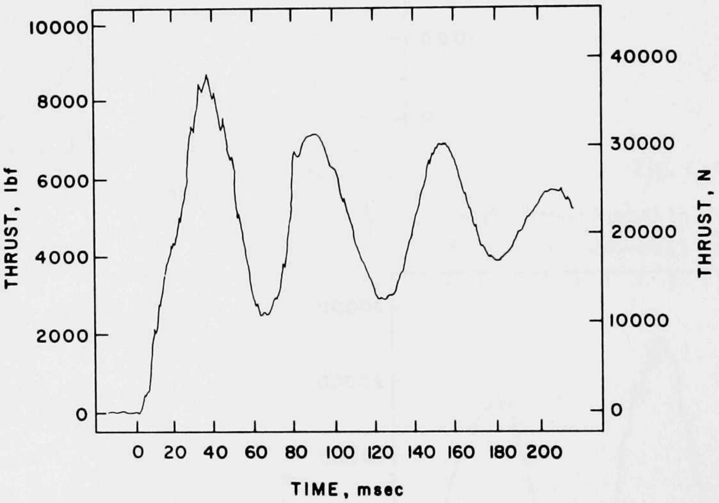

Fig. C.9. Thrust Signal at the Initiation of Test 2.
ANL Neg. No. 900-5014.

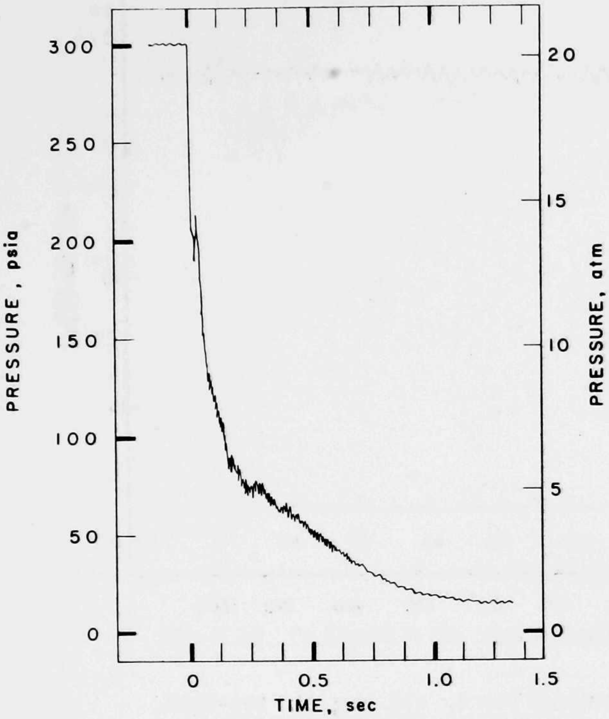

Fig. C.10

Overall P_1 Signal in the Calibration Test. ANL Neg. No. 900-5042.

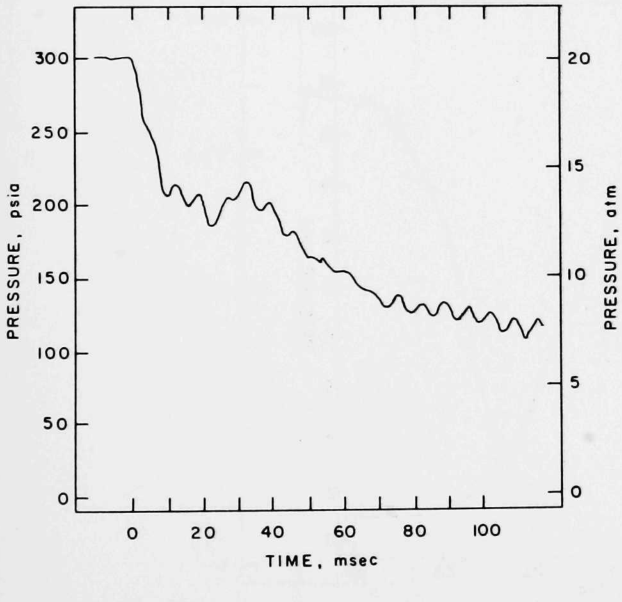

Fig. C.11. P_1 Signal at the Initiation of the Calibration Test. ANL Neg. No. 900-5016.

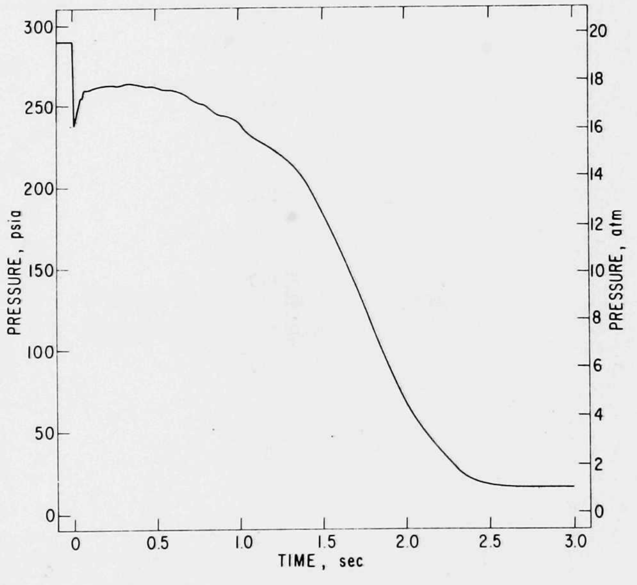

Fig. C.12. Overall P_2 Signal in Test 1. ANL Neg. No. 900-4999.

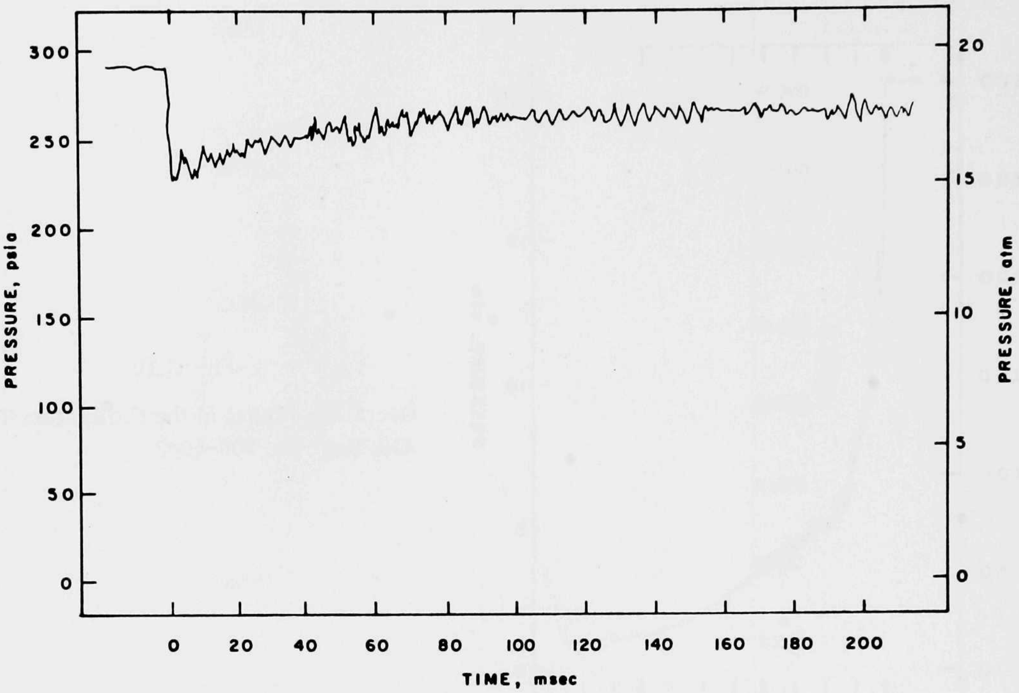

Fig. C.13. P_2 Signal at the Initiation of Test 1. ANL Neg. No. 900-5023.

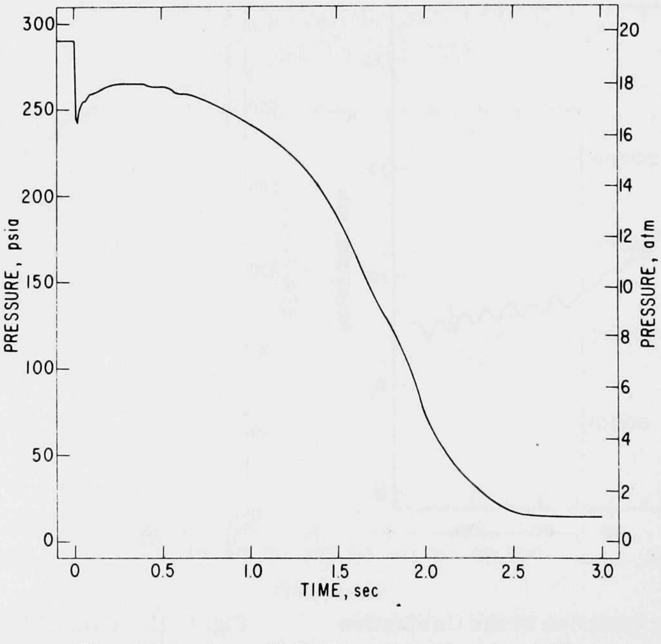

Fig. C.14. Overall P_3 Signal in Test 1. ANL Neg. No. 900-5000.

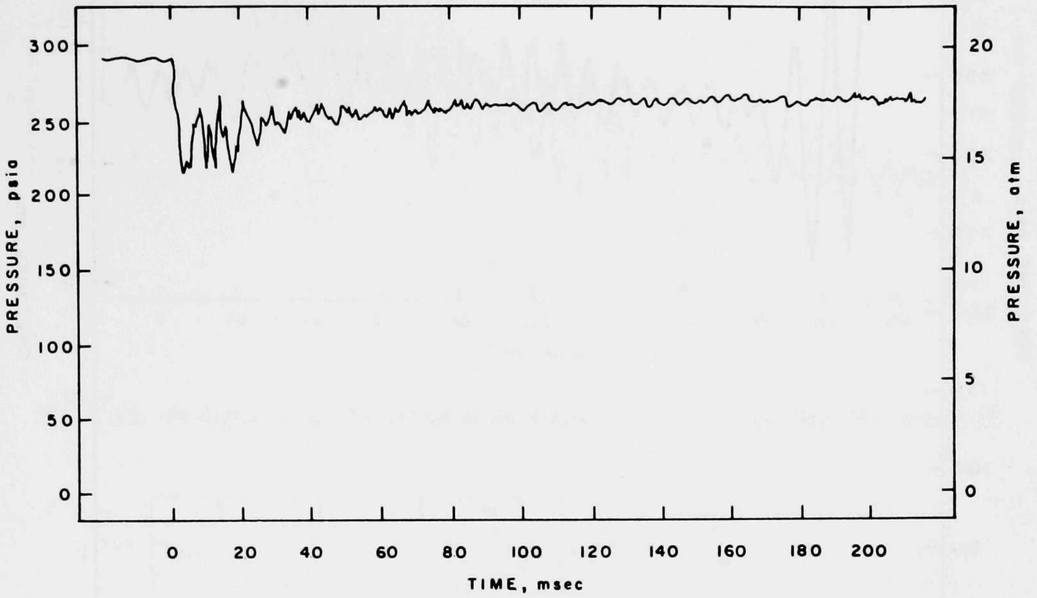

Fig. C.15. P3 Signal at the Initiation of Test 1. ANL Neg. No. 900-5024.

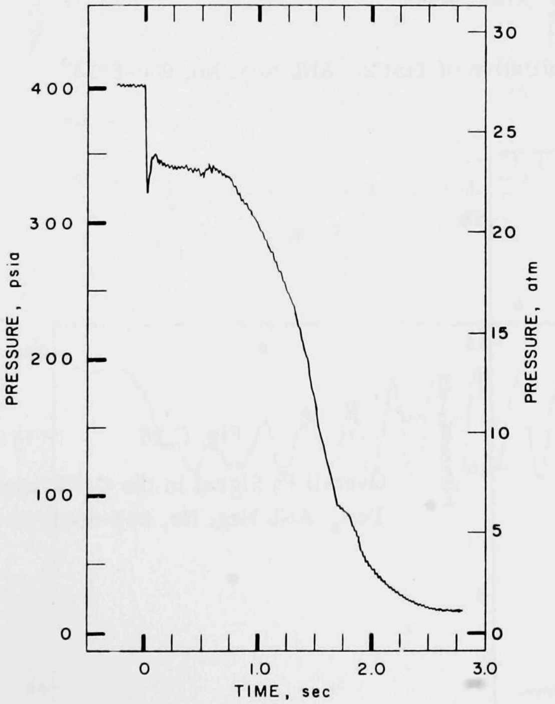

Fig. C.16

Overall P_1 Signal in Test 2. ANL Neg. No. 900-5013 Rev. 1.

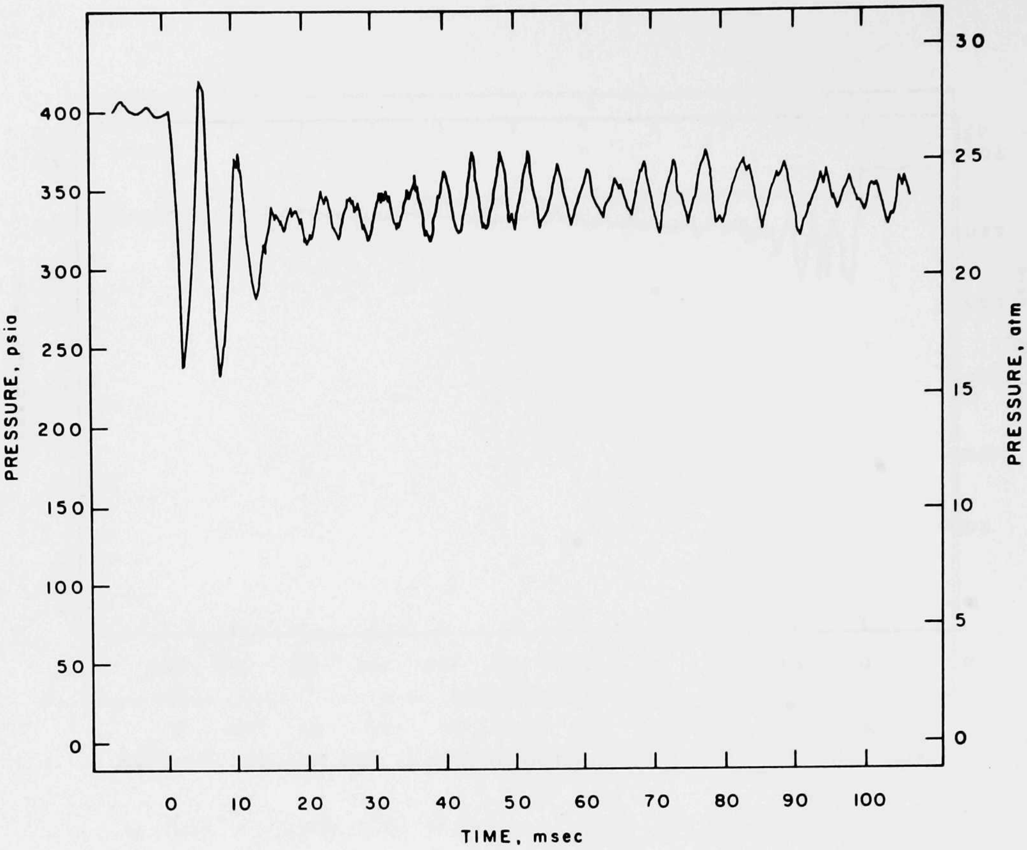

Fig. C.17. P_1 Signal at the Initiation of Test 2. ANL Neg. No. 900-5018.

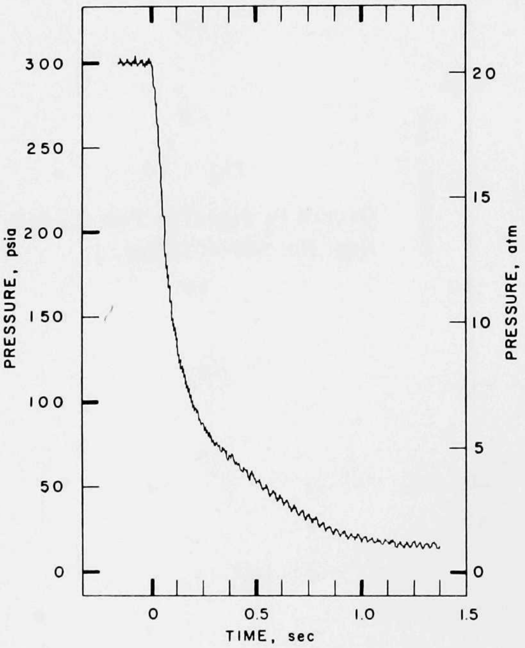

Fig. C.18

Overall P_8 Signal in the Calibration Test. ANL Neg. No. 900-5041.

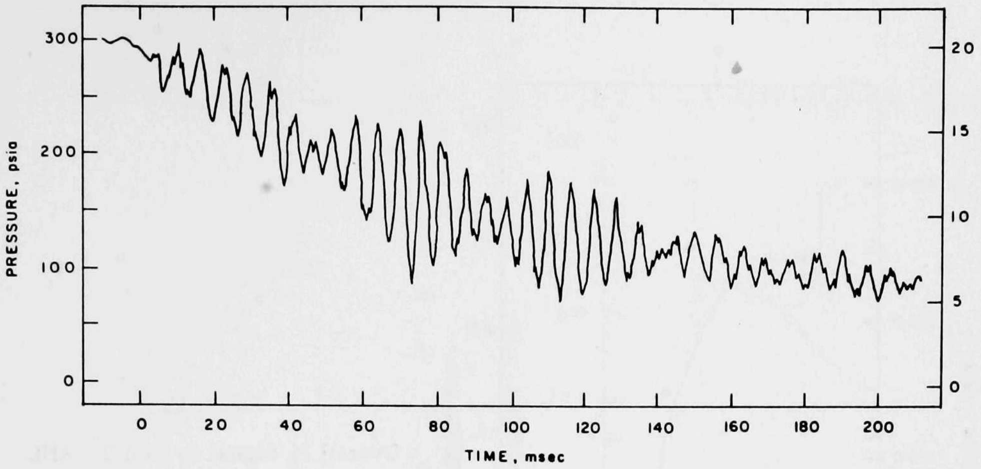

Fig. C.19. P_8 Signal at the Initiation of the Calibration Test. ANL Neg. No. 900-5021.

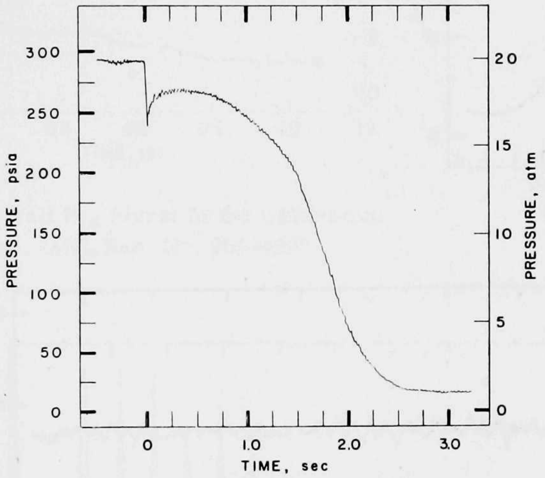

Fig. C.20

Overall P_8 Signal in Test 1.
ANL Neg. No. 900-5040.

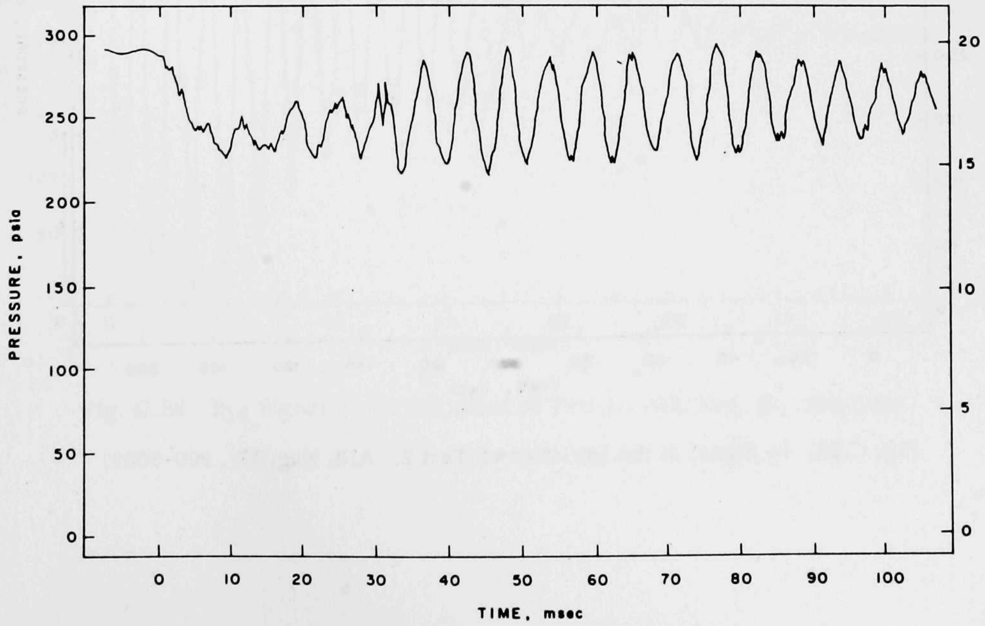

Fig. C.21. P_8 Signal at the Initiation of Test 1. ANL Neg. No. 900-5019.

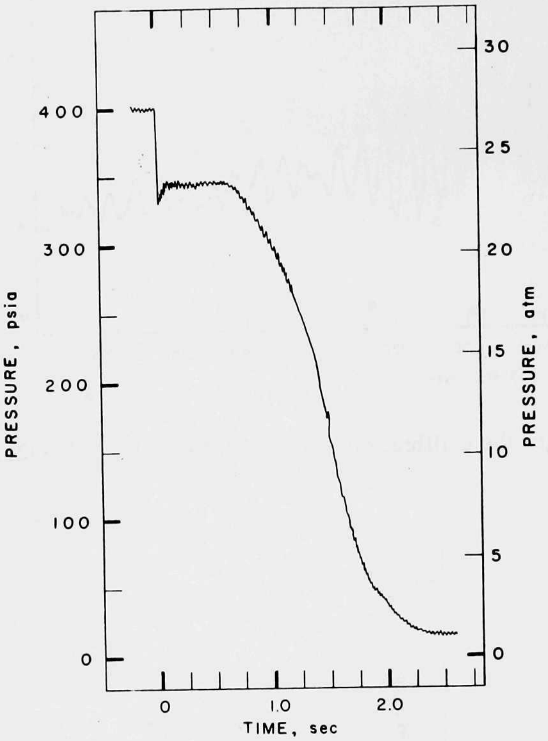

Fig. C.22

Overall P_8 Signal in Test 2. ANL Neg. No. 900-5012 Rev. 1.

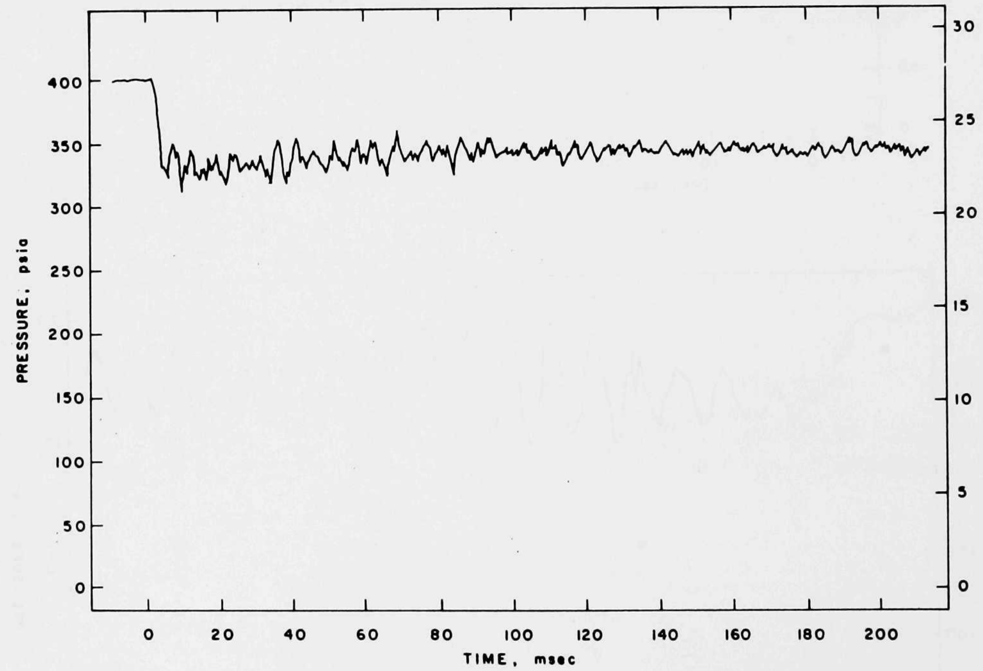

Fig. C.23. P_8 Signal at the Initiation of Test 2. ANL Neg. No. 900-5022.

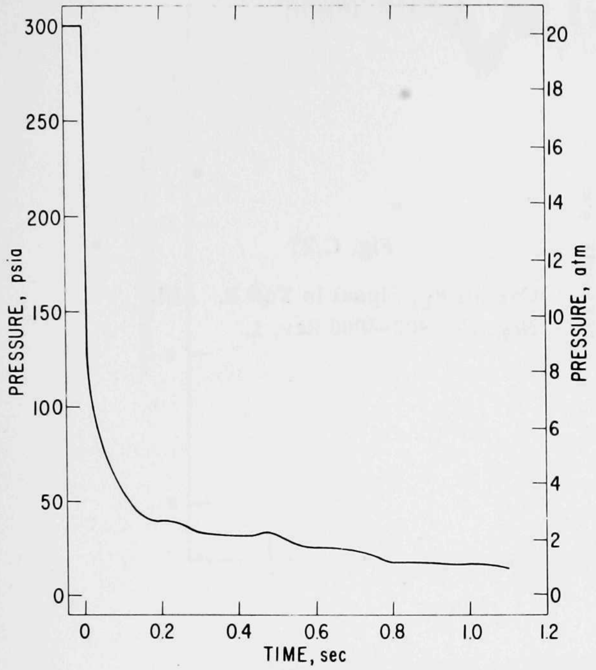

Fig. C.24. Overall P_{14} Signal in the Calibration Test. ANL Neg. No. 900-4990.

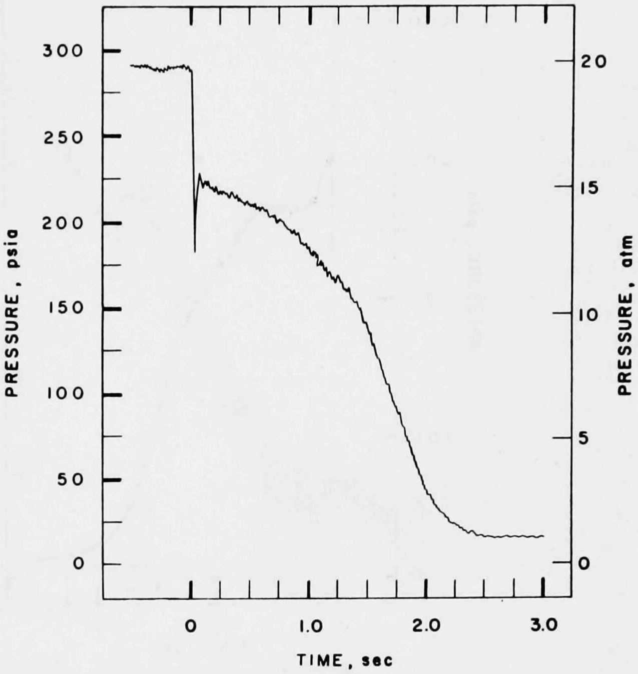

Fig. C.25. Overall P_{14} Signal in Test 1. ANL Neg. No. 900-5015.

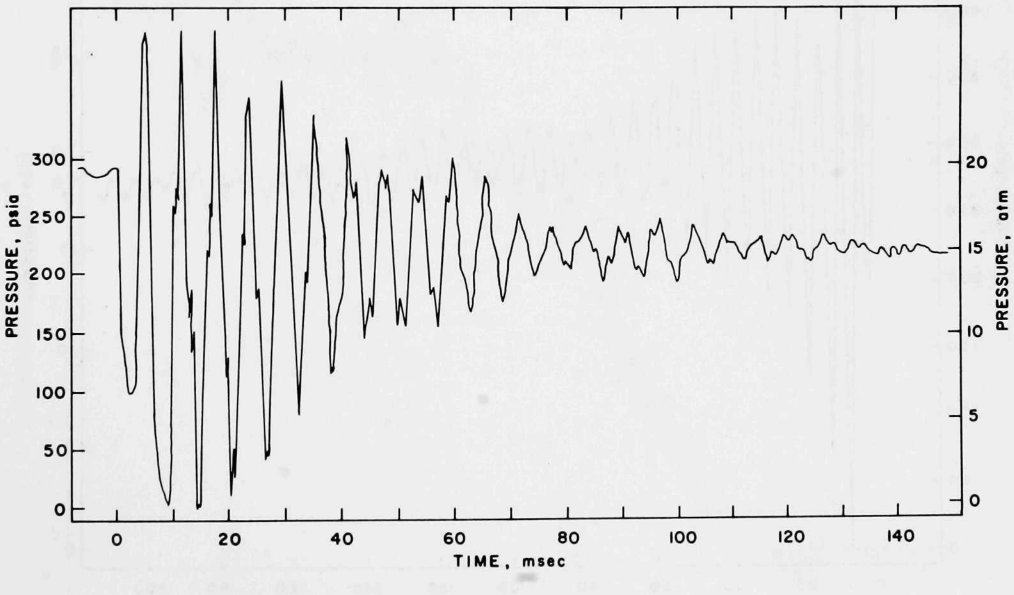

Fig. C.26. P_{14} Signal at the Initiation of Test 1. ANL Neg. No. 900-5038.

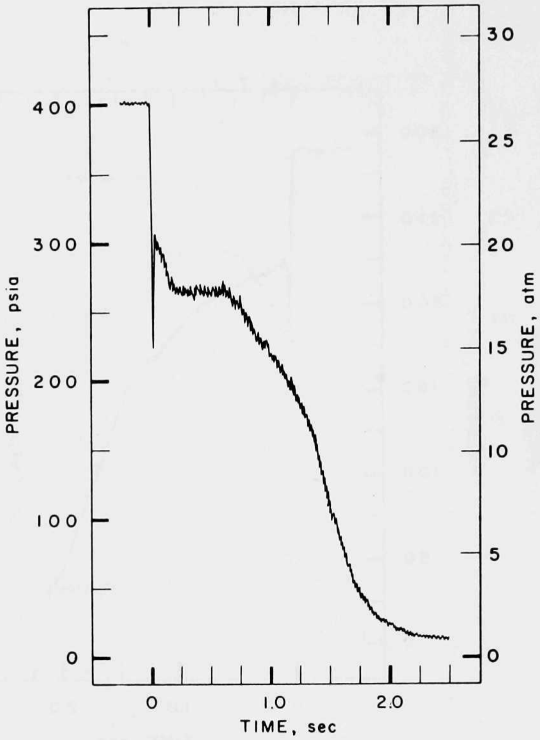

Fig. C.27

Overall P_{14} Signal in Test 2. ANL Neg. No. 900-5008 Rev. 1.

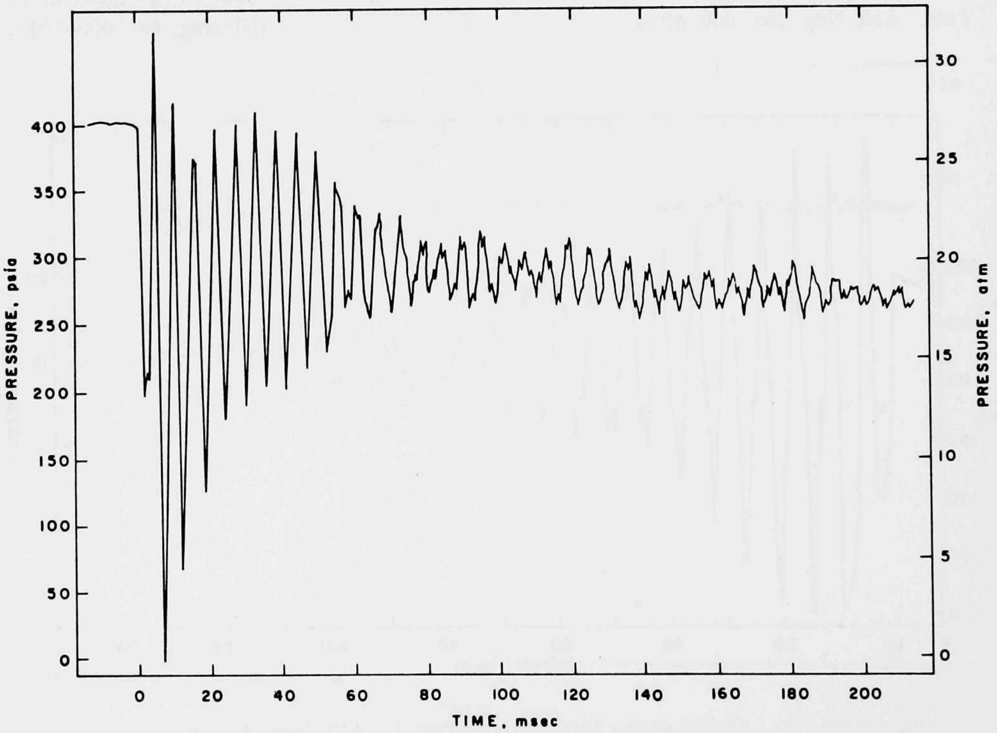

Fig. C.28. P_{14} Signal at the Initiation of Test 2. ANL Neg. No. 900-5039.

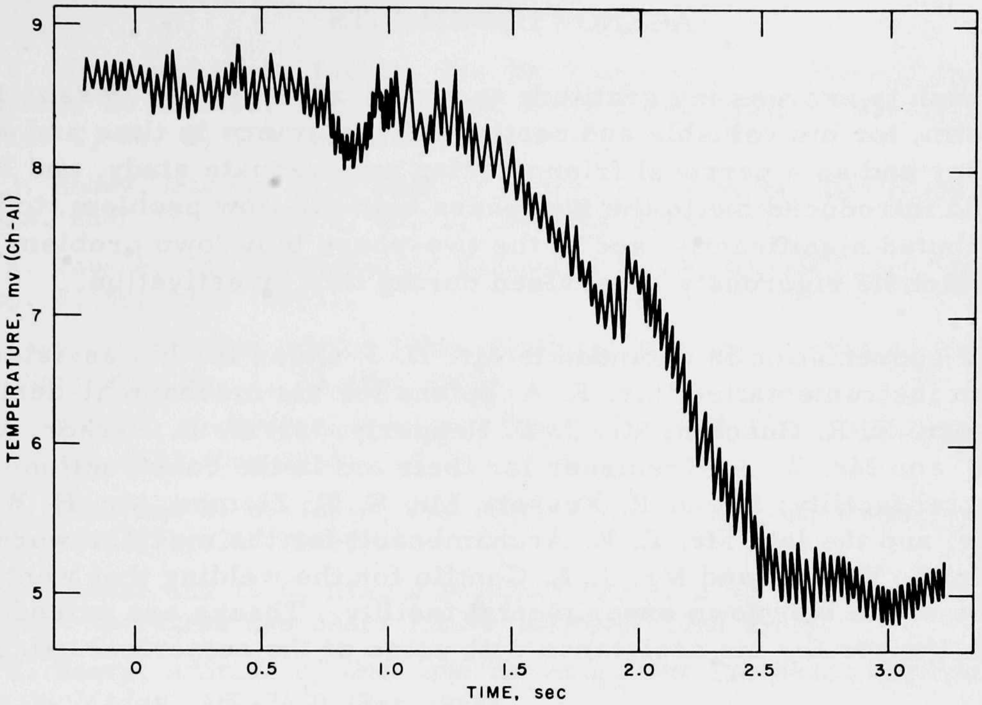

Fig. C.29. Overall T_8 Signal in Test 1. ANL Neg. No. 900-5086.

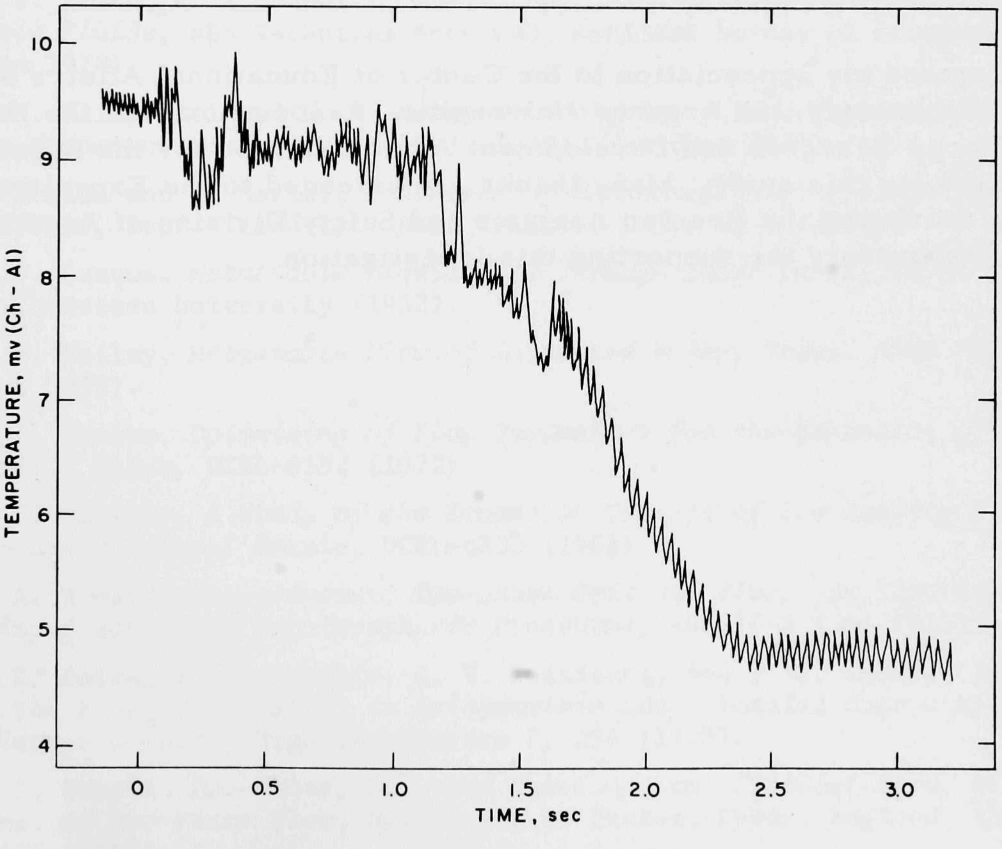

Fig. C.30. Overall T_7 Signal in Test 2. ANL Neg. No. 900-5098.

ACKNOWLEDGMENTS

I wish to express my gratitude to my co-advisors, Professor D. E. Wollersheim, for his valuable and continuous assistance in time and knowledge as a teacher and as a personal friend during my graduate study, and Dr. R. E. Henry, who introduced me to the two-phase critical-flow problem, to which he has contributed significantly, and to the two-phase blowdown problem in particular, which he rigorously supervised during this investigation.

My appreciation is extended to Mr. D. J. Quinn for his assistance with the system instrumentation; Mr. E. A. Spleha for his mechanical-design assistance; Mr. E. R. Gunchin, Mr. J. T. Hepperly, Mr. N. E. Parker, Mr. L. M. McUmber, and Mr. W. A. Kremsner for their aid in the construction of the experimental facility; Mr. J. R. Fessett, Mr. E. T. Ziemba, Mr. H. W. Laschober, and the late Mr. E. K. Archambeault for the machine work; and also to Mr. L. E. Cole and Mr. J. E. Cantlin for the welding that went into the fabrication of the blowdown experimental facility. Thanks are extended to Mr. G. M. Hauser for his assistance with some of the numerical calculations.

Acknowledgment is extended to Dr. S. R. Bull, Director of Graduate Studies in Nuclear Engineering, University of Missouri-Columbia, for providing me with my initial introduction to Argonne National Laboratory where this investigation was performed.

I extend my appreciation to the Center of Educational Affairs of Argonne National Laboratory, the Argonne Universities Association, and the United States Energy Research and Development Administration for the fellowship awarded me for this study. Many thanks are extended to the Experiment Modeling Section of the Reactor Analysis and Safety Division of Argonne National Laboratory for supporting this investigation.

REFERENCES

1. R. E. Henry and H. K. Fauske, *The Two Phase Critical Flow of One Component Mixtures in Nozzles, Orifices, and Short Tubes,* ASME J. Heat Transfer *93,* Series C, No. 2, 179 (May 1971).
2. F. J. Moody, *Maximum Flow Rate of a Single Component, Two Phase Mixture,* Trans. ASME *87,* Series C, No. 1, 134 (Feb 1965).
3. H. K. Fauske, *The Discharge of Saturated Water Through Tubes,* Chem. Engr. Symp. *61*(59), 210 (1965).
4. S. Levy, *Prediction of Two Phase Critical Flow Rate,* ASME J. Heat Transfer *87,* Series C, No. 1, 53 (Feb 1965).
5. H. K. Fauske, *Contribution to the Theory of Two-phase, One-component Critical Flow,* ANL-6633 (Oct 1962).
6. P. C. Chen and H. S. Isbin, *Two Phase Flow Through Apertures,* Energia Nucleare *13*(7), 347 (1966).
7. H. K. Fauske and T. C. Min, *A Study of the Flow of Saturated Freon-11 through Apertures and Short Tubes,* ANL-6667 (Jan 1963).
8. R. E. Henry, *A Study of One- and Two-component Two-phase Critical Flows at Low Qualities,* ANL-7430 (Mar 1968).
9. M. R. Prisco, *The Nonequilibrium, Two-phase Critical Discharge of Nearly Saturated and Subcooled CCl_3F through Short Tubes,* ANL-75-9 (Feb 1975).
10. R. V. Smith, K. R. Randall, and R. Epp, *Critical Two Phase Flow for Cryogenic Fluids,* NBS Technical Note 633, National Bureau of Standards (Jan 1973).
11. W. J. Klingebiel and R. W. Moulton, *Analysis of Flow Choking of Two Phase, One Component Mixtures,* AIChE J. *17*(2), 383 (Mar 1971).
12. H. Uchida and H. Nariai, *Discharge of Saturated Water Through Pipes and Orifices,* Proc. Third Int. Heat Transfer Conf. *5,* 1 (1966).
13. P. F. Pasqua, *Metastable Liquid Flow Through Short Tubes,* Ph.D. thesis, Northwestern University (1952).
14. J. F. Bailey, *Metastable Flow of Saturated Water,* Trans. ASME *73,* 1109 (Nov 1951).
15. K. F. Neusen, *Optimizing of Flow Parameters for the Expansion of Very Low Quality Steam,* UCRL-6152 (1972).
16. D. J. Maneely, *A Study of the Expansion Process of Low Quality Steam Through a DeLaval Nozzle,* UCRL-6230 (1962).
17. P. A. Howard, *One-component Two-phase Critical Flow: An Experimental Study Using Freon-11 at Subatmospheric Pressures,* ANL-75-8 (Jan 1975).
18. M. E. Deich, V. S. Danilin, G. V. Tsiklauri, and V. K. Shanin, *Investigation of the Flow of Wet Steam in Axisymmetric Laval Nozzles Over a Wide Range of Moisture Content,* High Temperature *7,* 294 (1969).
19. H. K. Fauske, *Two-Phase, Two- and One-Component Critical Flow,* Proc. of Symp. on Two-Phase Flow, University of Exeter, Devon, England, Vol. 3, SG101 (1965).

20. H. S. Isbin, J. E. Moy, and A. J. R. Cruz, *Two-Phase, Steam-Water Critical Flow*, AIChE J. *3*, 361 (1957).

21. D. W. Faletti and R. W. Moulton, *Two-Phase Critical Flow of Steam-Water Mixtures*, AIChE J. *9*, 247 (1963).

22. F. R. Zaloudek, *The Low-Pressure Critical Discharge of Steam-Water Mixtures from Pipes*, HW-68936 (1961).

23. F. R. Zaloudek, *The Critical Flow of Hot Water Through Short Tubes*, HW-77594 (1963).

24. F. R. Zaloudek, *Steam-Water Critical Flow from High Pressure Systems*, Interim Report HW-80535 (1964).

25. F. R. Zaloudek, *The Low Pressure Critical Discharge of Steam-Water Mixtures from Pipe Elbows and Tees*, BNWL-34 (1965).

26. E. S. Startman, V. E. Schrock, K. F. Neusen, and D. J. Maneely, *Expansion of a Very Low Quality Two-Phase Fluid Through a Convergent-Divergent Nozzle*, Trans. ASME, J. of Basic Engineering, Series D *86*(2), 247 (June 1964).

27. J. E. Cruver, *Metastable Critical Flow of Steam-Water Mixtures*, Ph.D. thesis, University of Washington (1963).

28. W. J. Klingebiel, *Critical Flow Slip Ratios of Steam-Water Mixtures*, Ph.D. thesis, University of Washington (1964).

29. J. C. Hesson and R. E. Peck, *Flow of Two-Phase Carbon Dioxide Through Orifices*, AIChE J. *4*, 207 (1958).

30. J. C. Hesson, *Flow of Two-Phase Carbon Dioxide Through Orifices*, Ph.D. thesis, Illinois Institute of Technology (1957).

31. H. M. Campbell and T. J. Overcamp, *Critical Flow Rate of Two-Phase Nitrogen*, NASA TM X-53492 (1966).

32. F. W. Bonnet, *Critical Two-Phase Flow of Nitrogen and Oxygen Through Orifices*, Adv. Cryog. Eng. *12*, 427 (1966).

33. D. J. Ryley and G. J. Parker, *Two-Phase Critical Flow Through Suction Slots in Low Pressure Steam Turbine Blades*, J. Mech. Eng. Sci. *10*, 337 (1968).

34. U. Simon, *Blowdown Flow Rates of Initially Saturated Water*, European Two Phase Flow Meeting in Riso, Denmark, June 1971.

35. T. A. Harris, *Analysis of the Coolant Expansion Due to a Loss of Coolant Accident in a Pressurized Water, Nuclear Power Plant*, Nucl. Sci. Eng. *6*, 238 (1959).

36. M. W. Benjamin and J. G. Miller, *The Flow of Flashing Mixture of Water and Steam Through Pipes*, Trans. ASME *64*, 657 (1942).

37. W. F. Allen, *Flow of a Flashing Mixture of Water and Steam Through Pipes and Valves*, Trans. ASME *73*, 257 (1951).

38. A. N. Nahavandi, *A Digital Computer Analysis of Loss of Coolant Accident for a Multicircuit Core Nuclear Power Plant*, Nucl. Sci. Eng. *14*, 272 (1962).

39. S. G. Margolis and J. A. Redfield, *FLASH: A Program for Digital Simulation of the Loss of Coolant Accident*, WAPD-TM-534 (1966).

40. K. V. Moore and H. W. Rettig, *RELAP2-A Digital Program for Reactor Blowdown and Power Excursion Analysis*, IDO-17263 (1968).

41. F. J. Moody, *Maximum Two Phase Vessel Blowdown from Pipes*, ASME J. Heat Transfer *88*, Series C, 285 (Aug 1966).

42. H. Goulding, *An Analytical-Experimental Comparison of the Initial Transient Response of High Enthalpy Water During Decompression*, ANS Meeting, Toronto, Canada (9 June 1968).

43. F. J. Moody, *Liquid-Vapor Action in a Vessel During Blowdown*, ASME J. Eng. Power *91*, Series A, No. 1, 53 (Jan 1969).

44. A. N. Nahavandi, *The Loss of Coolant Accident Analysis in Pressurized Water Reactors*, Nucl. Sci. Eng. *36*, 159 (1969).

45. N. P. Wilburn, *Void Fraction Profile in a Nuclear Reactor Vessel During Coolant Blowdown*, BNWL-1295 (Apr 1970).

46. J. A. Redfield, J. H. Murphy, and V. C. Davis, *FLASH-2: A FORTRAN IV Program for the Digital Simulation of a Multinode Reactor Plant During Loss of Coolant*, WAPD-TM-666 (Apr 1967).

47. *Nuclear Safety Quarterly Report for July, August, September, and October 1967*, BNWL-754 (June 1968).

48. *Nuclear Safety Quarterly Report for August, September, and October 1968*, BNWL-926 (Dec 1968).

49. *Nuclear Safety Quarterly Report for November, December, 1968, January 1969*, BNWL-1009 (Mar 1969).

50. G. Hoppner, *Experimental Study of Phenomena Affecting the Loss of Coolant Accident*, Ph.D. thesis, University of California at Berkeley (1971).

51. S. Banerjee, W. T. Hancox, R. B. Jeffries, and M. T. Sulatisky, *Transient Two Phase Flow and Heat Transfer During Blowdown from Subcooled Conditions with Heat Addition*, 15th National Heat Transfer Conf., ASME (Aug 1975).

52. T. R. Wilson, O. M. Hauge, and G. B. Matheney, *Feasibility and Conceptual Design for the STEP Loss of Coolant Facility*, IDO-16833 (1963).

53. S. G. Forbes and T. R. Wilson, *Loss of Coolant Accident Investigations*, IDO-17272 (1968).

54. S. G. Forbes, T. R. Wilson, and G. F. Brockett, *Semiscale Blowdown and ECC*, IDO-17258C (1969).

55. S. G. Forbes, T. R. Wilson, and K. A. Dietz, *Quarterly Technical Report LOFT Program Office*, IDO-17303 (1970).

56. G. F. Brockett, H. D. Curet, and H. W. Heiselmann, *Experimental Investigations of Reactor System Blowdown*, IN-1348 (1970).

57. J. C. Haire and G. F. Brockett, *Technical Assistance in Reactor Safety Analysis*, IN-1383 (1970).

58. D. J. Olsen, C. M. Moser, and H. W. Heiselmann, *Semiscale Blowdown and Emergency Core Cooling Project Test Report--Tests 824 and 825*, IN-1481 (June 1971).

59. D. J. Olsen and J. F. Whitbeck, *Semiscale Blowdown and Emergency Core Cooling Project Test Report--Tests 822 and 823*, IN-1393 (Oct 1970).

60. D. J. Olsen, *Semiscale Blowdown and Emergency Core Cooling Project Test Report--Tests 848, 849, and 850,* ANCR-1036 (June 1972).

61. T. E. Curry, *Semiscale Project Test Data Report--Test 851,* ANCR-1065 (July 1972).

62. C. H. Robbins, *Test of a Full Scale 1/48 Segment of the Humboldt Bay Pressure Suppression Containment,* GEAP-3596 (Nov 1960).

63. *Preliminary Hazards Summary Report, Bodega Bay Atomic Park Unit No. 1,* Pacific Gas and Electric Co. (Dec 1962).

64. H. Fugie, A. Yamanauchi, N. Sagawa, H. Ogasawara, and T. Tagami, *Studies for Safety Analyses of Loss of Coolant Accidents in Light Water Reactors,* J. Japan Soc. Mech. Eng. *69*(571), 1068 (Aug 1966).

65. T. Tagami, *Interim Report on Safety Assessments and Facilities Establishment Project in Japan for Period Ending June 1965 (No. 1),* Interim Report, Bureau of Atomic Energy, Japan (Feb 28, 1966).

66. J. P. Etheimer, *Beitrage zu den Problemen der Heibwasserrakete,* Mitt. Forsch. Inst. Physik Strahlantriebe *20,* Stuttgart (1959).

67. E. Ungerer, *Uber den Heibwasserstrahlantrieb,* Duetsche Luft-und Raumfahrt, Forschungsbericht 66-43 (DVL-Bericht Nr. 517) (1966).

68. R. Carzaniga, *Preliminary Experiments on the Blowdown of a Pressure Vessel,* CREST Meeting, Frankfurt, Germany (June 1969).

69. R. F. White, *Results of Two Phase Blowdown Experiments Part I: Straight Tube Test Section,* AECL-3664 (1970).

70. R. T. Allemann, A. J. McElfresh, A. S. Neuls, W. C. Townsend, N. P. Wilburn, and M. E. Witherspoon, *Experimental High Enthalpy Water Blowdown from a Simple Vessel Through a Bottom Outlet,* BNWL-1411 (June 1970).

71. E. V. Gallagher, *Water Decompression Experiments and Analysis for Blowdown of Nuclear Reactors,* IITRI-578-P-21-39 (July 1970).

72. J. Kober, G. Leistner, and M. Zimmermann, *Untersuchungen zur Simulation der Druckentlastung von Siedewasserreaktoren, Vorversuche mit einem Modellbehalter aus Glas,* Battelle Institut, Germany (Aug 1968).

73. G. Leistner, B. Rudiger, C. Sauberlich, K. Stein, and M. Zimmermann, *Untersuchungen zur Simulation der Druckentlastung von Siedewasserreaktoren, Vorversuche mit einem Glasbehalter,* Battelle Institut, Germany (Feb 1969).

74. G. Leistner and M. Zimmermann, *Untersuchungen zur Simulation der Druckentlastung von Siedewassereaktoren, Beschreibung der Hauptversuchsanlage,* Battelle Institut, Germany (Feb 1969).

75. M. Zimmermann, K. Stein, and B. Rudiger, *Der Grobbehalterprufstand zur Simulation der Druckentlastung wassergekuhlter Reaktoren,* Battelle Institut, Germany (Aug 1970).

76. J. Koehn, C. Sauberlich, R. Skoutajan, and B. Rudiger, *Untersuchung der Vorgange bei der Druckentlastung wassergekuhlter Reaktoren,* Battelle Institut, Germany (June 1971).

77. T. Kanzleiter, J. Koehn, C. Sauberlich, K. Stein, and M. Zimmermann, *Untersuchung der Vorgange bei der Druckentlastung wassergekuhlter Reaktoren,* 8. Bericht, Band I, Battelle Institut, Germany (July 1971).

78. W. Christ, T. Kanzleiter, J. Koehn, C. Sauberlich, K. Stein, and M. Zimmermann, *Untersuchung der Vorgange bei der Druckentlastung wassergekuhlter Reaktoren,* 8. Bericht, Band II, Battelle Institut, Germany (July 1971).

79. R. T. Allemann, A. J. McElfresh, A. S. Neuls, W. C. Townsend, N. P. Wilburn, and M. E. Witherspoon, *Coolant Blowdown Studies of a Reactor Simulator Vessel Containing a Perforated Sieve Plate Separator,* BNWL-1463 (Feb 1971).

80. B. Rudiger, *Experimental Blowdown Studies of a Reactor Simulator Vessel Containing Simplified Internals,* CREST Meeting on Emergency Core Cooling for Light Water Reactors, Munich, Germany, Vol. 1 (18 Oct 1972).

81. H. Shimamune, M. Shibe, H. Adachi, K. Namatame, and M. Sobajima, *A Present Status of Rosa Program,* CREST Meeting on Emergency Core Cooling for Light Water Reactors, Munich, Germany, Vol. 1 (18 Oct 1972).

82. M. Tokumitsu, *Full Scale Safety Experiments of FUGEN,* CREST Meeting on Emergency Core Cooling for Light Water Reactors, Munich, Germany, Vol. 1 (18 Oct 1972).

83. Bettis Flask Experiment, Aerojet Nuclear Co., private communication.

84. D. K. Choi, *Prediction of Reactor Coolant Blowdown by Similitude,* Ph.D. thesis, Iowa State University, University Microfilms, Ann Arbor, Mich. No. 74-525 (1973).

85. J. C. M. Leung, *Occurrence of Critical Heat Flux During Blowdown with Flow Reversal,* M.S. thesis, Northwestern University (1975).

86. A. H. Shapiro, *The Dynamics and Thermodynamics of Compressible Fluid Flow,* Ronald Press, Vol. 1, p. 100 (1953).

87. J. E. Cruver and R. W. Moulton, *Critical Flow of Liquid-Vapor Mixtures,* AIChE J. *13*(1), 53 (Jan 1967).

88. M. Giot and A. Fritte, *Two Phase, Two and One Component, Critical Flows with the Variable Slip Model,* Prog. Heat Mass Transfer *6,* 651 (1972).

89. H. Adachi, *High Speed Two Phase Flow (I), Theory of Axial Change of Flow Parameters and Critical Flow,* Heat Transfer, Japanese Research *3*(4), 75 (Oct-Dec 1974).

90. H. Adachi and N. Yamamoto, *High Speed Two Phase Flow (II), Flashing Flow Through a Convergent-Divergent Nozzle,* Heat Transfer, Japanese Research *3*(4), 89 (Oct-Dec 1974).

91. R. F. Tangren, C. H. Dodge, and H. S. Seifert, *Compressibility Effects in Two Phase Flow,* J. Appl. Phys. *20,* 736 (1949).

92. J. A. Vogrin, *An Experimental Investigation of Two-phase, Two-component Flow in a Horizontal Converging-Diverging Nozzle,* ANL-6754 (July 1963).

93. J. A. Perry, *Critical Flow Through Sharp Edged Orifices,* Trans. ASME *71,* 757 (1949).

94. B. T. Arnberg, *Review of Critical Flowmeters for Gas Flow Measurements,* Trans. ASME, J. Basic Eng., Series D *84*(4), 447 (Dec 1962).

95. A. T. Olsen, *Nozzle Discharge Coefficients-Compressible Flow,* ASME Paper No. 73-WA/FE-7 (1973).

96. R. E. Henry, *Two Phase Critical Discharge of Initially Saturated and Sub-Cooled Liquid,* Nucl. Sci. Eng. *41*, 336 (1970).

97. J. E. Shigley, *Mechanical Engineering Design*, McGraw-Hill Book Co., New York (1963), p. 42.

98. Lord Rayleigh, *Pressure Due to Collapse of Bubbles*, Phil. Mag. *34*, 94 (1917).

99. M. S. Plesset and J. A. Zwich, *The Growth of Vapor Bubbles in Superheated Liquids*, J. Appl. Phys. *25*, 493 (1954).

100. L. E. Scriven, *On the Dynamics of Phase Growth*, Chem. Eng. Sci. *10*, 1 (1959).

101. R. Cole and W. M. Rohsenow, *Correlation of Bubble Departure Diameters for Boiling of Saturated Liquids*, Chem. Eng. Prog. Sym. Series, AIChE *65*, 92 (1969).

102. S. G. Bankoff, "Simulation in Boiling Heat Transfer," *Cocurrent Gas-Liquid Flow*, Plenum Press, p. 283 (1969).

103. S. G. Bankoff, *Ebullition from Solid Surfaces in the Absence of a Pre-existing Gaseous Phase*, Trans. ASME *79*, 735 (1957).

104. F. Kreith, *Principles of Heat Transfer*, International Textbook Co., Second Edition, Fourth Printing, p. 563 (July 1968).

105. O. C. Jones and N. Zuber, *Statistical Methods for Measurement and Analysis of Two Phase Flow*, Proc. 5th Int. Heat Transfer Conf., Vol. 4, p. 200, Tokyo, Japan (3 Sept 1974).

106. N. A. Radovcich and R. Moissis, *The Transition from Two Phase Bubble Flow to Slug Flow*, MIT Report 7-7673-22 (1962).

107. M. A. Grolmes and H. K. Fauske, *Propagation Characteristics of Compression and Rarefaction Pressure Pulses in One Component, Vapor-Liquid Mixtures*, Nucl. Eng. Design *11*(1), 137 (Feb 1970).

108. A. H. Gibson, *Hydraulics and Its Applications*, Van Nostrand Book Co., Fourth Edition, p. 93 (1930).

ARGONNE NATIONAL LAB WEST
3 4444 00024131 5